

An Investigation of Relaxor Ferromagnets

A thesis submitted in part fulfilment of the requirements for the degree of

Doctor of Philosophy in Inorganic Chemistry

at the University of Oxford

Chun Mann Chin

St. Catherine's College

University of Oxford

September 2019

An Investigation of Relaxor Ferromagnets

A thesis submitted for the degree of

Doctor of Philosophy in Inorganic Chemistry

Chun Mann Chin September 2019 St. Catherine's College

Abstract

Q–dependent diffuse scattering was observed at low angles in a neutron diffraction experiment performed on the relaxor ferromagnet $La_3Ni_2SbO_9$ using a spin–polarised beam. The nuclear component could be modelled using direct Monte–Carlo methods if it was assumed that short (~5.5 Å) Sb–Sb contacts were energetically disfavoured. The magnetic component of the diffuse scattering at 110 K (T_C = 108 K) was analysed using both direct and reverse Monte–Carlo techniques. When antiferromagnetic nearest–neighbour coupling was assumed to be dominant in this perovskite, second neighbour coupling was found to be weak but non–zero with third–neighbour coupling being negligible. The short–range structural and magnetic orderings were found to have correlation lengths of 15 and 9 Å, respectively.

The consequences of replacing d^{10} Sb^{5+} by d^0 pentavalent cations were investigated; all the compounds reported are isostructural with $La_3Ni_2SbO_9$. $La_3Ni_2TaO_9$ was found to be a relaxor ferromagnet but $La_3Ni_2NbO_9$ behaved as a spin glass below 35 K. Solid solutions $La_3Ni_2Sb_xTa_yNb_{1-x-y}O_9$ were synthesised and characterised. It was again shown that the relaxor behaviour is incompatible with the presence of Nb^{5+} in the system. In contrast, doping $La_3Ni_2B'O_9$ (*B*' = Sb, Ta or Nb) with Cu^{2+} cations was found to increase T_C and the bulk magnetisation. For example, $La_3Ni_{1.75}Cu_{0.25}NbO_9$ exhibits ferrimagnetic behaviour below ~90 K with the development of long–range G–type magnetic ordering. It is proposed that relaxor regions and long–range ordered regions coexist in this system.

The sensitivity of cation ordering, and hence magnetic behaviour, to the charge difference between Ni^{2+} and the diamagnetic six–coordinate cation was studied by replacing Sb^{5+} by Te^{6+} or W^{6+}. Electron microscopy revealed a significant level of cation disorder in a severely–twinned sample of $SrLa_2Ni_2TeO_9$; spin–glass and antiferromagnetic phases coexist below 35 K. The Ni^{2+} cations in $CaLn_2Ni_2WO_9$ (*Ln* = La, Pr or Nd) form a spin glass, although the behaviour of each composition reflects the magnetic properties of Ln^{3+}.

Acknowledgment

I would like to express my greatest gratitude towards Professor Peter Battle. Not only has he been a fantastic supervisor throughout my DPhil, his mentorship has been second to none. All the academic consultations with him have been inspiring. He has also enlightened me as a person with his enthusiasm and wisdom. I appreciate his guidance and patience throughout my eight years at Oxford as they have been nothing but invaluable to me. I thank Professor Andrew Goodwin and Professor Joke Hadermann and her group members for their expertise on diffuse scattering and electron microscopy, respectively. I am extremely grateful to Dr Maxim Avdeev for the neutron powder diffraction data collected at ANSTO. Thanks to Professor Steve Blundell and his group members for conducting muon-spin rotation experiments. I would also like to thank Dr Emily Hunter for the valued discussions during her time at the Battle group. Contributions from Yawei and Diming have also been remarkable. I was also overwhelmed by the support of the Croucher Foundation for granting me the University of Oxford Croucher Scholarship to fund my DPhil studies and the opportunities to broaden my horizons.

I would like to thank all my students who have made my teaching experience as a college lecturer at St. Catherine's College very enjoyable. I would like to thank Dr Simon Cassidy, Dr Josh Hill and Dr Midori Amano Patino for their advice and encouragement, especially when I was writing up my thesis. Outside of laboratory, the life experiences shared by Gary have been marvellous. I would like to thank Alice for always brightening up my day with her laughter. My brother Bowen has been the best companion, not only for my visits to football stadia, but also through my ups and downs. I am, of course, indebted to my parents; a blessing for which I can never thank enough. They have always been there when I was most in need. Their support and love have been the best treasure of mine.

Table of Content

Chapter 1: Introduction 1

1.1 Prologue 1

1.2 Structural Chemistry of Perovskites 2

1.3 Magnetic Properties of Perovskites 8

1.4 Overview of the thesis 21

Chapter 2: Experimental techniques 23

2.1 Synthetic routes to mixed–metal oxides 23

2.2 Crystallography 25

2.3 Diffraction 26

2.4 Diffractometers 35

2.5 Rietveld Analysis 40

2.6 Micro Structural Determinations: Electron Microscopy 44

2.7 Diffuse scattering 46

2.8 Analysis of diffuse scattering 48

2.9 Muon and muon–spin rotation (μSR) 49

2.10 SQUID magnetometry 51

Chapter 3: Analysis of the short–range cation ordering in $La_3Ni_2SbO_9$ 55

3.1 Introduction 55

3.2 Experimental 58

3.3 Results 59

3.4 Discussion 80

3.5 Conclusion 83

Chapter 4: Comparative study of the magnetic properties of $La_3Ni_2B'O_9$ (*B*' = Sb, Ta or Nb) 85

4.1 Introduction 85

4.2 Experimental 86

4.3 Results 88

4.4 Discussion 106

4.5 Conclusion 111

Chapter 5: The studies of the solid solutions of $La_3Ni_2Sb_xTa_yNb_{1-x-y}O_9$ 112

5.1 Introduction 112

5.2 Experimental 113
5.3 Results 115
5.4 Discussion 135
5.5 Conclusion 139
Chapter 6: An investigation of Cu–doped perovskites 140
6.1 Introduction 140
6.2 Experimental 141
6.3 Results 143
6.4 Discussion 157
6.5 Conclusion 160
Chapter 7: Structural chemistry and magnetic properties of $SrLa_2Ni_2TeO_9$ 162
7.1 Introduction 162
7.2 Experimental 162
7.3 Results 164
7.4 Discussion 175
7.5 Conclusion 178
Chapter 8: A study of Ca*Ln*$_2$Ni$_2$WO$_9$ (*Ln* = La, Pr or Nd) 180
8.1 Introduction 180
8.2 Experimental 181
8.3 Results 182
8.4 Discussion 196
8.5 Conclusion 199
Chapter 9: Conclusion 200
Bibliography 203

Appendices

Appendix 1: Supporting information for Chapter 3 i
Appendix 2: Supporting information for Chapter 4 v
Appendix 3: Supporting information for Chapter 5 xi
Appendix 4: Supporting information for Chapter 6 xxii
Appendix 5: Supporting information for Chapter 7 xxxiv
Appendix 6: Supporting information for Chapter 8 xli

Chapter 1: Introduction

1.1 Prologue

Research into materials which adopt perovskite–related structures has grown markedly in recent decades because of their extensive range of physical properties. For example, the light–harvesting properties demonstrated by some hybrid organic–inorganic perovskites such as $CH_3NH_3PbI_3$[1] and $(NH_2)_2CHPbI_3$[2] have led to their emergence as potential candidates for photovoltaics, and hence solar–cell materials. Research groups in this field have devoted their efforts to designing environment–friendly perovskites of high efficiency and low cost[3-5]. Other applications should not be overlooked. The anion–deficient perovskite $YBa_2Cu_3O_{7-\delta}$ was found to be a high–temperature superconductor with a transition temperature above 77 K, the boiling point of liquid nitrogen[6]. This finding came as a surprise as it defied the Bardeen–Cooper–Schrieffer (BCS) theory that predicts the transition temperature should not exceed ~40 K[7, 8]. In $La_xA_{1-x}MnO_3$, where *A* is a divalent cation with x ~0.3, magnetoresistance properties were observed[9-11]. Magnetoresistance is when the conductivity of a ferromagnetic material increases in an applied magnetic field. It is believed that this phenomenon is related to the presence of manganese cations of mixed valency. Vasala and Karppinen recently reviewed the magnetic and dielectric properties of perovskites[12], listing numerous perovskites as examples of ferromagnets or ferroelectrics. Materials that are both ferromagnetic and ferroelectric are known as multiferroics; this behaviour is exemplified by Pb_2FeTiO_6 at room temperature[13]. It is not surprising that the chemical composition of a functional material usually dictates the physical properties. However, the structural features can sometimes be a decisive factor in determining the magnetic nature of the material. This thesis will describe the synthesis and characterisation

of new magnetic perovskites. In order to set the scene, the structural chemistry and magnetic properties of the existing members of this family of compounds will be reviewed.

1.2 Structural Chemistry of Perovskites

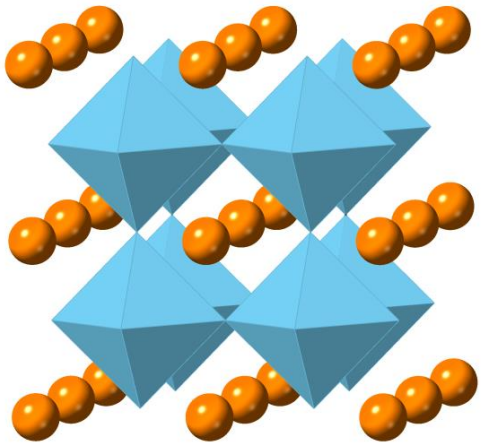


Figure 1.1. The cubic structure of $SrTiO_3$[14]. The orange spheres represent the Sr^{2+} cation and the TiO_6 octahedra are shown in sky blue with the oxide anion omitted.

Perovskites belong to a family of materials in which the composition generally has the formula ABO_3. In a simple cubic cell, the *A*–site cation is coordinated by 12 anions at the vertices of a cuboctahedron whereas the geometry around the *B* site is octahedral. Each anion is surrounded by four *A* cations and two *B* cations. In this description, the *A*–site cation sits in the centre of a cube with eight corner–sharing BO_6 octahedra at the vertices. Figure 1.1 shows the structure of a simple cubic perovskite, $SrTiO_3$[14]. Another way of visualising the structure is to have the *B*–site cation occupying all the octahedral holes formed solely by oxide ions in a pseudo–cubic closed packed array comprised of the oxides anions and the *A*–site cations. The structure can accommodate a wide range of elements and consequently it can have a large range of chemical compositions. The *A*–site cation is usually a large alkaline earth or lanthanide cation, although examples are known in which the *A* site cation is an organic ion instead[15, 16]. In these hybrid perovskites the anion sites are usually occupied by relatively large halide anions. The oxide anions can

also be replaced by a hydride ion via reduction; $SrV_{1-x}Ti_xO_{1.5}H_{1.5}$ was a product of a reaction between $SrV_{1-x}Ti_xO_3$ with CaH_2[17]. The *B* site is usually occupied by *p*– or *d*–block elements and the identity of the *B* site cation usually governs the physical properties of the material. *s*–block elements, for example Ca, have been observed to occupy the octahedral hole in some cases[18-20].

1.2.1 Octahedral Tilting

In a perovskite a deviation from cubic symmetry can be caused by octahedral tilting. This originates from differences in the ionic radii of the *A*– and *B*– site cations, causing the octahedra in the crystal to tilt to compensate for the difference in size so as to maintain the stability of the structure. Goldschmidt[21] proposed a dimensionless parameter called the tolerance factor, *t.f.*, as a means to predict whether the octahedron of the perovskite will tilt. The tolerance factor can be expressed as follow:

$$t.f. = \frac{r_A + r_X}{\sqrt{2}(r_B + r_X)} \qquad \text{Equation 1.1}$$

where r_A and r_B are the ionic radii of the *A* and *B* site cation respectively and r_X is the ionic radius of the anion. An ideal cubic perovskite will result in *t.f.* = 1. If the geometric ratio lies in the range of $0.8 \leq t.f. \leq 1$, the perovskite can usually be stabilised by tilting of the octahedra. Alternative structures are usually adopted by the materials whose *t.f.* lies outside this particular range.

Glazer suggested the use of a notation system to classify the rotation of the octahedra[22]. The system contains two parameters. The first parameter is a set of three letters which specify the magnitude of the tilts about the Cartesian axes in the order [100], [010] and [001]. The use of the same letter represents an equal tilting in two or three directions. The second parameter is a superscript denoting the direction of tilting of a particular layer

compared to the adjacent one. A positive sign indicates the rotation is in phase while a negative sign suggests that the rotation is out of phase. The number zero is used if no rotation occurs about an axis. Successive octahedra in directions perpendicular to a specific axis must have opposite tilts about that axis. However, such a constraint is absent for the consecutive octahedral along that specific axis.

Take $a^+b^-b^-$ as an example. The octahedra along the [100] axis rotate in the same direction whereas those along [010] and [001] axes rotate out of phase in the opposite direction. The letters indicate the magnitude of tilt is the same along the [010] and [001] axes but different from that of [100]. Overall, octahedral tilting leads to a lowering in symmetry in the unit cell.

1.2.2 Cation ordering in Perovskites

The variability of the composition of perovskites has facilitated the synthesis of many compounds with a general formula of *AA*'*BB*'O_6, which are also known as "double perovskites". The Glazer tilting system can still be applied to this type of perovskite[23]. For the tolerance factor, r_A and r_B will become the weighted average ionic radii of the ions involved in the formula. The flexibility in composition has enabled researchers to alter the constitutional elements in a perovskite when attempting to synthesise materials with particular physical properties. Moreover, different arrangements of these *A*/*A*' and/or *B*/*B*' cations within a crystal structure are now possible. As a rule of thumb, if the discrepancy between the size and/or the charge of the two cations is large, cation ordering is more likely.

There are three important types of *B*–site cation ordering, namely rock–salt, column and layered ordering[24-26]. Rock–salt ordering involves a 1:1 checkerboard ordering of *B* and *B*' cations over the octahedral sites in all three directions. The arrangement mimics the rock–

salt crystal structure. From an electrostatic point of view, rock–salt ordering is the most favourable as the BO_6 and $B'O_6$ octahedra are arranged in a fashion such that the separation between the cations with the higher charge is maximised[24], see Figure 1.2. There is an abundance of double perovskites which adopt such ordering over the *B*/*B*' sites[27-30]. Layered and columnar orderings are less common in the perovskite family. Figure 1.3 shows the *B*–site cation ordering in La_2CuSnO_6 where alternating CuO_6 and SnO_6 layers are found[31]. Given that Cu^{2+} has an electronic configuration of d^9, a Jahn–Teller distortion is expected[32, 33]. It was proposed that the difference in coordination geometries between the Sn^{4+} and Cu^{2+} cation is the driving force for the layered ordering while the small difference in charge and electronegativity suppressed the rock–salt ordering. Care must be taken when predicting the ordering in double perovskite cuprates. The importance of the electrostatic factor can outweigh the geometry requirement if the charge difference between the *B* and *B*' cation is greater than two[25]; Ba_2CuUO_6[34], for example, has a rock–salt arrangement of the *B*–site cations whereas there is a lack of long–range ordering in $SrLaCuRuO_6$[35]. Columnar ordering of Mn^{3+} and Mn^{4+} in the *ac*–plane in $La_{0.5}Ca_{0.5}MnO_3$ is stabilised by the Jahn–Teller distortion arising from the high–spin d^4 Mn^{3+} cation[36]. Such ordering is not found in $Nd_{0.5}Sr_{0.5}MnO_3$ when there is a quasi–absence of a Jahn–Teller distortion[37].

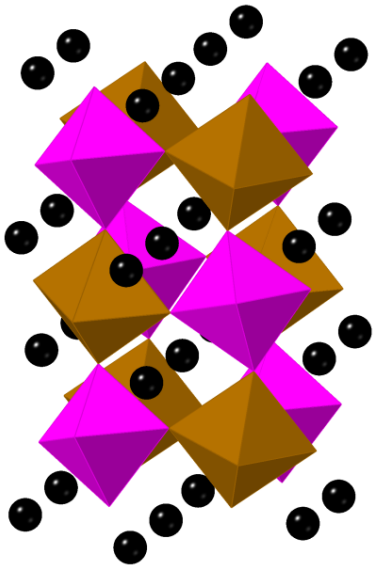


Figure 1.2. The structure of Ca_2FeMoO_6[28]. The black spheres represent the Ca^{2+} cations; the FeO_6 and MoO_6 octahedra are shown in brown and magenta, respectively. The oxide anions are omitted.

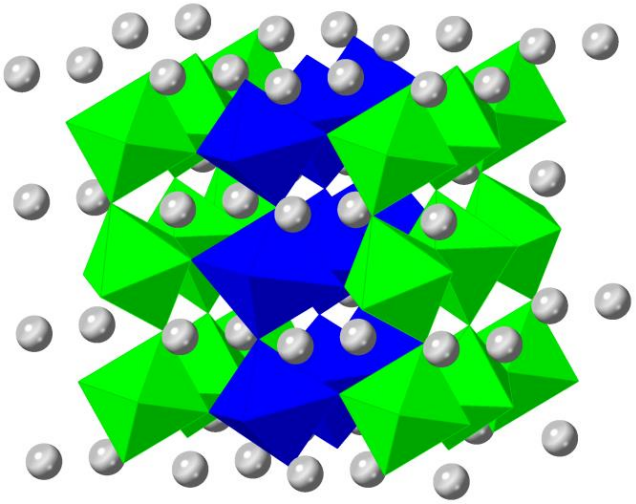


Figure 1.3. The structure of La_2CuSnO_6[31]. The light grey spheres represent the La^{3+} cations; the CuO_6 and SnO_6 octahedra are shown in blue and light green, respectively. The oxide anions are omitted.

It is interesting to note that *A*–site cation ordering is far less common than *B*–site cation ordering even though there is no shortage of perovskites with compositional variation over the *A* site[24]. One of the reasons is that the charge variation of the *A*–site cations is much smaller. However, based on the same electrostatic argument, rock–salt ordering should be more favourable if *A*–site ordering does occur. Yet, it is found that layered ordering over

the *A* site is more common. The key lies in the anion environment of an $AA'B_2O_6$ perovskite[24]. A fraction of the anions can displace from their original position to accommodate the size difference between *A* and *A*' cations only if the perovskite adopts a layered ordering over the *A* site.

Simultaneous ordering over both the *A* and *B* sites of a perovskite is unusual, with $NaLaMgWO_6$ being one of the rare examples of a doubly–ordered $AA'BB'O_6$ perovskite[38, 39]. There is a layered ordering between the Na^+ and La^{3+} cation whereas rock–salt ordering is observed over the *B* site between the divalent Mg^{2+} and the hexavalent W^{6+} cations, see Figure 1.4. Knapp suggested that a displacement of W^{6+} in the WO_6 octahedra stabilises the layered order in the *A* site because the distortions are synergistic[39].

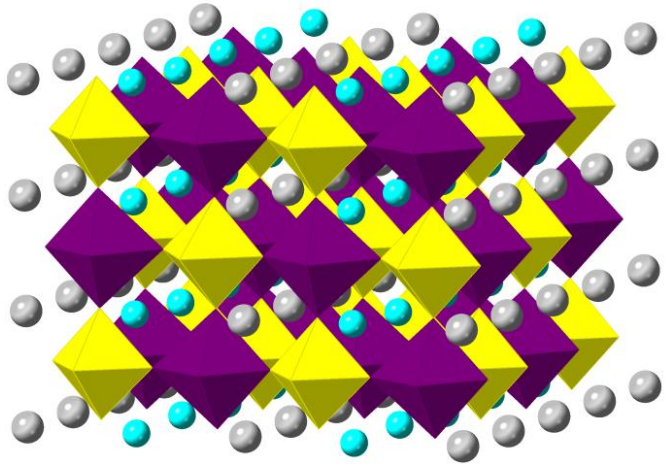


Figure 1.4. The structure of $NaLaMgWO_6$[39]. The light grey and cyan spheres represent the La^{3+} and the Na^+ cations, respectively; the MgO_6 and WO_6 octahedra are shown in purple and yellow. The oxide anions are omitted.

The flexibility of perovskite allows the *B*/*B*' ratio to deviate from unity, and consequently $A_3BB'_2O_9$ and $A_4BB'_3O_{12}$ perovskites can be formed. Judging from the stoichiometric ratio of *B*–site cations, 1:2 and 1:3 orderings are expected to occur in these perovskites. $Ba_3SrTa_2O_9$[40], $La_3LiTi_2O_9$[41] and $Sr_3Fe_2TeO_9$[42] are perovskites which demonstrate 1:2 ordering over the *B* site. $Ba_4BSb_3O_{12}$ (*B* = Li or Na) were the first examples of a 1:3

ordering in cubic perovskites[43]. $Sr_4NaSb_3O_{12}$ is an example of a monoclinic perovskite with the same ordering pattern[44]. However, a 1:1 ordering scheme is also possible for some "triple perovskites" despite their 2:1 ratio of chemical composition at the *B* site. The well–known lead–based relaxor ferroelectric $Pb_3MgNb_2O_9$ has a 1:1 positional ordering within the crystal structure and the cation distribution can be rationalised by a random–site model[45-47]. In this case, there are two crystallographically distinct octahedral sites. One of them is occupied predominately by the Nb^{5+} cation whilst the remaining Nb^{5+} and all the Mg^{2+} cations are randomly distributed in a 1:2 ratio over the other octahedral site. Another example is $La_3Ni_2SbO_9$[48], which will be discussed later in this thesis, see Chapter 3. A comparison between $Pb_3MgNb_2O_9$ and $La_3Ni_2SbO_9$ will also be presented therein.

1.3 Magnetic Properties of Perovskites

Perovskites have been the focus for many solid–state chemists because of their ability to demonstrate novel magnetic properties. In this section the basic principles of magnetism, and how the interesting and useful magnetic properties of perovskites arise, will be discussed.

1.3.1 Diamagnetism and Paramagnetism

Diamagnetism is independent of temperature and can be found in all materials, regardless of the constitutional elements present, because this phenomenon arises from the modified motion of the electrons in an applied magnetic field. Electrons orbiting around the nuclei are often considered as if they are electric currents, and therefore a magnetic moment is induced when an external magnetic field is applied. According to Lenz's law, the current induced will create a magnetic field to oppose the original inducing magnetic field. Despite its presence in all materials, the contribution from diamagnetism is normally weak enough

to be ignored and is often overshadowed by the stronger paramagnetism[49]. Therefore, the diamagnetic correction is omitted throughout this thesis.

In contrast, paramagnetism is temperature–dependent and has its origins in an assembly of unpaired electron spins present in the material. The electrons in an atom possess spin and orbital angular momenta, ***s*** and ***l*** respectively. For a multi–electron system, the spin and orbital angular momenta, ***S*** and ***L***, are the sum of the contributions from the individual electrons and they couple with each other to give a total angular momentum, ***J***.

$$\boldsymbol{J} = \boldsymbol{S} + \boldsymbol{L} \qquad \text{Equation 1.2}$$

The magnetic quantum number, m_J, can take values in the range $-J \leq m_J \leq +J$. In an applied magnetic field the occupation of the m_J states is non–random and the mean moment in the field direction is

$$\langle \mu \rangle = \sum_{m_J} g_J \mu_B m_J P(m_J) \qquad \text{Equation 1.3}$$

where $g_J = \frac{3}{2} + \frac{S(S+1)-L(L+1)}{J(J+1)}$ and is the Landé g–factor, μ_B is the Bohr magneton and $P(m_J)$ is the relative population of a given m_J state. It can then be shown[50] that $\langle \mu \rangle$ is given by

$$\langle \mu \rangle = g_J J \mu_B F(J, y) \qquad \text{Equation 1.4}$$

where

$$F(J, y) = \left(1 + \frac{1}{2J}\right) \coth\left[\left(1 + \frac{1}{2J}\right) y\right] - \left(\frac{1}{2J}\right) \coth\left(\frac{y}{2J}\right), \qquad \text{Equation 1.5}$$

$$y = \frac{J g_J \mu_B H}{k_B T}, \qquad \text{Equation 1.6}$$

H is the external magnetic field and k_B is the Boltzmann constant. $F(J,y)$ is the Brillouin function and it is plotted for different J values in Figure 1.5. For small values of y, that is at low fields and high temperatures,

$$F(J,y) = \frac{y(J+1)}{3J} \qquad \text{Equation 1.7}$$

So for a mole of atoms the molar magnetisation is

$$N_A\langle\mu\rangle = N_A g_J J \mu_B \frac{J+1}{3J}\left(J g_J \mu_B \frac{H}{k_B T}\right) \qquad \text{Equation 1.8}$$

where N_A is the Avagadro's constant. Let $M_m = N_A\langle\mu\rangle$ and by rearrangement the left hand side of Equation 1.8,

$$M_m = N_A {g_J}^2 {\mu_B}^2 \frac{J(J+1)}{3k_B}\frac{H}{T} \qquad \text{Equation 1.9}$$

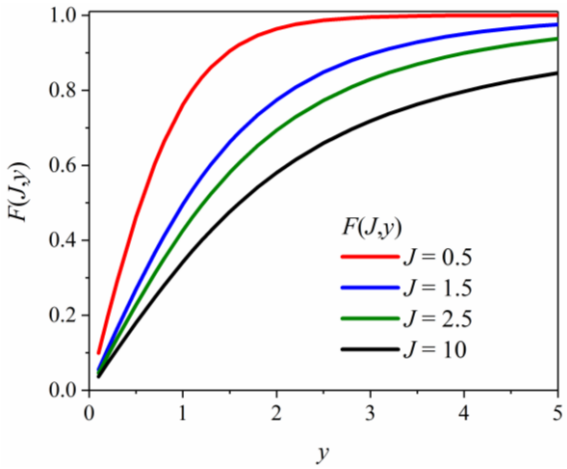


Figure 1.5. A plot of Brillouin function $F(J,y)$ for J = 0.5, 1.5, 2.5 and 10 against y, where $y = \frac{Jg_J\mu_B H}{k_B T}$.

This implies that the molar magnetisation is linearly proportional to $\frac{H}{T}$ as long as the latter is small enough. However, the more common parameter which is used to define the magnetic behaviour of a compound is the molar magnetic susceptibility, χ_m. It is defined as

$$\chi_m = \frac{M_m}{H} \qquad \text{Equation 1.10}$$

Therefore,

$$\chi_{\mathrm{m}} = \frac{N_{\mathrm{A}}{\mu_B}^2}{3k_{\mathrm{B}}T}{\mu_{\mathrm{eff}}}^2 \qquad \text{Equation 1.11}$$

where

$$\mu_{\mathrm{eff}} = g_J\sqrt{J(J+1)} \qquad \text{Equation 1.12}$$

and is called the effective magnetic moment of the ion. Paramagnetic materials that are observed within this region are considered to obey the Curie law

$$\chi_{\mathrm{m}} = \frac{C_{\mathrm{m}}}{T} \qquad \text{Equation 1.13}$$

where C_{m} is the molar Curie constant and is expressed as

$$C_{\mathrm{m}} = \frac{N_{\mathrm{A}}{\mu_B}^2}{3k_{\mathrm{B}}}{\mu_{\mathrm{eff}}}^2 \qquad \text{Equation 1.14}$$

When this quantity is expressed in c.g.s. units, C_{m} is estimated to be:

$$C_{\mathrm{m}} = \frac{1}{8}{\mu_{\mathrm{eff}}}^2 \qquad \text{Equation 1.15}$$

This allows us to deduce the effective magnetic moment of a free atom. However, if the atom or ion is in a crystalline material, caution should be applied. For transition metals, especially those in the first row, the orbital angular momentum is usually partially, if not completely, quenched. Therefore, $\boldsymbol{L}$ can be assumed to take the value of zero in the extreme cases, leaving the spin–only formula to describe the magnetic moment of the ion concerned:

$$\mu_{spin-only} = 2\mu_{\mathrm{B}}\sqrt{S(S+1)} \qquad \text{Equation 1.16}$$

However, for rare–earth elements, since the 4*f* orbital has no radial node and is much more contracted than the *d* orbitals, there is next to no quenching of the orbital angular momentum. As a consequence, g_J has to be calculated from appropriate quantum numbers *L*, *S* and *J* in order to estimate the magnetic contribution of a rare–earth cation in a bulk material. Take $NdGaO_3$ as an example. This perovskite remains paramagnetic below 300 K in an applied magnetic field of 4 Oe[51]. The magnetometry data was fitted with the Curie law and the μ_{eff} per Nd^{3+} cation was deduced to be 3.62 μ_B. This value is the same as the theoretical value calculated from the $^4I_{\frac{9}{2}}$ ground state of Nd^{3+} ion.

The theory presented above assumes that the atomic magnetic moments in a crystal are independent of each other. In practice this is not the case. The interactions between them give rise to the physical properties that make perovskites interesting. In the following sections the phenomena that occur and how they arise will be discussed.

1.3.2 Ferromagnetism

When, below some critical temperature (the Curie temperature, T_C), the interatomic interactions cause the unpaired spins of the ions in a crystal to co–align with each other over long distances, even in the absence of an external magnetic field, the sample is considered to be a ferromagnet, see Figure 1.6.

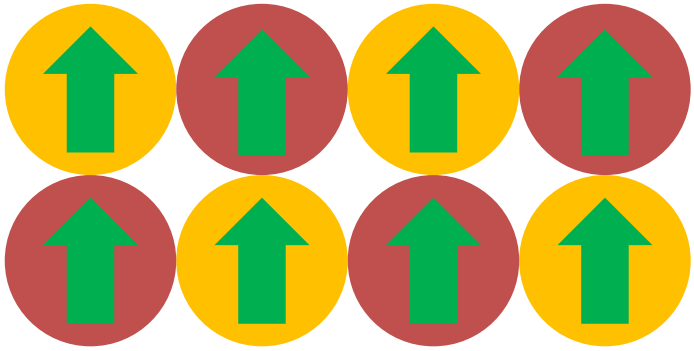


Figure 1.6. The arrangement of unpaired spins in a ferromagnet below Curie temperature, T_C.

However, this is a simple explanation of a complex phenomenon. The spins are actually aligned parallel within a relatively small magnetic domain, and in this region the magnetisation is saturated. These domains are separated by domain walls, meaning the net magnetisation of a particular domain does not necessarily align with its neighbouring magnetic domains in the absence of an external magnetic field. Thus, the bulk sample can have a low overall magnetisation due to the cancellation of the magnetic vectors from different domains. When a ferromagnet is placed in an applied magnetic field below the Curie temperature, the domains aligned with the magnetic field grow at the expense of the others. This gives rise to a large bulk magnetisation. The alignment between the spins is discouraged by the thermal fluctuations as temperature increases. At the Curie temperature, the spins are completely randomised and the crystalline material reverts to being a paramagnet. Because of the nature of the coupling between these ions, the ferromagnet then no longer follows the Curie Law, but the Curie–Weiss Law:

$$\chi = \frac{C}{T-\theta_{\mathrm{W}}} \qquad \text{Equation 1.17}$$

where θ_{W} is the Weiss Temperature. For a ferromagnet, θ_{W} is usually positive. For example, ferromagnetic ordering of Mn^{3+} ions in the insulator La_2GaMnO_6 was found to develop below 70 K with a reported θ_{W} of +126.7(8) K[52], even though the Ga^{3+} and Mn^{3+} cations are randomly distributed over the *B* sites.

1.3.3 Antiferromagnetism

An antiferromagnet is a material in which the interatomic interactions cause the atomic moments to order over long distances such that $\sum_{i=1}^{N} \boldsymbol{m}_i = 0$, where $\boldsymbol{m}_i$ is the atomic moment of the i^{th} atom in a unit cell containing *N* atoms. This ordering occurs on cooling below a critical temperature known as the Néel temperature, T_{N}. For an ideal crystal at

absolute zero (T = 0 K), the cancellation of the magnetic moments results in zero net magnetisation even when a magnetic field is applied. As in a ferromagnet above T_C, the electron spins will be randomised and paramagnetic above T_N. Since the coupling between neighbouring spins is predominantly antiferromagnetic, the compound follows the Curie–Weiss Law but with a negative θ_W. There are many examples of perovskites behaving as antiferromagnets due to nature favouring an antiparallel spin orientation as a consequence of the Pauli Exclusion Principle. For instance, there is an antiferromagnetic transition near 12 K for La_2MgIrO_6 with a θ_W = –24.0 K[53] whereas Sr_2CoTeO_6 becomes an antiferromagnet at approximately 15 K with θ_W = –146(21) K[54].

1.3.4 Magnetic Structures

Within the perovskite structure there are many different ways to arrange the atomic moments on the *B*–site cations to satisfy the condition $\sum_{i=1}^{N} \boldsymbol{m}_i = 0$. Wollan[55] listed several possible arrangements and some of them are shown in Figure 1.7. G–type ordering is observed when the antiferromagnetic coupling between nearest–neighbour cations dominates in all three directions and it is exemplified by the magnetic structure of $La_{0.8}Ca_{0.2}FeO_{3-\delta}$[56]. $CaCrO_3$ exhibits a C–type ordering which can be achieved by replacing the antiferromagnetic coupling in one direction in the G–type structure with ferromagnetic coupling instead[57]. In an A–type arrangement the cations couple ferromagnetically within layers but antiferromagnetically between layers. Such an ordering pattern is adopted by $LaMnO_3$ below 140 K[55]. Note that the magnetic unit cell can sometimes be larger than the structural unit cell due to the involvement of the spins.

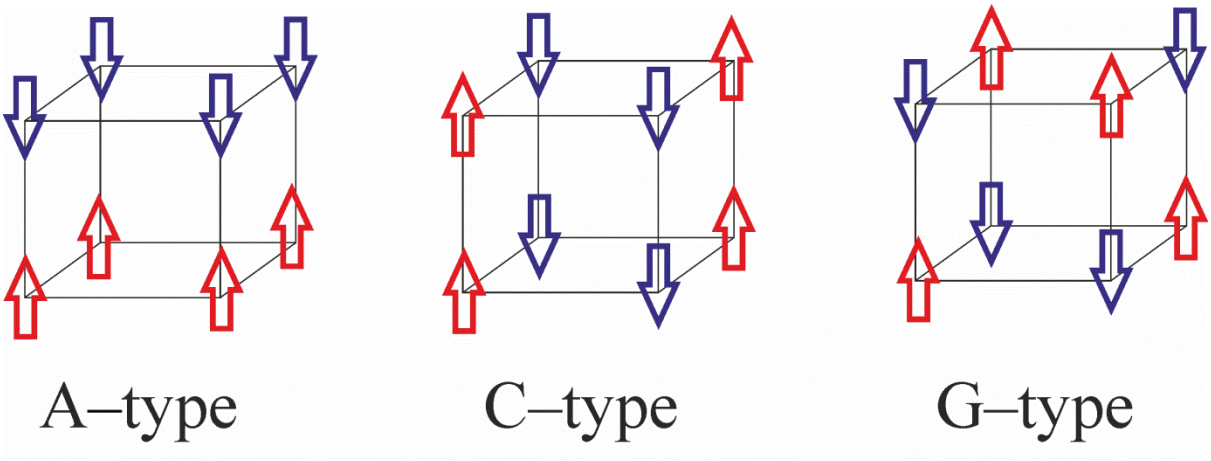


Figure 1.7. Three different types of magnetic ordering in a primitive cubic structure; A–, C– and G–type.

1.3.5 Ferrimagnetism

A ferrimagnet is a material in which the dominant cation–cation interactions are antiferromagnetic, but for some reason the vector sum of the atomic moments is non–zero. For example, two ferromagnetic sublattices might couple antiferromagnetically but if they do not have equivalent magnetic vectors a net magnetisation will result, as in Fe_3O_4[58]. Ferrimagnetism can also be a consequence of cation ordering as in $SrLa_2FeCoSbO_9$[59]. This material adopts a perovskite structure which has two crystallographically–distinct octahedral sites. The Co^{2+} and diamagnetic Sb^{5+} cations are distributed in a rock–salt type arrangement across the two *B* sites whereas the Fe^{3+} cations are present in equal concentration on both six–coordinate sites. Hence, when the two sublattices couple antiferromagnetically to each other the resultant magnetisation is non–zero.

1.3.6 Magnetically Frustrated Systems: Spin glasses

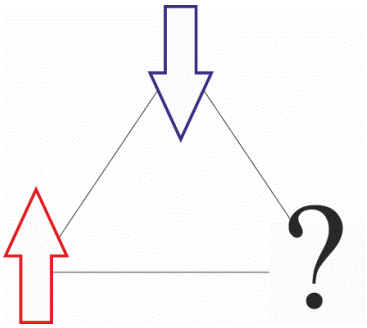


Figure 1.8. A simple system to explain magnetic frustration. Assuming all interactions between two spins are antiferromagnetic, the spin at the bottom right corner is magnetically frustrated as its direction is ambiguous.

A spin glass is a material with magnetic frustration, which is usually caused by disorder or competition between different interatomic interactions, each of which would favour a different magnetic structure. The magnetic ordering in a spin glass is short–range whereas ferromagnets and antiferromagnets have long–range magnetic ordering within the crystals. Magnetic frustration can be illustrated using a triangle of three spins, see Figure 1.8. Assuming only the nearest–neighbour interaction is available and the interaction is antiferromagnetic in nature, the spin sitting at the bottom right corner is now "frustrated" because the direction of this particular spin cannot be uniquely determined. Like all other magnetic systems, the frustrated coupling competes with the thermal energy. Above a certain temperature, known as the freezing temperature (T_f), the material is in a paramagnetic state.

Disorder, or randomness, can be created by cation distribution (occupancy) since the distance between each pair of paramagnetic cations in the crystal varies purely from a statistical point of view. Frustrated magnetic behaviour is therefore not uncommon in double perovskites, especially for those which have significant *B*–site cation disorder as this gives rise to a range of competing interactions. For example, Sr_2FeTaO_6 and

Sr_2FeNbO_6[60, 61] have a disordered arrangement of *B*–site cations and were both found to transform to a spin–glass state below 23 and 20 K respectively.

1.3.7 Origin of Exchange Interaction

In order to understand the magnetism in perovskites, one must consider the interaction between a pair of cations with unpaired electrons. There are a number of ways in which two paramagnetic cations can interact within a crystal. The dominant mechanism in the insulating ionic compounds discussed in this thesis is known as the superexchange interaction. Superexchange involves the virtual transfer of an electron between two magnetic cations that are separated by a non–magnetic anion; the participating orbitals are non–orthogonal to each other. The strength of the superexchange interaction relies on the degree of the orbital overlap between the metal cation (usually the *d* orbital) and the anion (usually the 2*p* orbital). It is not surprising that both the bond length and the bond angle of the superexchange pathway play an important role in this mechanism. The electronic configuration of the magnetic cation is undoubtedly a crucial factor in determining the type of superexchange interaction. The main operational pathway in perovskite is often found to be linear, see Figure 1.9.

To understand the superexchange mechanism, consider an octahedral transition metal oxide complex. The degeneracy of the *d* orbitals is destroyed by the crystal field splitting. Figure 1.9 illustrates the overlapping of the orbitals of two metal cations sitting on the same axis with the intervening anion in between. The overlap is bigger between the e_g set of orbitals and the 2*p* orbitals of the oxide anion than between the t_{2g}–O2*p* orbitals as the $d_{x^2-y^2}$ and d_{z^2} orbitals are pointing directly towards the ligands. These two types of interactions are known as the σ– and π–superexchange interactions respectively.

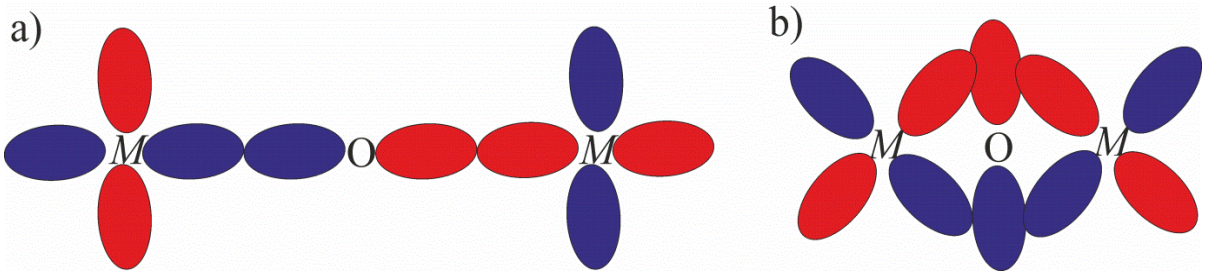


Figure 1.9. The overlapping of the *d* orbital from a metal cation (*M*) and the 2*p* orbital from the oxide anion for a) the σ– and b) the π– *M*–O–*M* interaction.

Now let us consider a few scenarios of a *M*–O–*M* bond with both metal cations (*M*) surrounded by an octahedral arrangement of oxide anions (O). We shall assume that the oxygen 2*s* orbital is too low in energy to be able to participate in the superexchange pathway. For a pair of cations with a d^8 electron configuration (e.g. Ni^{2+} cations), the t_{2g} orbitals are filled and are highly unlikely to be involved in any virtual electron transfer. As a result, the only possible superexchange interaction is of the σ–type. Here, if the net spin on the first cation is up, then, by the Exclusion Principle, a spin down electron from the anion 2*p* orbital will take part in the overlap. The remaining spin–up electron on the anion will then "migrate" towards the second metal cation. Due to the Exclusion Principle, the second metal cation must therefore have a net spin moment anti–parallel to the first one. This coupling is labelled as antiferromagnetic. Take NiO as an example. It has been confirmed by neutron scattering that the interaction between the nearest neighbours in NiO is antiferromagnetic, with the coupling constant J_1/k_B estimated as –221 K[62]. This magnetic interaction is dominant in NiO, and hence NiO is an antiferromagnet below 525 K. Another case is when the metal cations have a d^3 electron configuration, for example Cr^{3+}. The empty e_g orbitals dictate that the superexchange interaction will predominantly be π–type. Following a similar argument to that laid out above, the coupling between two d^3 metal cations will be antiferromagnetic in this linear pathway. Such an interaction was found to be dominant in $LaCrO_3$ as it adopts a G–type magnetic structure[63]. The third

scenario is where the metal cation has an electron configuration of d^5 in a high–spin state. Examples include Mn^{2+} and Fe^{3+} ions. Here both the e_g and t_{2g} orbitals are half–filled. Consequently, both σ– and π–interactions are expected to participate. Nevertheless, both interactions via the linear pathway will be antiferromagnetic for the reasons discussed above and it was confirmed by experimental data collected on MnO[64, 65].

So far the two metal cations in the *M*–O–*M* bond presented have the same electron configurations. It is of course possible to have two metal cations with different electron configurations, especially in a double perovskite where the *B* and *B*' cations are different. The situation is then more complex. First of all, the linear superexchange pathway has to involve two oxygen anions and can now be mediated by a cation with a different electron configuration, see Figure 1.10. The probability of *M*' being different from *M* depends on the distribution of cations on the *B* and *B*' sites in the crystalline material, and so the extent of the cation ordering should be considered when discussing the nature of the magnetic interactions present in a sample. For example, $Sr_2LaCr_2SbO_9$ adopts a triclinic structure where Cr^{3+} is present on both octahedral sites[66]. The dominant interaction in this Cr–containing perovskite is the antiferromagnetic nearly–linear coupling Cr–O–Cr. It is a ferrimagnet because of the imbalance in the distribution of Cr^{3+} over the two six–coordinate sites. Secondly, non–linear *M*–O–*M*'–O–*M* superexchange pathways should also be taken into account as these right–angled pathways, as illustrated in Figure 1.10, can be competitive with respect to the linear pathway. Furthermore, reports have suggested that it is possible that the *M*' cation may not be involved in the superexchange pathway if its outer orbitals are too low in energy to mix with the O 2*p* orbitals[67, 68]. This particular superexchange route will then become *M*–O–O–*M* instead. For example, the non–linear Cr–O–O–Cr superexchange route is thought to be dominant in the antiferromagnetic Sr_2CrSbO_6, where the Cr^{3+} and Sb^{5+} ions are fully ordered on the two crystallographically

distinct *B* sites[69]. However, the presence of cation order does not guarantee long–range magnetic ordering; Sr_2MgReO_6 was found to behave as a spin glass below 14 K despite the Mg^{2+} and Re^{6+} ions being ordered at the *B* site[70]. It is of course possible that the *M*' cation can have unpaired electron(s). Although Ca_2NiOsO_6 and Ca_2CoOsO_6 are both ferrimagnets, the coupling between Os^{6+} and the nearest–neighbour Ni^{2+}/Co^{2+} were found to be antiferromagnetic[71].

The above discussion can be summarised by the Goodenough–Kanamori rules[72-74]. They state that the interaction between two overlapping orbitals which are half–filled is antiferromagnetic. The coupling becomes ferromagnetic if the virtual transfer of an electron is from a half–filled orbital to an empty orbital. However, the rules do not give an indication regarding the relative strength of the interactions. As a result, competition among different types of superexchange interactions is expected to exist in a crystal.

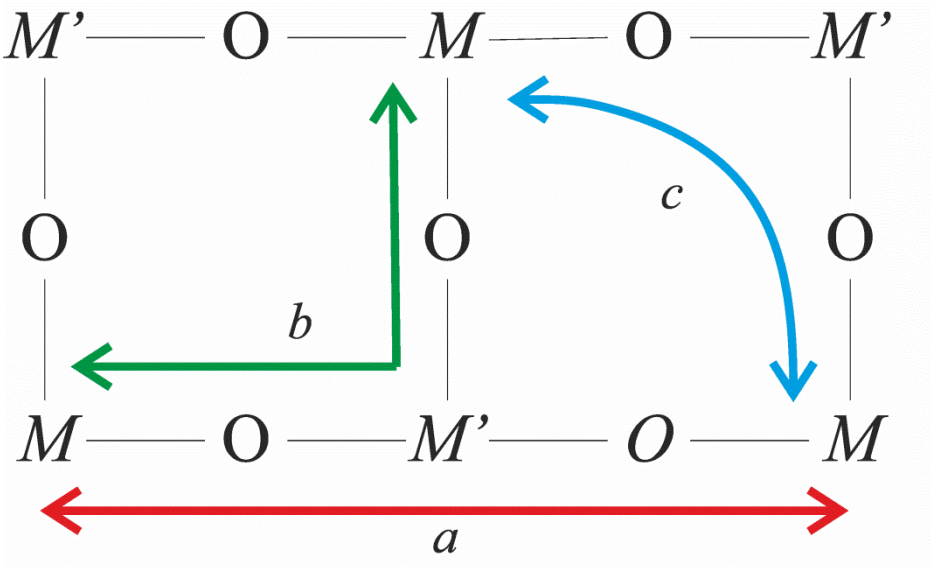


Figure 1.10. Three possible superexchange pathways in a double perovskite. It is assumed the *M* and *M*' cations are ordered in rock–salt arrangement and that *M*' is non–magnetic. Pathways *a* and *b* represent the linear and perpendicular *M*–O–*M*'–O–*M* superexchange pathways whilst pathway *c* is the *M*–O–O–*M* superexchange route.

1.4 Overview of the thesis

This thesis is principally concerned with perovskites that have the general formula $A_{3-x}A'_xNi_2B'O_9$ where A/A' = Ca^{2+}, Sr^{2+}, La^{3+}, Pr^{3+}, Nd^{3+} and B' = Sb^{5+}, Ta^{5+}, Nb^{5+}, Te^{6+} and W^{6+}. The work was motivated by two reports suggesting that $La_3Ni_2SbO_9$ is a relaxor ferromagnet, a magnetic analogue of the well–known relaxor ferroelectrics, for example $Pb_3MgNb_2O_9$[48, 75]. The magnetic domains in the former are small with respect to the coherent length of neutron; this is similar to the fact that the atomic displacement was undetectable using X-ray in a relaxor ferroelectric. In Chapter 3, the result of an experiment conducted on $La_3Ni_2SbO_9$ using polarised neutron scattering in an attempt to determine the nature of the short–range magnetic and nuclear ordering is presented. Monte–Carlo (MC) and Reverse Monte–Carlo (RMC) methods were used to model the data. The rest of the thesis describes a systematic investigation of the wide range of factors which are expected to influence the magnetic properties of $A_{3-x}A'_xNi_2B'O_9$ compounds. The structural and magnetic properties of $La_3Ni_2TaO_9$ and $La_3Ni_2NbO_9$ are discussed and compared with those of $La_3Ni_2SbO_9$ in Chapter 4. The idea behind this comparative study was to study the changes in behaviour that occur when a diamagnetic cation with an empty *d*–shell (d^0) replaces d^{10} Sb^{5+} in the superexchange pathway. The mixed d^0/d^{10} system $La_3Ni_2Sb_xTa_yNb_{1-x-y}O_9$ was subsequently synthesised and the results of that study are presented in the following chapter. An investigation of the effect of partially substituting the paramagnetic cation Ni^{2+} in $A_{3-x}A'Ni_2B'O_9$ with Cu^{2+} is presented in Chapter 6 for B' = Sb, Ta or Nb. It was thought that because Cu^{2+} is an anisotropic cation, the local environment could be severely distorted, and consequently the magnetic properties of the resultant compositions may differ considerably from those of the parent compound. To study the effect of having d^0 and d^{10} diamagnetic cations, with different charges, the pentavalent cations were replaced by hexavalent cations, namely the Te^{6+} (d^{10}) and W^{6+}

(d^0), in the investigations described in Chapters 7 and 8 respectively. To compensate for the change in charge, one–third of the La^{3+} in $La_3Ni_2B'O_9$ (*B*' = Sb, Ta or Nb) was substituted by divalent cations. The structural chemistry and magnetic properties of $SrLa_2Ni_2TeO_9$ are described in Chapter 7 and a similar study on $CaLa_2Ni_2WO_9$ is reported in Chapter 8, which also includes an account of the effect of substituting the diamagnetic La^{3+} cation with paramagnetic Nd^{3+} or Pr^3 in $CaNd_2Ni_2WO_9$ and $CaPr_2Ni_2WO_9$, respectively. The general conclusions that can be drawn from this work are summarised in Chapter 9.

Chapter 2: Experimental techniques

2.1 Synthetic routes to mixed–metal oxides

Mixed–metal oxides can be synthesised in many different ways. Subject to the availability of apparatus and reactants, the most suitable synthetic method can be determined by the experimenters. The traditional solid–state route is by far the most accessible option and consequently the most used. This method simply involves grinding a powdered mixture using an agate mortar and pestle or a ball mill machine. There are, however, some difficulties with this approach. Firstly, the nucleation of the reaction is difficult due to the amount of structural reorganisation involved. Bonds between atoms have to be broken in the starting materials and a new set of bonds must be formed in the product phase after the atoms have successfully migrated through the contacting surfaces of the granules. Furthermore, the discrepancy in the structure between the reactants and the product discourages the growth of the latter since the atoms involved have to diffuse to an environment which will alter their potential energy. For instance, the crystal field stabilisation energy decreases when a transition metal cation migrates from an octahedral environment to a tetrahedral hole in the product. It is believed that there are three main factors that govern the rate of a solid–state reaction. These include the contact surface areas of the granules, the rate of nucleation of the product phase and the rate of diffusion of the ions[76]. As a result, solid–state reactions normally occur at high temperatures as increasing the temperature facilitates the rate of diffusion and nucleation. The starting reagents are thoroughly crushed into fine powders to increase the surface area of the granules. Pelletisation is another way to accelerate the synthesis because the diffusion distance between ions is shortened and the contact surface area is larger.

There are a variety of approaches which facilitate crystal growth at a lower reaction temperature by decreasing the diffusion distance. For example, the sol–gel method involves the use of solvent to dissolve the reactants and often requires the formation of a precursor to act as a template for a network–like product. The hydrothermal method utilises the unique nature of water under pressure to provide a pressure–transmitting medium. The reagents are partially soluble in water under pressure and the reaction takes place in the liquid and/or vapour phase. High pressure synthesis is another option. It allows researchers to study phase transition as a function of pressure. It has been claimed that the physical properties of the same solid material may differ if the samples are made using different synthetic routes[77-79].

Nevertheless, the perovskites reported in this thesis were synthesised using the traditional ceramic method. As no purification process is involved, high purity (Puratronic, purity ≥ 99.99 %) starting materials were required for all reactions. Furthermore, lanthanide oxides (La_2O_3, Pr_6O_{11} and Nd_2O_3) were dried in a furnace at 800 °C overnight because of their tendency to absorb moisture and carbon dioxide from the atmosphere. Stoichiometric quantities of metal oxides or carbonates were then weighted out accurately within ± 0.0001 g. After that, the reactants were ground thoroughly in an agate pestle and mortar for 30 minutes to ensure a highly homogeneous mixture was formed, which was later pelletised with a 2–tonne press. The pellet was then heated in an alumina crucible at between 1000 and 1300 °C. In the cases where carbonates were involved, the mixture was first fired as a loose powder at 800 °C for one day to allow the release of carbon dioxide from the carbonates before being pelletised. All reaction mixtures were re–pelletised after each heating cycle which normally lasted for 48 to 72 hours. X–ray powder diffraction was used to monitor the progress of a reaction. As a consequence of the poor efficiency of the mass transfer between granules and the overall nature of this synthetic method, impurities which

are thermodynamically stable at the reaction temperatures can sometimes form. Nevertheless, a reaction was considered to be finished if no observable improvement was present when two successive diffraction patterns were compared and the sample contained less than 2 wt. % of impurities.

2.2 Crystallography

A crystal consists of a regular arrangement of atoms in three dimensions. It is best described in terms of a three–dimensional lattice of points that are arranged periodically in space. A group of atoms, the basis, is located on each lattice point, the same group on every point. Hence a structure is a combination of a basis and a lattice. It can be represented by a repeating unit that contains the constituent atoms in certain specific locations and the smallest repeating unit from which the crystal can be built up is defined as the unit cell. The geometric shape of a unit cell is governed by the presence or absence of symmetry elements in the structure. A symmetry element can be a rotational axis, a mirror plane or an inversion centre. Translational symmetry elements, including a screw axis and a glide plane, can also be found in a unit cell. As a result, there are seven unique unit cell shapes a structure can have in three dimensions; each is known as a crystal system. For example, a cubic unit cell will have four three–fold rotational axes and all the sides of the cube will be automatically equal with each face of the cube sitting at a right angle to each other. An orthorhombic unit cell possesses three mutually orthogonal mirror planes or two–fold axes but the sides are inequivalent to each other. A monoclinic unit cell can be considered to be a distortion of an orthorhombic unit cell; there is only one two–fold rotational axis parallel to one of the axes of the unit cell, and this particular axis is referred to as the unique axis. A unit cell is defined as primitive if it contains only one lattice point. Other lattice types contain between two and four lattice points. The

combination of the crystal system and the lattice type can generate fourteen possible Bravais lattices.

A unit cell has six crystallographic parameters[80]. The edges on a unit cell are labelled as *a*, *b* and *c* respectively. The angles between the edges and the plane which they are perpendicular to are known as α, β and γ. The "seventh" parameter is the origin of the unit cell. It can lie anywhere within the period arrangement of atoms as long as the aforementioned six parameters of the unit cells remain unchanged. The locations of the atoms within the unit cell are described in terms of fractional coordinates (*x*, *y*, *z*) which are the fractions of each of the unit–cell parameters *a*, *b*, and *c*. In fact, multiple atoms can be generated by symmetry from an individual atom located at a particular position in a unit cell. This atom can be labelled with Wyckoff positions, which are denoted by a number and a letter. The former represents the multiplicity of an atom whereas the latter is the Wyckoff site. For example, an atom located at a 2*c* site indicates there are two symmetrically equivalent atoms in a unit cell.

2.3 Diffraction

Crystal structures often hold the key to the observed magnetic properties of materials. An experimental technique involving diffraction turns out to be the most important experimental technique for solid–state chemists to study the crystal structure as it is a non–destructive technique that can be used to characterise the reaction products. Diffraction is a phenomenon observed when a wave travels through a periodic arrangement of scattering centres whose separation is comparable with the wavelength of the incident wave. In solid–state chemistry, the incident beams interacts with the atoms in a sample, resulting in both constructive and destructive interference, provided that the wavelength of the incoming beam is comparable with the separation between lattice points. It can also be understood by

considering the scattered radiation to be a consequence of the incoming beam being "reflected" by sets of parallel planes, known as the lattice planes. These imaginary planes contain the atoms which are responsible for scattering the incoming radiation. Lattice planes are often described by a triplet of numbers, (*hkl*), which are known as the Miller indices. The (*hkl*) planes cut the *a*, *b* and *c* axes *h*, *k* and *l* times, respectively, per unit cell. Miller indices can either be positive or negative, depending on the direction a plane intersects the axes relative to the origin. The planes in a particular (*hkl*) set are all a constant distance apart, d_{hkl}. Figure 2.1 illustrates the "reflection" of the X–ray by a set of (*hkl*) planes with a *d*–spacing equal to d_{hkl}.

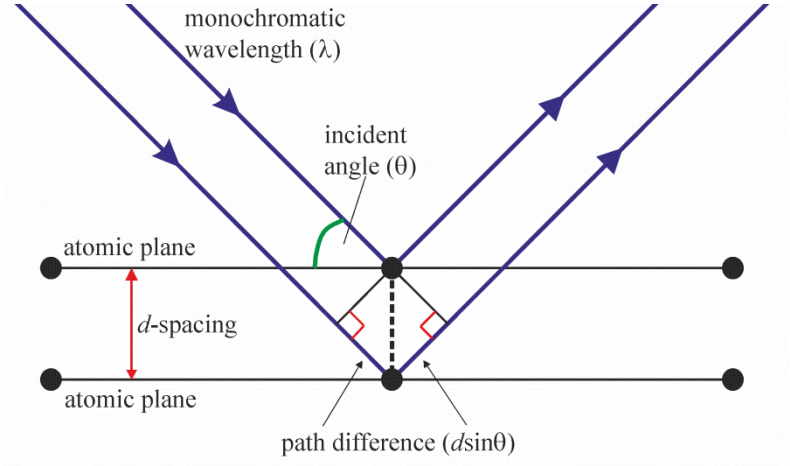


Figure 2.1. Monochromatic wavelength being diffracted by a periodic pattern.

Due to the nature of "reflection", the angle between the incident radiation and a lattice plane is the same as the angle of reflection, both here denoted as θ. In order to produce constructive interference, the radiation reflected from the adjacent lattice planes have to be in phase with each other. This relies on the fact that the path difference, $2d\sin\theta$, travelled by the incident and reflected waves must be equal to an integer multiple of the wavelength. Applying geometry in Figure 2.1 leads to the Bragg's Law:

$$\lambda = 2d_{hkl} \sin\theta \qquad \text{Equation 2.1}$$

where λ is the wavelength of the radiation, d_{hkl} is the distance between adjacent lattice planes and θ is the angle of incidence. When the wavelength is known and kept constant, one can calculate the *d*–spacing corresponding to a particular 2θ value. The interplanar spacing can be expressed as a function of the lattice parameters of a unit cell. The relationship, however, depends on the Bravais lattice type of the unit cell. For example, Equation 2.2 states the relationship between the *d*–spacing and the lattice parameters of a monoclinic unit cell.

$$\frac{1}{d^2} = \frac{1}{\sin^2\beta}\left(\frac{h^2}{a^2} + \frac{k^2\sin^2\beta}{b^2} + \frac{l^2}{c^2} - \frac{2hl\cos\beta}{ac}\right) \qquad \text{Equation 2.2}$$

Directions within a crystal are referred to using a triplet of numbers [*hkl*]; in an orthogonal unit cell the [*hkl*] direction is perpendicular to the (*hkl*) planes.

2.3.1 X–ray diffraction

X–rays are a common radiation for diffraction experiments because their wavelength is comparable to the interatomic spacings in solids, they are non–destructive in nature and they are easily accessible in a laboratory. They are normally produced by bombarding a metal target with a beam of high–energy electrons which ionise the electron from the K–shell of the targeted element. The vacancy generated will then be occupied by the relaxation of an electron from L (2*p*) or M (3*p*) levels, and the energy of the photon released lies in the X–ray section of the electromagnetic spectrum (labelled as K_α and K_β respectively). Due to the spin state in the *p* sub–shell, both transitions are in fact doublets ($K_{\alpha1}$, $K_{\alpha2}$, $K_{\beta1}$ and $K_{\beta2}$). As these two (four) radiations are generated simultaneously, usually a filter is used to give rise to a monochromatic X–ray beam for use in a diffraction experiment. Since the energy of an electron in an atom is quantised, the wavelength emitted is known precisely, and hence *d*–spacings, can be deduced with great precision.

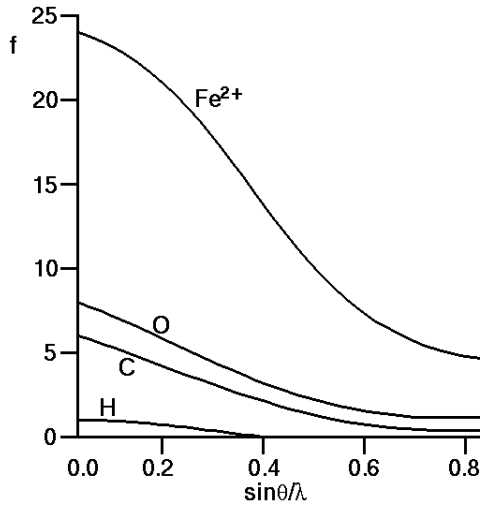


Figure 2.2. The X–ray scattering factors of a few elements[81]. Note all of them decrease with increasing sinθ.

Regarding the interaction between the X–ray beam and the sample, consider an X–ray as an electromagnetic wave with an oscillating electric field[76]. An elastic collision between the wave and the electrons of an atom induces vibrations, causing "electron cloud" to act as a secondary source of X–ray by emitting radiation which is in phase with the incident beam. As a result, the intensity of the scattered radiation is determined by the number of electrons an atom possesses; the contributions from heavier elements will overshadow these from lighter elements like oxygen in the materials reported in this thesis, making it very difficult to identify accurately the atomic position of the latter by using X–ray diffraction only. The ability of each element to scatter the incident X–ray beam is known as the scattering factor, *f*. Since isoelectronic ions such as K^+ and Cl^- scatter the X–ray radiation equally, they both have the same scattering factor at $\frac{\sin\theta}{\lambda} = 0$. Moreover the subtle difference in the location of different electrons in an atom, *i.e.* the finite size of the electron cloud compared to the wavelength, results in partial destructive interference. Consequently the scattering intensity diminishes with increasing scattering angle, see Figure 2.2.

Although Bragg's Law can be used to explain the positions of the diffraction peaks observed in a diffraction pattern, the equation provides no information with respect to the intensities of any peak. The intensity of a given set of *hkl* plane is given as follows:

$$I_{hkl} = K(L_{hkl}\, p_{hkl}\, A_{hkl})F_{hkl}^2 \qquad \text{Equation 2.3}$$

where the Lorentz factor L_{hkl} and p_{hkl} are factors that depends on the geometry of the apparatus. A_{hkl} is the absorption correction.

From Equation 2.3, the intensity of the reflection from a given set of plane is proportional to the square of the structural factor, which can be written as:

$$F_{hkl} = \sum_{j=1}^{N} a_j f_j exp\left[2\pi i\left(hx_j + ky_j + lk_j\right)\right] exp\left[-8\pi^2 U_{j,\mathrm{ISO}}\left(\frac{sin\,\theta}{\lambda}\right)^2\right] \qquad \text{Equation 2.4}$$

where a_j is the occupancy of the atom concerned at a crystallographic site (x, y, z), $U_{j,\mathrm{ISO}}$ is the isotropic displacement factor, f_j is the scattering factor of the ion j and other symbols have the same meanings as previously. The first exponential term indicates the contribution to the intensity of the *hkl* reflection from a static atom at (x, y, z). In theory, the X–ray should be diffracted by all sets of *hkl* planes. However, the intensity for each reflection may not necessarily be non–zero if the lattice type is non–primitive. The second exponential term is known as the Debye factor or the temperature factor. An atom vibrates as temperature increases. Consequently, the atom looks "larger" in size, and thus leads to a similar effect to that produced by the scattering factor, that is the intensity decreases with increasing scattering angle.

It is worth noting that for a powdered sample, all the reflections can only be measured on a one–dimension parameter which is the Bragg angle, or the *d*–spacing of the lattice planes in the crystal. Therefore, according to the Bragg's law, lattice planes with the same *d*–spacing should all contribute to the intensity of a Bragg peak observed at a particular 2θ

value as the intensities of the reflections originating from these lattice planes are additive. The number of equivalent lattice planes that superimpose onto one Bragg peak is known as the multiplicity. This value of this variable is determined by the symmetry of the structure.

2.3.2 Neutron diffraction

Diffraction experiments can also be conducted using neutron beams instead of X–rays. Due to the difference in the production of this neutron beam, there are two types of neutron source; reactors and pulsed neutron sources. For the former, a neutron beam is produced when neutrons are produced after countless collisions with atoms within a nuclear reactor. These fast neutrons of mass *m* are then slowed down by a moderator at a specific temperature *T* before emerging from the reactor with a root mean squared velocity υ. The kinetic energy of these neutrons can be expressed as follow:

$$\frac{1}{2}m\upsilon^2 = \frac{3}{2}\mathrm{k_B}T \qquad \text{Equation 2.5}$$

where $\mathrm{k_B}$ is the Boltzmann's constant. De Broglie's equation, given in Equation 2.6, allows us to calculate the wavelength λ of the neutrons travelling with the velocity υ.

$$\lambda = \frac{\mathrm{h}}{m\upsilon} \qquad \text{Equation 2.6}$$

Here, h is the Planck's constant. By combining the particle and wave properties of a neutron, the wavelength at a specific temperature *T* can be expressed as follow:

$$\lambda^2 = \frac{\mathrm{h}^2}{3m\mathrm{k_B}T} \qquad \text{Equation 2.7}$$

At thermal equilibrium, the distribution of the velocities of the neutron can be described by a Maxwellian distribution. A neutron beam of the desired wavelength can be obtained by inclining a monochromating crystal to the white beam at a fixed Bragg angle. The

wavelength selected should be carefully chosen so as to minimise contamination of the beam by neutrons having a wavelength of $\frac{\lambda}{2}$.

Pulsed neutron sources are based on proton spallation, for example at ISIS in Harwell, England[82]. A pulsed proton beam is generated by passing H^- ions through an aluminium oxide stripping foil which removes the electron from the anion. The proton beam is then accelerated in a proton synchrotron at a frequency of approximately 50 Hz. The highly energetic protons are then extracted and allowed to hit at a heavy metal target in order to produce neutrons with very high velocities. Hydrogenous moderators are used to slow the neutrons down to an energy level where they can be useful for condensed–matter studies.

A time–of–flight (TOF) technique is employed when a pulsed neutron source is used for neutron diffraction[83]. After leaving the moderators, the pulsed neutrons travel a certain distance before being scattered by a sample. The neutrons then arrive at the detectors which are some distance away from the sample tank at certain fixed 2θ angles. Let L be the total flight path of the neutrons and t be the total flight time. Neutrons with velocity of v reaches a detector after $t = \frac{L}{v}$. By substituting the de Brogile's equation into the Bragg's law, the relationship between the d–spacing, as well as the reciprocal vector Q, of the material and the total flight time t are given in Equation 2.8.

$$\lambda = \frac{h}{mv} = \frac{ht}{mL} = 2d \sin\theta = \frac{4\pi \sin\theta}{Q} \qquad \text{Equation 2.8}$$

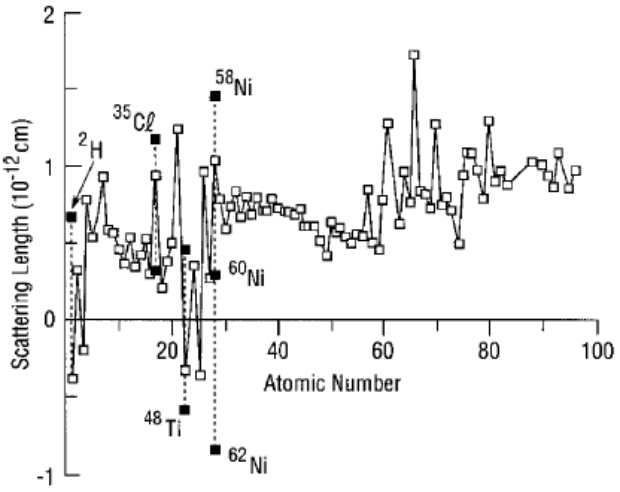


Figure 2.3. The neutron scattering length of various elements[84].

Similar to X–rays, a neutron beam can also be diffracted by a crystalline material because of its wave properties. Neutron scattering can be separated into two parts, potential and resonance scattering[84], and constructive interference is produced at some well–defined angles according to the Bragg's law. However, the neutron mainly interacts with the nucleus, instead of the cloud of electrons, of an atom with the exception of magnetic materials. The neutron scattering amplitude is then governed by the scattering length, b_n, of an atom. This quantity can be treated as a replacement of the scattering factor f in X–ray diffraction. As shown in Figure 2.3, the variation of the scattering length is now no longer dependent of the atomic number Z due to the superposition of the random effects of resonant scattering on the potential scattering. In other words, light atoms such as oxygen are not masked by the heavier elements in a diffraction pattern. Note that the values of the scattering length, b_n, for most elements are positive, with a few exceptions such as hydrogen and lithium which have negative values. A positive b_n indicates that there is a phase shift of 180° between the incident and scattered neutron waves. However, with the presence of a resonance level whose energy is greater than that of the thermal neutron, the value of b_n will become negative. Moreover, since the dimensions of the nucleus are extremely small in comparison with the wavelength of the radiation, the nucleus can be

considered to be a point scatterer. As a consequence, in contrast to X–ray scattering, the scattering amplitude of the neutron is independent of the Bragg angle. The neutron scattering lengths of some selected elements are shown in Table 2.1.

Table 2.1. The neutron scattering lengths of some selected elements[85].

Element	Atomic number (*Z*)	Scattering length / fm
O	8	5.803
Ca	20	4.7
Ni	28	10.3
Cu	29	7.718
Sr	38	7.02
Nb	41	7.054
Sb	51	5.57
Te	52	5.80
La	57	8.24
Pr	59	4.58
Nd	60	7.69
Ta	73	6.91
W	74	4.86

Furthermore, since a neutron has a spin quantum number of $\frac{1}{2}$, it enables us to extract additional information from a magnetic sample. The magnetic moment of the neutrons interact with the unpaired electrons in a material. However, this interaction produces Bragg scattering only if the magnetic moments of the atoms of interest align in a periodic manner; that is when long–range magnetic ordering is present in the crystal. If the neutron beam is unpolarised, the nuclear and magnetic scattering intensities are additive. A common technique in NPD is first to compare the intensities of the NPD patterns recorded below

and above a magnetic transition temperature and then to assume that any additional intensities are magnetic in origin. The magnetic structure of the crystal can then be deduced. Similarly to X–ray diffraction, since this particular interaction is between the neutrons and electrons, the scattering grows weaker with increasing 2θ. In other words, extra diffraction peaks or intensities attributable to magnetic ordering within the material are more easily observed in the low angle region.

2.4 Diffractometers

As discussed before, diffraction is crucial to extract structural information about a crystal. In this section, different diffractometers which were used during the course of this study will be described. All neutron diffractometers listed here use neutron beams of constant wavelength unless specified.

2.4.1 PANalytical Empyrean Alpha–1 X–ray Diffractometer

All X–ray powder diffraction patterns shown in this thesis were recorded on this in–house diffractometer. It operates at 45 kV and 40 mA to generate an X–ray beam. A Johansson monochromator with a symmetrically cut, curved germanium (111) crystal[86] ensures the production of pure Cu $K\alpha_1$ radiation (λ = 1.54051 Å). For all data collections reported here, a pair of 0.04° Soller slits, a 10 mm beam mask and a fixed 1° divergence slit were used to collimate the X–ray beam and optimise the intensity and resolution.

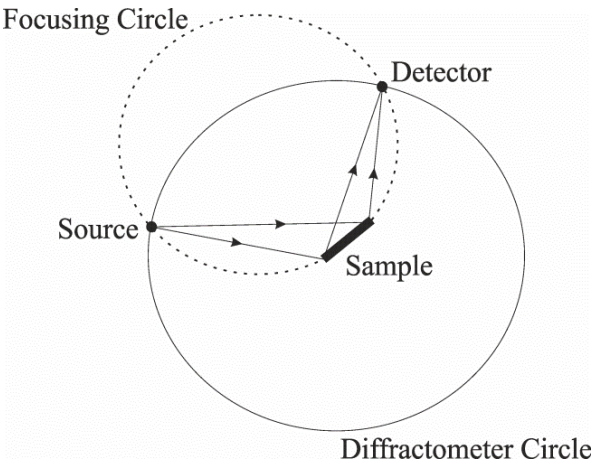


Figure 2.4. Bragg–Brentano diffraction geometry[76].

This diffractometer makes use of Bragg–Brentano geometry to collect diffraction data and the geometry is depicted in Figure 2.4. During a measurement, both the source and the detector have to sit on the circumferences of the two interpenetrating circles, namely the focusing circle and the diffractometer circle. The sample should always stay tangential to the former and at the centre of the latter. To maintain this geometry, the detector should rotate along the circumference of the diffractometer circle twice as fast as the sample rotates.

The sample was mounted on a flat aluminium plate during preliminary data collections to monitor the progress of a reaction. Each measurement roughly lasted for 30 minutes and covered an angular range of $10 \leq 2\theta/° \leq 90$ with a step size of $\Delta 2\theta = 0.0131°$. High–quality data were collected subsequently if the sample was deemed to be pure enough. With the help of high vacuum grease, a small amount of sample was gelled onto a silicon wafer cut parallel to (110) to prevent any contamination by Bragg peaks from silicon. The wafer was then placed onto a spinner and spun at a rate of one revolution per second to reduce the effects of preferred orientations of the powder. The high–resolution measurement covered a wider angular range, $5 \leq 2\theta/° \leq 125$, with a smaller step size of $\Delta 2\theta = 0.0066°$ and lasted for at least 9 hours.

2.4.2 Neutron diffractometer ECHIDNA

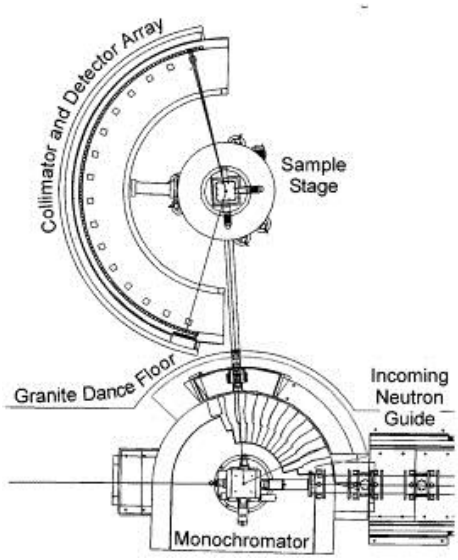


Figure 2.5. Schematic drawing of ECHIDNA diffractometer[87].

ECHIDNA, located at the Australian Nuclear Science and Technology Organisation (ANSTO) in Australia, is a neutron diffractometer designed for studying atomic and magnetic structure of materials. A schematic drawing of ECHIDNA is shown in Figure 2.5[87]. All diffraction measurements done using ECHIDNA were kindly carried out by Dr Maxim Avdeev. The angular range covered was $8 \leq 2\theta/° \leq 160$ with a step size of $\Delta 2\theta$ = 0.05° and the wavelength used was either 1.622 or 2.4395 Å. The wavelength was selected by rotating the germanium crystals to the (115) or the (335) plane respectively. The longer wavelength was employed in the hope of finding any extra Bragg peaks, with relatively large *d*–spacings, attributable to long–range magnetic order in the sample. The monochromators of ECHIDNA have variable take–off angles and there are 128 detectors. The neutron flux at the sample position can reach up to 10^7 n cm^{-1} s^{-1}. Moreover, the sample space is large and versatile, allowing ancillary equipment, for example a magnet to be mounted. Therefore, diffraction patterns can be collected with the sample in an applied magnetic field.

2.4.3 Neutron diffractometer D2b

D2b is a high–resolution powder diffractometer located at Institut Laue–Langevin (ILL) in France. Its design is very similar to ECHIDNA. The polychromatic beam passes through a collimator and is diffracted by monochromators with a high take–off–angle 135°. The desired wavelength for an experiment can be obtained by rotating the germanium crystals within the (*hhl*) plane. The crystals were rotated to the (335) lattice plane to provide neutron beams with a wavelength of 1.594 Å during the investigations presented in this thesis. The samples studied were loaded into 6 or 8 mm vanadium canisters and the scattered neutrons were collected by 128 detectors with an interval of 1.25° between each pair. The diffraction pattern collected covers an angular range of $5 \leq 2\theta/° \leq 165$ with a step size of $\Delta 2\theta = 0.05°$. Although the data were recorded by the detectors which are 200 mm high, only the data collected at the centre of these detectors were analysed in the work presented in this thesis. For diffraction data collected at low temperature, the sample was mounted inside a cryostat. The use of a rotating sample stage enables the cooling of one sample when another sample is being measured at room temperature.

2.4.4 Neutron diffractometer D1b

D1b is a high intensity powder diffractometer located at ILL. Its schematic drawing is shown in Figure 2.6. Neutron beams with wavelength of 2.52 Å is made available when pyrolyic (002) graphite monochromator with take–off angle at 44.22° is used. The corresponding neutron flux at the sample is about 7.9×10^6 n cm^{-2} s^{-1}. The high neutron flux is achieved at the expense of the resolution in a powder diffraction pattern, and D1b is therefore a good diffractometer to use in order to study weak magnetic Bragg scattering arising from a magnetic sample. The angular range covered by D1b is $0.8 \leq 2\theta/° \leq 128.8$ and the scattered neutrons are captured by a multi–detector with 1280 cells 0.1° apart from

each other. In contrast to D2b, the detector of D1b remains static while a measurement is in progress. A cryostat was again used to cool the sample to a temperature lower than its magnetic transition temperature.

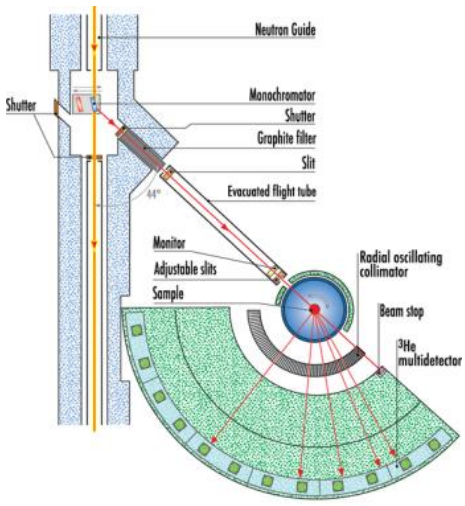


Figure 2.6. Schematic drawing of D1b diffractometer[88].

2.4.5 TOF diffractometer GEneral Material (GEM)

The TOF diffractometer GEM is located at ISIS at Rutherford–Appleton Laboratory. Figure 2.7 shows a schematic drawing of the GEM beamline[89]. The length of the primary flight path of GEM is 17 m, reducing the TOF and flight path contributions to the resolution[89]. Moreover, three disc choppers are installed to ensure the high quality of neutron diffraction pattern. There are eight detector banks on GEM, covering scattering angles from 1.2° to 171.4°. This extensive angular range enables GEM to study disordered materials. Nevertheless, only diffraction data collected from banks 3 (located at 2θ = 34.96°) to 6 (2θ = 154.40°) were analysed.

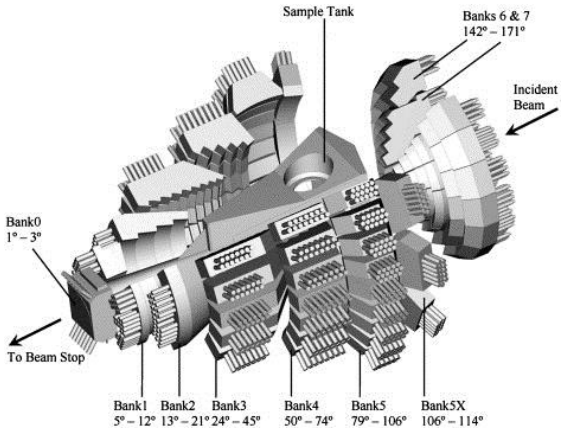


Figure 2.7. Schematic drawing of GEM diffractometer[89].

2.5 Rietveld Analysis

After the collection of diffraction data, it is important to find a way to interpret the patterns accurately. Integration of the total area under the peak could yield the desired crystallographic information[90]. Although this works well for cubic materials, in low symmetry systems multiple reflections can be grouped under one broad peak due to the fact that the data collected is projected onto one–dimension (2θ) and this method will not then be able to solve the problem. Rietveld suggested that the profile intensity at each measured point in a diffraction experiment could be used as the basis for a least–squares refinement of the structure[91, 92]. The prerequisite for a successful Rietveld refinement is a reasonably accurate starting model which consists of the atomic coordinates, unit cell parameters and space group of the material. It is also necessary to know the instrumental peak shape and peak width, otherwise divergence in the iteration process during the refinement will become a possibility[93]. All Rietveld refinements presented in this thesis was done using the General Structure Analysis System (GSAS)[94] with EXPGUI as the interface[95].

In a refinement, the primary goal is to minimize the weighted difference between the observed intensity, $y_{i,O}$, and the calculated intensity, $y_{i,C}$, at the i^{th} step of a diffraction

pattern. The presence of the weighting factor, w_i, is of prime importance as it ensures all points have equal significance in the refinement. This prevents the fit from being dominated by the most intense points. There are several parameters, namely the (un)weighted profile parameter, (R_p)R_{wp} and the reduced chi–squared, χ^2, which indicate how good an account of the data collected the proposed model gives. These dimensionless parameters are labelled as goodness–of–fit parameters and are calculated as follows[96]:

$$R_{\mathrm{wp}} = \sqrt{\frac{\sum_i w_i (y_{i,C} - y_{i,O})^2}{\sum_i w_i y_{i,O}{}^2}} \qquad \text{Equation 2.9}$$

$$\chi^2 = \left(\frac{R_{\mathrm{wp}}}{R_{\mathrm{exp}}}\right)^2 \qquad \text{Equation 2.10}$$

$$R_{\mathrm{exp}} = \sqrt{\frac{N}{\sum_i w_i y_{i,O}{}^2}} \qquad \text{Equation 2.11}$$

where w_i is the weighting factor, R_{exp} is the expected R factor and N is the number of data points collected. In an ideal case, the calculated intensity would be completely superimposed onto the observed intensity, making the difference curve a flat line lying at zero intensity. The goodness–of–fit parameters R_{wp} and χ^2 will then equal 0 and 1 respectively. Note that when reporting the value of R_{wp} it is normally listed as a percentage.

The order of which variables are refined can be crucial. Since the observed intensity in an X–ray powder diffraction (XRPD) pattern has a strong correlation with the atomic number of the element due to the nature of the interaction between X–ray and the material, elements with higher Z values are usually given higher priority in the refinement process. The instrumental parameters tend to vary little and thus they are normally refined at a later stage.

Each reflection generated by the proposed model couples with a background function to account for the calculated intensity $y_{i,C}$ which is also expressed as[97]:

$$y_{i,C} = s\sum_{hkl} L_{hkl}|F_{hkl}|^2\varphi(2\theta_i - 2\theta_{hkl})\,P_{hkl}A_{hkl} + y_{i,B} \qquad \text{Equation 2.12}$$

where s is the scale factor, L_{hkl} is a combination of the Lorentz, polarisation and multiplicity factors, φ is the profile function for the *hkl* reflection, P_{hkl} is the preferred orientation function, A_{hkl} is the absorption factor and $y_{i,\mathrm{B}}$ is the background intensity at the i^{th} step.

The inclusion of a background function is necessary to fit the observed intensity in regions of the pattern where there are no Bragg reflections. A Chebyshev polynomial of the first kind was employed to model the background intensity. Regarding the number of different background terms, it is sample–dependent but normally a 12–term Chebyshev polynomial should be sufficient to model the background intensity recorded.

A more complex feature in the Rietveld refinement is the modelling of the peak shape. As can be seen from above, the peak shape is a function of 2θ. A pseudo–Voigt function, a linear combination of Gaussian (*G*) and Lorentzian (*Lz*) functions, is often used to model the peak shape and can be expressed as[94]:

$$psuedo - Voigt = \eta G + (1-\eta)Lz \qquad \text{Equation 2.13}$$

where η is a weighting factor.

Before proceeding any further, it is worth noting that the profile parameters used for a constant wavelength refinement are slightly different from those of a TOF refinement. For a constant wavelength refinement, the Gaussian (σ) and Lorentzian (γ) components, which model the peak shape, are described by:

$$\sigma^2 = U\tan^2\theta + V\ \tan\theta + W + \frac{P}{\cos^2\theta} + \cdots \quad \text{Equation 2.14}$$

$$\gamma^2 = \frac{X}{\cos\theta} + Y\ \tan\theta + \cdots \quad \text{Equation 2.15}$$

where *U*, *V* and *W* are coefficients proposed by Caglioti *et al*[98] and are labelled as *GU*, *GV* and *GW* in GSAS. *P* is the Sherrer coefficient which describes the broadening effect on a Gaussian peak. *X* and *Y* are parameters which represent broadening effects arising from particle size and strain respectively. The relationship between *X* and the particle size *p* is given in Equation 2.16.

$$p = \frac{18000K\lambda}{\pi X} \quad \text{Equation 2.16}$$

Here λ is the wavelength of the source and *K* is the Sherrer constant. It varies from sample to sample. Nevertheless, a typical value of *K* is 0.9 and the broadening effect was assumed to be isotropic throughout all the refinements reported here. Furthermore, a zero–point correction for the diffractometer should also be included in a Rietveld analysis.

For a TOF refinement, the Gaussian and Lorentzian components are described using a different set of parameters:

$$\sigma^2 = {\sigma_0}^2 + {\sigma_1}^2 d^2 + {\sigma_2}^2 d^4 + \cdots \quad \text{Equation 2.17}$$

$$\gamma = \gamma_0 + \gamma_1 d + \gamma_2 d^2 + \cdots \quad \text{Equation 2.18}$$

where σ_0, σ_1, σ_2, γ_0, γ_1, γ_2 are related to broadening effect from the sample and *d* is the *d*–spacing of the material. Moreover, the diffractometer constants for TOF refinement are different from those in the constant wavelength refinement and are given as follow:

$$t = DIFC\ d + DIFA\ d^2 + ZERO \quad \text{Equation 2.19}$$

where *DIFC*, *DIFA* and *ZERO* are three refinable parameters, *t* is the time of flight in μs. The first term represents the ideal TOF relation between *t* and *d*. The second term is a correction for peak shifts due to neutron absorption and *ZERO* stands for the standard zero point error.

2.6 Micro Structural Determinations: Electron Microscopy

The full structural complexity of a material can be revealed by studying its micro–structure with an electron microscope. Preliminary XRPD analysis had suggested that $Sr_3Fe_2TeO_9$ adopts a tetragonal structure, but an electron microscope study has revealed the co–existence of both tetragonal and trigonal phases in this perovskite[42]. The wavelength of the accelerated electrons in an electron microscope can be as short as 0.037 Å when the accelerating voltage is 100 keV, leading to atomic resolution in the diffraction patterns and/or images. Since the electrons are scattered by the atomic potentials of the atoms in the sample, the scattering power falls off more sharply with $\frac{\sin\theta}{\lambda}$ when compared to X–ray. The types of interactions between the electrons and the matter are summarised in Figure 2.8. Transmission electron microscopy (TEM) was used to study most of the samples reported herein in order to reveal the local structure of each composition and the relationship with the associated magnetic properties. In this section, each specific TEM technique employed in the investigation will be discussed. All the related experiments were carried out by Dr Robert Paria Sena, Ms Mylène Hendrickx and Professor Joke Hadermann at the University of Antwerp.

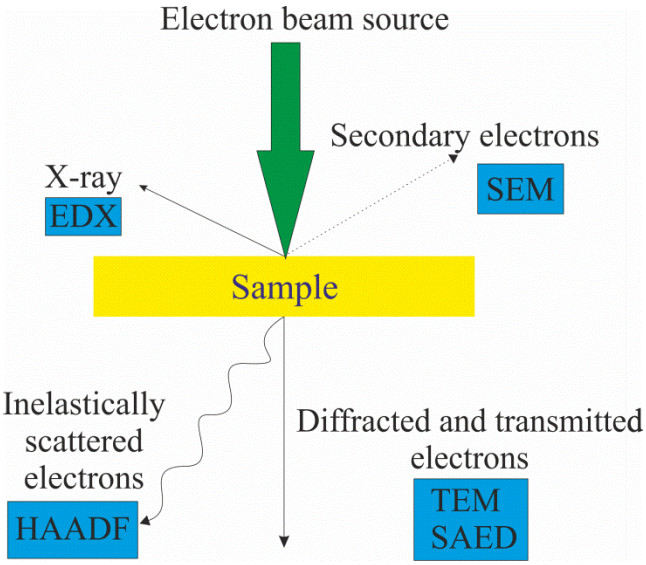


Figure 2.8. Potential applications of using electron as the beam source.

2.6.1 Selected Area Electron Diffraction

Selected area electron diffraction (SAED) is a technique where a particularly selected area of a sample is studied by transmitting a beam of electrons through it. This is achieved by inserting an aperture directly below the selected area of the sample. The SAED patterns included in this thesis were taken with Philips CM20 and EFI Tecnai G2 instruments.

2.6.2 High angle annular dark field scanning transmission electron microscopy

High angle annular dark field (HAADF) imaging allows researchers to study the local arrangement of ions in the sample[99]. This technique involves the selection of a particular type of scattered electrons after their interaction with the material. The image produced from the scattered high–angle electrons in a dark field can reveal the short–range arrangement of atoms in the scanned area. In a dark field image, the heavier elements appear brighter than the lighter because of the stronger scattering with the electron beam. Since the scattering intensity is proportional to the square of the atomic number Z of the ion[100], it enables us to distinguish the atomic identities as long as the difference between different Z values is large enough.

2.6.3 Energy dispersive X–ray scanning transmission electron microscopy

In a way similar to the production of X–rays in an in–house diffractometer, the accelerated electron beam can also excite an electron from the inner shell of the atoms in the sample. The relaxation of the electrons will then emit X–ray photons with an energy which is characteristic of the element itself, allowing qualitative analysis of the sample to be carried out. This is the principle of energy–dispersive X–ray (EDX) analysis.

The EDX detector is often combined with the HAADF–STEM detector. Consequently, when scanning over the sample, an "elemental map" can be produced together with the HAADF images. Both the maps and the HAADF–STEM images presented in this thesis were taken using an FEI Titan 80–300 "cubed" microscope which operates at 300 kV and is equipped with a Super–X detector.

2.6.4 Scanning electron microscopy

Scanning electron microscopy (SEM) makes use of the intensity of the secondary electrons emitted from different parts of the specimen. SEM images were acquired with a JEOL 5590 microscope on a smeared sample over tape which was mounted on a stub of metal. These images were used to study the size of the particles of interest.

2.7 Diffuse scattering

The intensities of the Bragg peaks in a diffraction pattern are weakened if disorder exists in the compound. Here, disorder is a phenomenon that indicates any deviation in a real crystalline material from the perfect periodic arrangement; it could be, for example, stem from thermal vibrations or random local displacements in a structure. The scattering from these "anomalies" appears in the background of the diffraction pattern and is labelled as diffuse scattering. If the disorder is completely random, then the level of diffuse scattering

is independent of the scattering angle. If the disorder involves the formation of regions of short–range order, for example atomic or magnetic clusters, then the diffuse scattering is a function of angle and has broad maxima that can be used to determine the nature of the short–range order.

2.7.1 D7

D7, see Figure 2.9, is a neutron diffractometer that was designed to study the diffuse scattering from a material with structural and/or magnetic short–range ordering[101]. The neutron beam is first monochromated by a double focusing pyrolytic graphite monochromator; wavelengths of 3.1, 4.8 or 5.8 Å are available. After passing through a Be filter, the beam is polarised into the *z* direction by a focusing, *m* = 2.8 Co/Ti Schärpf bender–type[102] supermirror polariser before being scattered by the sample. After the initial data collection, the measurement is repeated with the polarised beam being spin–flipped by a Mezei–type flipper. This is to account for the spin–dependent scattering amplitudes, a component arising from the interaction between the neutron and the nuclei. Afterwards, the same procedure is repeated with the neutron spin having been rotated to the ±*x* and ±*y* directions with the help of three orthogonal XYZ Helmholtz coils. A total of six points is thus collected and the diffraction data can be analysed using the 6–point method[103].

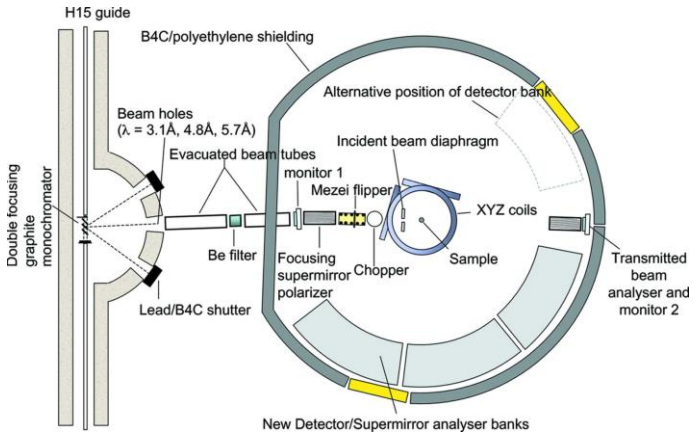


Figure 2.9. Schematic drawing of D7 diffractometer[101].

2.8 Analysis of diffuse scattering

One of the most formidable challenges in modelling for the disorder in a material using diffuse scattering data is to establish an initial model which can accurately represent the average randomness. For example, given there is a lack of any long–range periodic arrangement, the size of the model cannot be easily determined. Certain criteria such as the dominant interaction have to be specified in order to govern the simulation. Two approaches are used in this thesis to simulate the data; direct Monte–Carlo (DMC) which is interaction–driven and reverse Monte–Carlo (RMC) which is data–driven.

DMC is a valuable approach when the parameters of the dominant interaction in a material can be well–defined in the initial model. An expression for the total energy of the system can be formulated and the energy of the initial model can be calculated. The energy of the system is then minimised to give an optimised model by refining variables such as the atomic distribution or spin configuration within the model. In order to achieve this, a move, for example a swap of a randomly chosen pair of cations, is proposed. This move is accepted if certain criteria are met. After several such moves, a comparison is made between the calculated and the observed scattering pattern. If the fit is unsatisfactory, the parameters involved in the energy calculation can be adjusted and the procedure is repeated until satisfactory agreement is achieved.

In contrast, the concept of the RMC, developed by McGreevy and Pusztai[104], emphasises minimizing the difference between the calculated and the observed scattering data. This can be achieved by calculating a goodness–of–fit parameter for the starting model. A new configuration is then computed and is either accepted or rejected by the Metropolis criterion[105]. The process is repeated until the goodness–of–fit parameter, instead of the total energy of the system, is minimised. This approach is gaining a lot of popularity as the

information regarding the dominant interaction is no longer required. It is the method of choice when studying systems in which the interactions are not well–defined.

In this thesis, the program SPINDIFF in the SPINVERT package[106] was employed to deduce the spin configuration of a disordered system using the RMC approach. The orientation, rather than the crystallographic positions, of the spins were given the freedom to vary during the simulation in order to fit the data. In each move, a randomly chosen spin is allowed to rotate by a small amount. The optimal spin configuration is that which gives a converged, minimum goodness–of–fit parameter.

2.9 Muon and muon–spin rotation (μSR)

A muon is a fermion whose spin quantum number is $\frac{1}{2}$. It can be either positively or negatively charged. The positive muon (μ^+) which has a lifetime of 2.2 μs is extremely useful for studying the magnetic properties of a material. This is because Coulombic interactions cause the μ^+ to temporarily occupy an interstitial site which has a negative potential and it can then act as a probe of its local environment[107]. Some of the compounds described in this thesis were studied in muon–spin rotation (μSR) experiments which were performed by Dr Franz Lang and Professor Steve Blundell of the Oxford Physics Department, and Dr Emily Hunter of this department.

In contrast to neutrons or X–rays in a diffraction experiment, the muon is not scattered. Instead, each muon loses all its energy within the crystal without being depolarised. The muon then decays into two neutrinos and one positron in after a time t with a probability proportional to $\exp(-t/\tau_\mu)$, where τ_μ is the lifetime of the muon, see Equation 2.20. As the decay involves the weak interaction, which leads to parity not being conserved, positrons are emitted predominately along the direction of the muon spin over an extensive range of angles.

$$\mu^+ \rightarrow e^+ + \upsilon_e + \bar{\upsilon}_\mu \qquad \text{Equation 2.20}$$

There are generally two scenarios when the muon is fired towards the sample. If the muon decays before reaching the material, a positron will be emitted preferentially into a backward detector (B). If the muon does arrive at the sample, the muon can precess in the presence of an applied magnetic field before its decay. The number of positrons collected by either the backward or the forward detector as a function of time can be described as $N_B(t)$ and $N_F(t)$ respectively. These two quantities combine to give the decay positron asymmetry function $A(t)$ which is defined as:

$$A(t) = \frac{\delta N_B(t) - N_F(t)}{\delta N_B(t) + N_F(t)} \qquad \text{Equation 2.21}$$

where δ is a constant obtained from experimental calibration. If the material is magnetic an external magnetic field is not required. The implanted muons undergo Larmor precession in the local magnetic field of the material. The signals generated will have a frequency which is proportional to the local magnetic field.

All muon–related experiments were carried out using the general purpose surface–muon (GPS) spectrometer[108] at the Paul Scherrer Institute (PSI) in Switzerland and the EMU spectrometer[109] at ISIS. This highlights the two different ways of performing a muon experiment. A continuous muon beam is used at PSI whereas pulsed muon beams are used at ISIS. For the former, muons arrive at the sample intermittently. The decay time is measured for each muon entering the experiment. However, the arrival of a second muon before the first one has decayed results in the event being disregarded as it is impossible to distinguish which muon the detected positron is emitted from. Regarding the pulsed muon beam, an intensive pulse of muons arrives at the sample and the time of each event is recorded with respect to the arrival of the pulse. A drawback of this technique is that there

is an upper limit on the precession frequency it can measure. All the data analyses presented herein were conducted by Professor Blundell and Dr Franz Lang.

2.10 SQUID magnetometry

A Supercoducting QUantum Interference Device (SQUID) is a crucial tool to study the magnetic properties of a material due to its sensitivity; it can measure changes in a magnetic field as small as 10^{-15} T, where 1 T is 10^4 Oe[110, 111]. All the data reported in this thesis were collected using a Quantum Design MPMS *XL* device.

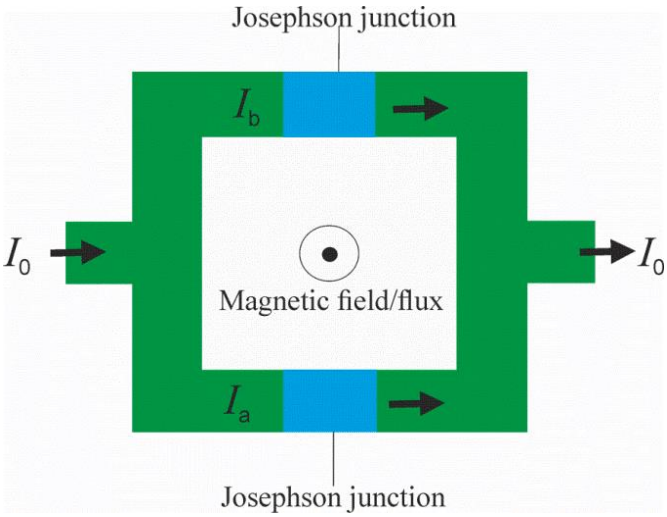


Figure 2.10. A schematic drawing of the SQUID device.

A schematic drawing of a SQUID device is illustrated in Figure 2.10. An input current, I_0, is split into two equal components when it passes through the superconducting loop, which contains two insulating Josephson junctions[112, 113], in the absence of an external magnetic field. If a magnetic field is now switched on, an induced current, I_i, which generates a magnetic field to oppose the external field is formed. One half on the ring will then has a current of $I_a = \frac{I_0}{2} + I_i$ whereas the other half $I_b = \frac{I_0}{2} - I_i$. When either one of the branches has a current that exceeds a critical value, I_c, the superconducting Cooper pairs of electrons[7, 8] penetrate the Josephson barrier by quantum tunnelling[114] and a voltage is

produced across the loop. If there is a perturbation on the magnetic field, or to be specific the magnetic flux Φ, the change in voltage ΔV can be measured. The perturbation can be caused by moving a sample through a set of detector coils or by applying an alternating magnetic field.

If the sample was considered to be pure enough, 30 – 50 mg of the reaction product was loaded into a gelatine capsule. This capsule was then mounted into a plastic straw, surrounded by four empty capsules under and above it. This was to ensure the sample environment was relatively constant. The empty capsules were pierced so that they could be evacuated, thus preventing paramagnetic oxygen from blemishing the measurement. The sample mounting was then attached to a rod such that it could be moved through the detector coils.

2.10.1 dc magnetometry

Two types of dc magnetometry measurements were carried out. Firstly, the magnetic moment of the sample was measured as a function of temperature with the sample having been cooled without (Zero–Field Cooling, ZFC) or with (Field Cooling, FC) the magnetic field switched on. The temperature range covered was $2 \leq T/\mathrm{K} \leq 300$ and the field used was 100 Oe unless otherwise specified. The magnetic moment recorded in each step was the average value from four scans.

Secondly, the field dependence of the magnetisation per formula unit (f.u.) of the sample was measured. The sample was first cooled to the desired temperature under a field of 50 kOe. The magnetic moment of the sample was then recorded with the field sweeping from 50 kOe to –50 kOe then back to 50 kOe. If a hysteresis loop formed, the coercive field and the remanent moment were determined.

2.10.2 ac magnetometry

The difference between ac and dc magnetometry experiments is the presence of an applied oscillating magnetic field with a frequency ω in the former. This oscillating field is normally very small in terms of strength; the drive field used in the measurements reported in this thesis was 3.5 Oe. The applied magnetic field now consists of two components: a static and a time–dependent component[115], see Equation 2.22. Therefore, the magnetic susceptibility is a function of both temperature and frequency.

$$H(t) = H_0 + H_1 \sin \omega t \qquad \text{Equation 2.22}$$

At low frequencies, the rate of spin–flip is fast enough that the change in the magnetisation of the sample responds in–phase with the field. This resembles the dc measurement. At a much higher frequency, the detected magnetic moment may lag behind the field due to the dynamic properties of the sample. As a result, two quantities are produced, namely the magnetic susceptibility χ and the phase difference φ. χ can be split into two components: the real component χ' which represents the dispersion of the sample and the imaginary component χ" which is usually referred to as the absorption susceptibility. The relations among these four quantities are shown below:

$$\chi' = \chi \cos \varphi \qquad \text{Equation 2.23}$$

$$\chi'' = \chi \sin \varphi \qquad \text{Equation 2.24}$$

$$\chi = \sqrt{\chi'^2 + \chi''^2} \qquad \text{Equation 2.25}$$

$$\varphi = \tan^{-1} \frac{\chi''}{\chi'} \qquad \text{Equation 2.26}$$

Ac magnetometry measurements were normally conducted over the temperature range $2 \leq T/\text{K} \leq 150$ unless specified. The range was selected to ensure the data collection could

capture the magnetic susceptibility below, at and above the transition temperature of the sample. The oscillating field was alternating at frequencies of 1, 10, 100 and 1000 Hz. However, the data collected at 1000 Hz may not necessarily be included in the data analysis due to a poor signal to noise ratio. Since the static field used was very weak (H_0 = 3 Oe), it was necessary to verify accurately the static magnetic field. To achieve this, the magnetic moment of some dried gadolinium oxide, Gd_2O_3, was measured with the weak dc field switched on at 300 K. The paramagnetic phase of Gd_2O_3 is well–documented, and so the static field can be measured accurately[116, 117]. The principal purpose of the ac magnetometry measurements described in this thesis was to distinguish between antiferromagnets, spin glasses and ferromagnets. An antiferromagnet has χ" = 0 and the susceptibility is independent of ω. Spin glasses and ferromagnets both have non–zero χ" and the ac susceptibility is a function of ω. However, the Curie temperature of a ferromagnet is independent of ω whereas the freezing temperature of a spin glass is a function of ω. Mydosh has proposed that the frequency shift of a spin glass can be expressed by a parameter, $\frac{\Delta T_f}{T_f \Delta(\log \omega)}$, where ΔT_f is the change in T_f and $\Delta(\log \omega)$ reflects the change in per decade ω[118]. A typical canonical spin glass is not very sensitive to the change in frequency and the value obtained from the equation above is approximately 0.01[118].

Chapter 3: Analysis of the short–range cation ordering in $La_3Ni_2SbO_9$

3.1 Introduction

$La_3Ni_2SbO_9$ was first described by Alvarez *et al.* as an orthorhombic structure with a random distribution of Ni^{2+} and Sb^{5+} over the octahedral *B* sites (space group: *Pbmn*)[119]. They concluded that spin canting was responsible for the ferromagnetic component observed in their magnetic susceptibility measurements, despite the fact that antiferromagnetic interactions are expected to dominate within the crystal structure. However, recent studies have revealed that the Ni^{2+} and Sb^{5+} cations are ordered in a rock–salt arrangement and the structure was assigned to the monoclinic space group $P2_1/n$[48, 120, 121]. In this structure, the *B* site in *Pbmn* is separated into two inequivalent sites and the distribution of Ni^{2+} and Sb^{5+} is similar to the positional ordering in the aforementioned relaxor ferroelectric $Pb_3MgNb_2O_9$ (PMN); one of the sites is fully occupied by Ni^{2+}, within standard deviation, and the remaining *B*–site cations are randomly distributed on the other site.

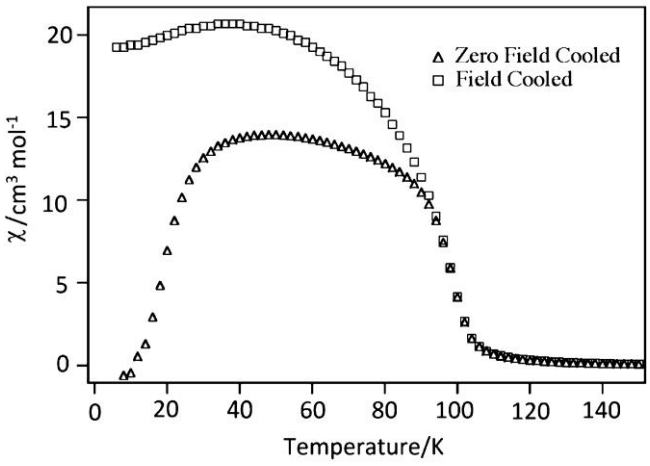


Figure 3.1. The temperature dependence of dc molar susceptibility of $La_3Ni_2SbO_9$[48].

The magnetic properties of $La_3Ni_2SbO_9$ were studied in detail by ac and dc magnetometry[48]. The magnetic susceptibility increases markedly below 105 K, see Figure 3.1, and the data collected under ZFC and FC conditions differ at low temperatures. The effective magnetic moment per Ni^{2+} cation and the Weiss temperature deduced from fitting the high temperature data to the Curie–Weiss Law were reported to be 2.2(1) μ_B and +159 K respectively. $M(H)$ was measured at 5 K in an applied field of $-50 \leq H/\text{kOe} \leq +50$ and a magnetisation of approximately 1.5 μ_B per formula unit was measured in a field of 40 kOe. The ac susceptibility is complex below the magnetic transition temperature, which is independent of the frequency of the oscillating magnetic field. It was proposed that, even though the dominant nearest–neighbour superexchange interaction is antiferromagnetic in nature, the fact that one of the octahedral sites is fully occupied by Ni^{2+} whereas the other is only 33 % occupied by Ni^{2+} creates an imbalance of spins aligning anti–parallel to each other, leading to the formation of a ferrimagnet. However, any magnetic Bragg scattering was too weak to be observable in a neutron diffraction pattern recorded in the absence of an applied magnetic field at 5 K using diffractometer D2b. This suggests that the antiferromagnetic interaction is short–range despite the presence of structural ordering between the Ni^{2+} and the Sb^{5+} cations. It was later discovered that the intensity of the magnetic Bragg peak increases with increasing strength of an applied magnetic field[75]. The local structure was examined using transmission electron microscopy, see Figure 3.2, and it shows the presence of Sb–rich regions within the crystal structure. It was proposed that these compositionally unusual regions act as domain walls which in turn disrupt the antiferromagnetic coupling between the Ni^{2+} cations as the concentration of nearest–neighbour Ni^{2+} cations is diluted. The next–nearest–neighbour magnetic interaction, and perhaps even the third–nearest–neighbour coupling, then becomes more influential. The competition among these interactions causes local spin frustration and long–range

magnetic ordering is only detectable when the net magnetic moments in each domain are aligned parallel by an applied magnetic field. Otherwise, the size of the magnetic domain could be too small to be detectable. PMN is structurally similar to $La_3Ni_2SbO_9$ and it contains nano–polar regions[122] which give rise to a net electric polarisation in the presence of an electric field. The structural distortion that gives rise to the ferroelectric properties of PMN occurs in small domains that do not give rise to Bragg peaks in an X–ray diffraction pattern[46] but the polarisations of these domains are aligned by an external electric field. The similarities between the relaxor ferroelectric PMN and $La_3Ni_2SbO_9$ lead to the latter being described as a "relaxor ferromagnet".

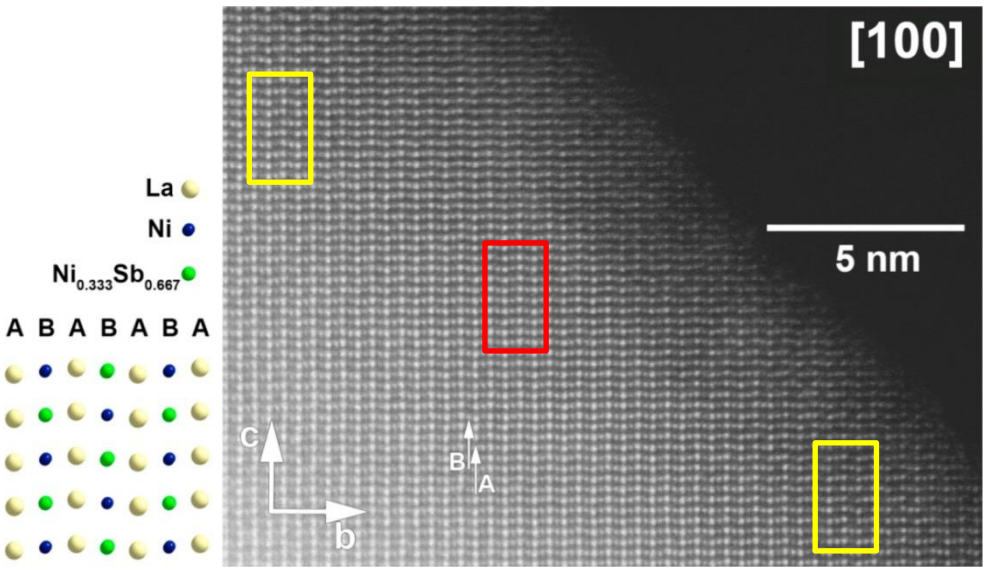


Figure 3.2. HAADF–STEM image of $La_3Ni_2SbO_9$. Areas of (*B,B′*) cation–ordering can be seen on the left and right of the image (yellow rectangles), but no such ordering is seen in the middle of the image (red rectangle). A [100] projection of the cation–ordered structure is shown to the left of the image[75].

Local deviations from the average crystal structure can also be investigated by analysing the diffuse scattering embedded in a diffraction pattern. In contrast to the sharp Bragg peaks that define the average structure, features in the diffuse scattering are usually broad and weak; consequently they are often treated as background scattering. However, analysis of this scattering can elucidate the short–range structural ordering present in a material and,

if a polarised neutron beam is used, short–range magnetic ordering can also be studied. Computational models can be constructed to simulate both the structural and magnetic scattering in order to elucidate the short–range order. In this chapter a study of $La_3Ni_2SbO_9$ carried out using this methodology is described.

3.2 Experimental

Approximately 5 g of polycrystalline $La_3Ni_2SbO_9$ were synthesised by the ceramic method described previously by Battle *et al.*[48] from a stoichiometric mixture of Sb_2O_5, NiO and pre–dried La_2O_3. The powder mixture was pelletised and heated at 1250 °C for nine days with intermediate grinding. X–ray powder diffraction pattern (XRPD) data were collected with Cu $K_{\alpha 1}$ radiation (λ = 1.54051 Å) using a PANalytical Empyrean diffractometer operating at room temperature. The angular range covered was $15 \leq 2\theta/° \leq 125$ with step–sizes, $\Delta 2\theta$, of 0.0066°. The XRPD patterns were analysed using the Rietveld method[92], as implemented in the GSAS program suite[94]. The background level of each pattern was modelled by a 12–term shifted Chebyshev function and the peak shapes were fitted with a pseudo–Voigt function[123]. The dc molar susceptibility and the field dependence of the magnetisation of the product were measured, as described in Chapter 2, to ensure that this sample was consistent with that used in the earlier studies.

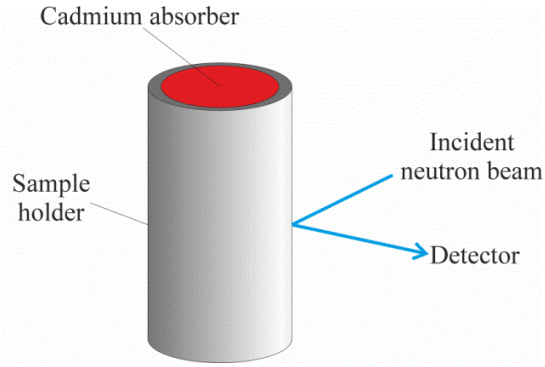


Figure 3.3. Calibration using cadmium. Cadmium is a strong neutron absorber, and hence the only signal the detector picks up should theoretically be those reflected from the sample holder.

Polarised neutron scattering data were collected with a wavelength λ = 4.853 Å using the D7[101] diffractometer located at ILL, Grenoble. The Q range covered was $0 \leq Q/\text{Å}^{-1} \leq 2.5$ with a step–size, $\Delta 2\theta$, of 0.5°. For each data point, an *xyz*–polarisation measurement was conducted. This method allows the separation of the structural and the magnetic contributions to the total neutron scattering pattern via mathematical calculation[103].

In order to maximise the efficiency of the data collection, the sample was mounted in an annular aluminium can. However, a number of calibration measurements were done before the sample was loaded. Firstly, data were collected from an empty can, and then from a can containing a neutron–absorbing cadmium rod[85], see Figure 3.3. These measurements allowed the determination of the intensity of the scattering from the can.

Further calibrations involved data collection from quartz (SiO_2) block. The diamagnetic nature of quartz means the neutron scattering from the block will be entirely nuclear in origin, and hence there should be no spin–flip scattering[124]. This enables a calibration to account for imperfect polarisation. Finally, the transmission of all the materials was measured to ensure that there were no undesired contributions to the scattering.

After all calibrations had been accomplished, the polarised neutron scattering experiment was carried out at 110 K, slightly above the magnetic transition temperature of 108 K[48]. Another set of data was collected at 175 K.

3.3 Results

Figure 3.4 shows the XRPD pattern of the polycrystalline $La_3Ni_2SbO_9$ sample. It could be modelled as a monoclinic crystal structure with space group $P2_1/n$. The refined unit cell parameters were a = 5.6037(1) Å, b = 5.6336(1) Å, c = 7.9326(1) Å, β = 90.01(1)° and V = 250.422(8) Å^3. These values are in good agreement with those published by Battle *et al*..

During the refinement the occupancy of Ni/Sb on the two distinct octahedral sites were fixed as per the model published before. The structural refinement parameters χ^2 and R_{wp} were 3.76 and 0.123 respectively. 0.20(6) wt. % of NiO[125] and 0.55(5) wt. % of La_3SbO_7[126] impurities were found in the mixture. The magnetic susceptibility and the field dependence of the magnetisation of the sample, see Figures S3.1 and S3.2, were consistent with the data presented in the literature.

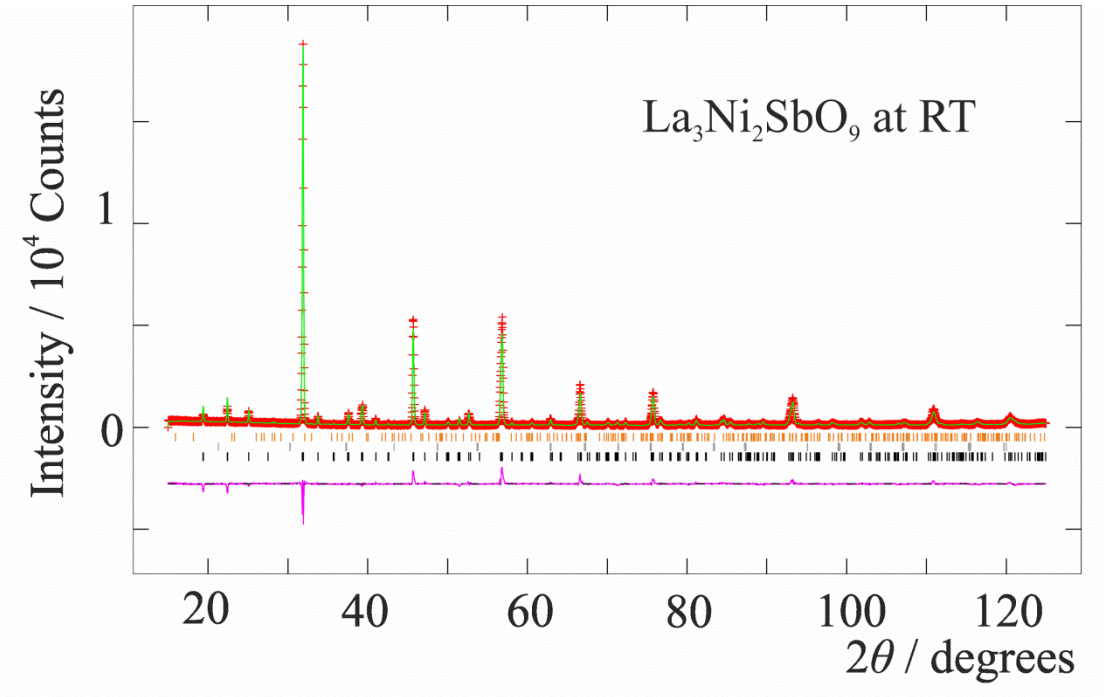


Figure 3.4. Observed (red crosses) and calculated (green line) XPRD profiles of $La_3Ni_2SbO_9$ at room temperature. A difference curve (purple) is shown below. Reflection markers are shown for the La_3SbO_7 (top, orange), NiO (middle, grey) and the principal perovskite phase (bottom, black).

Figure 3.5 shows the nuclear coherent and isotopic incoherent scattering, which are inseparable using the *xyz* method[103]. As a result of the presence of two impurity phases, all intensity data in this chapter are presented in arbitrary units rather than in absolute units. Apart from the broad scattering observed at $0.5 \leq Q/\text{Å}^{-1} \leq 1.0$, which is emphasised in the inset of Figure 3.5, the diffraction pattern was compatible with the previous result[48]. A Bragg peak from the La_3SbO_7 impurity[126] is located at Q ~2.0 Å^{-1}.

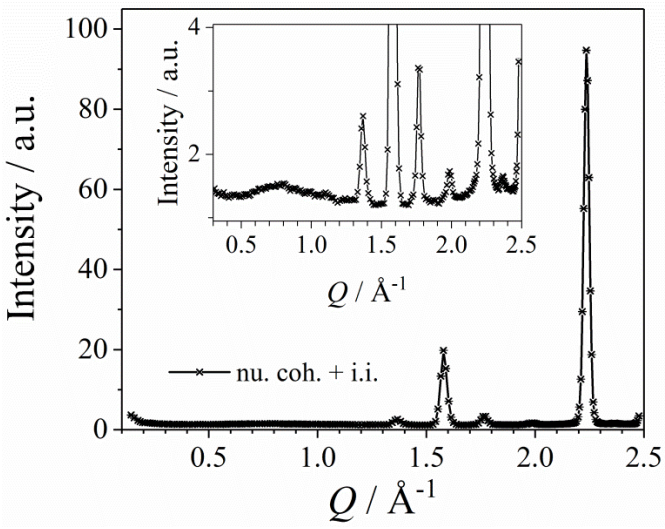


Figure 3.5. The nuclear coherent and isotopic incoherent scattering pattern for $La_3Ni_2SbO_9$ at 110 K, information regarding short–range order of the sample is embedded in the broad peak observed at $0.5 \leq Q/Å^{-1} \leq 1.0$, see inset.

The analysis of the scattering data was split into two parts; the nuclear and the magnetic scattering datasets. Analysis of the former focussed on the broad diffuse scattering, which is partially embedded with the background scattering, rather than on the sharp Bragg reflections. The diffuse scattering occurs in the range $0.5 \leq Q/Å^{-1} \leq 1.0$, and it contains information regarding the short–range distribution of Ni/Sb over the six–coordinate site that they both occupy. In order to determine the short–range structural information, a model which would give rise to the observed scattering was generated using a Monte–Carlo (MC) approach. A cubic perovskite supercell with a chosen number of octahedral sites along each cell edge was set up as the structural template for direct Monte–Carlo (DMC) simulations. The ratio of the total number of Ni^{2+} cations to Sb^{5+} cations was fixed at 2:1 in order to be consistent with the chemical composition of $La_3Ni_2SbO_9$. Given that the well–ordered La^{3+} and O^{2-} sublattices do not contribute to the diffuse scattering, these two types of ions were omitted at this stage of the analysis for simplicity. Alternate sites along the three cube axes were constrained to be occupied by Ni^{2+} cations. This represents

the fact that there is a 100 % chance, within statistical error, of having a Ni^{2+} cation at the 2*c* site in $La_3Ni_2SbO_9$[48]. Then the remaining Ni^{2+} and Sb^{5+} cations were distributed over the remaining sites (2*d* sites) of the supercell in a random fashion. Once the initial model was set up, the initial energy E_0 was calculated. This was done by assigning Sb^{5+} and Ni^{2+} cations to have pseudo–charges represented by $e = +1$ and $e = 0$, respectively. The energy of the system was then taken to be summation of the product of all the next–nearest–neighbour pairs:

$$E = \sum_{i \neq j}^{n} e_i e_j \qquad \text{Equation 3.1}$$

Here, e_i and e_j represent the pseudo–charges of the ions at the sites *i* and *j* respectively. Repeating pairs were ignored to avoid double calculation of the energy. It was then assumed that the energy of the supercell was governed only by the electrostatic interactions between the highly charged Sb^{5+} cation and the number of Sb^{5+}–Sb^{5+} pairs with a separation of $\sqrt{2}a_p$, where a_p is the unit cell parameter of a primitive cubic perovskite, was therefore minimised during the simulation. This was achieved by increasing the total energy of the supercell whenever such a pair was created within the MC process which began when a random Sb^{5+} cation on a 2*d* site was chosen to swap with a Ni^{2+} cation on a different 2*d* site. The energy of the new configuration, E_1, was then calculated. The modified structure was accepted if E_1 was lower than E_0. Otherwise, a number was randomly generated and treated as a probability. The destabilising exchange of Ni/Sb cations was only accepted when this number was less than 0.005, a value that functioned as an effective temperature in the MC simulations. Every successful or accepted swap was considered as a "move". This process was repeated until the MC loop had performed a selected number of moves. At this stage the La^{3+} and O^{2-} ions were added to the model and a diffraction pattern was then generated using CrystalDiffract[127]. This whole process was

repeated to give a total of ten independently–generated cation configurations. The ten generated patterns were then normalised against the data collected. A *Q*–dependent background function was also inserted in each case. This function can be divided into three parts and is expressed as follows:

$$f(Q) = \begin{cases} -0.1306Q + 1.394 & at \quad 0.5 \leq Q \leq 1.45 \\ 1.2 & at \quad 1.45 < Q \leq 2.1 \\ 1.35 & at \quad 2.1 < Q < 2.5 \end{cases} \qquad \text{Equation 3.2}$$

This process was repeated using supercells of different size and with different numbers of allowed moves.

Figure 3.6 shows the simulated nuclear diffuse scattering patterns generated from a *n*×*n*×*n* cubic supercell with *n* being 8, 12, 16 and 20. The simulated diffuse scattering is a function of both the size of the supercell and the number of moves in the DMC loop. All of these DMC simulations were firstly done with a fixed number of moves (2000). When *n* is below 16, the simulated patterns consists of a small number of discrete, relatively intense peaks that do not model the broad feature observed in the nuclear diffuse scattering in a satisfactory manner. When the supercell is large enough to give meaningful results, different combinations of cell size and the number of allowed moves can provide reasonable fits to the observed data. Various combinations were tested and the best nuclear model was produced from a 20×20×20 supercell with 3000 moves allowed in the DMC simulations. There was no significant improvement when the number of allowed moves was increased further. The scattering patterns shown in Figure 3.6 are, in each case, the average of the patterns calculated from the ten DMC calculations that were performed for each value of *n* in order to minimise statistical errors. Figure 3.7 shows the cation distribution in a slice of one of the ten cells generated in the calculations with *n* = 20. There are regions showing hints of a checkerboard arrangement of Ni/Sb in this supercell,

see the blue rectangle in Figure 3.7. This does not represent a failure of the energy constraint set in the DMC calculations because there is no way to arrange the cations so as to completely avoid Sb/Sb next–nearest–neighbour pairs and, furthermore, the simulation was performed at a finite temperature so violations must be allowed. This is compensated for by regions which can be considered to be Ni clusters, see the orange square in Figure 3.7. This particular nuclear configuration was analysed using a site correlation function and was chosen to be the nuclear template for the magnetic diffuse scattering analysis, see below. The average of the nuclear diffuse scattering patterns calculated for n = 20 from the ten independent nuclear configurations, with an appropriate background function included, were normalised and plotted against the observed data at 110 K, see Figure 3.8. The diffraction pattern of La_3SbO_7 was also included; no Bragg peaks characteristic of NiO were observed.

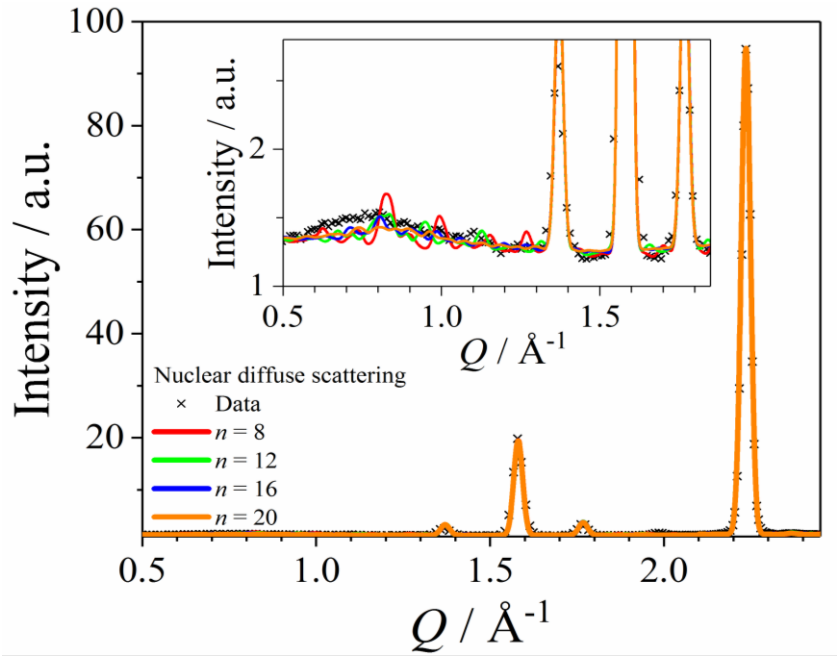


Figure 3.6. The simulated nuclear diffraction pattern for supercells of $La_3Ni_2SbO_9$ of different dimensions after DMC simulation of 2000 moves. n is the number of octahedral sites present on each edge of the cubic supercell. The red, green, blue and orange lines represent the diffraction patterns when n = 8, 12, 16 and 20 respectively. The crosses are the observed data points.

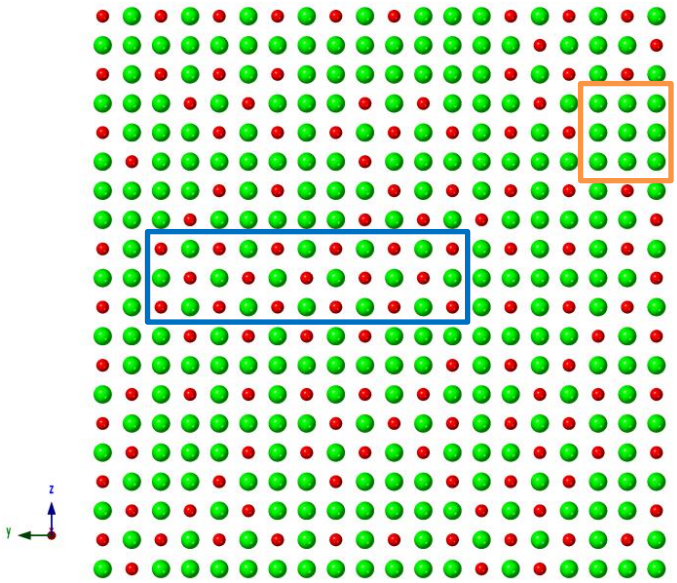


Figure 3.7. The view of a slice of the supercell ($0.3 \leq x \leq 0.35$, $0 \leq y \leq 1$, $0 \leq z < 1$) of $La_3Ni_2SbO_9$ with n = 20 in the x–direction. It shows the Ni/Sb distribution after a DMC simulation. The green and red spheres represent the Ni^{2+} and Sb^{5+} cations, respectively. The blue rectangle indicates a region with 5.5 Å Sb–Sb contacts whereas the orange square shows a Ni–cluster which compensate for the existence of an Sb–rich region.

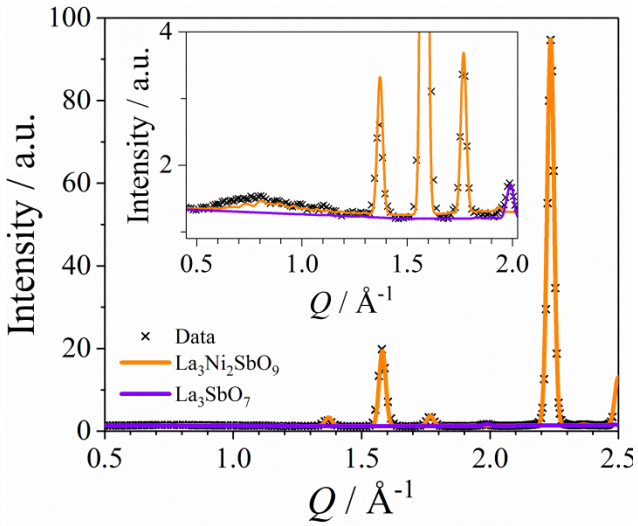


Figure 3.8. The simulated nuclear diffraction pattern for supercells of $La_3Ni_2SbO_9$ when n = 20. The DMC simulation was terminated after 3000 moves. The orange and violet curves represent the average diffraction pattern of ten independent supercells of $La_3Ni_2SbO_9$ and the diffraction pattern of La_3SbO_7[126]. A simple variable background function was included in the simulated diffraction pattern. The crosses are the observed data points at 110 K.

The site correlation function of this particular nuclear configuration is displayed in Figure 3.9. It was calculated using a program written by Professor Andrew Goodwin of this department, primarily for calculating spin–correlation functions. In order to use it to calculate an atomic distribution function, Ni^{2+} and Sb^{5+} were assigned pseudo–spin vectors of $\begin{pmatrix}0\\0\\1\end{pmatrix}$ and $\begin{pmatrix}0\\0\\-1\end{pmatrix}$ respectively. The function $g(r_{ij})$ in this case can be understood as the summation of all the possible atomic pairing combinations at distance r_{ij}:

$$g(r_{ij}) = \sum P_i s_i P_j s_j \qquad \text{Equation 3.3}$$

Here P_i (P_j) and s_i (s_j) represent the probability of having either a Ni^{2+} or Sb^{5+} cation at site i (j) and the corresponding assigned virtual pseudo–spin vector, respectively. As can be seen in Figure 3.9, the correlation function reaches $\frac{-1}{3}$ at almost every alternate point. Each of these distances corresponds to the pairing between a Ni^{2+} cation at a 2*c* site and a cation, either a Ni^{2+} or Sb^{5+} cation, at a 2*d* site. The probability of having a pseudo–spin 'up' vector $\begin{pmatrix}0\\0\\1\end{pmatrix}$ at the 2*c* site is unity. Since the ratio of Ni to Sb at the 2*d* site was fixed as 1:2 because of the chemical composition of $La_3Ni_2SbO_9$, the probabilities of having spin 'up' and 'down' vectors at this site will be $\frac{1}{3}$ and $\frac{2}{3}$, respectively. Taking the negative sign in the spin 'down' vector into account, $g(r_{ij})$ for this 2*c*–2*d* pairing is:

$$g(r_{ij}) = \left(\frac{1}{3}\right)(+1)(1)(+1) + \left(\frac{2}{3}\right)(-1)(1)(+1)$$

$$= -\frac{1}{3} \qquad \text{Equation 3.4}$$

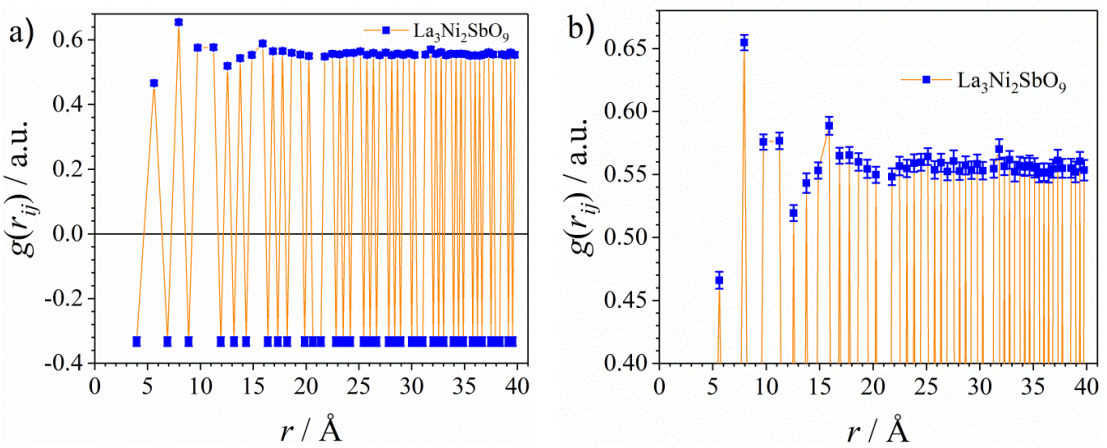


Figure 3.9. (a) The site correlation function of a particular nuclear configuration of an n = 20 supercell after a DMC simulation. (b) An expansion of the range of $0.4 \leq g(r_{ij}) \leq 0.68$.

For 2*c*–2*c* and 2*d*–2*d* pairings, when there is no correlation between two *B* sites, the probability of having either a Ni^{2+} or Sb^{5+} is entirely governed by the stoichiometric ratio at sites *i* and *j*. Consequently, $g(r_{ij})$ can be calculated as follows:

$$g(r_{ij}) = [(2d - 2d)\ pairings] + [(2c - 2c)\ pairings]$$

$$= [(\mathrm{Ni}_{2d} - \mathrm{Sb}_{2d})\ pairings + (\mathrm{Sb}_{2d} - \mathrm{Sb}_{2d})\ pairings + (\mathrm{Ni}_{2d} - \mathrm{Ni}_{2d})\ pairings] + [(\mathrm{Ni}_{2c} - \mathrm{Ni}_{2c})\ pairings]$$

$$= \frac{1}{2}\left[\left(\frac{1}{3}\right)(+1)\left(\frac{2}{3}\right)(-1) + \left(\frac{2}{3}\right)(-1)\left(\frac{1}{3}\right)(+1) + \left(\frac{2}{3}\right)(-1)\left(\frac{2}{3}\right)(-1) + \left(\frac{1}{3}\right)(+1)\left(\frac{1}{3}\right)(+1)\right] + \frac{1}{2}[(1)(+1)(1)(+1)]$$

$$= \frac{+5}{9} \qquad \text{Equation 3.5}$$

Hence, with the exception of the 2*c*–2*d* site pairings described by Equation 3.4, $g(r_{ij})$ is expected to take a value of $\frac{+5}{9}$ in the absence of short–range ordering. In fact, $g(r_{ij})$ fluctuates around $\frac{+5}{9}$ when $r < 15$ Å and $g(r_{ij}) \sim \frac{+5}{9}$ when $r > 15$ Å. The data thus show that short–range correlations exist in the cation distribution when $r < 15$ Å. When $g(r_{ij}) < \frac{+5}{9}$, it

indicates that the interatomic vectors are more likely to have a Ni^{2+} cation at one end and an Sb^{5+} cation at the other end. In contrast, there is a high probability of having the same type of cations at both ends of the vector if $g(r_{ij}) > \frac{+5}{9}$.

The magnetic scattering from $La_3Ni_2SbO_9$, after appropriate initial processing and binning, is shown in Figure 3.10. A broad peak can be seen where $1.0 \leq Q/Å^{-1} \leq 1.7$; this peak lies under a non–magnetic Bragg peak when the experiment is performed using unpolarised neutrons. Thus there is a magnetic contribution to the diffraction pattern even though the sample was slightly above the transition temperature. No magnetic scattering from the NiO impurity was observed. Both DMC and reverse Monte–Carlo (RMC) approaches were then used to study the spin configuration of the paramagnetic Ni^{2+} cations.

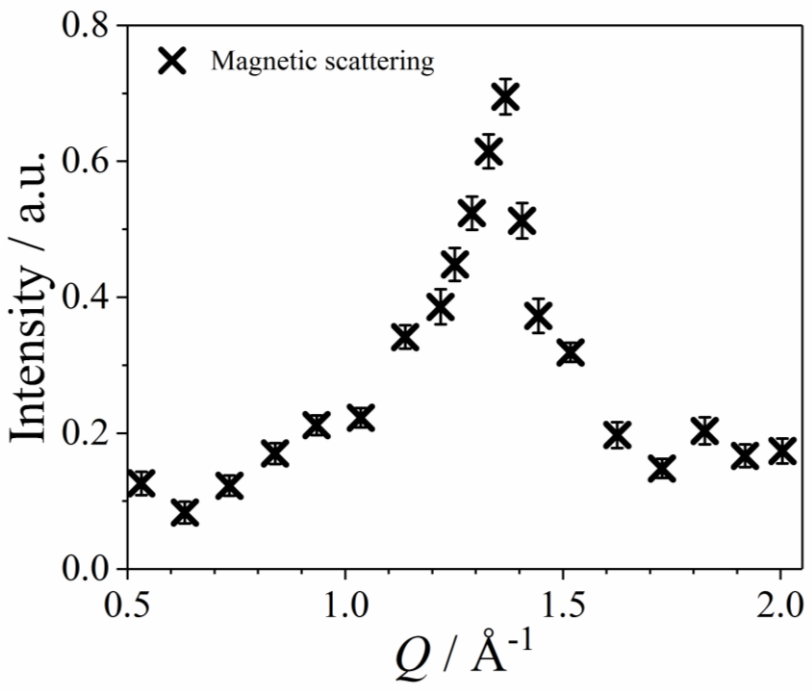


Figure 3.10. Magnetic scattering from $La_3Ni_2SbO_9$ at 110 K.

The magnetic scattering was first analysed using the program SPINDIFF in the SPINVERT package[106], which implements a RMC algorithm[104]. A supercell of 20×20×20 octahedral sites was populated with one of the ten Ni/Sb distributions generated by refining

the nuclear diffuse scattering as described above. Since the Sb^{5+} cation is diamagnetic, only the paramagnetic Ni^{2+} cations, and hence a total of 5334 spin vectors, were present in this cell. Each Ni^{2+} cation was assigned a random spin orientation and the corresponding scattering pattern was calculated. The sum of squared residuals $\chi_{\mathrm{RMC}}{}^2$ was calculated as follows:

$$\chi_{\mathrm{RMC}}{}^2 = W \sum_Q \left[\frac{sI_{\mathrm{calc}}(Q) - I_{\mathrm{expt}}(Q)}{\sigma(Q)}\right]^2 \qquad \text{Equation 3.6}$$

where $I_{\mathrm{calc}}(Q)$ and $I_{\mathrm{expt}}(Q)$ represent the calculated and experimental values of powder–averaged magnetic scattering intensity, $\sigma(Q)$ is an experimental uncertainty, s is a refined overall scale factor and W is an empirical weighting factor. The latter is a parameter which determines how closely the refinement will attempt to fit the data[106]. The spin vector of a Ni^{2+} cation was then chosen randomly and was allowed to rotate by a small amount. This proposed move was either accepted or rejected according to the METROPOLIS algorithm[128]. This process was repeated until no further reduction in $\chi_{\mathrm{RMC}}{}^2$ was observed. 100 proposed moves per spin were performed in all refinements, and all the calculated magnetic diffuse scattering patterns were averaged over ten independent initial spin configurations in order to minimise the statistical noise. Two different values were used for W, 100 and 10000.

DMC simulations were also performed to study the magnetic short–range ordering in $La_3Ni_2SbO_9$ at 110 K. The DMC and RMC simulations shared the same nuclear template, and hence there was again a total of 5334 spins in the supercell. A spin configuration was initialised with random spin orientations in an algorithm which subsequently cooled the sample at a rate of:

$$T_i = (0.9)^i T_0 \qquad \text{Equation 3.7}$$

where T_i is the temperature at the i^{th} step of the algorithm and T_0 is the initial temperature which was set to 200 K in all DMC simulations. Spins were allowed to rotate at each temperature for equilibration. If equilibrium was not reached, the simulations were terminated. After each move, the energy was calculated using Equation 3.8

$$E = -\frac{1}{2}\sum_n \sum_{i,j} J_n \boldsymbol{S}_i . \boldsymbol{S}_j \,, \qquad \text{Equation 3.8}$$

where J_n is the superexchange constant between n^{th} nearest neighbours and $\boldsymbol{S}_i$and $\boldsymbol{S}_j$ represent the spins of the n^{th} nearest neighbours at the i^{th} and j^{th} sites. Different ratios of the relative strength of the superexchange interactions were used in different DMC runs. The magnetic diffuse scattering was calculated using SPINDIFF from six independent spin configurations generated by successive DMC simulations.

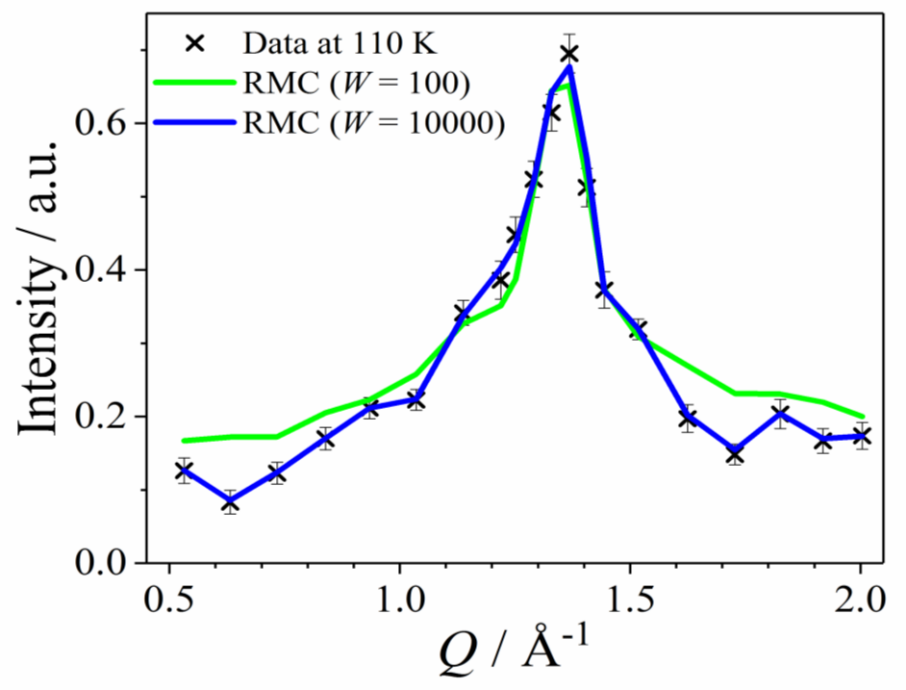


Figure 3.11. The simulated magnetic scattering pattern for $La_3Ni_2SbO_9$ using RMC simulations. The green and blue curves represent the RMC simulation with the weighting factor *W* being 100 and 10000. The crosses represent the data points at 110 K with the associated error bars.

Magnetic diffuse scattering patterns were calculated from various spin configurations which had been generated using the RMC approach with the weighting factor, *W*, being 100 or 10000, see Figure 3.11. In latter case, the calculated pattern fitted both the width and the intensity of the peak.

Although the RMC calculations described above account for the observed scattering, they give no information about the relative strengths of the magnetic coupling constants, J_n, that operate within the structure. However, this information can be deduced from the results of the DMC calculations.

In contrast to the RMC approach, the magnetic exchange constants between pairs of spins J_n must be defined before a DMC simulation. Figure 3.12 illustrates the four shortest distances between a Ni^{2+} cation occupying a 2*c* site (bottom left corner) and other Ni^{2+} cations. J_1 is the interaction between nearest–neighbour Ni^{2+} cations and this interaction was assumed to be as strongly antiferromagnetic as are the Ni–O–Ni interactions found in NiO[62]. However, this analogy is not perfect because the bond distances and bond angles in $La_3Ni_2SbO_9$ are slightly different from those in NiO. The local environment could also have an effect on the strength of this magnetic interaction. Nevertheless, J_1/k_B was given a fixed value of –221 K[62] in all cases. J_3 is the interaction with the third–nearest–neighbour paramagnetic cation which is approximately 6.9 Å away. The distance between them is relatively long. Moreover, the superexchange pathway for J_3 involves at least three oxide anions. As a result, J_3 was considered to make a negligible contribution to the magnetic coupling and was given a value of zero in all DMC simulations. J_2 and J_4 are the 90° and linear Ni–O–*B*'–O–Ni superexchange interactions, respectively. They can be significant in an ordered double perovskite if the *B*' cation is diamagnetic, for example[129, 130] W^{6+} or Te^{6+}. DMC calculations were performed with a number of different values for J_2 and J_4.

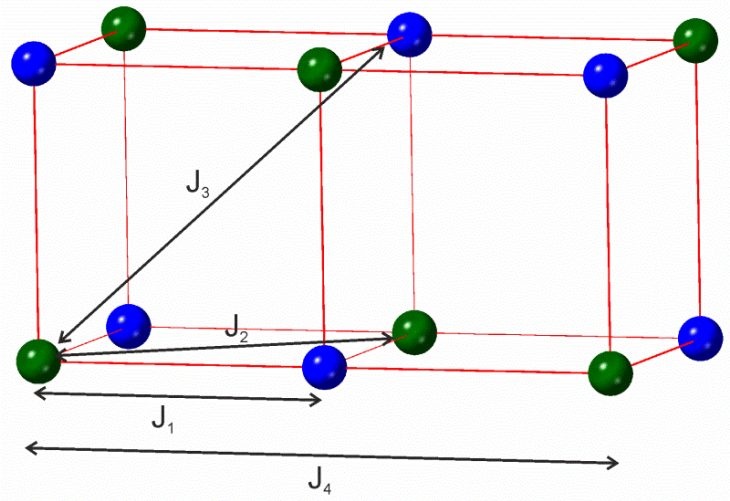


Figure 3.12. An illustration of the four nearest neighbour interactions. The green and blue spheres represent the Ni^{2+} cations located at the 2*c* and 2*d* sites respectively. Note that the red line does not represent the unit cell.

Literature values obtained from a nickel–containing ordered double perovskite were used for J_2 or J_4 or both; values for Sr_2NiWO_6 and Sr_2NiTeO_6 were reported by Blasse and Iwanaga[129, 130], see Table 3.1. The magnitudes of these magnetic interactions, together with the fixed J_1/k_B value, were applied to the selected structural model to generate three independent magnetic diffuse scattering patterns using the program SPINDIFF, see Figure 3.13. Neither the width nor the maximum intensity of the peak is ideally matched by any pair of J_2 and J_4 values. Clearly further adjustment of the J_n values was necessary. By inspection of Figure 3.13, the ratio of $\frac{J_2}{J_4}$ for Sr_2NiTeO_6 provided the best simulations among these three cases. It is worth noting that despite the presence of different types of diamagnetic *B*' cations in Sr_2NiWO_6 and Sr_2NiTeO_6, the J_2/k_B values reported are very similar. Hence, it was decided to fix J_2/k_B –7.1 K and to optimise the J_4/k_B value for $La_3Ni_2SbO_9$ manually by trial and error. The result of this "refinement" is shown in Figure 3.14. Preliminary analyses showed that J_4/k_B is approximately 0 K or slightly positive when J_1/k_B and J_2/k_B were fixed at –221 and –7.1 K, respectively, indicating that the linear

superexchange interaction which is mediated by a diamagnetic Sb^{5+} cation has little effect on the magnetic coupling. A plausible explanation is that the outer orbital in Sb^{5+} cation is too low in energy for mixing with the O^{2-} 2*p* orbital to be significant, and consequently, the superexchange pathways J_1 and J_2 are the only ones that should be considered.

Table 3.1. Superexchange coupling constants for Sr_2NiTeO_6 and Sr_2NiWO_6 from literature.

Composition	J_2/k_B (K)	J_4/k_B (K)
Sr_2NiTeO_6[129]	–6.7	–4.4
Sr_2NiWO_6[129]	–7.6	–12.8
Sr_2NiWO_6[130]	–7.6	–6.7

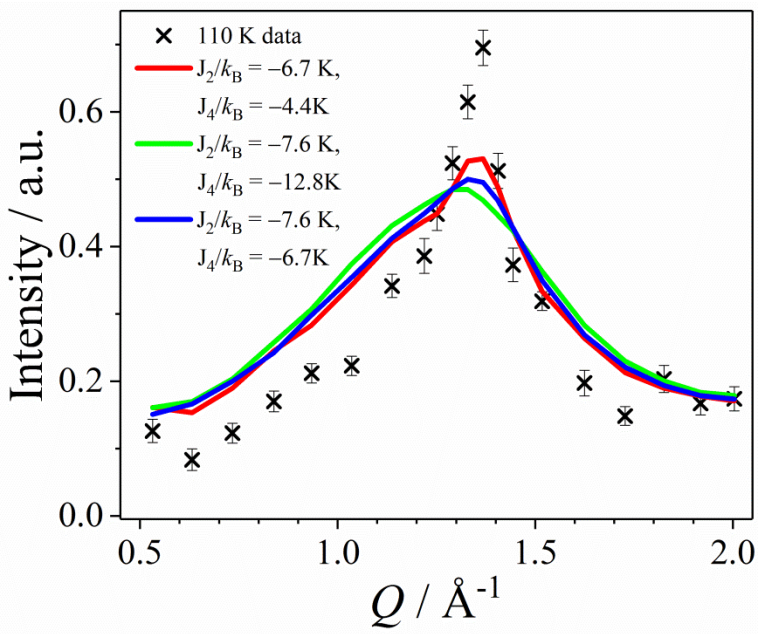


Figure 3.13. The simulated magnetic scattering patterns generated with J_1/k_B being fixed at –221 K and some reported ratios of $\frac{J_2}{J_4}$. The crosses represent the magnetic scattering data collected at 110 K.

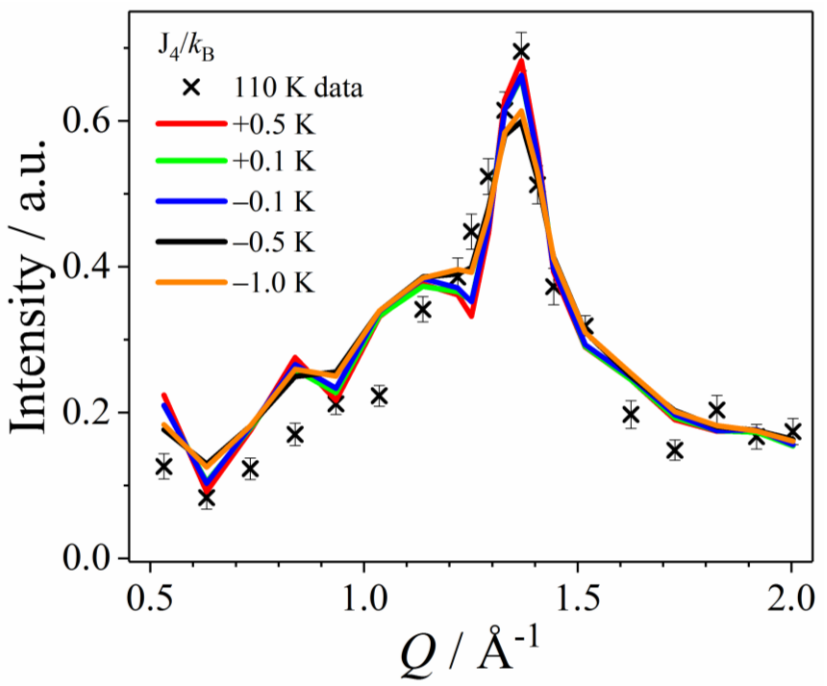


Figure 3.14. The simulated magnetic scattering patterns generated with J_1/k_B and J_2/k_B being fixed at –221 and –7.1 K, respectively, and some values for J_4/k_B. The crosses represent the magnetic scattering data collected at 110 K.

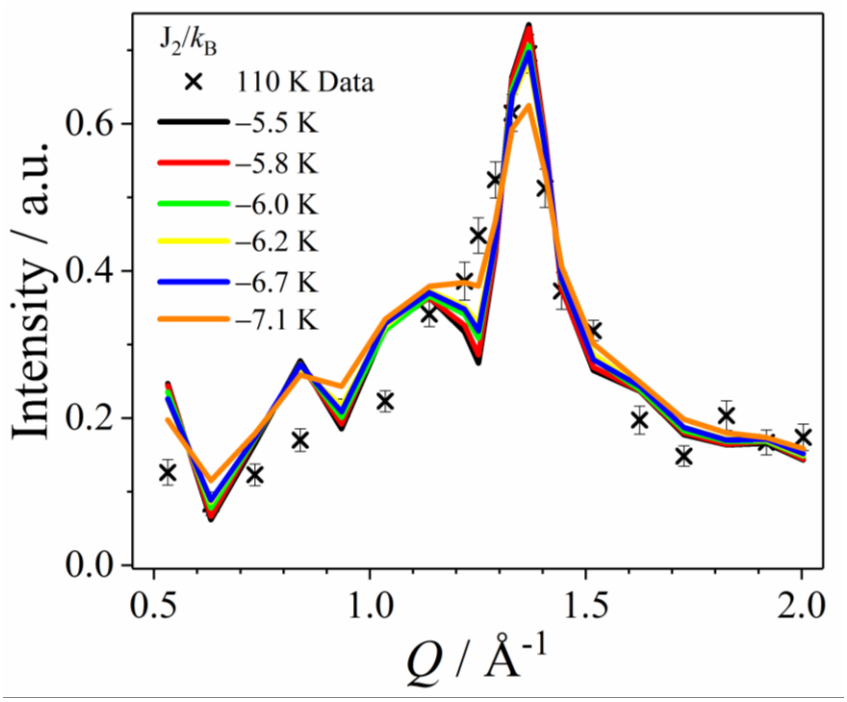


Figure 3.15. The simulated magnetic scattering patterns generated with J_2/k_B being a variable and J_1/k_B fixed to be –221 K. The crosses represent the magnetic scattering data collected at 110 K.

Further calculations were carried out with J_4/k_B set to be 0 K, and therefore the J_2/k_B value (or the ratio of $\frac{J_1}{J_2}$) was the only variable. This parameter was manually adjusted due to the lack of least–squares refinement algorithm for systems with disordered magnetic sites. A range of J_2/k_B values were used and the corresponding calculated patterns, together with the observed data, are plotted in Figure 3.15. The simulated magnetic diffuse scattering pattern generated with J_1/k_B and J_2/k_B being –221 and –6 K, respectively, gives a satisfactory fit to the data at 110 K. Both the peak width and intensity of the simulated pattern are in a good agreement with the data collected. The optimised value for J_2/k_B is close to that reported by Blasse and Iwanaga for Sr_2NiWO_6 and Sr_2NiTeO_6[129, 130].

In order to investigate the magnetic ordering over short distances, spin configurations produced in the RMC and DMC simulations were drawn using CrystalMaker program[127]. Unfortunately, it is extremely difficult to identify a particular spin pattern (if any) from such a diagram, see Figures S3.3 – S3.6. As a result, a spin correlation function, $g(r)$, was calculated in order to provide a better overview of how the spins couple with each other. The function $g(r)$ can be understood as follows: assume there is a Ni^{2+} cation at r = 0 Å. This atom will interact with its nearest magnetic neighbour, and they will couple ferromagnetically or antiferromagnetically. If the coupling is, on average, antiferromagnetic, $g(r)$ will be negative; the function will have a positive value if the coupling is ferromagnetic. The second point in $g(r)$ represents the nature of the coupling between the atom located at r = 0 Å and its next–nearest neighbours, and so forth. For comparative purposes, $g(r)$ was plotted for all simulated models, see Figure 3.16. The algorithm for calculating the spin correlation function was written by Professor Andrew Goodwin in this Department.

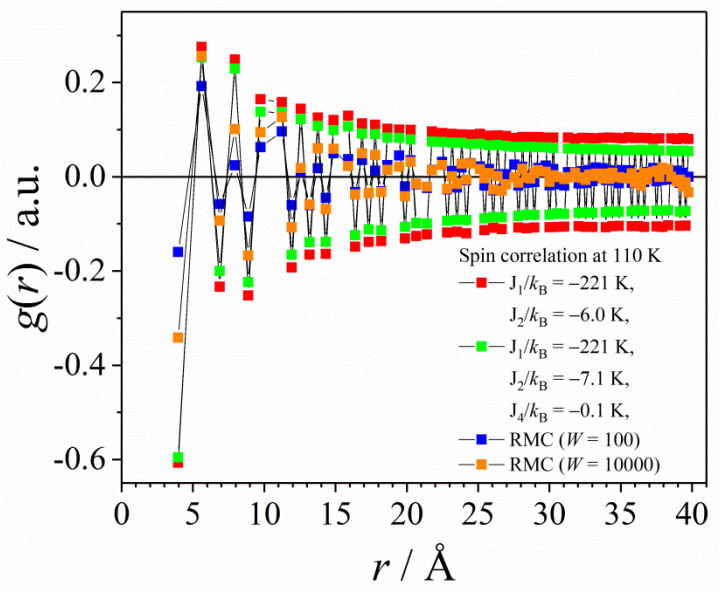


Figure 3.16. The spin correlation function of the RMC model and three DMC models with different J_ns ratios.

In each case $g(r)$ shows a similar feature; a decaying oscillation as a function of r. Apart from a few exceptions, the sign of $g(r)$ alternates as r increases. The alignment between nearest–neighbour Ni^{2+} cations is found to be antiferromagnetic in all simulations whereas the positive value of $g(r)$ at ~5.5 Å shows that the coupling between the next–nearest–neighbours is, on average, ferromagnetic. In all the RMC simulations, $g(r)$ decays towards zero, indicating the spin vectors lose the correlation at large distances. This can be explained by the fact that the RMC approach will always give the most disordered model which is consistent with the data. Therefore, the correlations will be damped accordingly. The spin correlations in the models generated using the DMC approach show many similarities; for example $g(r)$ is generally of the same order of magnitude as those deduced from an RMC approach. However, the DMC calculations predict much stronger antiferromagnetic coupling between nearest–neighbours (r ~ 4 Å) than do the RMC calculations. This might be an indication that the magnitude of J in NiO is larger than the true value in $La_3Ni_2SbO_9$. The over–estimation of J_1 might be responsible for the failure of

$g(r)$ to decay to zero in the DMC case, see Figure 3.16. The envelope of each curve shown in Figure 3.16 was fitted to the function

$$g(r) = Ae^{-r/\xi} + c, \qquad \text{Equation 3.9}$$

where ξ represents the magnetic correlation length of $La_3Ni_2SbO_9$, A is a scale factor and c is the value of $g(r)$ at infinite r, see Figure S3.7. The non–zero value of c obtained for the DMC fits is a consequence of the relatively narrow width of the principal maximum, which implies that magnetic ordering persists over longer distances, see Figures 3.11 and 3.15. In all cases the curves were well described by a value $\xi \sim 9$ Å.

Attempts were made to analyse the corresponding data collected at 175 K using an approach similar to that described above. Figure 3.17 shows the nuclear and isotopic incoherent scattering recorded at 110 and 175 K. The two patterns are superimposable, and the nuclear template established from the 110 K data was therefore used to analyse the magnetic scattering observed at 175 K.

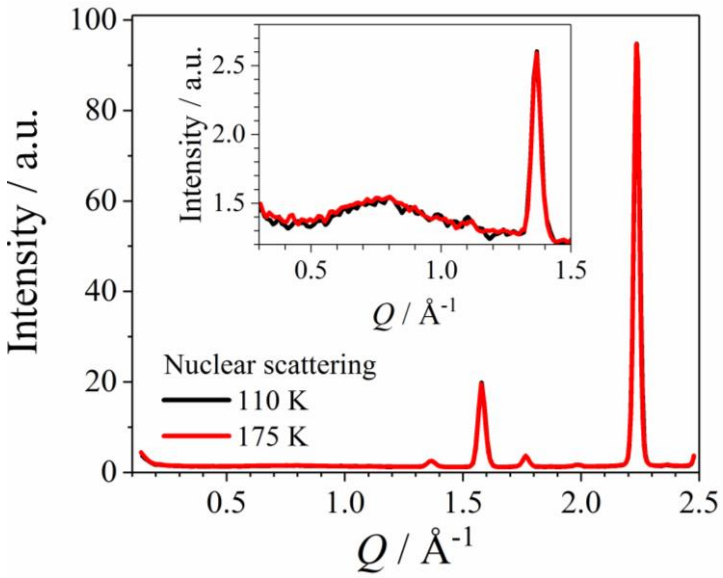


Figure 3.17. The nuclear coherent and isotopic incoherent scattering patterns for $La_3Ni_2SbO_9$ at 110 K (black) and 175 K (red). The inset shows that the nuclear diffraction patterns are superimposable.

The magnitude of the magnetic scattering was weaker at 175 K than that at 110 K, see Figure 3.18. This could be a consequence of increased fluctuation of the spins in $La_3Ni_2SbO_9$ as the temperature increased. Although the intensity of the scattering observed at 175 K is significantly lower than that recorded at the lower temperature the magnetic data were binned in the same way.

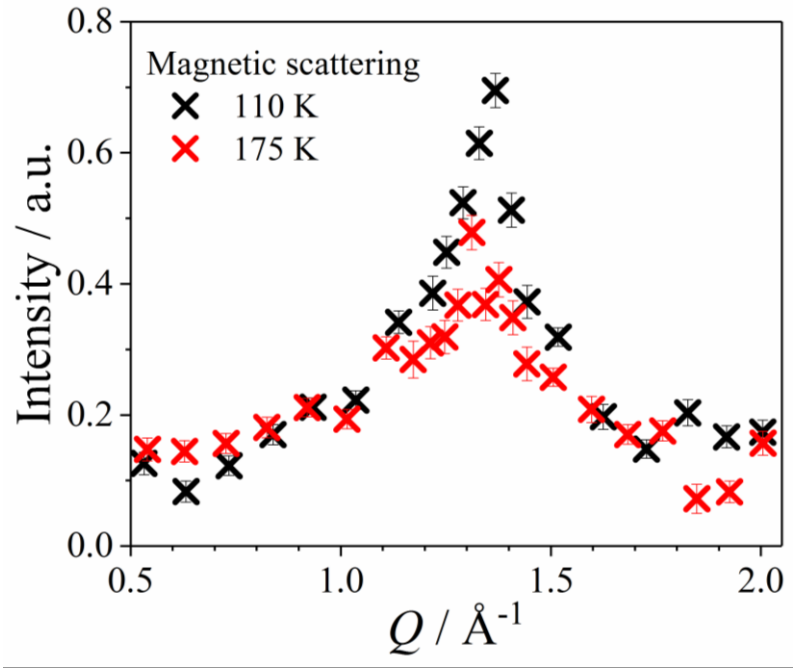


Figure 3.18. The average magnetic scattering patterns for $La_3Ni_2SbO_9$ at 110 K (black) and 175 K (red).

Four magnetic scattering patterns were produced using both the DMC and RMC approaches, see Figure 3.19. For the former, two independent models were used; one of them included the linear Ni–O–*B*'–O–Ni superexchange pathway (J_1/k_B = –221 K, J_2/k_B = –7.1 K and J_4/k_B = –0.1 K) whereas the other used only J_1 and J_2 (J_1/k_B = –221 K and J_2/k_B = –6 K). Both cases generated unsatisfactory fits to the data collected at 175 K, implying that the ratios of the superexchange constants, J_n, deduced previously are not applicable here, and the parameters could possibly be a function of temperature. It is perhaps more likely that the over–estimation of J_1 discussed above has a greater effect on the fit at higher temperatures. Due to the counting statistics, it was deemed to be impossible to

quantitatively obtain the ratios of J_n at 175 K. In contrast, given that the RMC calculation is data–driven, this methodology provided two fits which account for the data.

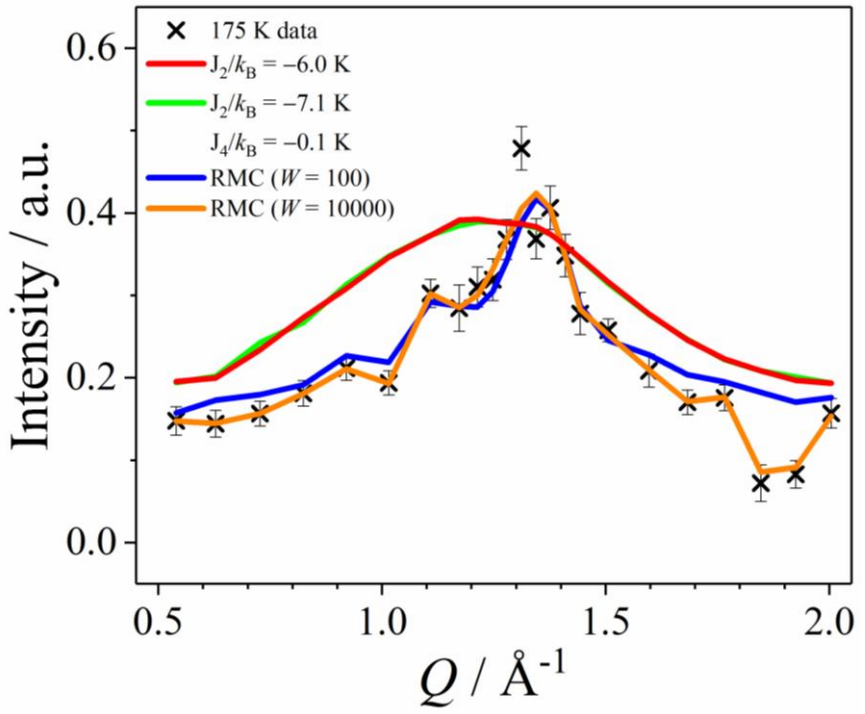


Figure 3.19. The magnetic scattering patterns generated using different approaches plotted against the data collected. The red and green curves represent the DMC methodology; the involvement of the linear Ni–O–*B*'–O–Ni (J_4/k_B) is the difference between the two. The blue and orange curves represent the RMC approach with different weighting factors, *W*.

The spin correlations $g(r)$ obtained using RMC approach at 110 and 175 K are shown in Figure 3.20. The $g(r)$ for each case oscillates and decays towards zero as r > 15 Å. Increasing the temperature has caused $|g(r)|$ to decrease at low values of r. The spin correlation of the nearest–neighbour Ni^{2+} cations (*i.e.* at r ~4 Å) is seen to be a function of the weighting factor *W*; at both temperatures $g(r)$ is more negative when *W* is 10000. However, whatever the weighting factor, the value of the correlation function for the nearest–neighbour interaction (r ~4 Å) does not change between 110 K and 175 K whereas that between next–nearest–neighbour at r ~5.5 Å clearly decreases.

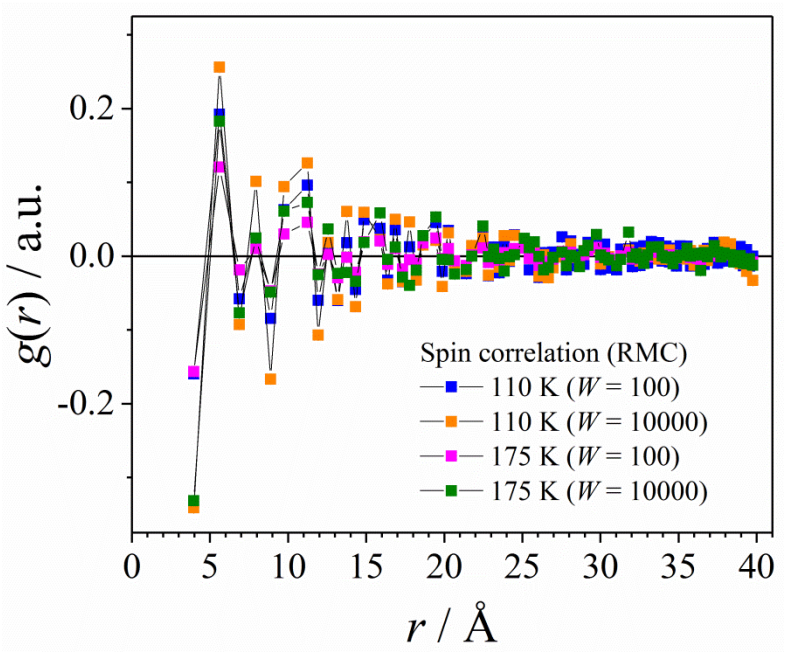


Figure 3.20. The spin correlation function as a function of temperature and weighting factor *W*.

3.4 Discussion

The X–ray diffraction and magnetometry data collected on the newly prepared sample of $La_3Ni_2SbO_9$ are consistent with those collected on the original sample[48] although there will certainly be some small variation in the degree of local ordering in two different samples.

The analysis of the nuclear scattering has provided information about the cation ordering on a local scale. The energy constraint used in the DMC calculation plays a crucial role in determining the Ni/Sb distribution. It is true that other interactions could have also been taken into account during the construction of the Hamiltonian in the simulation so as to provide a more complete description of the sample. However, satisfactory models were obtained when the electrostatic next–nearest–neighbour Sb^{5+}–Sb^{5+} repulsions were used as the only energy constraint, suggesting that the other interactions are not needed to account for the observed diffuse scattering. The use of a supercell allows the Ni^{2+} and Sb^{5+} cations to be distributed over the 2*d* sites in a non–random manner and hence generates scattering that is not modelled in the usual unit cell.

Apart from those points fixed at a value of $\frac{-1}{3}$, $g(r_{ij})$ deviates from the value of $\frac{+5}{9}$ at $r < 15$ Å. This demonstrates that Ni^{2+} and Sb^{5+} are not randomly distributed over the 2*d* sites. This is consistent with the observation of variations in the cation distribution in the previous TEM experiments[75], but the nature of the variation is different. For example, the Sb–rich regions observed by microscopy in one particular crystallite of $La_3Ni_2SbO_9$ appears to extend over a distance of ~ 80 Å, see Figure 3.2, whereas the diffuse scattering data, both structural and magnetic, suggest that the short–range order observed on the 2*d* sites which give rise to Ni–rich regions persists over only ~ 15 Å. Of course the TEM experiment sampled only a small number of local regions whereas the neutron scattering experiment sampled the bulk material. It is possible to reconcile the two observations by postulating that Sb–rich regions occur in the domain boundaries to compensate for Ni–rich regions within the domains, but further experimental work would be necessary in order to prove this.

The DMC calculations have shown that the linear, approximately 8 Å, superexchange pathway Ni–O–*B*'–O–Ni is insignificant in $La_3Ni_2SbO_9$ at 110 K. If the *B*' cation is Sb^{5+}, there will be a mismatch in energy between the low–lying filled Sb^{5+} 4*d* orbital and 2*p* orbitals of O^{2-}, and if the *B*' cation is Ni^{2+}, J_4 will be small compared to the strongly antiferromagnetic J_1 interaction which would then dominate. The low value found for J_2/k_B might indicate that the mean next–nearest–neighbour magnetic interaction actually depends on the Ni/Sb distribution. If the *B*' cation is a diamagnetic Sb^{5+} cation, the coupling between the next–nearest–neighbour Ni^{2+} cation (Ni–O–O–Ni) is expected to be antiferromagnetic and J_2/k_B should then be negative. However, there is a 33 % probability that a Ni^{2+} cation will be on the *B*' site. In this case, the superexchange pathway is slightly different; it should now involve an additional Ni^{2+} cation between the two oxide anions, and the J_2 interaction will be expected to be positive, as it is in NiO[62]. As a result, the mean

J_2 interaction is much less antiferromagnetic than might be expected. Nevertheless, further adjustment of the J_n is required as the $\frac{J_2}{J_1}$ ratio deduced from the data collected at 110 K did not result in a satisfactory model to the magnetic data collected at 175 K. This seems to indicate that the magnetic interactions are temperature dependent. However, the spin correlation function, see Figure 3.16, suggests that the interaction between nearest–neighbour Ni^{2+} cations may not be as antiferromagnetic as in the case of NiO[62]. Moreover, it implies that there might well be other combinations of J_1 and J_2 which could model the magnetic diffuse scattering at 110 K in a satisfactory fashion. Again, the absolute values of J_1/k_B and J_2/k_B for $La_3Ni_2SbO_9$ cannot be obtained without a least–squares refinement algorithm. The spin correlation functions $g(r)$ calculated using both the DMC and RMC approaches, see Figure 3.16, show that the spin vectors start to be randomised at r ~15 Å, the same distance as that calculated for the structural short–range order. It seems there is a correlation between the nuclear and magnetic ordering in $La_3Ni_2SbO_9$.

The nuclear scattering data collected at 175 K match those collected at 110 K, meaning the nuclear template is temperature independent. In other words, no phase transition or significant redistribution of Ni/Sb at the 2*d* site was observable within the resolution of the diffractometer D7. This is not surprising. In contrast, the diminished intensity in the magnetic scattering data recorded at the higher temperature shows that the extent of short–range magnetic ordering decreased as the temperature increased. The spin correlation function shown in Figure 3.20 indicates the magnetic correlation length is not a function of temperature as $g(r)$ decays towards zero at a similar value of r at both temperatures. On the other hand, the degree of spin correlation between next–nearest–neighbour cations (r ~ 5.5 Å) decreases with temperature faster than that between nearest neighbours with the weighting factor W being the same. An explanation for this feature is that the increase in the thermal energy gained by the spins reduces the correlation between the spins at the

relatively longer distance. Future work is required to study the spin correlation in a more quantitative manner.

3.5 Conclusion

The polarised neutron experiments reported herein allow the separation of the nuclear and magnetic diffuse scattering from $La_3Ni_2SbO_9$. 10 independent supercells of size 20×20×20 octahedral sites, each with a specific Ni/Sb distribution, were generated using a DMC approach. Their simulated scattering patterns were averaged and the resulting pattern provides a satisfactory fit to the nuclear diffuse scattering observed at both 110 and 175 K. It can be seen by inspection that the cation ordering at the octahedral sites is short–range and regions of uneven Ni/Sb distribution are present. This is consistent with a more rigorously calculated site correlation function.

Both DMC and RMC approaches were employed to study the magnetic diffuse scattering. The former provides an insight into the relative strength of the superexchange interactions involved in $La_3Ni_2SbO_9$. The rock–salt ordering of Ni^{2+} and Sb^{5+} cations complicates the deduction of the strength of the magnetic interactions, especially the non–linear superexchange pathway (J_2), as the nature of this magnetic interaction depends on the local distribution of the Ni/Sb cations at the 2*d* site. Nevertheless, when the nearest–neighbour interaction was assumed to be the same as that in NiO[62], J_2/k_B was found to be approximately –6 K. Spin correlation functions suggested that this assumption might overestimate the J_1 interaction. However, the lack of least–squares refinement algorithm for systems with disordered magnetic sites has prevented optimisation of the values of J_1/k_B and J_2/k_B. It is interesting to note that both the site and spin correlation functions decay towards a constant value at $r \sim 15$ Å.

Data collected at a higher temperature (175 K) showed no significant variation in the atomic structure of the sample. In contrast, the intensity of magnetic diffuse scattering was seen to decrease with increasing temperature. The analysis presented here suggests the next–nearest–neighbour interactions weaken more rapidly than those between nearest neighbours.

Chapter 4: Comparative study of the magnetic properties of $La_3Ni_2B'O_9$ (B' = Sb, Ta or Nb)

4.1 Introduction

One of the factors that affects the magnetic properties of some perovskites is the identity of the diamagnetic *B*' cation. For example, both Sr_2FeTaO_6 and Sr_2FeNbO_6 were found to adopt the same space group *Pbnm*, in which the *B*/*B*' cations are randomly distributed. However, replacing the d^0 diamagnetic cation with a d^{10} cation (*i.e.* Sb) induces a partial rock–salt ordering between the Fe^{3+} and Sb^{5+} over the two octahedral sites[61, 131]. This change in the composition, and subsequently the structure, leads to magnetic ordering in Sr_2FeSbO_6. Substituting the d^0 W^{6+} cation in Sr_2NiWO_6 with a d^{10} Te^{6+} cation lowers the magnetic transition temperature at which they both transform to spin glasses from 54 to 35 K[129]. The effect of altering the electron configuration in "triple perovskites" is slightly more subtle. Despite being isostructural, $La_3Co_2TaO_9$ and $La_3Co_2NbO_9$ become ferromagnetic at 72(2) and 62(2) K respectively whereas $La_3Co_2SbO_9$ is a spin glass with a field–dependent freezing temperature, T_f[77, 132, 133]. Competition between antiferromagnetic and ferromagnetic interactions was suggested as the reason for the magnetic frustration observed in $La_3Co_2SbO_9$ and it was proposed that the occurrence of partial electron density transfer leads to ferromagnetic coupling mediated by the d^0 Ta or Nb cation in $La_3Co_2TaO_9$ or $La_3Co_2NbO_9$, although the evidence does not seem to be conclusive.

In this chapter, the influence of the electron configuration of the diamagnetic *B*' cation on the structural and magnetic properties of $La_3Ni_2B'O_9$ (B' = Sb, Ta or Nb) is discussed. These compositions have been investigated through a combination of X–ray and neutron

diffraction, electron microscopy, magnetometry and muon spin relaxation. Earlier results[48, 75] on $La_3Ni_2SbO_9$ are discussed for purposes of comparison.

4.2 Experimental

Polycrystalline samples of $La_3Ni_2TaO_9$ and $La_3Ni_2NbO_9$ were synthesized using the traditional ceramic method. Stoichiometric quantities of pre–dried La_2O_3, NiO and Ta_2O_5 or Nb_2O_5 were mixed and ground together in an agate mortar and pestle. The mixture was then pelletised and heated in air inside an alumina crucible. The tantalum–containing mixture was heated at 800 °C for 24 hours then at 1250 °C for 11 days whilst that containing niobium was initially heated at 1200 °C for 7 days and finally at 1250 °C for 8 days. The pellets were ground and reformed every 48–72 hours.

X–ray and neutron powder diffraction patterns were collected from both reaction products. XPRD data were collected with Cu $K_{\alpha 1}$ radiation (λ = 1.54051 Å) using a PANalytical Empyrean diffractometer operating at room temperature. NPD data were collected at selected temperatures using the diffractometer D2b (λ ~ 1.59 Å) at ILL, Grenoble; unit cell parameters determined by X–ray diffraction were used to determine accurately the neutron wavelength. The angular ranges covered were $15 \leq 2\theta/° \leq 125$ and $10 \leq 2\theta/° \leq 150$ respectively, with step–sizes, $\Delta 2\theta$, of 0.0066° and 0.05°. The Rietveld method[92], as implemented in the GSAS[94] program suite, was used to analyse the diffraction patterns. In all refinements, the background and peak shapes were modelled by a 12–term shifted Chebyshev function and a pseudo–Voigt function[123], respectively. Further high–intensity NPD patterns were collected using the diffractometer D1b (λ ~2.52 Å) at ILL.

Both compounds were also studied by TEM and SEM. Specimens for TEM were prepared by crushing the powder in ethanol and depositing a few drops of this solution on a copper grid covered with a holey carbon film. Selected area electron diffraction (SAED) patterns

were taken with Philips CM20 and FEI Tecnai G2 instruments. High angle annular dark field stem (HAADF–STEM) images and energy dispersive X–ray (EDX) maps were acquired with an FEI Titan 80–300 "cubed" microscope equipped with a Super–X detector and operated at 300 kV. Specimens for SEM were prepared by smearing the powder over tape which was mounted on a stub of metal. SEM images were collected using a JEOL 5590 microscope.

The temperature dependence of the dc molar magnetic susceptibilities of both $La_3Ni_2TaO_9$ and $La_3Ni_2NbO_9$ was measured in fields of 10, 100 and 1000 Oe over the temperature range $2 \leq T/K \leq 300$ after cooling the sample in zero field (ZFC) and after cooling in the measuring field (FC) using a SQUID magnetometer. The variation of the magnetisation per formula unit (f.u.) with applied magnetic field was measured at 5, 150 and 220 K over the range $-50 \leq H/kOe \leq 50$. The ac susceptibility was measured in an oscillating field of amplitude 3.5 Oe over the temperature range $2 \leq T/K \leq 150$ at frequencies of 1, 10 and 100 Hz.

Zero–field muon–spin relaxation (ZF μSR) measurements were made on polycrystalline samples of $La_3Ni_2B'O_9$ (B'= Sb, Ta or Nb) using the general purpose surface (GPS)[108] spectrometer at the Swiss Muon Source and the EMU instrument[109] at the STFC ISIS facility. For the measurement, the samples were mounted in silver foil packets and placed on silver backing plates. As previously described, the observed property in a μSR experiment is the time evolution of the positive muon spin polarisation. Recording the time dependence of the positron emission directions therefore allows the determination of the spin–polarization of the ensemble of muons.

In the case of $La_3Ni_2TaO_9$, NPD data were also collected in an applied magnetic field using the diffractometer ECHIDNA[87] at the Bragg Institute, ANSTO, Australia. The sample was

made into a pellet which was then broken into fragments, each just small enough to be loaded into a standard vanadium container. This was done to prevent movement of the sample in the magnetic field. The vanadium container was then mounted in a vertical–field cryomagnet. Data were collected over the angular range $10 \leq 2\theta/° \leq 158$ at 5 K in fields of 0, 4, 20 and 50 kOe using a neutron wavelength of 2.4395 Å. In order to study the reversibility of any change in the magnetic scattering a final pattern was recorded in 0 kOe after the magnet had been switched off. The NPD patterns were also analysed using the Rietveld method[92] as implemented in the GSAS program suite[94]. The peak shape was modelled using a pseudo–Voigt function[123] and the background was fitted with a 15–term shifted Chebyshev function. Regions where the patterns were contaminated by the aluminium in the cryomagnet were excluded from the refinements.

4.3 Results

Preliminary analysis of the XRPD data of both reaction products suggested that each was dominated by the desired perovskite–like phase, the reflections from which could be accounted for in the monoclinic space group $P2_1/n$ with $a \sim b \sim \sqrt{2}a_p$, $c \sim 2a_p$ and $\beta \sim 90°$ where a_p is the cell parameter of a primitive cubic perovskite. The crystal structures thus contain two crystallographically distinct octahedral sites, 2*c* and 2*d*, which are occupied by Ni^{2+} and the diamagnetic, pentavalent cations. The La^{3+} cations are accommodated on a single 4*e* site and three distinct 4*e* sites are occupied by oxide ions.

The room–temperature crystal structure of each of the two compounds was refined with both XRPD data and NPD data from D2b being analysed simultaneously. Apart from the usual atomic parameters, the distribution of Ni^{2+} and Ta^{5+} or Nb^{5+} over the six–coordinate sites was allowed to vary. The cation distribution determined in these refinements was held constant during refinements of the crystal structure based on D2b data collected at lower

temperatures, see below. The structural models deduced from the D2b data were then used in the analysis of the D1b data.

Simultaneous profile analysis of the XRPD and NPD patterns collected at room temperature gave a satisfactory account of the structures of both compounds. Small amounts of diamagnetic impurities were detected in each sample; and 0.4(2) wt % of La_3TaO_7[134] in $La_3Ni_2TaO_9$ and 0.8(1) wt % of $LaNbO_4$[135] in $La_3Ni_2NbO_9$. No Bragg peaks attributable to unreacted NiO were observed in either case. The observed and calculated room–temperature XPRD and NPD patterns of $La_3Ni_2TaO_9$ and $La_3Ni_2NbO_9$ are displayed in Figures 4.1 and 4.2, respectively. The structural parameters of $La_3Ni_2TaO_9$ and $La_3Ni_2NbO_9$ derived from these analyses are presented in Table 4.1. In order to achieve a satisfactory fit to the data collected from $La_3Ni_2NbO_9$ it was necessary to include a parameter to model the effect of a small particle size on the shape of the Bragg peaks and, for comparison purposes, this parameter was also included in refinements of $La_3Ni_2TaO_9$. The ratio of the parameters determined from the X–ray data suggested that the Ta:Nb particle size ratio was 1.67(7):1.

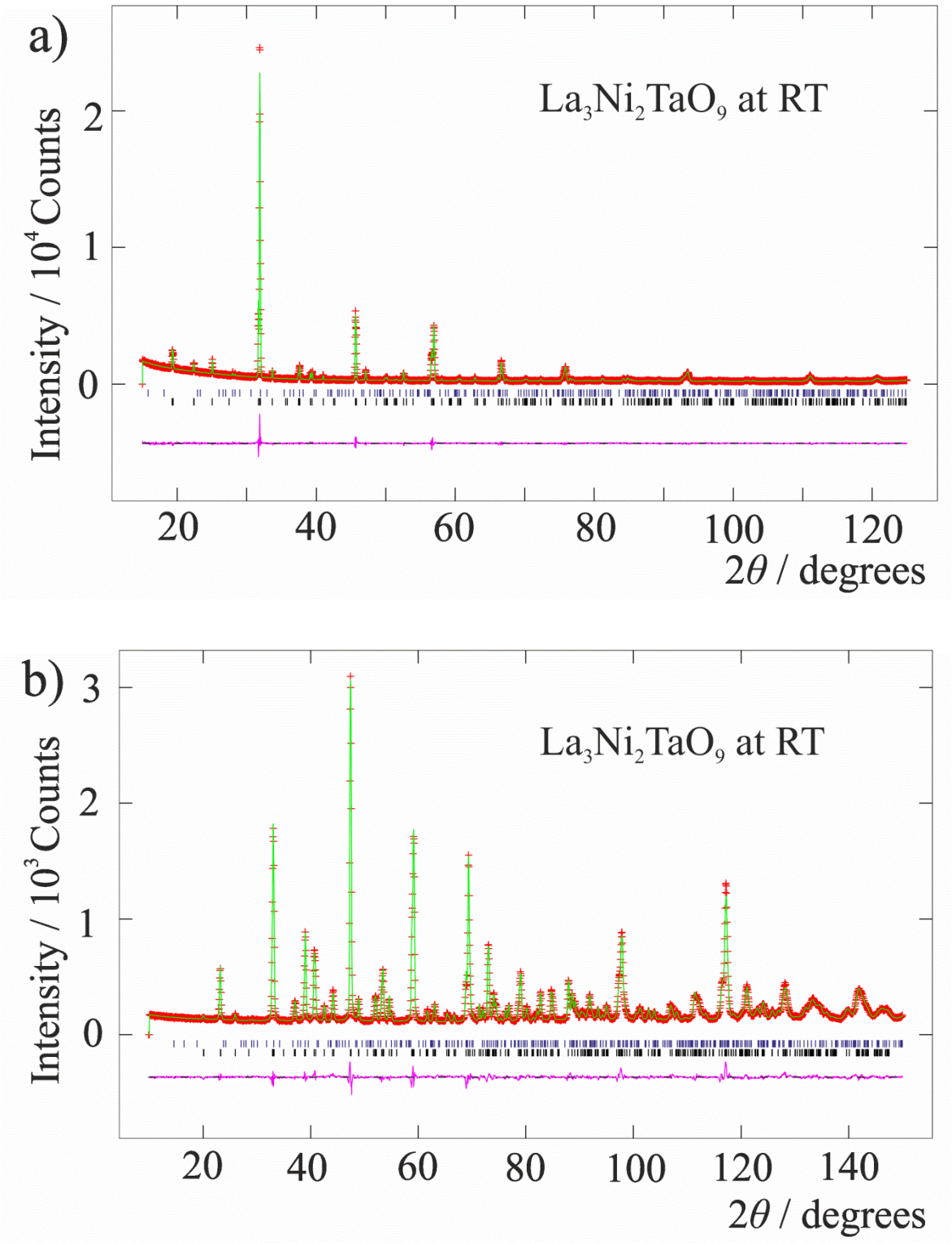


Figure 4.1. Observed (red crosses), calculated (green line) and difference (purple) (a) XPRD and (b) NPD profiles of $La_3Ni_2TaO_9$ collected at room temperature. Reflection markers are shown for La_3TaO_7 (blue) and $La_3Ni_2TaO_9$ (black).

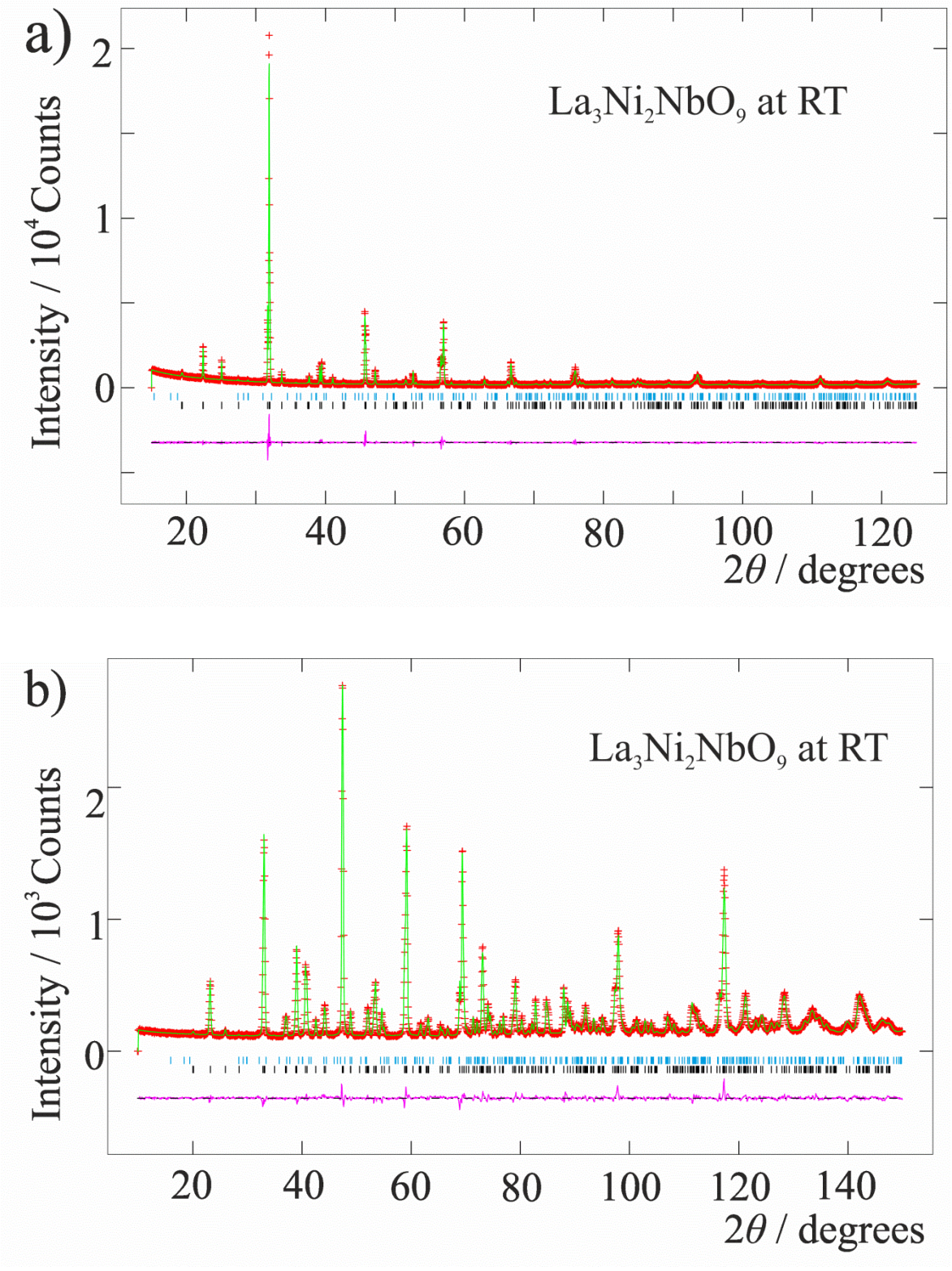


Figure 4.2. Observed (red crosses), calculated (green line) and difference (purple) (a) XPRD and (b) NPD profiles of $La_3Ni_2NbO_9$ collected at room temperature. Reflection markers are shown for $LaNbO_4$ (cyan) and $La_3Ni_2NbO_9$ (black).

Table 4.1. Structural parameters of $La_3Ni_2B'O_9$ (B' = Ta or Nb) at RT (Space group $P2_1/n$).

		B' = Ta	B' = Nb
a / Å		5.5902(1)	5.5865(1)
b / Å		5.6407(1)	5.6400(1)
c / Å		7.9222(1)	7.9165(1)
β / °		90.034(3)	90.012(5)
V / Å^3		249.806(6)	249.435(6)
$R_{wp}\|_{XRPD}$ / %		6.46	7.62
$R_{wp}\|_{NPD}$ / %		4.72	4.56
Total R_{wp} / %		5.76	6.25
χ^2		2.317	2.293
La	x	0.4924(3)	0.4921(3)
4*e* (*x y z*)	y	0.4613(1)	0.4610(1)
	z	0.2507(2)	0.2501(3)
	U_{ISO} / Å^2	0.0224(2)	0.0195(2)
Ni/*B*'1	U_{ISO} / Å^2	0.0048(1)	0.0032(1)
2*c* (0 ½ 0)	Ni occupancy	0.982(1)	0.964(7)
	B' occupancy	0.018(1)	0.036(7)
Ni/*B*'2	U_{ISO} / Å^2	0.0048(1)	0.0032(1)
2*d* (½ 0 0)	Ni occupancy	0.351(1)	0.369(7)
	B' occupancy	0.649(1)	0.631(7)
O1	x	0.7886(7)	0.7912(9)
4*e* (*x y z*)	y	0.7950(6)	0.7965(7)
	z	–0.0374(5)	–0.0366(5)
	U_{ISO} / Å^2	0.0041(8)	0.0059(10)
O2	x	0.7093(8)	0.7119(9)
4*e* (*x y z*)	y	0.2851(7)	0.2835(7)
	z	–0.0469(5)	–0.0472(5)
	U_{ISO} / Å^2	0.0148(11)	0.0087(10)
O3	x	0.5769(3)	0.5766(3)
4*e* (*x y z*)	y	0.0172(3)	0.0168(3)
	z	0.252(1)	0.250(1)
	U_{ISO} / Å^2	0.0132(3)	0.0121(3)

SAED patterns of both compounds are shown in Figure 4.3. The patterns can be indexed using the cell parameters obtained from the XRPD and NPD data. The derived reflection conditions correspond with space group $P2_1/n$. Reflections can be seen in [100] and [001] at $h00$, $0k0$ and $00l$ with respectively h, k and l odd, which would contradict the $P2_1/n$ symmetry. However, these reflections are due to double diffraction, since they disappear when the sample is tilted around the relevant axes. The cation ordering that occurs over the six–coordinate position is clear from the HR–EDX images in Figure 4.4. The order is long range, as seen in the HAADF–STEM images of Figure 4.5. No systematic presence of disordered areas could be found. The different appearance between the HAADF–STEM images of $La_3Ni_2TaO_9$ and $La_3Ni_2NbO_9$ is due to the difference in atomic number Z between Ta and Nb: on such images, the brightness of the dots increases with increasing total Z of the column. Therefore, the difference between columns with only Ni (Z = 28) or with approximately $\frac{1}{3}$ Ni + $\frac{2}{3}$ Ta ($Z_{average}$ = 58) is larger than the difference between Ni columns and $\frac{1}{3}$ Ni + $\frac{2}{3}$ Nb columns ($Z_{average}$ = 37), giving a clearer alternating contrast at the six–coordinate sites for the tantalum–containing sample.

Both materials show the presence of structured diffuse scattering, see Figure 4.6, most probably connected to short–range ordering at the 2*d* position, which is occupied by approximately $\frac{1}{3}$ Ni and $\frac{2}{3}$ either Ta or Nb. By eye, there is no systematic difference in the shape or intensity of this diffuse scattering between the Ta and Nb containing compounds. After a thorough search of literature, it appears that no protocol to quantify diffuse intensities from electron diffraction patterns has yet been developed; a detailed investigation of the precise structural modifications responsible for the diffuse intensity is therefore beyond the scope of this thesis.

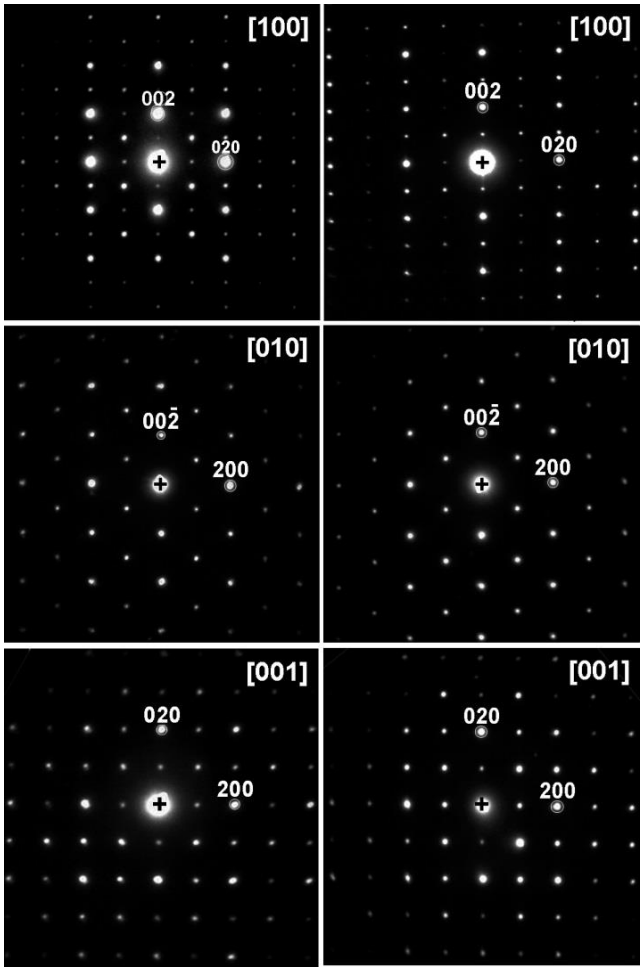


Figure 4.3. Representative SAED patterns of the main zones of $La_3Ni_2TaO_9$ (left column) and $La_3Ni_2NbO_9$ (right column).

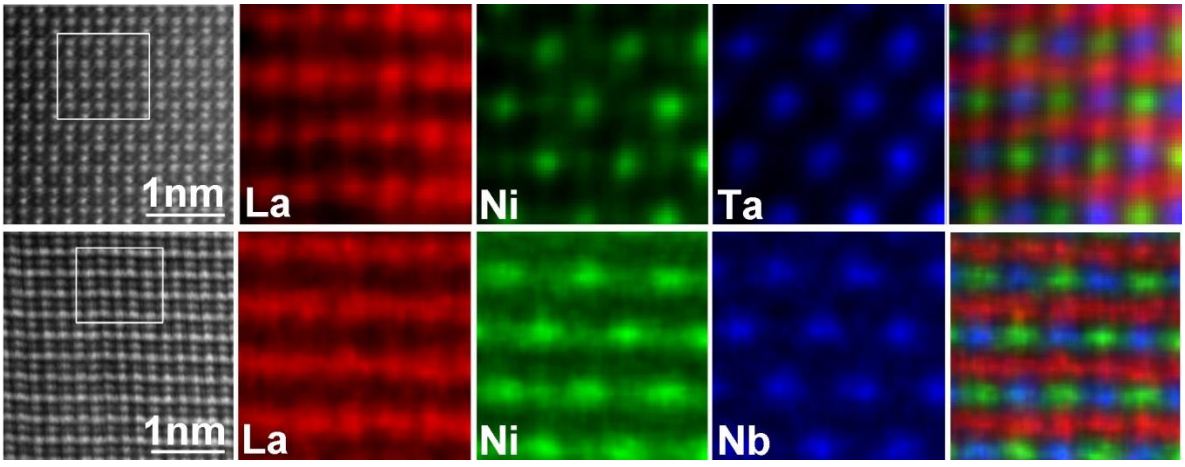


Figure 4.4. High resolution EDX maps along [010], showing the distribution of the different elements within the unit cells of $La_3Ni_2TaO_9$ (top row) and $La_3Ni_2NbO_9$ (bottom row).

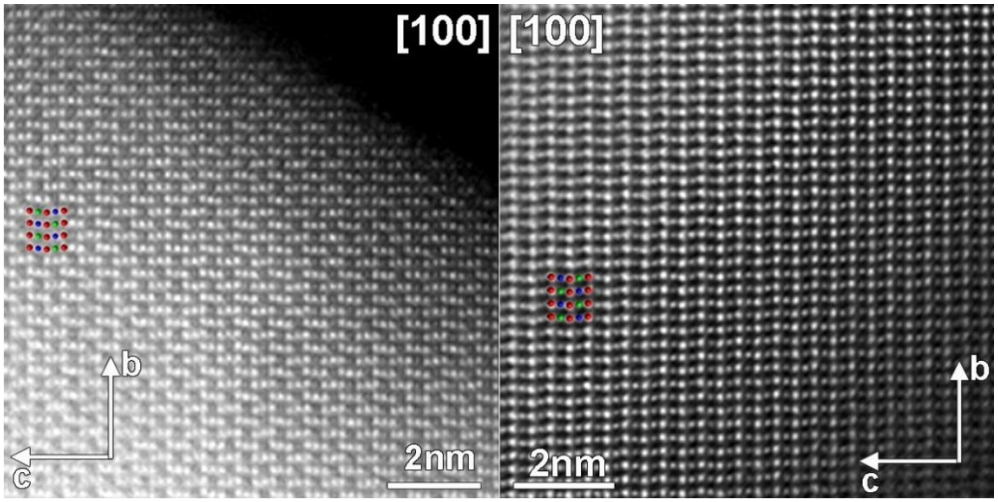


Figure 4.5. HAADF–STEM images of the most informative zone [100] of $La_3Ni_2TaO_9$ (left) and $La_3Ni_2NbO_9$ (right). An overlay of the model is shown, using the same colour scheme as the high resolution EDX maps of Figure 4.4, *i.e.* red is La, green is Ni and blue is Ta or Nb.

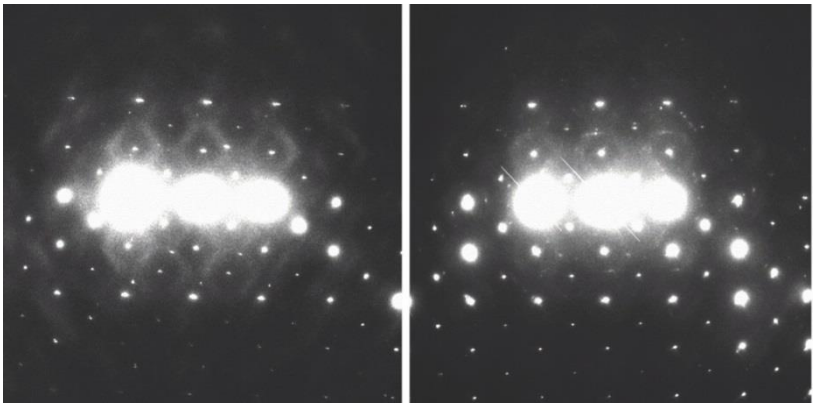


Figure 4.6. SAED patterns along the [100] zones of $La_3Ni_2TaO_9$ (left) and $La_3Ni_2NbO_9$ (right), showing clear structured diffuse scattering. The patterns are tilted out of zone to increase the visibility of the diffuse scattering.

The sizes of the particles were analysed using SEM. As can be clearly seen on Figure S4.1, the $La_3Ni_2NbO_9$ particles are slightly larger than those of $La_3Ni_2TaO_9$. The sizes were quantified using Digital Micrograph[136] to determine a value for the diameter of the particles, using either the mean diameter along two perpendicular directions or using a spherical particle approximation. The average sizes were in both approximations about 580(20) and 670(30) nm for $La_3Ni_2TaO_9$ and $La_3Ni_2NbO_9$, respectively, but for both

compounds there is a large range in sizes, varying over several hundred nanometers, see Figure S4.2.

The temperature dependence of the ZFC and FC molar magnetic susceptibilities of $La_3Ni_2TaO_9$ and $La_3Ni_2NbO_9$ measured in 100 Oe are shown in Figure 4.7. The inverse magnetic susceptibility of each sample is linear above ~175 K but neither sample behaves as a Curie paramagnet below that temperature. The effective magnetic moment, μ_{eff}, and the Weiss temperature, θ_W, derived from fitting the data collected above 200 K to the Curie–Weiss law are listed in Table 4.2, along with the corresponding parameters for $La_3Ni_2SbO_9$[48]. The ZFC susceptibility of each compound reaches a maximum at a temperature T_{MAX}, see Table 4.2, and below this temperature there is a clear difference between the ZFC and FC susceptibilities. The FC susceptibilities, χ_{FC}, measured in 10, 100 and 1000 Oe are shown in Figure 4.8. Note that χ_{MAX} is an order of magnitude greater in $La_3Ni_2TaO_9$ and that hysteresis persists somewhat above T_{MAX} in that compound. Furthermore, the susceptibility of $La_3Ni_2TaO_9$ is strongly field dependent at all temperatures below 85 K whereas that of the niobium analogue is essentially independent of field above T_{MAX} and shows a relatively weak field dependence below that temperature. Figure 4.9 shows the $M(H)$ for each compound and the values of the remanent magnetisation (M_R) and coercive field (H_C) observed at 5 K are included in Table 4.2. $M(H)$ is not a linear function for either compound at 150 K but it is linear for both at 220 K. The deviation from linearity at 150 K is greater in the case of $La_3Ni_2TaO_9$ even though both compounds show their susceptibility maximum below 100 K. The temperature and frequency dependence of the ac molar susceptibilities of $La_3Ni_2TaO_9$ and $La_3Ni_2NbO_9$ are shown in Figure 4.10. The data in Figure 4.10a show anomalous behaviour in $La_3Ni_2TaO_9$ below 85 K, the temperature below which hysteresis is observed in the dc susceptibility and well above T_{MAX}. The ac susceptibility is complex below the transition temperature,

which shows no clear frequency dependence. However, in the case of $La_3Ni_2NbO_9$ the temperature of the susceptibility maximum is frequency dependent and the susceptibility is again complex below this temperature. The parameter $\Delta T_f/[T_f\Delta(\log \omega)]$ takes a value of 0.0167, indicating that $La_3Ni_2NbO_9$ can be classified as a canonical spin glass. The temperature of the maximum in χ' corresponds closely to T_{MAX} observed in the dc susceptibility. The two compounds clearly have very different magnetic properties.

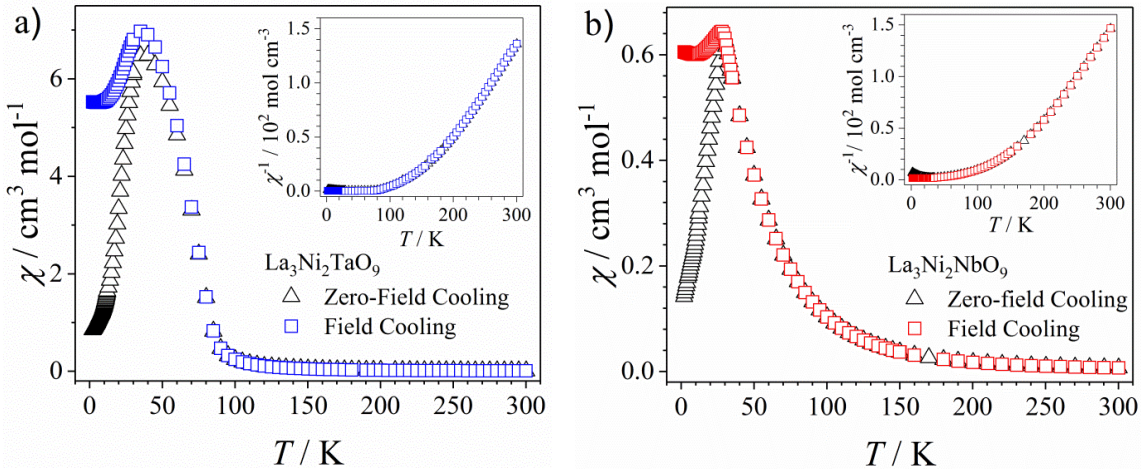


Figure 4.7. The temperature dependence of dc molar susceptibility and (inset) inverse susceptibility of (a) $La_3Ni_2TaO_9$ and (b) $La_3Ni_2NbO_9$ measured in 100 Oe as a function of temperature.

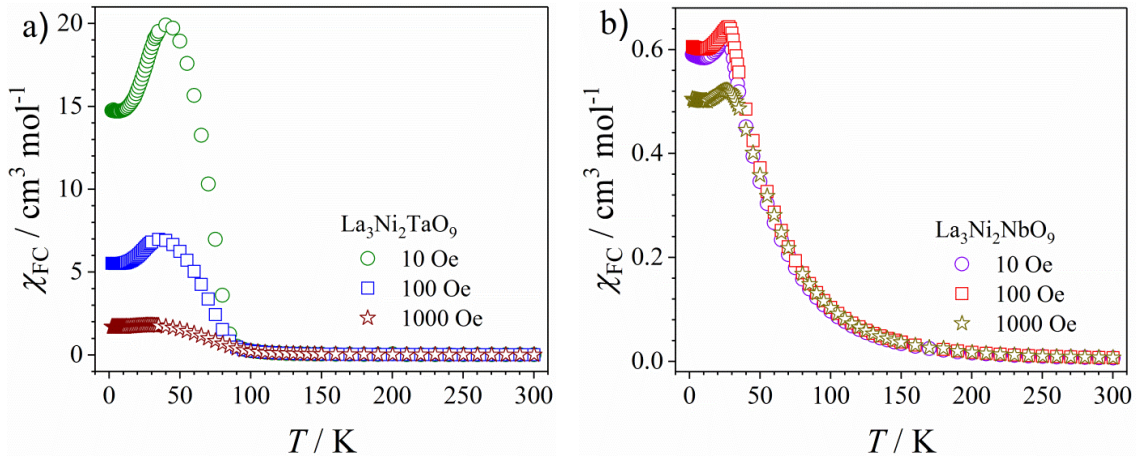


Figure 4.8. The FC dc molar susceptibility of (a) $La_3Ni_2TaO_9$ and (b) $La_3Ni_2NbO_9$ measured in 10, 100 and 1000 Oe as a function of temperature.

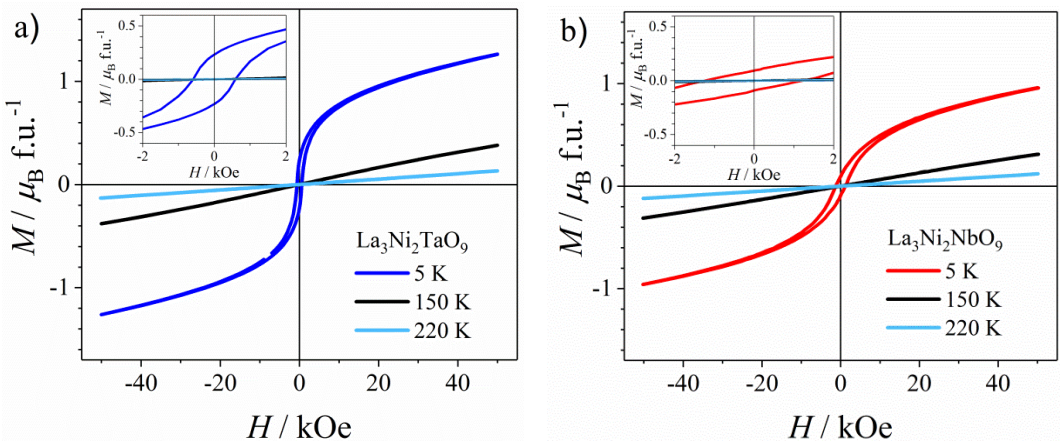


Figure 4.9. The magnetisation per formula unit as a function of magnetic field of (a) $La_3Ni_2TaO_9$ and (b) $La_3Ni_2NbO_9$ at 5 (red or blue), 150 (black) and 220 (cyan) K. The inset shows the function for $-2 \leq H/\text{kOe} \leq 2$.

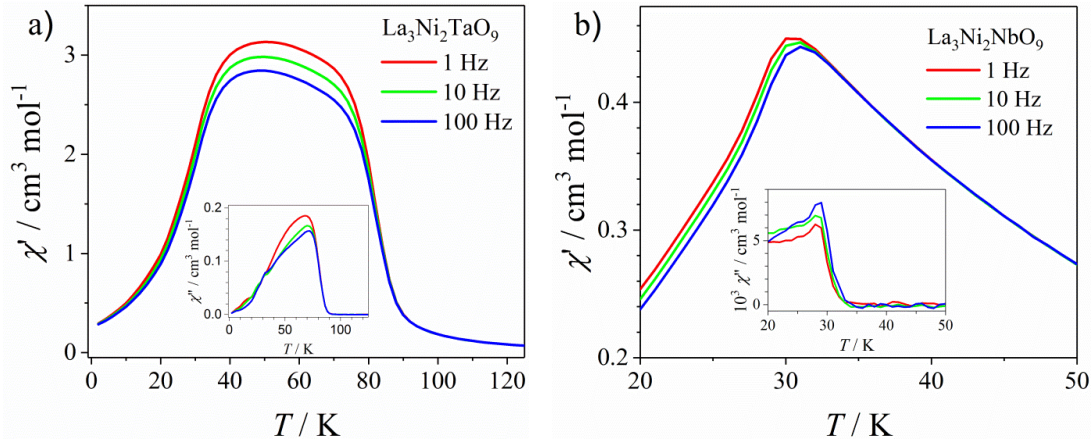


Figure 4.10. The real and imaginary components of the ac susceptibility of (a) $La_3Ni_2TaO_9$ and (b) $La_3Ni_2NbO_9$ as a function of temperature measured at 1 (red), 10 (green) and 100 (blue) Hz.

Table 4.2. Magnetic parameters of $La_3Ni_2B'O_9$ (B' = Sb, Ta or Nb).

Composition	μ_{eff} / μ_B	θ_W / K	M_R / μ_B	H_C / kOe	T_{MAX} / K
$La_3Ni_2SbO_9$	2.2(1)	+159	0.5	0.5	45
$La_3Ni_2TaO_9$	2.15(1)	+144(2)	0.2	0.6	35
$La_3Ni_2NbO_9$	2.12(1)	+137(3)	0.1	1.3	29

No additional Bragg peaks that could have a magnetic origin were detected in any of the NPD patterns collected below room temperature on D2b or D1b, despite the enhanced counting statistics of the latter. The results of the analysis of the data collected at 5 K on D2b are shown in Figure S4.3 and the refined structural parameters of $La_3Ni_2TaO_9$ and $La_3Ni_2NbO_9$ at 5 K are listed in Table 4.3, respectively. Some selected bond lengths and angles at room temperature and 5 K are listed in Tables 4.4 and 4.5, respectively. To facilitate comparison, the corresponding quantities reported by Battle *et al.* for $La_3Ni_2SbO_9$[48] are also included in these tables. The results of the analyses of NPD data collected on D1b for $5 < T/K < 300$ can be found in Figures S4.4 and S4.5; the structural parameters resulting from the analysis of data collected on D2b at intermediate temperatures are listed in Tables S4.1 and S4.2.

Table 4.3. Structural parameters of $La_3Ni_2B'O_9$ (B' = Ta or Nb) at 5 K (Space group $P2_1/n$).

		B' = Ta	B' = Nb
a / Å		5.5782(2)	5.5755(1)
b / Å		5.6372(2)	5.6383(1)
c / Å		7.9067(2)	7.9029(2)
β / °		90.064(6)	90.024(9)
V / Å^3		248.63(2)	248.44(2)
$R_{wp\|NPD}$ / %		4.60	4.72
χ^2		3.350	4.618
La	x	0.4919(5)	0.4918(5)
4*e* (*x y z*)	y	0.4597(2)	0.4588(2)
	z	0.250(1)	0.250(1)
	U_{ISO} / Å^2	0.0143(3)	0.0140(3)
Ni/*B*'1	U_{ISO} / Å^2	0.0012(2)	0.00182)
2*c* (0 ½ 0)	Ni occupancy	0.982	0.964
	B' occupancy	0.018	0.036
Ni/*B*'2	U_{ISO} / Å^2	0.0012(2)	0.0018(2)
2*d* (½ 0 0)	Ni occupancy	0.351	0.369
	B' occupancy	0.649	0.631
O1	x	0.790(1)	0.792(1)
4*e* (*x y z*)	y	0.798(1)	0.797(1)
	z	–0.0386(7)	–0.0383(7)
	U_{ISO} / Å^2	0.0018(13)	0.0012(12)
O2	x	0.710(1)	0.712(1)
4*e* (*x y z*)	y	0.284(1)	0.284(1)
	z	–0.0462(8)	–0.0464(8)
	U_{ISO} / Å^2	0.0062(15)	0.0084(15)
O3	x	0.5781(5)	0.5786(4)
4*e* (*x y z*)	y	0.0180(4)	0.0174(4)
	z	0.251(1)	0.252(1)
	U_{ISO} / Å^2	0.0081(5)	0.0086(5)

Table 4.4. Selected bond lengths (Å) and angles (°) in $La_3Ni_2B'O_9$ (*B'* = Sb, Ta or Nb) at RT.

	$La_3Ni_2SbO_9$	$La_3Ni_2TaO_9$	$La_3Ni_2NbO_9$
La–O1	2.815(9)	2.745(4)	2.733(4)
La–O1	2.687(7)	2.721(4)	2.733(4)
La–O1	2.384(8)	2.452(4)	2.446(4)
La–O2	2.799(9)	2.831(4)	2.838(5)
La–O2	2.478(8)	2.433(4)	2.440(5)
La–O2	2.686(8)	2.648(5)	2.632(5)
La–O3	2.561(2)	2.549(2)	2.549(2)
La–O3	2.448(4)	2.429(2)	2.430(2)
2*c*–O1	2.094(5)×2	2.062(3)×2	2.059(4)×2
2*c*–O2	2.055(6)×2	2.061(4)×2	2.054(4)×2
2*c*–O3	2.071(10)×2	2.016(6)×2	2.028(9)×2
2*d*–O1	2.007(6)×2	2.007(3)×2	2.012(4)×2
2*d*–O2	2.012(6)×2	2.023(4)×2	2.024(4)×2
2*d*–O3	1.993(10)×2	2.042(6)×2	2.026(9)×2
O1–2*c*–O2	89.7(3)×2	89.8(2)×2	89.2(3)×2
O1–2*c*–O3	88.9(2)×2	88.8(1)×2	88.8(1)×2
O2–2*c*–O3	89.4(2)×2	88.0(1)×2	87.7(1)×2
O1–2*d*–O2	87.6(3)×2	88.1(2)×2	87.2(3)×2
O1–2*d*–O3	87.8(2)×2	89.8(1)×2	89.8(1)×2
O2–2*d*–O3	89.2(2)×2	88.9(1)×2	88.9(1)×2
2*c*–O1–2*d*	151.62(1)	154.7(2)	154.3(2)
2*c*–O2–2*d*	155.62(1)	152.9(2)	153.4(2)
2*c*–O3–2*d*	155.12(1)	154.9(1)	155.04(9)

Table 4.5. Selected bond lengths (Å) and angles (°) in $La_3Ni_2B'O_9$ (*B'* = Sb, Ta or Nb) at 5K.

	$La_3Ni_2SbO_9$	$La_3Ni_2TaO_9$	$La_3Ni_2NbO_9$
La–O1	2.833(8)	2.743(10)	2.732(10)
La–O1	2.658(7)	2.712(9)	2.718(8)
La–O1	2.401(8)	2.439(9)	2.435(9)
La–O2	2.767(9)	2.819(10)	2.826(10)
La–O2	2.463(8)	2.438(9)	2..449(9)
La–O2	2.693(8)	2.639(9)	2.624(9)
La–O3	2.545(3)	2.536(3)	2.535(2)
La–O3	2.463(4)	2.421(4)	2.418(3)
2*c*–O1	2.088(5)×2	2.070(5)×2	2.059(5)×2
2*c*–O2	2.050(6)×2	2.060(5)×2	2.050(6)×2
2*c*–O3	2.036(10)×2	2.020(9)×2	2.013(11)×2
2*d*–O1	2.011(5)×2	2.001(5)×2	2.014(6)×2
2*d*–O2	2.012(5)×2	2.014(6)×2	2.021(6)×2
2*d*–O3	2.025(10)×2	2.034(9)×2	2.039(11)×2
O1–2*c*–O2	89.8(3)×2	89.5(3)×2	89.0(4)×2
O1–2*c*–O3	89.0(2)×2	88.9(2)×2	88.9(2)×2
O2–2*c*–O3	89.7(2)×2	88.1(2)×2	88.1(2)×2
O1–2*d*–O2	87.5(3)×2	87.4(4)×2	87.1(4)×2
O1–2*d*–O3	87.6(2)×2	89.7(2)×2	90.0(2)×2
O2–2*d*–O3	89.2(2)×2	89.2(2)×2	89.2(2)×2
2*c*–O1–2*d*	151.3(3)	153.8(3)	153.6(3)
2*c*–O2–2*d*	155.7(3)	153.4(4)	153.7(4)
2*c*–O3–2*d*	154.7(2)	154.5(1)	154.4(1)

The muon asymmetry for $La_3Ni_2B'O_9$ (*B'* = Sb, Nb or Ta) is plotted in Figure 4.11 for a representative set of temperatures (data collected at the Swiss Muon Source). For each compound, heavily–damped oscillatory behaviour is found at low temperatures, proving the presence of a static spin system in all three compositions. The heavy damping suggests that the muons experience a range of fields and is consistent with the presence of either long–range or short–range magnetic order. The observed asymmetry at low temperatures is well described by a fitting function of the form:

$$A_1 \cos(\gamma_\mu B_\mu t)\, exp(-\lambda_1 t) + A_2 \exp(-\lambda_2 t) + A_3 \exp(-\lambda_3 t), \qquad \text{Equation 4.1}$$

where γ_μ is the muon gyromagnetic ratio (= $2\pi \times 135.5$ MHz/T) and λ_i are relaxation rates. The first term models the oscillatory signal and its fitted amplitude A_1 is much larger than those of the non–oscillating terms (A_2 and A_3), signifying that the majority of the muons indeed stop at a site which is directly sensing the static spin system. It is believed that the smaller non–oscillatory terms can be attributed to a combination of muons stopping in regions in which the local field is along the muon polarization direction and muons stopping in the cryostat tails. The exponentials account for temporal fluctuations of the local magnetic field. At higher temperatures a single, non–oscillatory exponentially relaxing component is sufficient to describe the muon asymmetry. The fitted values for the mean local field $B_\mu(T)$ as a function of temperature are presented in Figure 4.12, and are shown together with fitted curves obtained from the phenomenological relation $B_\mu(T) = B_0(1–(T/T_C)^\alpha)^\beta$. These fitted curves yield values for the transition temperature T_C of 95 K for *B*' = Sb, 38 K for *B*' = Nb and 30 K for *B*' = Ta, and show that $B_\mu(0)$ = 290(10) mT for all three compounds.

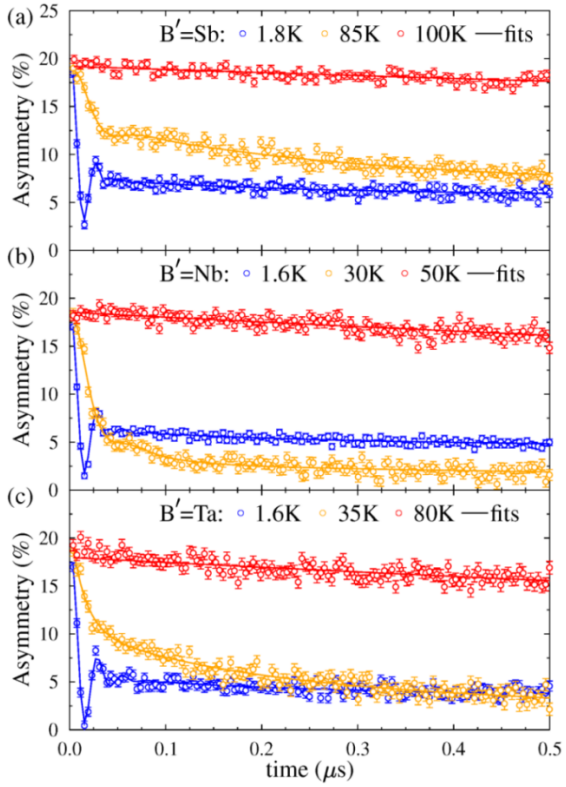


Figure 4.11. Muon asymmetry of $La_3Ni_2B'O_9$ (B'=Sb, Nb, Ta) measured at the General Purpose Spectrometer (GPS) at the Swiss Muon Source for representative temperatures: well below, slightly above and well above T_c. The solid lines represent the curves fitted using the formulae described in the main text.

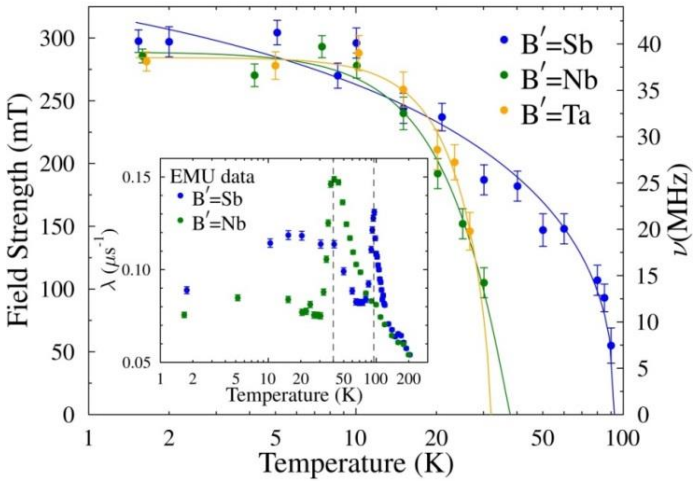


Figure 4.12. Mean local field measured at the muon site as extracted from the muon precession signals. The solid lines are obtained by fitting a phenomenological order parameter equation: $B_\mu(T)=B_0(1-(T/T_C)^\alpha)^\beta$. The inset shows the relaxation rates obtained the EMU spectrometer at ISIS. The peaks in the relaxation rates due to critical slowing down near T_C are in good agreement with the values of T_C obtained from the fits to $B_\mu(T)$.

Further muon data were obtained on two of the compounds, *B*' = Sb and Nb, at the EMU muon spectrometer at STFC ISIS. However, the large value of B_μ precludes direct measurement of precession signals at a pulsed muon source such as ISIS where the frequency resolution is more limited. Nevertheless, a critical slowing down of the fluctuations near the transition temperature can be observed when fitting a single exponential with relaxation rate λ to the data. Fitted values for the relaxation rate λ are presented in the inset of Figure 4.12 and a peak analysis finds the maxima in λ (inversely proportional to the magnetic fluctuation rate) to be in good agreement with the transition temperatures of about 95 K for *B*' = Sb and 38 K for *B*' = Nb.

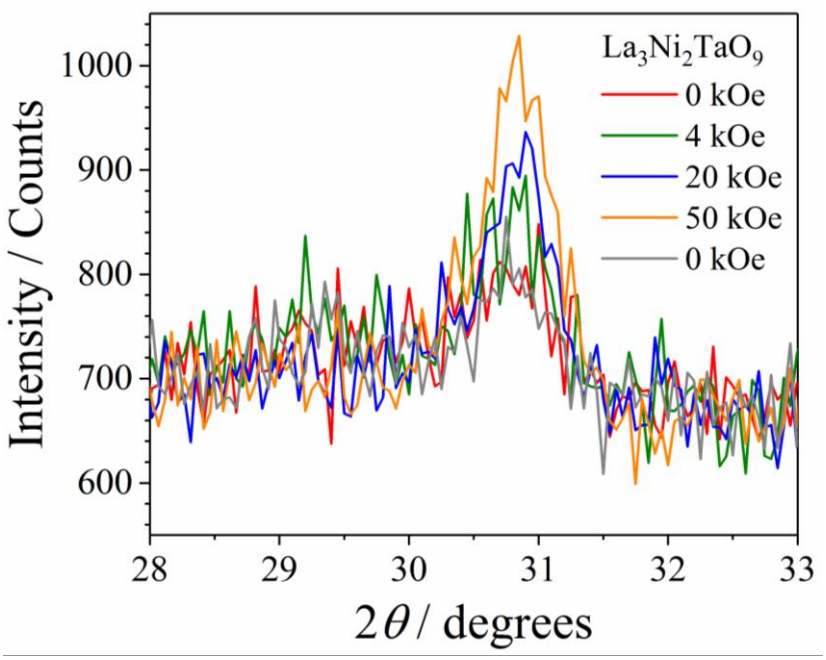


Figure 4.13. The observed neutron scattering from $La_3Ni_2TaO_9$ at 5 K in applied magnetic fields of 0 (red), 4 (olive), 20 (blue), 50 (orange) and back to 0 (grey) kOe.

The structural model derived using D2b diffractometer at 5 K was employed in the analysis of the NPD data collected at ANSTO. It gave a good account of the data collected in the absence of a magnetic field. When a magnetic field was applied, the intensity of the 011 Bragg reflection at 2θ ~31° increased with increasing field strength, see Figure 4.13. The

additional intensity could be accounted for by assuming that the field causes the Ni^{2+} cations on the 2*c* and 2*d* sites to order in a G–type magnetic structure, which is with nearest–neighbour cations having antiparallel moments. With the magnetic sublattice being pseudo–cubic, the magnetic moment of the Ni^{2+} cation was arbitrarily assigned to be along the *c* axis. The magnitude of the magnetic moment of Ni^{2+} was refined by Rietveld analysis of the in–field diffraction patterns. The moment was found to be 0.79(9), 1.07(7) and 1.34(6) μ_B per Ni^{2+} cation in fields of 4, 20 and 50 kOe, respectively. The diffraction pattern collected after the magnetic field had been switched off could be superimposed on the initial, zero–field pattern.

4.4 Discussion

Analysis of the X–ray and neutron diffraction data resulted in a structural model similar to that derived previously in the case of $La_3Ni_2SbO_9$[48]. In other words, no structural phase transition was observed by replacing the Sb^{5+} cation with a d^0 pentavalent diamagnetic cation. As a consequence of the differences in size and charge of Ni^{2+} and B'^{5+}, the Ni^{2+} cations and the pentavalent cations in both $La_3Ni_2NbO_9$ and $La_3Ni_2TaO_9$ order over the six–coordinate sites of the perovskite structure such that the 2*c* site is occupied almost entirely by the former and the 2*d* site by Ni^{2+} and B'^{5+} in an approximately 1:2 ratio; the deviation from the ideal distribution is greater in the niobium–containing compound, although it is lower than that reported in a previous study[137]. On the other hand, the structure of $La_3Ni_2TaO_9$ displayed here has a lower symmetry than previously reported by Kato *et al.*[138]. The marginally longer bond lengths around the 2*c* site, see Tables 4.4 and 4.5, reflect the size difference between the two cation species. The La–O bond lengths and the bond angles within the framework of octahedra are typical of those found in oxide perovskites. The monoclinic structure described above is also consistent with the electron diffraction patterns shown in Figure 4.3. The HAADF–STEM image of $La_3Ni_2TaO_9$, see

Figure 4.5, demonstrates clearly the cation ordering over the two six–coordinate sites but as a consequence of the reduced contrast, this is not so clear in the image of $La_3Ni_2NbO_9$. However, the EDX map in Figure 4.4 confirms that, in the selected area, the cation ordering is present. A quantitative analysis of the spot intensities in the columns of cations in Figure 4.5 did not reveal any extended regions in which the cation ordering was absent, although there were some local fluctuations in both compounds.

The magnetometry data collected on the crystalline sample of $La_3Ni_2NbO_9$ are in good agreement with those presented previously by Dey *et al.*[139]. Above 35 K the temperature dependence of the susceptibility of $La_3Ni_2NbO_9$, see Figures 4.7 and 4.8, is characteristic of a paramagnet with relatively strong interactions. The positive Weiss temperature, see Table 4.2, suggests that a transition to a ferro– or ferrimagnetic phase might occur at low temperatures but below 35 K the susceptibility is actually characteristic of a spin glass. In order to account for similar behaviour in other cation–disordered perovskites it was proposed that the frustration necessary for the formation of a spin glass results from competition between nearest–neighbour and next–nearest–neighbour superexchange interactions that favour the adoption of different magnetic structures[131]. The relative strengths of the different interactions within a particular region of a crystallite will be determined by the local composition. It seems likely that the same factors are involved in the case of $La_3Ni_2NbO_9$, where the random distribution of Ni^{2+} and Nb^{5+} over the 2*d* sites will cause local fluctuations in composition. The absence of magnetic Bragg scattering in the neutron diffraction data can then be explained by postulating that a particular pattern of cation ordering is never maintained over distances long enough to allow the development of islands of coherent magnetic order that can be detected by neutron diffraction. However, the diffuse scattering apparent in Figure 4.6 suggests that cation ordering is present over short distances. The *M(H)* behaviour of $La_3Ni_2NbO_9$, see Figure 4.9, can be explained by

the alignment of small ferromagnetic domains in an applied magnetic field, the same argument which was used to elucidate the characteristics of the antimony–containing counterpart[48, 75]; the magnetisation per f.u. is never saturated, indicating those ferromagnetic domains are not completely aligned even with a large field. The observation of oscillations in the μSR data below 35 K, see Figures 4.11 and 4.12, is consistent with this explanation. The presence of oscillations proves that static spins are present at low temperatures but their rapid damping suggests that they may be ordered only in relatively small regions.

Like $La_3Ni_2NbO_9$, $La_3Ni_2TaO_9$ has a relatively large and positive Weiss temperature in the paramagnetic region. However, below approximately 100 K $\chi(T)$ behaves in a manner that is reminiscent of the relaxor ferromagnet $La_3Ni_2SbO_9$ rather than the niobium–containing composition. In common with the latter, the dc susceptibility measured in 100 Oe has a clear maximum at T_{MAX} ~35 K but the magnitude of the susceptibility is an order of magnitude greater in $La_3Ni_2TaO_9$. Furthermore, hysteresis is clearly apparent in $\chi(T)$ between T_{MAX} and ~80 K whereas none was detected in the data collected on $La_3Ni_2NbO_9$ above 30 K. The temperature dependence of the ac susceptibility is also markedly different, see Figure 4.10. The frequency dependence of the real component and the appearance of an imaginary component, taken together with the presence of hysteresis in the dc data, suggest that magnetised domains are present below ~80 K. Another piece of evidence of the existence of magnetic domains is the NPD data collected in an applied magnetic field. The increase in intensity can be attributed to the alignment of numerous ferromagnetic regions with the external field. These domains grow in size and are thus large enough to be detected in neutron diffraction. It is clear that $La_3Ni_2SbO_9$ and $La_3Ni_2TaO_9$ share similarities. The difference lies in the moment deduced at 0 kOe. The magnetic moment per Ni^{2+} cation in the former was found to be approximately 1 μ_B

whereas the corresponding G–type ordering is absent in the latter. This can be explained by the fact that the magnetic ordering in $La_3Ni_2TaO_9$ occurs over shorter distances than in $La_3Ni_2SbO_9$ in the absence of an external magnetic field. The coercive field is smaller in $La_3Ni_2TaO_9$ than in $La_3Ni_2SbO_9$, suggesting that the domain size is different in the two materials. However, the μSR data in Figure 4.12 suggest that the spins only become static on a microsecond timescale below 35 K. In order to account for these data it is proposed that extensive short–range magnetic ordering, resulting in the formation of relatively–large rapidly–relaxing ferrimagnetic clusters, is well–established at ~80 K in $La_3Ni_2TaO_9$. On further cooling the larger clusters become blocked, giving rise to hysteresis. The spins become static after being cooled below 35 K, but are still in clusters which are too small to be detected in a neutron diffraction experiment. Studying the short–range ordering using the appropriate neutron scattering techniques will now be the crucial to understand the underlying principles of the magnetic properties of $La_3Ni_2TaO_9$.

The differences in the magnetic behaviours of $La_3Ni_2SbO_9$, $La_3Ni_2TaO_9$ and $La_3Ni_2NbO_9$ are striking, given that they are apparently isostructural compounds and the changes in chemical composition along the series do not involve the magnetic species. It is not surprising that $La_3Ni_2SbO_9$ and $La_3Ni_2NbO_9$ behave differently but $La_3Ni_2TaO_9$ would be expected to lie closer to the latter rather than the former. Local structural variations in these "triple perovskites" should then be investigated to explain the behaviour of these three compounds.

One factor that could be important is the extent to which the B'^{5+} and Ni^{2+} cations order over the six–coordinate sites. The neutron diffraction experiments reported above determine the average site occupancies across the crystallites; they do not identify local deviations from the mean distribution. When judged on the former length scale, the degree of ordering increases in the sequence Nb < Ta < Sb but the differences are small and the 2*d*

site is still 96.4(7) % occupied by Ni^{2+} in the most heavily disordered niobium–containing sample.

The structures over shorter length scales that are not probed in a neutron diffraction experiment therefore become more important in order to understand the magnetic behaviour and TEM has been used to look for local anomalies in the cation–ordering pattern. Disordered regions found in $La_3Ni_2SbO_9$ were considered as magnetic domain walls between neighbouring ordered regions. No comparable feature has been observed in the TEM studies of $La_3Ni_2NbO_9$ which shows spin–glass–like behaviour at low temperature. However, nor have they been observed in $La_3Ni_2TaO_9$, despite the fact that the magnetic behaviour of that compound is somewhat similar to that of $La_3Ni_2SbO_9$. The difference in the coercive fields derived from $M(H)$, together with the apparent inconsistency in the relative particle size as determined by SEM and X–ray diffraction, are the only indication of a difference between the microstructure of $La_3Ni_2TaO_9$ and that of $La_3Ni_2NbO_9$. The observation of a small particle size in $La_3Ni_2NbO_9$ is consistent with the findings of Inprasit *et al.*[140] but, interestingly, subsequent SEM measurements found that the particle size in the sample of $La_3Ni_2NbO_9$ discussed herein was actually greater than that in the sample of $La_3Ni_2TaO_9$.

However, changes in the chemical bonding brought about by the differences in the electronic structure of the diamagnetic, pentavalent cation can also be one possible cause. Comparative studies of the perovskites Sr_2NiWO_6 and Sr_2NiTeO_6[129, 141] and other pairs of d^0 and d^{10} compounds have shown that the magnetic structure adopted at low temperatures is partly dependent on whether the diamagnetic cation on the six–coordinate sites has empty *d* orbitals available to take part in the superexchange interactions. In order to understand the influence of the electron configuration of the diamagnetic, pentavalent cation in the superexchange interactions, and hence the competition among them, a study

of the solid solution $La_3Ni_2Sb_xTa_yNb_{1-x-y}O_9$ will be presented in the following chapter. A more detailed explanation of the variation of the magnetic behaviour of $La_3Ni_2B'O_9$ where B' = Sb, Ta or Nb will be presented therein.

4.5 Conclusion

Marked differences are apparent in the magnetic properties of $La_3Ni_2SbO_9$, $La_3Ni_2TaO_9$ and $La_3Ni_2NbO_9$ even though they all crystallise in the same monoclinic space group $P2_1/n$ and show similar degrees of cation ordering over the six–coordinate sites. Surprisingly, the contrast between the Sb^{5+} (d^{10}) and Ta^{5+} (d^0) compounds is less than that between those containing Ta^{5+} and Nb^{5+} (d^0). It is evident that the tantalum–containing perovskite is another example of a relaxor ferromagnet.

This work has been published as *C.–M. Chin, P. D. Battle, S. J. Blundell, E. C. Hunter, F. Lang, M. Hendrickx, R. Paria Sena and J. Hadermann, Journal of Solid State Chemistry, 2018, **258**, 825-834*[142].

Chapter 5: The studies of the solid solutions of $La_3Ni_2Sb_xTa_yNb_{1-x-y}O_9$

5.1 Introduction

The synthesis of multiple compositions in a solid solution is a valuable approach to the study of perovskites containing different *B*–site cations, especially when the end members show differences in their magnetic properties. For example, Sr_2CuWO_6 and Sr_2CuMoO_6 were reported to have quasi–two–dimensional magnetic behaviour with broad maxima located at T = 83 and 95 K, respectively[143, 144]. The magnetic properties of the solid solution of $Sr_2CuW_{1-x}Mo_xO_6$ showed a variation with composition; the temperature of the susceptibility maximum increases with increasing Mo content[143]. However, due to the energetically low–lying d^{10} orbital of Te^{6+} cation, hybridisation with the O^{2-} 2*p* orbital is not possible in Sr_2CuTeO_6 and hence the linear Cu–O–Te–O–Cu superexchange interaction is not allowed[67, 68, 145-147]. This leads to interesting magnetic properties for the members in the $Sr_2CuTe_yW_{1-y}O_6$ solid solution. In contrast to the $Sr_2CuW_{1-x}Mo_xO_6$ system, in which the electron configurations of all the hexavalent cations is d^0, the temperature of the susceptibility maximum is not in a linear relationship with the composition[147]. It was found that the magnetic frustration arising from the competition between the nearest–neighbour and the next–nearest–neighbour antiferromagnetic interactions is strongest when there are approximately equal amounts of Te^{6+} and W^{6+} cations present in the sample; the composition $Sr_2CuTe_{0.5}W_{0.5}O_6$ was reported to be a spin–liquid, a state where the spins remain dynamic near absolute zero[148].

The synthesis and characterisation of the solid solution $La_3Ni_2Sb_xTa_yNb_{1-x-y}O_9$ is presented in this chapter. As demonstrated in previous chapters, the bulk magnetic properties of the

triple perovskite $La_3Ni_2B'O_9$ series were found to be surprising; $La_3Ni_2SbO_9$ and $La_3Ni_2TaO_9$ were relaxor ferromagnets whereas $La_3Ni_2NbO_9$ is a spin glass, even though both Ta^{5+} and Nb^{5+} are d^0 cations. Studies of the solid solution have allowed an investigation of how the magnetic behaviour alters according to the composition. The comparison between members in the $La_3Ni_2Sb_xTa_yNb_{1-x-y}O_9$ system is of particular interest because of the presence of both d^0 and d^{10} diamagnetic cations in samples of a solid solution, the end members of which have significantly different magnetic properties. XRPD, magnetometry, NPD and electron microscopy were employed in the report described below.

5.2 Experimental

Polycrystalline samples of compositions containing two pentavalent cations were prepared using the traditional ceramic method. Stoichiometric amounts of NiO, B'_2O_5 (B' = Sb, Ta or Nb) and pre–dried La_2O_3 were thoroughly mixed and ground in an agate mortar and pestle. Each mixture was pelletised and heated in air at 1200 to 1250 °C for up to 16 days. The pellet was ground and reformed every 2–4 days. In all, three new compositions in each of the three series Sb/Nb, Sb/Ta and Ta/Nb were prepared. X–ray powder diffraction (XRPD) was used to monitor the progress of the reactions and to characterise the final products. Data were collected at room temperature (RT) using a PANalytical Empyrean diffractometer with Cu $K_{\alpha 1}$ radiation (λ = 1.54051 Å). Data were collected over an angular range of $15 \leq 2\theta/° \leq 125$ with a step–size, $\Delta 2\theta$, of 0.0066°. The XRPD patterns were analysed using the Rietveld method[92], as implemented in the GSAS program suite[94]. The background level of each pattern was modelled by a 15–term shifted Chebyshev function and the peak shapes were fitted with a pseudo–Voigt function[123].

A SQUID magnetometer was employed to study the magnetic properties of the $La_3Ni_2Sb_xTa_yNb_{1-x-y}O_9$ series. 30 – 50 mg of the sample was first cooled to 5 K in the absence of a magnetic field (Zero–Field Cooling, ZFC) and then the dc susceptibility was measured in a field of 100 Oe as the sample was warmed to 300 K. This was repeated after the sample had been cooled to 5 K in a field of 100 Oe (Field Cooling, FC). The field dependence of the magnetisation per formula unit (f.u.) was measured over the range $-50 \leq H/\text{kOe} \leq 50$ at 5, 150 and 220 K.

All of the compositions containing two pentavalent cations were characterised by X–ray diffraction and dc magnetometry as described above. However, three of them (i.e. $La_3Ni_2Ta_{0.75}Nb_{0.25}O_9$, $La_3Ni_2Sb_{0.75}Ta_{0.25}O_9$ and $La_3Ni_2Sb_{0.75}Nb_{0.25}O_9$) were studied in greater detail using ac magnetometry, electron microscopy and neutron diffraction. Their ac susceptibilities were measured over the temperature range $2 \leq T/\text{K} \leq 150$ in a magnetic field of amplitude 3.5 Oe oscillating at frequencies of 1, 10, 100 and 1000 Hz.

The homogeneity of these selected reaction products was studied by performing low–magnification energy–dispersive X–ray (EDX) measurements on a 200 kV FEI Osiris microscope equipped with a Super–X detector. Specimens were prepared by dispersing a crushed polycrystalline sample in ethanol and depositing a few drops of this suspension on a copper grid covered with a holey carbon film. The L–lines were used for the quantification of La (~ 4.6 keV), Sb (~3.6 keV) and Nb (~2.2 keV) and the K–lines for the quantification of Ni (~1.7 keV). In the case of Ta there was a choice of two line series, the M–lines (~1.7 keV) and the L–lines (~8.1 keV), which overlap with Si peaks arising from the sample preparation or Cu peaks arising from the support, respectively. The L–line was chosen for all measurements as there was less peak overlap compared to the M–line and it produced results closer to the expected stoichiometry. The oxygen content, which cannot be accurately quantified by EDX, was excluded from the analysis. The compositions of

between 36 and 53 regions were measured across multiple grains of each sample in order to determine the average stoichiometry. In the light of the results of these experiments $La_3Ni_2Sb_{0.75}Ta_{0.25}O_9$ and $La_3Ni_2Sb_{0.75}Nb_{0.25}O_9$ were studied further. Selected area electron diffraction (SAED) patterns were taken with an FEI Tecnai G2 microscope and further HAADF–STEM images, along with high–resolution EDX (HR–EDX) maps were acquired with an FEI Titan 80–300 "cubed" microscope equipped with a Super–X detector and operated at 300 kV.

Neutron powder diffraction (NPD) patterns of $La_3Ni_2Ta_{0.75}Nb_{0.25}O_9$, $La_3Ni_2Sb_{0.75}Ta_{0.25}O_9$ and $La_3Ni_2Sb_{0.75}Nb_{0.25}O_9$ were recorded using the diffractometer ECHIDNA. Data were collected at RT and 3.5 K (3 K in the case of $La_3Ni_2Sb_{0.75}Nb_{0.25}O_9$). The measurements covered an angular range of $10 \leq 2\theta/° \leq 158$ with $\Delta 2\theta = 0.05$ ° and used a wavelength of either 1.622 or 2.4395 Å. The data collected using the shorter and longer wavelengths were primarily for use in the analysis of the nuclear and magnetic Bragg scattering, respectively. The NPD patterns were analysed by the Rietveld method as implemented in GSAS.

5.3 Results

The XRPD patterns collected from the reaction products containing two pentavalent cations were dominated by a monoclinic, perovskite–like phase which adopts the space group $P2_1/n$ with $a \sim b \sim \sqrt{2}a_p$, $c \sim 2a_p$, $\beta \sim 90$ ° where a_p is the unit cell parameter of a primitive cubic perovskite. Some compositions were contaminated by a small trace of $LaTa_pNb_{1-p}O_4$ (< 1 wt. %). The crystal structure of the perovskites thus contains two crystallographically distinct octahedral sites, 2*c* and 2*d*. In the initial analysis of the cation distribution over the two six–coordinate sites the coordinates of the weakly–scattering oxide ions were not refined and it was assumed there was no site ordering between the different pentavalent cations. These Rietveld refinements showed that the 2*c* site of all the

compositions is mainly occupied by the larger Ni^{2+} cation (≥95 %) while the remaining Ni^{2+} cations share the 2*d* site with the pentavalent cations that are present. The distribution of the B'^{5+} cations was then allowed to vary whilst the occupancy of Ni^{2+} over the two sites was held constant in order to establish whether there was any ordering among the pentavalent cations. These refinements did not yield any significant improvement in the fits and the XRPD data thus provide no evidence for long–range site ordering among the different species of pentavalent *B*' cations (Nb/Ta, Sb/Ta or Sb/Nb). Fitted XRPD patterns of selected compositions are shown in Figure S5.1; the unit cell parameters of those not discussed in more detail below are listed in Table S5.1.

The temperature dependence of the dc molar susceptibility and the inverse susceptibility of each composition studied is shown in Figures S5.2 – S5.4. In every case $\chi(T)$ reaches a maximum value at a temperature T_{MAX} < 60 K, see Tables 5.1 – 5.3, and the ZFC and FC susceptibilities differ below this temperature; in some cases a difference is also apparent at temperatures between T_{MAX} and 100 K. $\chi^{-1}(T)$ of all the compositions except $La_3Ni_2Sb_{0.75}Nb_{0.25}O_9$ is linear above 220 K (240 K in the case of $La_3Ni_2Sb_{0.75}Nb_{0.25}O_9$), indicating that they become paramagnetic on warming. The data collected in the linear region of $\chi^{-1}(T)$ were fitted to the Curie–Weiss Law in order to derive the effective magnetic moment of each Ni^{2+} cation, μ_{eff}, and the Weiss temperature, θ_W, which are listed in Tables 5.1 – 5.3. The field dependence of the magnetisation per formula unit (f.u.), $M(H)$, at selected temperatures is also shown in Figures S5.2 – S5.4. At 5 K, hysteresis is apparent in every compound. The values of the coercive field (H_C) and remanent magnetisation (M_R) observed at this temperature are included in Tables 5.1 – 5.3. Hysteresis is not apparent in $M(H)$ at 150 or 220 K although the function is nonlinear at the lower of these temperatures. The composition dependence of the FC susceptibility, χ_{FC}, and $M(H)$ at 5 K within each solid solution can be seen in Figures 5.2 and 5.3.

The temperature and frequency dependence of the ac molar susceptibility of $La_3Ni_2Sb_{0.75}Ta_{0.25}O_9$, $La_3Ni_2Sb_{0.75}Nb_{0.25}O_9$ and $La_3Ni_2Ta_{0.75}Nb_{0.25}O_9$ are illustrated in Figure 5.4. The data from the former two compositions show the same general features. The real component, χ', increases relatively smoothly with temperature between 2 K and ~90 K and is frequency–dependent above 30 K. The positive slope of $\chi'(T)$ becomes steeper above ~90 K and the function reaches a well–defined maximum at a frequency–independent temperature of 95 K before falling sharply as the temperature increases to ~100 K. The imaginary component χ" is an order of magnitude weaker but shows the same general features as χ'. However, a change in gradient can be observed in the χ" at approximately 50 K, indicating the possibility of a second magnetic transition. The behaviour of $La_3Ni_2Ta_{0.75}Nb_{0.25}O_9$ is very different to that of the two Sb–containing compositions. $\chi'(T)$ and $\chi''(T)$ are frequency–dependent over the temperature range $20 < T/K < 75$ and both show a broad maximum at a frequency–independent temperature of ~50 K.

Table 5.1. Magnetic parameters of $La_3Ni_2Sb_xTa_yO_9$.

x:y	μ_{eff} / μ_B	θ_W / K	M_R / μ_B	H_C / kOe	T_C / K	T_{MAX} / K
1:0	2.08(1)	+164(2)	0.5	0.46	100	45
0.75:0.25	2.11(1)	+163(3)	0.51	0.4	105	50
0.5:0.5	2.08(1)	+159(2)	0.42	0.4	100	45
0.25:0.75	2.07(1)	+155(2)	0.4	0.4	95	45
0:1	2.13(1)	+146(1)	0.2	0.6	85	35

Table 5.2. Magnetic parameters of $La_3Ni_2Sb_xNb_{1-x}O_9$.

x	μ_{eff} / μ_B	θ_W / K	M_R / μ_B	H_C / kOe	T_C / K	T_{MAX} / K
1	2.08(1)	+164(2)	0.5	0.46	100	45
0.75	2.07(1)	+166(2)	0.51	0.38	100	45
0.5	2.09(1)	+156(3)	0.36	0.46	95	40
0.25	2.10(1)	+149(2)	0.22	0.76	80	35
0	2.10(1)	+140(1)	0.1	1.3	29	29

Table 5.3. Magnetic parameters of $La_3Ni_2Ta_yNb_{1-y}O_9$.

y	μ_{eff} / μ_B	θ_W / K	M_R / μ_B	H_C / kOe	T_C / K	T_{MAX} / K
1	2.13(1)	+146(2)	0.2	0.6	85	35
0.75	2.07(1)	+147(2)	0.2	0.66	70	35
0.5	2.11(1)	+144(2)	0.16	0.83	33	33
0.25	2.10(1)	+139(1)	0.12	1.1	32	32
0	2.10(1)	+140(1)	0.1	1.3	29	29

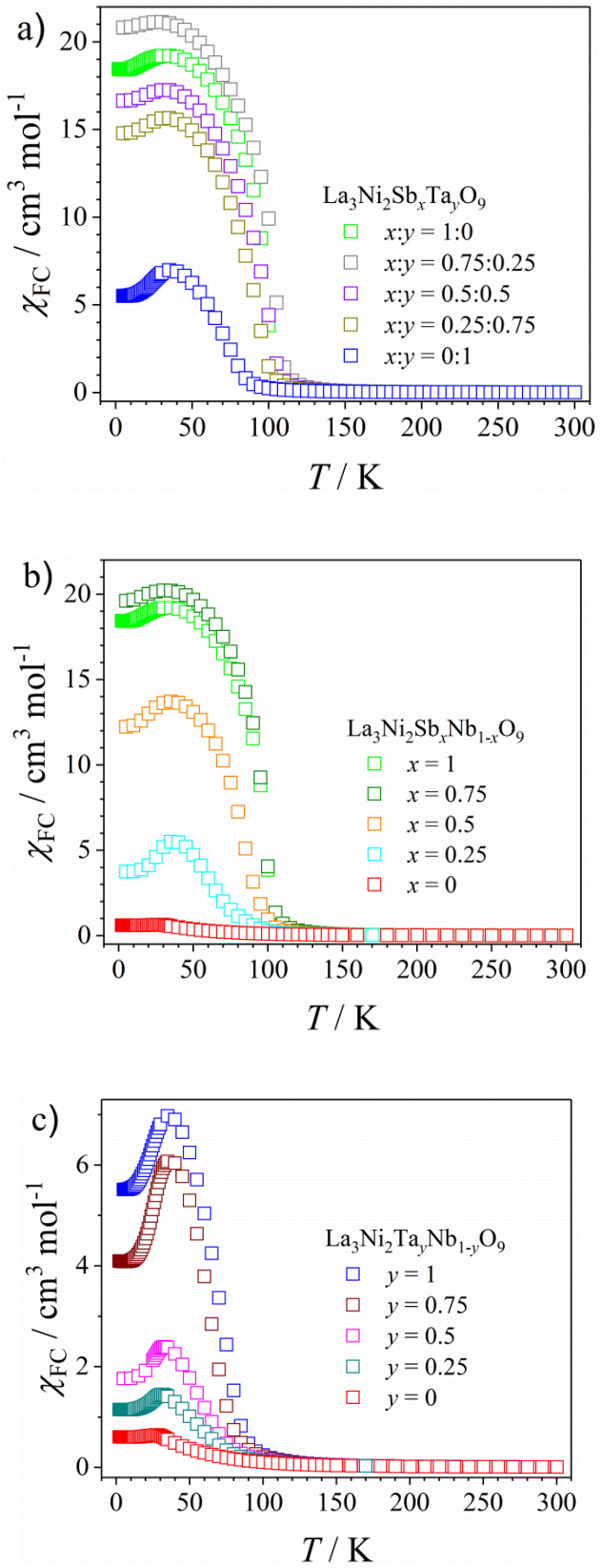


Figure 5.2. Temperature dependence of the FC molar susceptibility of (a) $La_3Ni_2Sb_xTa_yO_9$, (b) $La_3Ni_2Sb_xNb_{1-x}O_9$ and (c) $La_3Ni_2Ta_yNb_{1-y}O_9$.

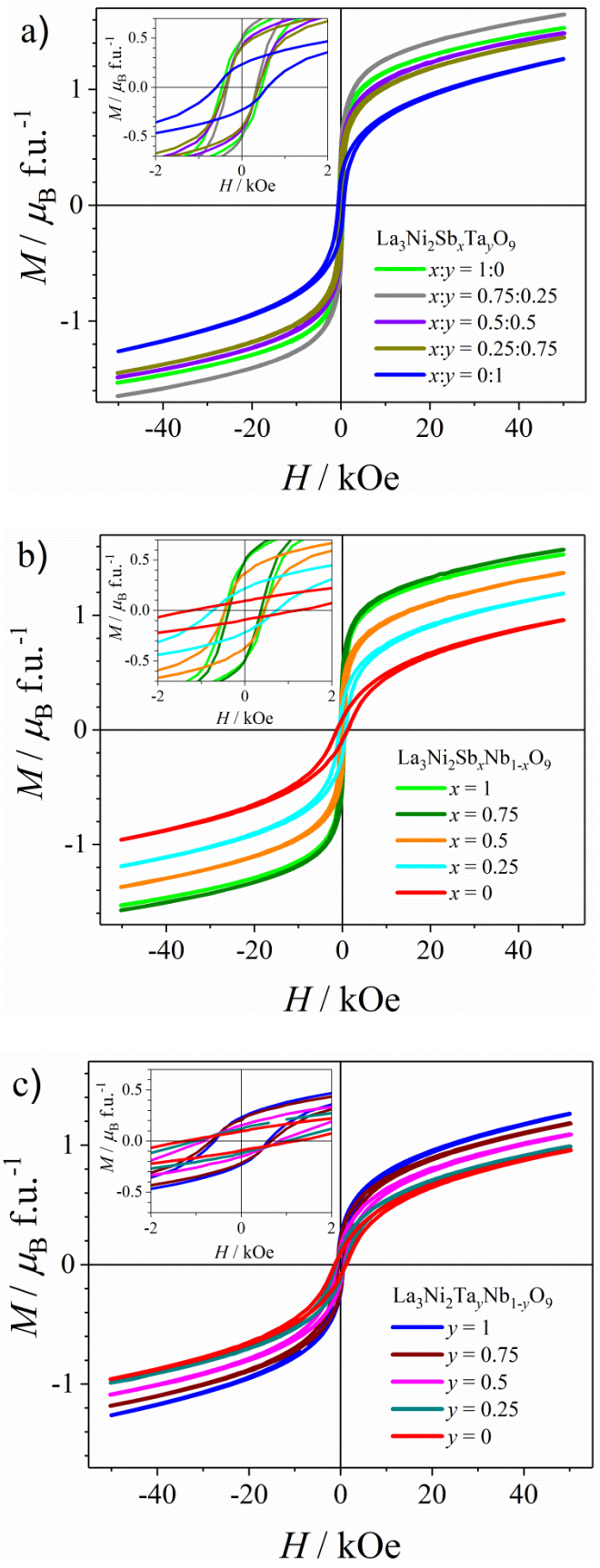


Figure 5.3. Field dependence of the magnetisation per formula unit of (a) $La_3Ni_2Sb_xTa_yO_9$, (b) $La_3Ni_2Sb_xNb_{1-x}O_9$ and (c) $La_3Ni_2Ta_yNb_{1-y}O_9$ at 5 K. The insets show the same function for $-2 < H/\text{kOe} < 2$.

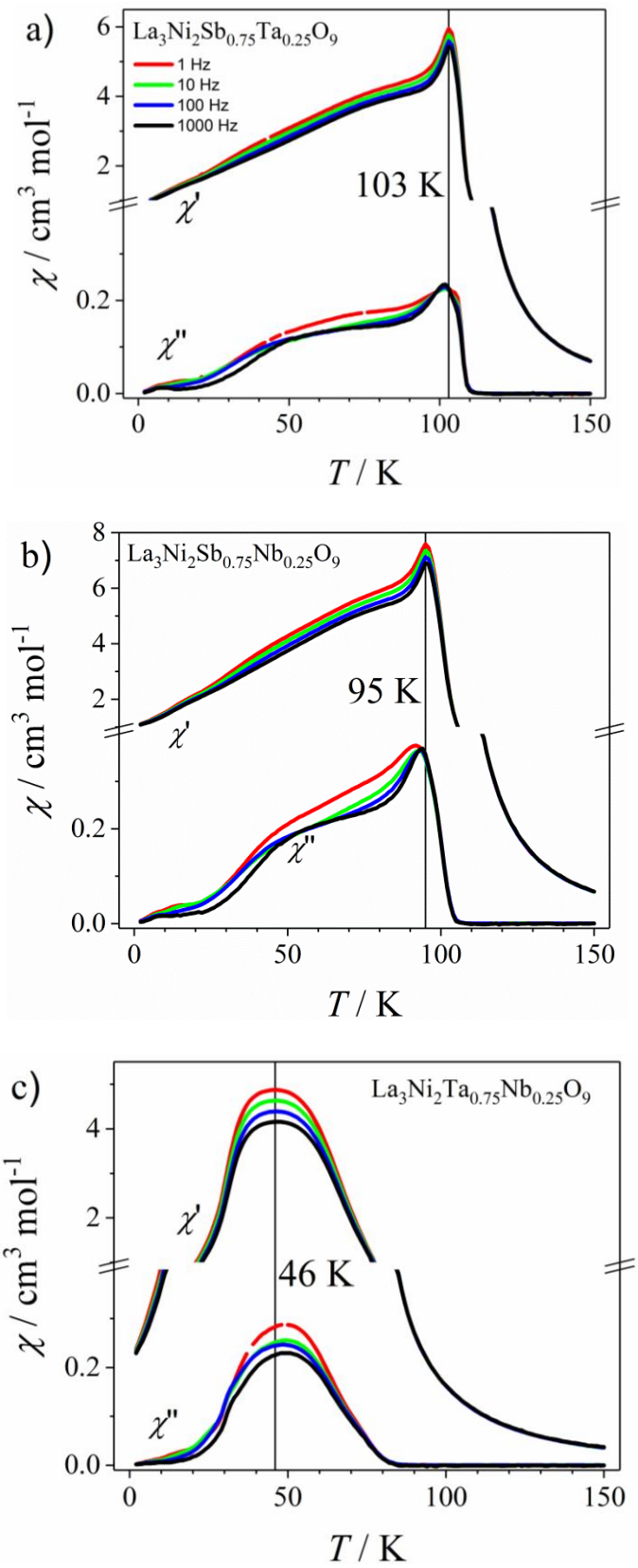


Figure 5.4. The temperature and frequency dependence of the real and (inset) imaginary components of the ac molar susceptibility of (a) $La_3Ni_2Sb_{0.75}Ta_{0.25}O_9$, (b) $La_3Ni_2Sb_{0.75}Nb_{0.25}O_9$ and (c) $La_3Ni_2Ta_{0.75}Nb_{0.25}O_9$ collected at 1 (red), 10 (green), 100 (blue) and 1000 (black) Hz.

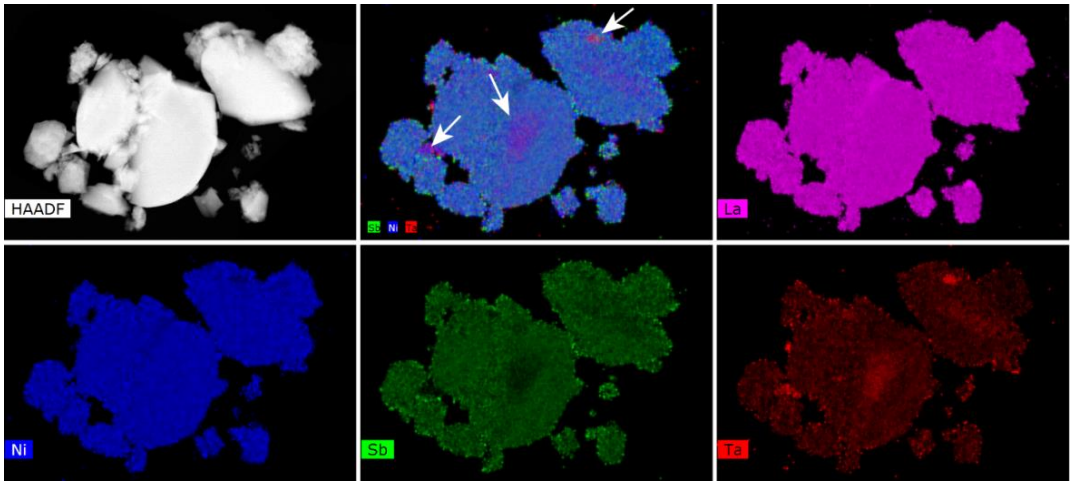


Figure 5.5. HAADF–STEM image of particles of $La_3Ni_2Sb_{0.75}Ta_{0.25}O_9$ with a mixed [Ni, Sb, Ta] and individual (La/Ni/Sb/Ta) element maps. The element maps are given in counts. The mixed element map clearly shows regions, marked by arrows, that contain much more Ta and less Sb.

The cation compositions derived from low–magnification EDX maps collected from the three samples chosen for more detailed study were $La_{0.51(1)}Ni_{0.30(1)}Sb_{0.12(2)}Ta_{0.06(2)}$ (*36*), $La_{0.52(1)}Ni_{0.30(1)}Sb_{0.14(2)}Nb_{0.04(2)}$ (*53*) and $La_{0.52(1)}Ni_{0.31(1)}Ta_{0.13(2)}Nb_{0.04(2)}$ (*38*); the italicized figure in brackets is the number of regions analysed in each case. The oxygen content was omitted here as the oxide anion cannot be reliably measured from EDX quantification on a powder sample. These formulations are in reasonable agreement with the targeted compositions, although the La and Ni contents are systematically high and low, respectively. The standard deviations indicate that while there is little variation in the atomic percentage of La and Ni in the different grains there is a greater deviation in the proportion of each of the two *B*' cations present. Figures 5.5, S5.5 and S5.6 show a representative EDX map of a grain from each sample. In the two Sb–containing samples there were a few grains, exemplified by the arrowed regions in Figure 5.5, where the ratio of the *B*'–site cations is inverted; no such extreme variations were seen in the Ta/Nb sample. Despite the compositional fluctuations, the overall ratio of the Ni to the *B*' cations remains 2:1 within error. Following the observation of regions in which the concentration

of pentavalent cations was inverted, SAED patterns were collected from the two Sb–containing compositions along the zone axes [100], [010], [001], [110] and [201], see Figures 5.6 and S5.7.

All the SAED patterns could be indexed using the cell parameters: $a \approx b \approx \sqrt{2}a_p$, $c \approx 2a_p$ and $\beta \approx 90°$, and showed the following reflection conditions: *hkl, 0kl, hk0: no conditions; h0l, h00, 00l: h+l = 2n; 0k0: k = 2n.* Reflections in conflict with the reflection conditions: *h00, 0k0, 00l: h, k, l = 2n and h0l: h+l = 2n,* are present in the [100], [001], [110] and [201] SAED patterns but are due to double diffraction; this was verified by tilting the crystal out of zone around the relevant axes. These reflection conditions and cell parameters show that $La_3Ni_2Sb_{0.75}Ta_{0.25}O_9$ and $La_3Ni_2Sb_{0.75}Nb_{0.25}O_9$ adopt the monoclinic space group $P2_1/n$, in agreement with the X–ray data described above. The HR–EDX maps collected from areas of $La_3Ni_2Sb_{0.75}Ta_{0.25}O_9$ and $La_3Ni_2Sb_{0.75}Nb_{0.25}O_9$ with the expected composition show a clear 1:1 order between Ni and *B*' in that Ni fully occupies one *B* site and the other is occupied by the remaining Ni and the two *B'* cations, see Figures 5.7 and S5.8. An atomic resolution EDX map from a region of inverted *B'* composition in $La_3Ni_2Sb_{0.75}Ta_{0.25}O_9$, see Figure 5.8, shows that the same 1:1 ordering occurs in the inverted composition with one *B* site being fully occupied by Ni and the other by Ni, Sb and Ta. The 1:1 ordering of the *B*–site cations can also be clearly observed in the HAADF–STEM images of both Sb–containing compounds taken along the [010] orientation, as shown in Figures 5.9 and S5.9. The brightness of the dots in the HAADF–STEM images increases with the increasing total atomic number, *Z*, of the column. The continuous rows of dots along the *a*–axis correspond to the *A* sites occupied by La. The rows with alternation of darker and brighter dots along the *x*–axis correspond to the alternating Ni and Ni/*B*' columns, respectively. From the images the *B*–site order appears to be long–range with no disordered regions or micro–twinning present. However, fast Fourier Transforms

(FFT's) corresponding to the HAADF–STEM images of $La_3Ni_2Sb_{0.75}Ta_{0.25}O_9$ and $La_3Ni_2Sb_{0.75}Nb_{0.25}O_9$ taken along various orientations clearly show, see Figures 5.10 and S5.10, the presence of structured diffuse scattering reminiscent of the diffuse scattering observed in $La_3Ni_2TaO_9$ and $La_3Ni_2NbO_9$[142]. It is likely that the diffuse scattering arises from short–range order at the 2*d* site between the $\frac{1}{3}$ Ni and $\frac{2}{3}$ *B'* cations.

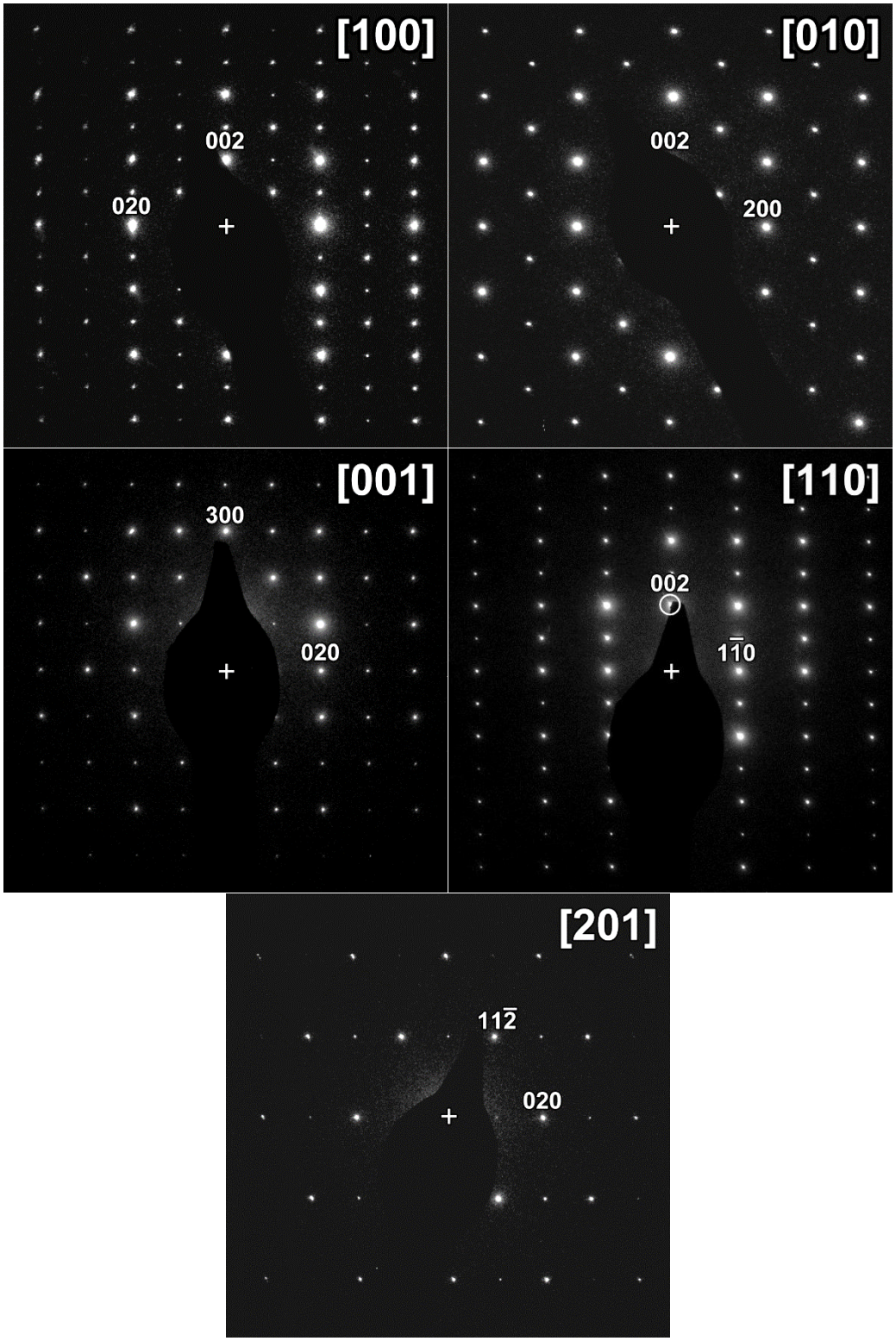


Figure 5.6. SAED patterns of the sample $La_3Ni_2Sb_{0.75}Ta_{0.25}O_9$ along the zone axes [100], [010], [001], [110] and [201] corresponding to space group $P2_1/n$.

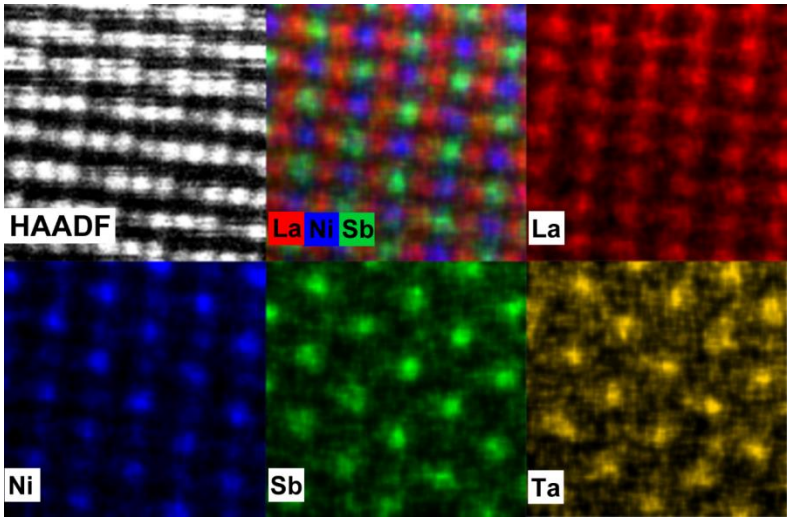


Figure 5.7. Atomic resolution EDX map along [010] the zone axis, of $La_3Ni_2Sb_{0.75}Ta_{0.25}O_9$ where La is presented in red and the cations Ni, Sb and Ta in respectively blue, green and yellow. The individual EDX maps of elements Ni, Sb and Ta show ordering between both Ni–Sb and Ni–Ta.

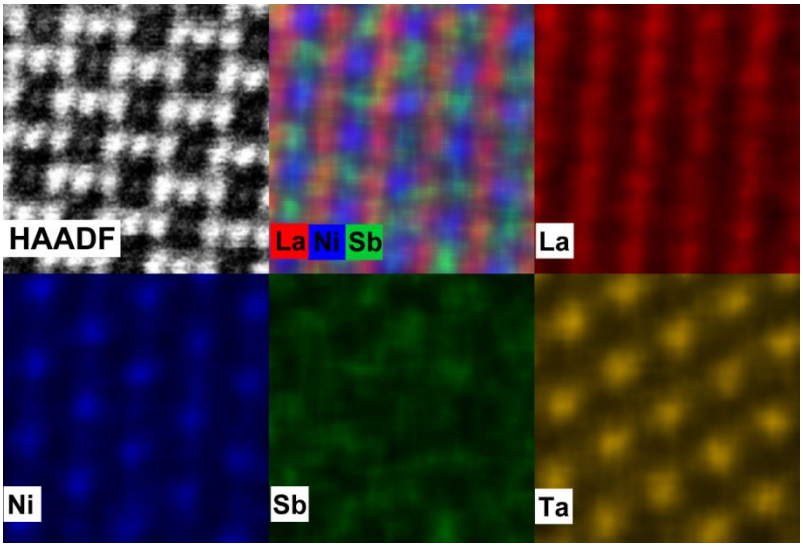


Figure 5.8. Atomic resolution EDX map along the [010] zone axis of a region of $La_3Ni_2Sb_{0.75}Ta_{0.25}O_9$ with an inverted composition of Sb and Ta, where La is presented in red and the cations Ni, Sb and Ta in respectively blue, green and yellow. The individual EDX maps of elements Ni, Sb and Ta show ordering between both Ni–Sb and Ni–Ta.

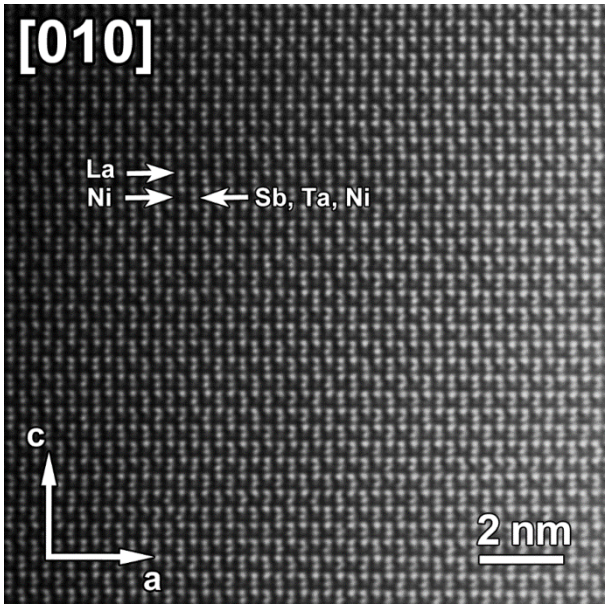


Figure 5.9. HAADF–STEM image of the $La_3Ni_2Sb_{0.75}Ta_{0.25}O_9$ sample along the [010] orientation. The rows of bright atomic columns correspond to the *A* cation La. The rows along the *a*–axis with alternating dark and bright atom columns correspond to Ni and (Sb, Ta and Ni), respectively. In order to reduce the scanning artefacts in the image, a "Gaussian blur" filter has been applied.

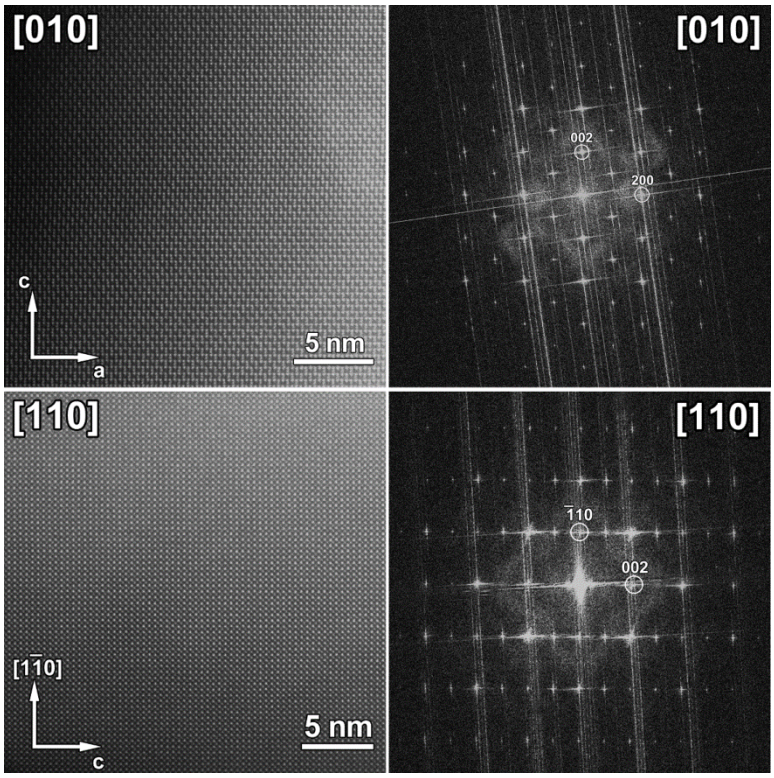


Figure 5.10. Left column: HAADF–STEM image along the [010] and [110] zone axes of the $La_3Ni_2Sb_{0.75}Ta_{0.25}O_9$ sample, where *B* cation ordering is clearly present. Right column: corresponding FFTs, in which diffuse intensities are observed.

NPD data were collected at room temperature (RT) and 3.5 or 3 K for $La_3Ni_2Sb_{0.75}Ta_{0.25}O_9$, $La_3Ni_2Sb_{0.75}Nb_{0.25}O_9$ and $La_3Ni_2Ta_{0.75}Nb_{0.25}O_9$. The data collected at room temperature using λ = 1.622 Å were consistent with the X–ray and electron diffraction data described above in that they could be accounted for using a monoclinic unit cell with an ordered arrangement of Ni^{2+} and the pentavalent cations. The fits are shown in Figure S5.11. Approximately 0.77(6) wt. % of $LaTa_pNb_{1-p}O_4$[135] was found in $La_3Ni_2Ta_{0.75}Nb_{0.25}O_9$ whereas no secondary phase was detected in the two Sb–containing compounds. The Ni/*B*' distribution over the two octahedral sites in each perovskite was refined from the data collected at RT and was then held constant during the analysis of the low temperature datasets. At low temperature, extra intensity was present in the 011 reflection of the two Sb–containing samples, $La_3Ni_2Sb_{0.75}Ta_{0.25}O_9$ and $La_3Ni_2Sb_{0.75}Nb_{0.25}O_9$. It could be accounted for by introducing a G–type[55] magnetic structure with the ordered moments aligned along [100]. The magnetic moments of the Ni^{2+} cations on the 2*c* and 2*d* sites were constrained to be equal. They refined to values of 1.08(4) and 1.18(4) μ_B per cation in $La_3Ni_2Sb_{0.75}Ta_{0.25}O_9$ and $La_3Ni_2Sb_{0.75}Nb_{0.25}O_9$, respectively. These values were determined by analysing the diffraction pattern collected using λ = 2.4395 Å; the atomic parameters were fixed at the values determined in the analysis of the data collected at the same temperature using λ = 1.622 Å. In contrast, no magnetic Bragg scattering was observed in the diffraction pattern of $La_3Ni_2Ta_{0.75}Nb_{0.25}O_9$ collected at 3.5 K. The patterns recorded at 3.5 K (3 K for $La_3Ni_2Sb_{0.75}Nb_{0.25}O_9$) and the calculated fits are presented in Figures 5.11 and S5.12 for λ = 2.4395 and 1.622 Å, respectively, whilst Tables 5.4 – 5.6 list the atomic parameters derived at RT and low temperature for each composition. Selected bond lengths and bond angles are shown in Tables 5.7 and 5.8.

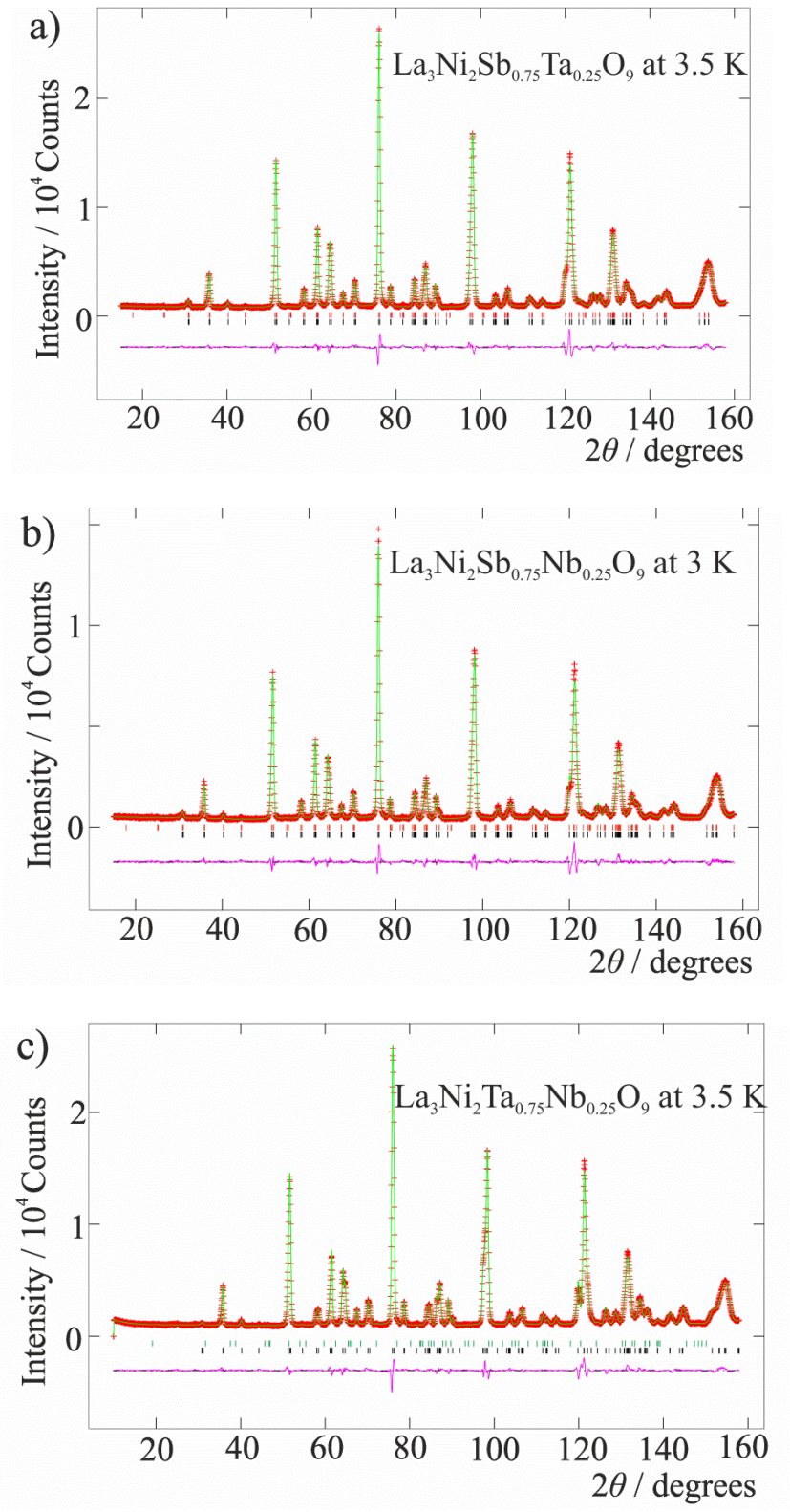


Figure 5.11. Observed (red crosses) and calculated (green line) NPD profiles of (a) $La_3Ni_2Sb_{0.75}Ta_{0.25}O_9$, (b) $La_3Ni_2Sb_{0.75}Nb_{0.25}O_9$ and (c) $La_3Ni_2Ta_{0.75}Nb_{0.25}O_9$ at low T recorded using λ = 2.4395 Å. A difference curve (purple) is shown below. Reflection markers are shown for the magnetic (red) and structural (black) phases and also for identified impurity phases: $LaTaO_4$ (green).

Table 5.4. Atomic parameters of $La_3Ni_2Sb_{0.75}Ta_{0.25}O_9$ at RT and 3.5 K (Space group $P2_1/n$).

		RT	3.5 K
a / Å		5.6010(1)	5.5907(1)
b / Å		5.6369(1)	5.6344(1)
c / Å		7.9299(2)	7.9178(2)
β / °		90.00(1)	90.02(1)
V / Å^3		250.37(1)	249.41(1)
$R_{wp\|NPD}$ / %		4.13	3.69
χ^2		2.650	3.287
La	x	0.4897(6)	0.4913(4)
4*e* (*x y z*)	y	0.4620(2)	0.4599(2)
	z	0.252(1)	0.251(1)
	U_{ISO} / Å^2	0.0183(3)	0.0149(2)
Ni/Sb/Ta1	U_{ISO} / Å^2	0.0032(2)	0.0007(1)
2*c* (0 ½ 0)	Ni occupancy	0.99(2)	0.99
	Sb occupancy	0.01(1)	0.01
	Ta occupancy	0.003(4)	0.003
Ni/Sb/Ta2	U_{ISO} / Å^2	0.0032(2)	0.0007(1)
2*d* (½ 0 0)	Ni occupancy	0.35(2)	0.35
	Sb occupancy	0.49(1)	0.49
	Ta occupancy	0.163(4)	0.163
O1	x	0.785(1)	0.780(1)
4*e* (*x y z*)	y	0.788(1)	0.796(1)
	z	–0.0479(6)	–0.0451(6)
	U_{ISO} / Å^2	0.0152(15)	0.0081(13)
O2	x	0.707(1)	0.701(1)
4*e* (*x y z*)	y	0.290(1)	0.286(1)
	z	–0.0346(5)	–0.0406(7)
	U_{ISO} / Å^2	0.004(1)	0.0006(15)
O3	x	0.5796(6)	0.5779(4)
4*e* (*x y z*)	y	0.0169(4)	0.0173(3)
	z	0.242(1)	0.251(1)
	U_{ISO} / Å^2	0.0125(5)	0.0087(4)

Table 5.5. Atomic parameters of $La_3Ni_2Sb_{0.75}Nb_{0.25}O_9$ at RT and 3 K (Space group $P2_1/n$).

		RT	3 K
a / Å		5.5993(1)	5.5891(1)
b / Å		5.6374(1)	5.6353(1)
c / Å		7.9286(2)	7.9165(2)
β / °		90.03(1)	90.08(1)
V / Å^3		250.27(1)	249.34(1)
$R_{wp\|NPD}$ / %		4.33	4.61
χ^2		2.243	2.617
La	x	0.4900(6)	0.4901(5)
4*e* (*x y z*)	y	0.4616(2)	0.4600(2)
	z	0.252(1)	0.249(1)
	U_{ISO} / Å^2	0.0186(4)	0.0146(3)
Ni/Sb/Nb1	U_{ISO} / Å^2	0.0033(2)	0.0011(2)
2*c* (0 ½ 0)	Ni occupancy	0.96(2)	0.96
	Sb occupancy	0.03(2)	0.03
	Nb occupancy	0.010(5)	0.010
Ni/Sb/Nb2	U_{ISO} / Å^2	0.0033(2)	0.0011(2)
2*d* (½ 0 0)	Ni occupancy	0.37(2)	0.37
	Sb occupancy	0.47(2)	0.47
	Nb occupancy	0.156(5)	0.156
O1	x	0.790(1)	0.786(1)
4*e* (*x y z*)	y	0.7930(9)	0.798(1)
	z	–0.0369(6)	–0.0411(8)
	U_{ISO} / Å^2	0.0024(11)	0.0025(12)
O2	x	0.711(1)	0.705(1)
4*e* (*x y z*)	y	0.284(1)	0.283(1)
	z	–0.0464(7)	–0.0419(8)
	U_{ISO} / Å^2	0.017(1)	0.007(1)
O3	x	0.5773(5)	0.5798(5)
4*e* (*x y z*)	y	0.0176(4)	0.0176(3)
	z	0.244(1)	0.247(1)
	U_{ISO} / Å^2	0.0121(5)	0.0075(5)

Table 5.6. Atomic parameters of $La_3Ni_2Ta_{0.75}Nb_{0.25}O_9$ at RT and 3.5 K (Space group $P2_1/n$).

		RT	3.5 K
a / Å		5.5890(1)	5.5777(1)
b / Å		5.6415(1)	5.6406(1)
c / Å		7.9193(2)	7.9063(1)
β / °		90.04(1)	90.03(1)
V / Å^3		249.70(1)	248.75(1)
$R_{wp\|NPD}$ / %		4.04	3.11
χ^2		2.539	2.555
La	x	0.4909(5)	0.4914(4)
4*e* (*x y z*)	y	0.4612(2)	0.4587(1)
	z	0.255(1)	0.250(1)
	U_{ISO} / Å^2	0.0181(3)	0.0144(2)
Ni/Ta/Nb1	U_{ISO} / Å^2	0.0023(2)	0.0006(1)
2*c* (0 ½ 0)	Ni occupancy	1	1
	Ta occupancy	0	0
	Nb occupancy	0	0
Ni/Ta/Nb2	U_{ISO} / Å^2	0.0023(2)	0.0006(1)
2*d* (½ 0 0)	Ni occupancy	0.3333	0.3333
	Ta occupancy	0.5	0.5
	Nb occupancy	0.1667	0.1667
O1	x	0.783(1)	0.793(1)
4*e* (*x y z*)	y	0.786(1)	0.797(1)
	z	–0.0422(8)	–0.0384(6)
	U_{ISO} / Å^2	0.0037(12)	0.0012(10)
O2	x	0.700(1)	0.711(1)
4*e* (*x y z*)	y	0.294(1)	0.285(1)
	z	–0.0393(7)	–0.0450(6)
	U_{ISO} / Å^2	0.0121(11)	0.0059(11)
O3	x	0.5783(5)	0.5787(3)
4*e* (*x y z*)	y	0.0173(4)	0.0175(3)
	z	0.241(1)	0.251(1)
	U_{ISO} / Å^2	0.0138(6)	0.0083(4)

Table 5.7. Selected bond lengths (Å) and angles (°) in $La_3Ni_2Sb_xTa_yNb_{1-x-y}O_9$ at RT.

	$La_3Ni_2Sb_{0.75}Ta_{0.25}O_9$	$La_3Ni_2Sb_{0.75}Nb_{0.25}O_9$	$La_3Ni_2Ta_{0.75}Nb_{0.25}O_9$
La–O1	2.836(9)	2.741(9)	2.782(9)
La–O1	2.643(8)	2.726(8)	2.670(8)
La–O1	2.410(8)	2.442(7)	2.441(7)
La–O2	2.757(8)	2.854(10)	2.776(8)
La–O2	2.479(7)	2.447(8)	2.443(7)
La–O2	2.717(7)	2.628(9)	2.713(6)
La–O3	2.560(3)	2.551(3)	2.554(3)
La–O3	2.433(4)	2.443(4)	2.429(4)
2*c*–O1	2.054(7)×2	2.050(5)×2	2.048(5)×2
2*c*–O2	2.040(5)×2	2.059(6)×2	2.062(4)×2
2*c*–O3	2.098(10)×2	2.078(9)×2	2.103(9)×2
2*d*–O1	2.033(6)×2	2.019(5)×2	2.016(4)×2
2*d*–O2	2.025(5)×2	2.022(6)×2	2.026(5)×2
2*d*–O3	1.971(10)×2	1.985(9)×2	1.957(8)×2
O1–2*c*–O2	87.8(3)×2	90.0(3)×2	86.4(3)×2
O1–2*c*–O3	88.8(2)×2	88.9(2)×2	90.0(2)×2
O2–2*c*–O3	89.3(2)×2	87.8(2)×2	89.8(2)×2
O1–2*d*–O2	90.0(3)×2	87.8(3)×2	88.2(3)×2
O1–2*d*–O3	88.1(2)×2	89.7(2)×2	89.0(2)×2
O2–2*d*–O3	87.9(2)×2	89.4(2)×2	89.2(2)×2
2*c*–O1–2*d*	152.9(3)	155.0(3)	155.5(3)
2*c*–O2–2*d*	155.6(3)	153.5(3)	152.5(3)
2*c*–O3–2*d*	154.1(2)	154.7(2)	154.4(1)

Table 5.8. Selected bond lengths (Å) and angles (°) in $La_3Ni_2Sb_xTa_yNb_{1-x-y}O_9$ at low *T*.

	$La_3Ni_2Sb_{0.75}Ta_{0.25}O_9$	$La_3Ni_2Sb_{0.75}Nb_{0.25}O_9$	$La_3Ni_2Ta_{0.75}Nb_{0.25}O_9$
La–O1	2.811(9)	2.780(10)	2.732(8)
La–O1	2.654(8)	2.684(8)	2.720(7)
La–O1	2.427(9)	2.433(9)	2.433(7)
La–O2	2.770(9)	2.785(10)	2.813(8)
La–O2	2.446(9)	2.445(9)	2.449(7)
La–O2	2.697(8)	2.675(9)	2.638(7)
La–O3	2.541(2)	2.543(2)	2.536(2)
La–O3	2.430(3)	2.426(4)	2.421(3)
2*c*–O1	2.101(5)×2	2.083(5)×2	2.057(4)×2
2*c*–O2	2.086(5)×2	2.081(4)×2	2.049(5)×2
2*c*–O3	2.023(8)×2	2.052(7)×2	2.021(8)×2
2*d*–O1	1.976(5)×2	1.994(4)×2	2.018(4)×2
2*d*–O2	1.991(6)×2	1.990(5)×2	2.024(4)×2
2*d*–O3	2.035(8)×2	2.011(7)×2	2.033(9)×2
O1–2*c*–O2	87.9(3)×2	89.7(3)×2	89.2(3)×2
O1–2*c*–O3	89.9(2)×2	89.3(2)×2	89.0(2)×2
O2–2*c*–O3	89.7(2)×2	89.4(2)×2	88.5(2)×2
O1–2*d*–O2	89.7(3)×2	88.2(3)×2	87.4(3)×2
O1–2*d*–O3	88.0(2)×2	89.4(2)×2	90.0(1)×2
O2–2*d*–O3	89.9(2)×2	89.8(2)×2	89.6(2)×2
2*c*–O1–2*d*	153.5(3)	153.5(3)	153.4(3)
2*c*–O2–2*d*	153.5(3)	154.3(4)	153.8(3)
2*c*–O3–2*d*	154.6(1)	154.0(1)	154.4(1)

5.4 Discussion

It has been shown that solid solutions containing two different pentavalent cations can be prepared for each of $x = 0$, $y = 0$ and $x + y = 1$. Compositions containing only antimony and tantalum show a strong low–field magnetisation below ~100 K but the introduction of niobium to form either Sb/Nb or Ta/Nb solid solutions decreases both the onset temperature, $T_{C,}$ and the magnitude of the magnetisation, see Figure 5.2 and Tables 5.1 – 5.3. Given the similarity in size and charge of Ta^{5+} and Nb^{5+}, the change is striking and in the discussion that follows the structural and electronic factors that might be responsible are considered.

The X–ray diffraction data suggest that in all cases the cations order over the two six–coordinate sites within the unit cell such that one is predominantly occupied by Ni^{2+} and the other by Ni^{2+} and pentavalent cations in a 1:2 ratio. Neutron diffraction has confirmed this for the three compositions studied in detail. Only in the case of $La_3Ni_2Sb_{0.75}Nb_{0.25}O_9$ was the refined concentration of pentavalent cations on the predominantly nickel–occupied 2*c* site significant at the 2σ level, see Table 5.5. The mean bond length around the nickel–rich 2*c* site at both room temperature and low temperatures is, as expected, larger than that around the site, 2*d*, containing the smaller, pentavalent cations. In each case the atomic displacement parameters of some of the oxide ions are large at both room temperature and low temperatures, suggesting that the anions show static displacements from their mean positions. The displacement parameters also provide evidence of disorder on the La^{3+} sublattice. The large displacement parameters on both of these sublattices are likely to stem from the different coordination requirements of Ni^{2+} and the pentavalent cations that together occupy the 2*d* site. Contrary to the widely–quoted published data[149], the unit–cell volumes of all[48, 142] these compounds suggest that the ionic radius of Sb^{5+} in six–coordination is greater than those of Ta^{5+} and Nb^{5+}.

The results from the electron microscopy study are in broad agreement with those produced by X–ray and neutron diffraction. Furthermore, they show, see Figures 5.5, S5.5 and S5.6, that all the samples have the desired overall compositions and that, with the exception of a few local regions, they are homogeneous and monophasic. They also provide, see Figures 5.7 and S5.8, direct evidence that the pentavalent cations do not occupy the 2*c* sites but that they are randomly distributed over the 2*d* sites. The long–range nature of the 2*c*/2*d* cation ordering is emphasised by Figures 5.9 and S5.9. Finally, the diffuse scattering in the diffraction patterns generated by taking the Fourier transform of the HAADF–STEM images, see Figures 5.10 and S5.10, indicates the presence of short–range structural ordering that is not included in the model derived from the neutron diffraction data. Similar diffuse scattering was observed in the previous study of $La_3Ni_2TaO_9$ and $La_3Ni_2NbO_9$[142]. Further experimental work will be necessary before the origin of this scattering can be fully explained.

$La_3Ni_2TaO_9$ was labelled as a relaxor ferromagnet in previous chapter and $La_3Ni_2SbO_9$ was described as a relaxor ferromagnet in which some of the domains are large enough for the magnetic ordering to be detected by zero–field neutron diffraction[75], albeit with a low mean magnetic moment, 0.87(9) μ_B, for the Ni^{2+} cations. The magnetometry presented in this chapter, as well as the in–field neutron diffraction data described in previous chapter, suggest that relaxor behaviour persists throughout the $La_3Ni_2Sb_xTa_yO_9$ ($x + y = 1$) solid solution. The neutron diffraction data show that the large domains are still present when $x = 0.75$, but the previous study of $La_3Ni_2TaO_9$, see Chapter 4, showed that they are absent for $x = 0$. It is thus possible that these domains are responsible for the relatively sharp transition seen at ~100 K in the ac susceptibility of both $La_3Ni_2SbO_9$[48] and $La_3Ni_2Sb_{0.75}Ta_{0.25}O_9$, see Figure 5.4, but not in that of $La_3Ni_2TaO_9$[142]. The introduction of 75 % Ta^{5+} reduces the magnetisation of $La_3Ni_2SbO_9$ in 100 Oe by only ~25 %, see Figure

5.2, but there is then a threefold reduction as the remaining antimony is removed. However, the maximum dc susceptibility of $La_3Ni_2TaO_9$ is an order of magnitude greater than that of the niobium analogue. Both neutron diffraction and ac magnetometry show that large magnetic domains are also present in $La_3Ni_2Sb_{0.75}Nb_{0.25}O_9$ and the temperature dependence and magnitude of the dc susceptibility suggests that relaxor behaviour persists in the 1:1 Sb:Nb composition. However, the introduction of 75 % Nb^{5+} into $La_3Ni_2SbO_9$ reduces the magnetisation in 100 Oe by ~75 %. It appears that the magnetisation is maximised by the presence of antimony, largely maintained after the introduction of tantalum and reduced markedly by the introduction of niobium. Furthermore, the magnetisation is largest when relatively large domains form.

The absence of magnetic Bragg scattering in the neutron diffraction pattern of $La_3Ni_2Ta_{0.75}Nb_{0.25}O_9$ recorded at 3.5 K signals the absence of large magnetic domains and is consistent with the data collected previously from $La_3Ni_2TaO_9$ and $La_3Ni_2NbO_9$. On the basis of the data presented previously and above, the former member of this pair is believed to be a relaxor ferromagnet and the latter to be a spin glass. The change in behaviour with composition thus entails a progression from short–range magnetic ordering, albeit in domains too small to be detected by neutron diffraction, to an absence of magnetic ordering. The susceptibility data in Figures 5.2 and 5.4 suggest that the introduction of 25 % niobium in place of tantalum is not sufficient to change the nature of the compound. However, the data in Table 5.3, along with Figures 5.2, 5.3 and S5.4, suggest that a change in the low–temperature behaviour of $La_3Ni_2Ta_yNb_{1-y}O_9$ begins in the composition range $0.5 < y < 0.75$. The parameters describing the behaviour of this series in the paramagnetic region are essentially constant across the entire composition range. As described above, the data collected on other compositions suggest that the short–range magnetic ordering is likely to involve the presence of ferrimagnetic G–type domains in which nearest–

neighbour interactions dominate. The formation of a spin glass requires the presence of magnetic frustration, which in turn implies that a second superexchange interaction must increase in importance and compete with the nearest–neighbour interaction as the concentration of niobium increases. This interaction, which must be uncompetitive in $La_3Ni_2SbO_9$ and $La_3Ni_2TaO_9$, could be either the second–nearest–neighbour interaction along an approximately 90º Ni–O–*B*'–O–Ni pathway, with a direct Ni–Ni distance of ~5.5 Å, or the third–nearest–neighbour interaction along a nearly–linear Ni–O–*B*'–O–Ni pathway of length ~7.8 Å. The adoption of a Type I antiferromagnetic structure by $SrLaNiSbO_6$[150] shows that the former pathway can be significant when *B*' = Sb, but it has also been shown[67, 141, 148] that the $4d^{10}$ shell of post–transition metals is too low in energy to play a part in the interaction, which therefore effectively takes place along a Ni–O–O–Ni pathway and so can operate whatever the identity of *B*'. However, the nearly–linear Ni–O–*B*'–O–Ni pathway can only operate with the participation of orbitals on the *B*' cation and so could be significant for *B*' = d^0 Ta^{5+} or Nb^{5+}, but not when *B*' = Sb^{5+}. In order to explain the greater significance of the competitive interaction in the niobium–rich compositions the energy of the empty 4*d* orbitals of Nb^{5+} is tentatively considered to be relatively close to that of the anion orbitals and they are therefore able to participate effectively in the linear superexchange but that the $5d^0$ orbitals of Ta^{5+} lie too high in energy to participate to the same degree. Consequently the magnetic frustration increases with increasing niobium content and $La_3Ni_2NbO_9$ adopts a spin–glass state at low temperatures. The competing superexchange interaction present in $La_3Ni_2TaO_9$ is not enough to prevent the formation of a relaxor state but the third–nearest–neighbour coupling might be strong enough to reduce both the size of the domains formed and the ordered moment measured by neutron diffraction. There may also be a structural difference that has consequences for the magnetic properties. More specifically, it has been shown[151] that Nb^{5+} is more likely to

move away from the centre of the coordination octahedron than is Ta^{5+}. In the compounds under discussion any such displacements would be local rather than cooperative, but they might still be partially responsible for the differences in the magnetic behaviour. It is interesting that the imaginary components of the ac susceptibilities of the antimony–containing, large–domain compositions show a change in gradient, see Figure 5.4, at the temperature at which those of the relaxor phases that do not contain large domains, *i.e.* $La_3Ni_2TaO_9$ and $La_3Ni_2Ta_{0.75}Nb_{0.25}O_9$, reach a maximum. This suggests that some regions of the sample order at ~100 K and that those smaller regions follow suit at lower temperatures.

5.5 Conclusion

Magnetometry and neutron diffraction have shown that the relaxor ferromagnetic behaviour persists in the solid solution $La_3Ni_2Sb_xTa_yNb_{1-x-y}O_9$ when $x + y = 1$ although the magnitude of the magnetisation decreases as y increases. However, the introduction of niobium causes a relatively rapid decrease in both the magnetisation and the onset temperature and eventually leads to the formation of a spin–glass phase when $x = y = 0$. Neutron diffraction and electron microscopy showed these samples to be well–ordered and homogeneous; there are no structural differences that might explain the magnetic changes that occur when niobium is introduced. The energies of the outer *d* orbitals of the pentavalent cations determine the ability of these cations to play a role in superexchange interactions and it is proposed that the differences in the *d*–orbital energies for Sb^{5+}, Ta^{5+} and Nb^{5+} are responsible for the observed variations in magnetic behaviour.

This work has been published as *C.–M. Chin, P. D. Battle, E. C. Hunter, M. Avdeev, M. Hendrickx and J. Hadermann, Journal of Solid State Chemistry, 2019,* ***273****, 175-185*[152].

Chapter 6: An investigation of Cu–doped perovskites

6.1 Introduction

It was shown in the previous chapters that the magnetic properties of an ordered perovskite can be influenced by the electronic configuration of the elements at the *B*' site. However, structural modification could also be one of the consequences when the perovskite accommodate different cations. For example, the CuO_6 octahedra in Ba_2CuWO_6 and Sr_2CuWO_6 were found to be tetragonally distorted; they consist of four short Cu–O bonds in the equatorial *ab* plane (~2 Å) whereas the remaining two axial Cu–O bonds are elongated along the *c* axis (~2.35 Å)[145, 153]. In other words, a square lattice is effectively formed around each Cu^{2+} cation as a result of Jahn–Teller distortion[32, 33]. The structural distortion is retained when W^{6+} is substituted with either a d^0 Mo^{6+} or a d^{10} Te^{6+} cation at the *B*'–site[143, 145], although the evidence does not seem conclusive. The shorter Cu–O bond lengths lead to relatively stronger magnetic interactions between neighbouring Cu cations which lie within the *ab* plane at the expense of the interactions in the *c* direction. As a result, these cuprate perovskites demonstrate quasi–low–dimensional magnetic behaviour; a broad maximum is observed in the temperature dependence of the magnetic susceptibility, and hence there is no clear indication of long–range magnetic order in these Cu–containing products.

The results of replacing Ni^{2+} with Cu^{2+} cations in $La_3Ni_2B'O_9$ (*B*' = Sb, Ta or Nb) will be presented and discussed in this chapter. The intention here is to investigate any structural change and study the possibility of lowering the magnetic dimensionality of the system. $La_3Ni_{1.75}Cu_{0.25}B'O_9$ (*B*' = Sb, Ta or Nb) and $La_3Ni_{1.5}Cu_{0.5}NbO_9$ were successfully synthesised. These compounds were then characterised using X–ray powder diffraction, neutron powder diffraction, electron microscopy and magnetometry.

6.2 Experimental

The traditional ceramic method was used to synthesise polycrystalline samples of $La_3Ni_{2-x}Cu_xB'O_9$ for x = 0.25; B' = Sb, Ta or Nb and x = 0.5; B' = Nb. Mixtures containing analytical–grade NiO, CuO, B'_2O_5 (B' = Sb, Ta or Nb) and pre–dried La_2O_3 in a stoichiometric ratio were thoroughly ground in an agate mortar and pestle, and then pelletised before being heated at 1100 or 1200 °C for several periods of two or three days. After each heating the pellets were ground up and then reformed. Different compositions needed a different number of heating cycles to optimise the purity of the perovskite but a typical synthesis took 5 – 6 cycles.

A PANalytical Empyrean diffractometer was used to record the X–ray powder diffraction (XRPD) patterns of the reaction products at room temperature. Data were collected, using Cu $K_{\alpha1}$ radiation (λ = 1.54051 Å), over the angular range $15 \leq 2\theta/° \leq 125$ with a step–size, $\Delta 2\theta$, of 0.0066°. Ni^{2+} and Cu^{2+} possess a similar number of electrons and, consequently, XRPD cannot distinguish between these cations. Conversely, the neutron scattering lengths of Ni and Cu, 10.3 and 7.72 fm, respectively, provide substantial contrast[85]. Neutron powder diffraction (NPD) patterns were therefore collected at various temperatures using the diffractometer ECHIDNA[87] at ANSTO, Australia. Data were collected over the angular range $10 \leq 2\theta/° \leq 158$ with $\Delta 2\theta$ = 0.05°. Wavelengths of 1.622 and 2.4395 Å were used, the latter in order to ensure that weak magnetic scattering at relatively long d–spacings was not overlooked. All diffraction patterns were analysed using the Rietveld method[92], as implemented in the GSAS program suite[94]. A 15–term shifted Chebyshev function and a pseudo–Voigt function[123] was employed to model the background level and peak shapes respectively.

The composition and homogeneity of each sample was studied by means of analytical transmission electron microscopy (TEM). The specimen was prepared by dispersing a crushed powder sample in ethanol and depositing a few drops of this suspension on a holey carbon film covering a molybdenum grid. Energy–dispersive X–ray (EDX) elemental maps were acquired using an FEI Osiris microscope equipped with a Super–X detector and operated at 200 kV. The intensities of the K lines were used to quantify the Cu and Ni content of each sample whereas the L lines were used to quantify La, Nb, Sb and Ta. In order to assess the homogeneity both from particle to particle and within an individual particle, different regions of a number of different particles were analysed. For each sample, a total of at least thirty regions were assessed. A more detailed electron–microscopy study was carried out on $La_3Ni_{1.75}Cu_{0.25}NbO_9$. Selected–area electron diffraction (SAED) and convergent–beam electron diffraction (CBED) patterns were collected using a CM20 microscope. High–angle, annular dark field scanning TEM (HAADF–STEM) images and high–resolution EDX (HR–EDX) analyses were acquired using an FEI Titan 80–300 "cubed" microscope equipped with a Super–X detector and operated at 300 kV and 200 kV for HAADF–STEM and HR–EDX, respectively.

The magnetic properties of these copper–doped perovskites were characterised using a SQUID magnetometer. The temperature dependence of the dc molar magnetic susceptibility, $\chi(T)$, was measured in a magnetic field of 100 Oe over a temperature range of $2 \leq T/\mathrm{K} \leq 300$ under both zero–field–cooled (ZFC) and field–cooled (FC) conditions. The ac susceptibility was measured in an oscillating field of amplitude 3.5 Oe over the temperature range $2 \leq T/\mathrm{K} \leq 150$ at frequencies, ω, of 1, 10, 100 and 1000 Hz. The magnetisation per formula unit (f.u.) was measured as a function of applied field and temperature. The field was cycled through the range $-50 \leq H/\mathrm{kOe} \leq 50$ at temperatures selected after consideration of the results of the dc and ac susceptibility measurements.

6.3 Results

The XRPD data showed that the principal component of each reaction product was a perovskite–like phase, see Figure S6.1. Weak, additional reflections revealed the presence of minor impurity phases which were identified as diamagnetic $La_3B'O_7$ (B' = Sb, Nb or Ta) and $LaNb_{1-y}Ta_yO_4$[126, 134, 135, 154]. The concentration of the impurity phases increased when attempts were made to prepare compositions containing a higher concentration of copper. Preliminary analysis of the patterns suggested that all the perovskite phases crystallise in the monoclinic space group $P2_1/n$ with $a \sim b \sim \sqrt{2}a_p$, $c \sim 2a_p$ and $\beta \sim 90°$ where a_p is the cell parameter of a primitive cubic perovskite. Comparison with the results of some earlier work[142] showed that several of the relatively–broad maxima seen in the diffraction patterns of the Cu–free compositions, for example $La_3Ni_2TaO_9$, are split in the patterns collected from the Cu–doped compounds, showing that the non–cubic strain is greater in the latter. The fits to the XRPD data shown in Figure S6.1 are based on a model in which the 2*c* sites are predominantly (~98 %) occupied by divalent *d*–block cations and the 2*d* sites by a random distribution of divalent and pentavalent cations. The La^{3+} cations occupy a 4*e* site and the oxide anions are distributed over three such sites.

The results of the TEM–EDX analyses are summarized in Table 6.1. Some particles with a La:Ta or La:Nb ratio of 3:1 or 1:1 were identified, which is consistent with the results of the X–ray diffraction experiments. However, significant deviations from the ideal composition were found in only a negligible number of particles and the samples can be considered to be homogeneous. The SAED patterns of $La_3Ni_{1.75}Cu_{0.25}NbO_9$ taken along the main zone axes [100], [010] and [001] can be indexed, see Figure 6.1, using the cell parameters $a \approx b \approx \sqrt{2}a_p$, $c \approx 2a_p$, where a_p is the unit cell parameter of a primitive cubic perovskite, and $\alpha, \beta, \gamma \approx 90°$. Using a combination of SAED, CBED and HAADF–

STEM, the space group $P2_1/n$ was conclusively derived from the TEM data; explanation can be found in the Appendix with the help of Figure S6.2 and S6.3. The [010] HAADF–STEM image shown in Figure 6.2 shows that a high degree of cation ordering is present in this sample. The continuous rows of bright dots along the *a*–axis correspond to columns of La^{3+} cations. The rows showing an alternation of brighter and darker dots along the *a*–axis correspond to alternating (Nb, Ni) and (Ni, Cu) columns respectively. (The intensity of the atom columns is proportional to the atomic number of the elements: $I \sim Z^2$.) The preference of the Cu^{2+} cations for the Ni^{2+}–rich 2*c* sites is shown by the atomic–resolution EDX maps in Figure 6.3. The *A*–site La^{3+} cations are indicated in red and the Ni^{2+}, Cu^{2+} and Nb^{5+} cations on the *B* sites are mapped in green, yellow and blue, respectively. $La_3Ni_{1.75}Cu_{0.25}NbO_9$ is seen to have Nb^{5+} cations on alternate sites along [100] rows, whereas Ni^{2+} is present on all *B* sites, but with a greater abundance on the sites not occupied by Nb^{5+}. The Cu^{2+} cations are less clearly mapped because of their low concentration in the compound, but it can be seen that they are predominantly found on the Ni–rich sites. This is best seen by comparing the overlapped Ni–Cu and Nb–Cu maps shown in Figure 6.3.

Table 6.1. Metal content (atomic %) of $La_3Ni_{2-x}Cu_xB'O_9$ (x =0.25 or 0.5; B' = Sb, Ta or Nb) determined by TEM–EDX.

Sample	% La	% Ni	% Cu	% *B*'
$La_3Ni_{1.75}Cu_{0.25}SbO_9$ *	50.5 ± 2.1	28.3 ± 1.7	5.0 ± 0.6	16.3 ± 1.0
$La_3Ni_{1.75}Cu_{0.25}TaO_9$ *	51.0 ± 1.4	27.3 ± 1.4	4.3 ±1.0	17.5 ± 1.5
$La_3Ni_{1.75}Cu_{0.25}NbO_9$ *	51.9 ± 1.2	29.4 ± 1.0	4.7 ±0.5	14.1 ±1.3
$La_3Ni_{1.5}Cu_{0.5}NbO_9$ **	52.8 ± 0.6	24.1 ± 0.6	8.3 ± 0.3	14.7 ± 0.7

* Expected; La 50, Ni 29.17, Cu 4.17, *B*' 16.66

** Expected; La 50, Ni 25, Cu 8.33, Nb 16.67

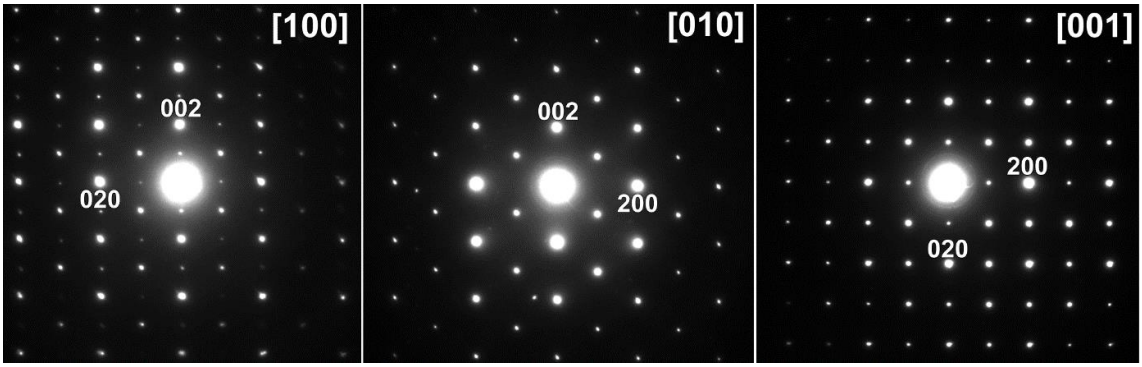


Figure 6.1. SAED patterns of $La_3Ni_{1.75}Cu_{0.25}NbO_9$ taken along the zone axes [100], [010] and [001].

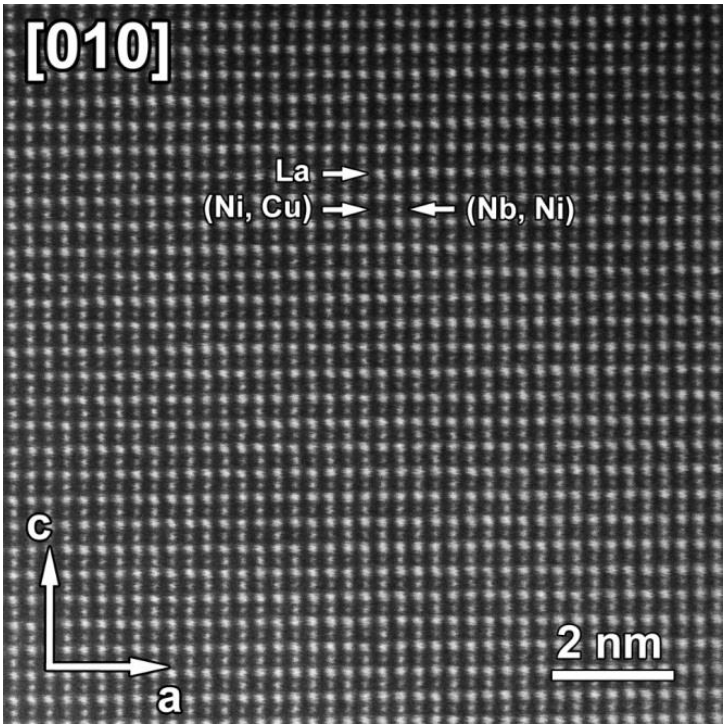


Figure 6.2. High resolution HAADF–STEM image of $La_3Ni_{1.75}Cu_{0.25}NbO_9$ along the [010] zones axis, where the continuous rows of bright dots along the *a*–axis are occupied by La. The rows with alternation of darker and brighter dots along the *a*–axis correspond to (Ni, Cu) and (Nb, Ni) atom columns, respectively.

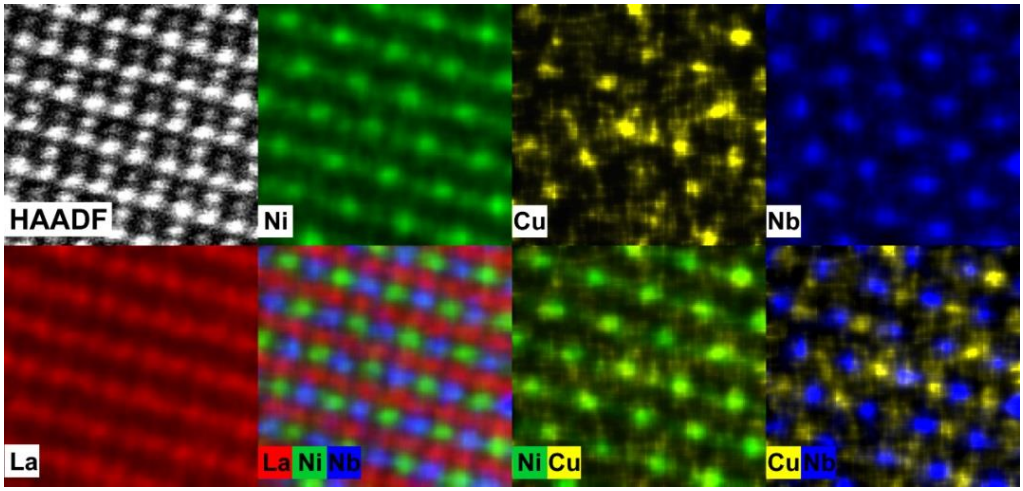


Figure 6.3. High–resolution HAADF–STEM image of $La_3Ni_{1.75}Cu_{0.25}NbO_9$ along [010] (top left) and atomic–resolution EDX maps, acquired for 17 min. Partial ordering is present between Ni and Nb, and Cu is located at the six–coordinate sites containing most Ni.

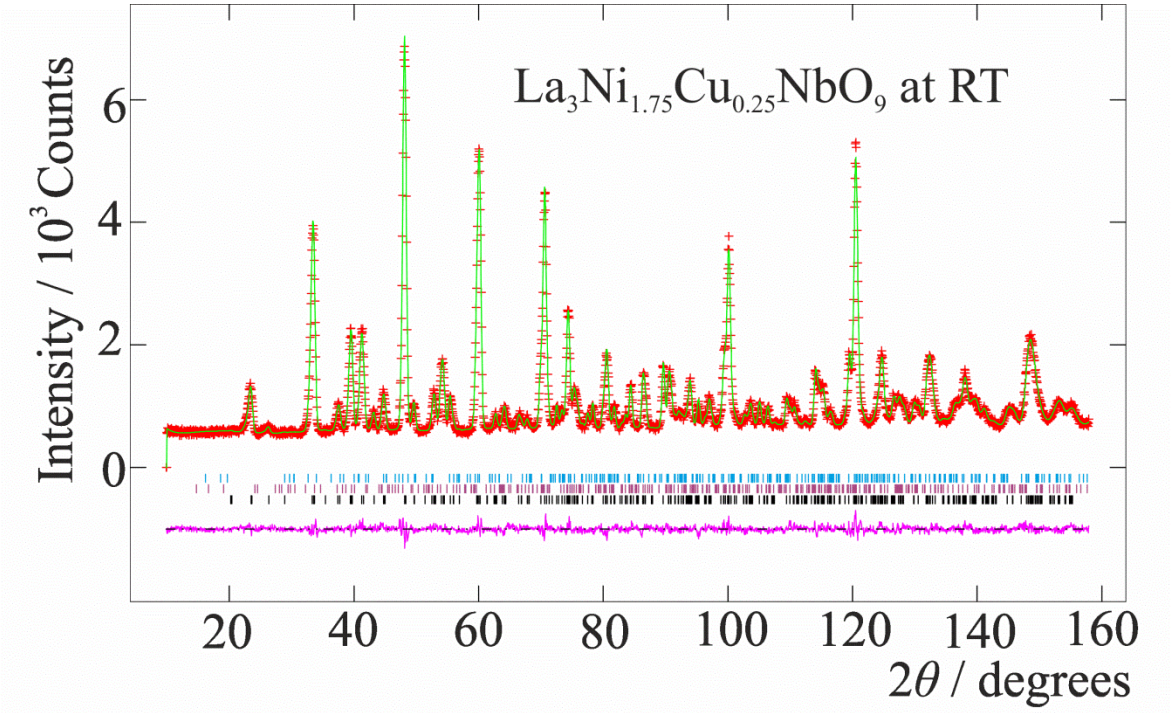


Figure 6.4. Observed (red crosses) and calculated (green line) NPD profiles of $La_3Ni_{1.75}Cu_{0.25}NbO_9$ at room temperature using λ = 1.622 Å. A difference curve (purple) is shown below. Reflection positions are marked for $LaNbO_4$ (top, cyan), La_3NbO_7 (middle, purple) and the principal perovskite phase (bottom, black).

The NPD patterns collected at room temperature (RT) using λ = 1.622 Å were analysed in order to determine if there was any Ni/Cu ordering over the *B*–site. The resulting fits are shown in Figures 6.4 and S6.4. Consistent with the analysis of the XRPD and TEM data reported above, it was found that the dominant perovskite phase in each compound adopts the space group $P2_1/n$ and that these compositions were contaminated with minimal (less than 1 wt. %) diamagnetic impurities, namely $La_3B'O_7$ (*B*' = Sb, Ta or Nb) and $LaNb_{1-y}Ta_yO_4$. On the basis of the model derived from the XRPD data, the pentavalent cations were assigned to the 2*d* site only, whereas the distribution of Ni^{2+} and Cu^{2+} over the 2*c* and 2*d* sites was allowed to vary so as to determine any site preference between these two cations. Preliminary refinements showed that, except in the case of $La_3Ni_{1.5}Cu_{0.5}NbO_9$, the Cu^{2+} cations only occupy the 2*c* site and they were excluded from the 2*d* site in the final refinements. The structural model, see Tables 6.2, S6.1 and S6.2, that has been derived from the NPD data collected at room temperature for the 12.5 % Cu–substituted compositions thus has Ni^{2+} and Cu^{2+} occupying the 2*c* sites and the remaining Ni^{2+} cations and the pentavalent B'^{5+} cations occupying the 2*d* sites. This is consistent with the high–resolution EDX map of $La_3Ni_{1.75}Cu_{0.25}NbO_9$ described above and shown in Figure 6.3. In the case of $La_3Ni_{1.5}Cu_{0.5}NbO_9$, the 2*c* site was found to contain Ni^{2+} and Cu^{2+} and 2*d* sites Ni^{2+}, Cu^{2+} and Nb^{5+}, see Table 6.3. The bond lengths and bond angles derived from the analyses of the neutron diffraction data are listed in Tables 6.4 and 6.5.

Table 6.2. Atomic parameters of $La_3Ni_{1.75}Cu_{0.25}NbO_9$ at RT and 3 K (Space group $P2_1/n$).

		RT	3 K
a / Å		5.5890(1)	5.5769(1)
b / Å		5.6516(1)	5.6503(1)
c / Å		7.9194(2)	7.9049(2)
β / °		90.04(1)	90.04(1)
V / Å^3		250.15(1)	249.09(1)
$R_{wp\|NPD}$ / %		4.10	3.84
χ^2		1.565	1.985
La	x	0.4915(6)	0.4910(4)
4*e* (*x y z*)	y	0.4593(2)	0.4571(2)
	z	0.246(1)	0.253(1)
	U_{ISO} / Å^2	0.0185(4)	0.0149(3)
Ni/Cu/Nb1	U_{ISO} / Å^2	0.0036(2)	0.0011(2)
2*c* (0 ½ 0)	Ni occupancy	0.833	0.833
	Cu occupancy	0.167	0.167
	Nb occupancy	0	0
Ni/Cu/Nb2	U_{ISO} / Å^2	0.0036(2)	0.0011(2)
2*d* (½ 0 0)	Ni occupancy	0.333	0.333
	Cu occupancy	0	0
	Nb occupancy	0.667	0.667
O1	x	0.793(1)	0.796(1)
4*e* (*x y z*)	y	0.797(1)	0.798(1)
	z	–0.0365(7)	–0.0378(6)
	U_{ISO} / Å^2	0.003(1)	0
O2	x	0.711(1)	0.712(1)
4*e* (*x y z*)	y	0.282(1)	0.283(1)
	z	–0.0465(8)	–0.0453(7)
	U_{ISO} / Å^2	0.015(1)	0.011(1)
O3	x	0.5786(5)	0.5801(4)
4*e* (*x y z*)	y	0.0185(4)	0.0179(3)
	z	0.244(1)	0.247(1)
	U_{ISO} / Å^2	0.0153(6)	0.0111(5)

Table 6.3. Atomic parameters of $La_3Ni_{1.5}Cu_{0.5}NbO_9$ at RT and 3 K (Space group $P2_1/n$).

		RT	3 K
a / Å		5.5915(1)	5.5793(1)
b / Å		5.6617(1)	5.6617(1)
c / Å		7.9203(2)	7.9055(2)
β / °		90.06(1)	90.05(1)
V / Å^3		250.74(1)	249.72(1)
$R_{wp\|NPD}$ / %		4.18	3.90
χ^2		2.140	2.651
La	x	0.4906(5)	0.4906(4)
4*e* (*x y z*)	y	0.4586(2)	0.4566(2)
	z	0.252(1)	0.253(1)
	U_{ISO} / Å^2	0.0177(3)	0.0140(3)
Ni/Cu/Nb1	U_{ISO} / Å^2	0.0037(2)	0.0013(2)
2*c* (0 ½ 0)	Ni occupancy	0.80(5)	0.80
	Cu occupancy	0.20(5)	0.20
	Nb occupancy	0	0
Ni/Cu/Nb2	U_{ISO} / Å^2	0.0037(2)	0.0013(2)
2*d* (½ 0 0)	Ni occupancy	0.20(5)	0.20
	Cu occupancy	0.13(5)	0.13
	Nb occupancy	0.667	0.667
O1	x	0.791(1)	0.792(1)
4*e* (*x y z*)	y	0.799(1)	0.800(1)
	z	–0.0356(6)	–0.0377(5)
	U_{ISO} / Å^2	0.006(1)	0
O2	x	0.707(1)	0.707(1)
4*e* (*x y z*)	y	0.284(1)	0.285(1)
	z	–0.0462(6)	–0.0459(6)
	U_{ISO} / Å^2	0.011(1)	0.012(1)
O3	x	0.5806(4)	0.5819(3)
4*e* (*x y z*)	y	0.0187(4)	0.0202(3)
	z	0.252(1)	0.252(1)
	U_{ISO} / Å^2	0.0152(5)	0.0103(4)

Table 6.4. Selected bond lengths (Å) and angles (°) in $La_3Ni_{1.75}Cu_{0.25}B'O_9$ at RT and 3 K.

	B' = Sb		*B*' = Ta		*B*' = Nb	
	RT	3 K	RT	3 K	RT	3 K
La–O1	2.745(10)	2.736(8)	2.701(9)	2.754(8)	2.7528(1)	2.701(8)
La–O1	2.726(9)	2.710(8)	2.751(8)	2.710(7)	2.7158(1)	2.742(6)
La–O1	2.450(8)	2.441(6)	2.418(7)	2.463(8)	2.4692(1)	2.417(7)
La–O2	2.849(11)	2.839(8)	2.882(9)	2.793(9)	2.8086(1)	2.835(9)
La–O2	2.445(8)	2.437(7)	2.465(8)	2.435(8)	2.4331(1)	2.473(7)
La–O2	2.631(9)	2.635(8)	2.608(9)	2.648(9)	2.6479(1)	2.612(7)
La–O3	2.554(3)	2.535(2)	2.554(3)	2.532(3)	2.5384(1)	2.532(2)
La–O3	2.437(4)	2.426(3)	2.429(5)	2.419(4)	2.4273(1)	2.417(3)
2*c*–O1	2.060(5)	2.059(5)	2.051(7)	2.057(5)	2.06096(4)	2.056(4)
2*c*–O2	2.068(5)	2.066(5)	2.061(7)	2.061(6)	2.0653(1)	2.052(5)
2*c*–O3	2.071(9)	2.040(8)	2.066(8)	2.085(12)	2.0806(1)	2.054(9)
2*d*–O1	2.014(5)	2.009(5)	2.021(6)	2.026(5)	2.0179(1)	2.027(4)
2*d*–O2	2.015(5)	2.023(6)	2.029(8)	2.023(6)	2.01558(4)	2.021(5)
2*d*–O3	1.997(9)	2.028(8)	2.000(8)	1.975(12)	1.9808(1)	2.003(9)
O1–2*c*–O2	89.5(3)	89.1(4)	89.9(4)	88.2(3)	88.742(2)	88.3(3)
O1–2*c*–O3	88.6(2)	88.4(2)	88.6(2)	88.9(2)	88.667(4)	88.9(2)
O2–2*c*–O3	88.0(2)	88.5(2)	88.1(2)	88.0(2)	87.791(5)	88.4(2)
O1–2*d*–O2	87.4(3)	88.8(4)	88.3(4)	86.6(3)	87.037(2)	86.8(3)
O1–2*d*–O3	89.4(2)	89.8(2)	89.4(2)	89.4(2)	89.430(6)	89.5(2)
O2–2*d*–O3	89.4(2)	89.5(2)	89.4(2)	90.0(2)	89.600(4)	89.8(2)
2*c*–O1–2*d*	154.8(3)	155.0(3)	155.0(4)	153.1(3)	153.984(1)	153.0(3)
2*c*–O2–2*d*	153.6(3)	152.4(3)	152.8(4)	154.2(4)	153.744(1)	154.1(3)
2*c*–O3–2*d*	154.3(2)	153.6(1)	154.0(2)	153.9(1)	154.291(1)	153.9(1)

Table 6.5. Selected bond lengths (Å) and angles (°) in $La_3Ni_{1.5}Cu_{0.5}NbO_9$ at RT and 3 K.

	RT	3 K
La–O1	2.714(7)	2.691(5)
La–O1	2.743(6)	2.749(5)
La–O1	2.445(6)	2.416(5)
La–O2	2.831(8)	2.848(6)
La–O2	2.449(6)	2.465(5)
La–O2	2.639(7)	2.607(5)
La–O3	2.541(2)	2.524(2)
La–O3	2.422(3)	2.412(3)
2*c*–O1	2.079(5)	2.067(4)
2*c*–O2	2.076(5)	2.058(4)
2*c*–O3	2.014(9)	2.004(7)
2*d*–O1	2.002(5)	2.019(4)
2*d*–O2	2.015(6)	2.028(5)
2*d*–O3	2.053(9)	2.060(7)
O1–2*c*–O2	89.3(3)	88.7(2)
O1–2*c*–O3	87.9(1)	88.0(1)
O2–2*c*–O3	88.6(2)	88.4(2)
O1–2*d*–O2	87.7(3)	87.2(2)
O1–2*d*–O3	89.4(2)	89.6(1)
O2–2*d*–O3	89.4(2)	89.7(1)
2*c*–O1–2*d*	154.2(2)	153.2(2)
2*c*–O2–2*d*	153.1(3)	153.1(3)
2*c*–O3–2*d*	153.7(1)	153.1(1)

The temperature dependence of the ZFC and FC molar magnetic susceptibility of $La_3Ni_{1.75}Cu_{0.25}B'O_9$ (B' = Sb, Ta or Nb) and $La_3Ni_{1.5}Cu_{0.5}NbO_9$ in an applied field of 100 Oe is shown in Figure 6.5. The data from all four compounds show the same general trends; the ZFC and FC curves do not overlie below 100 K and both the ZFC and FC molar susceptibilities decrease sharply on heating through the temperature range $75 \leq T/\mathrm{K} \leq 150$. Note that under FC conditions $\chi_{MAX} > 15$ cm^3 mol^{-1} for all compositions. These compounds appear to be paramagnetic above 200 K, where $\chi^{-1}(T)$ is linear. The data collected in the range $200 \leq T/\mathrm{K} \leq 300$ were fitted to the Curie–Weiss law to yield the molar Curie constant, C_m, and the Weiss temperature, θ_W. These parameters are listed in Table 6.6. The former has contributions from both the Ni^{2+} and Cu^{2+} cations and the observed values, C_m, are therefore compared to the calculated value, C_m^{calc}, where

$$C_m^{calc} = \frac{2-x}{8}\left(\mu_{so}^{Ni}\right)^2 + \frac{x}{8}(\mu_{so}^{Cu})^2. \qquad \text{Equation 6.1}$$

Here the μ_{so}^{Ni} and μ_{so}^{Cu} represent the spin–only effective moments of the Ni^{2+} and Cu^{2+}. The temperature and frequency dependences of the ac molar susceptibilities of $La_3Ni_{1.75}Cu_{0.25}B'O_9$ (B' = Sb, Ta or Nb) and $La_3Ni_{1.5}Cu_{0.5}NbO_9$ are shown in Figure 6.6. The real component, χ', has a maximum at the temperature where χ_{dc} rises significantly and χ'' has a maximum at the same temperature or a slightly lower temperature. Moreover, for all compositions other than $La_3Ni_{1.75}Cu_{0.25}NbO_9$, a secondary maximum in χ'' is observed at ~60 K. Note that $\frac{d\chi''}{d\omega}$ is positive at the principal maximum and negative at the secondary maximum. The field dependence of the magnetisation per formula unit, $M(H)$, of each compound is shown in Figure 6.7. In no case is hysteresis apparent at either 150 or 220 K although $M(H)$ is always nonlinear at 150 K. However, hysteresis is present at 5 K in each compound and the values of the coercive field (H_C) and remanent magnetisation (M_R) observed at this temperature are included in Table 6.6. For each perovskite, $M(H)$ was also

recorded at the temperature at which a local minimum was observed in the imaginary component of the ac magnetic susceptibility. Hysteresis was less apparent at these temperatures, especially in the case of $La_3Ni_{1.75}Cu_{0.25}NbO_9$.

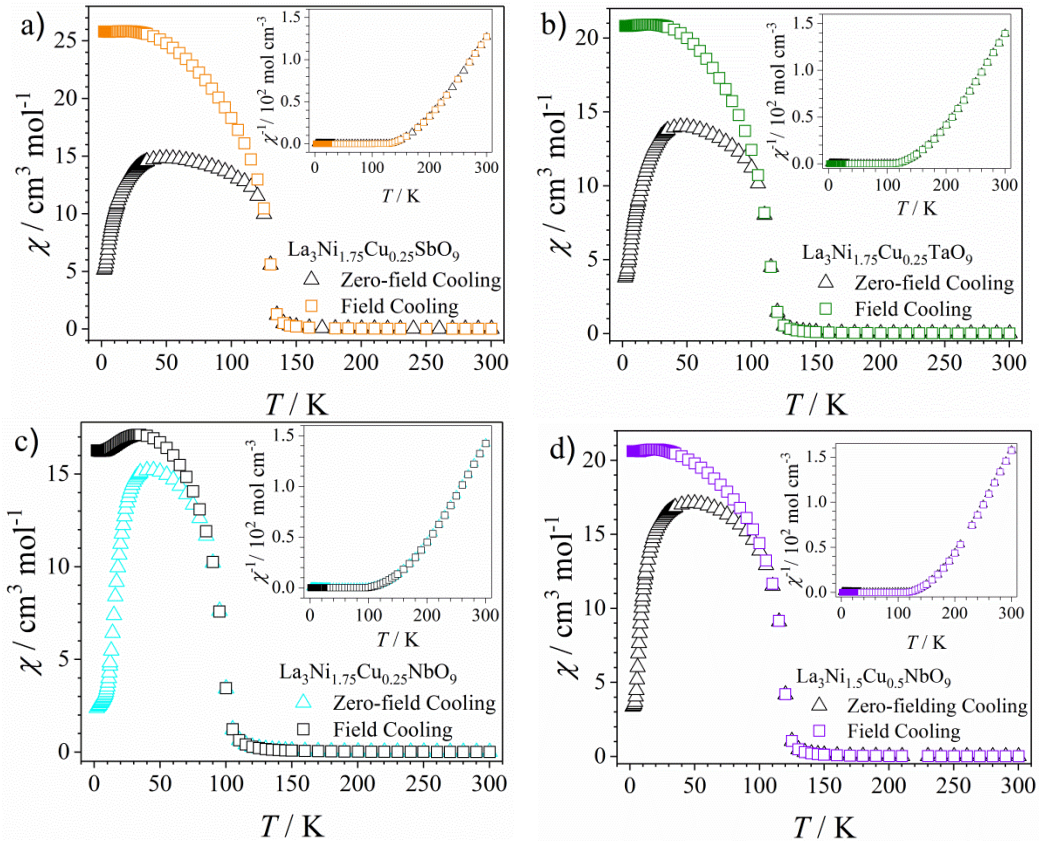


Figure 6.5. Temperature dependence of the dc molar susceptibility and inverse susceptibility of (a) $La_3Ni_{1.75}Cu_{0.25}SbO_9$, (b) $La_3Ni_{1.75}Cu_{0.25}TaO_9$, (c) $La_3Ni_{1.75}Cu_{0.25}NbO_9$ and (d) $La_3Ni_{1.5}Cu_{0.5}NbO_9$.

Table 6.6. Magnetic parameters of $La_3Ni_{2-x}Cu_xB'O_9$.

B'	*x*	C_m^{calc}	C_m	θ_W/K	M_R/μ_B	H_C/kOe	T_C/K	T_{MAX}/K	M_O/μ_B*
Sb	0.25	1.84	1.05(1)	+169(4)	0.38	0.2	130	50	1.22(4)
Ta	0.25	1.84	1.01(1)	+161(3)	0.18	0.32	110	45	1.15(5)
Nb	0.25	1.84	1.02(1)	+156(3)	0.42	0.35	90	45	0.94(6)
Nb	0.5	1.69	0.87(1)	+165(4)	0.3	0.2	110	50	0.83(6)

* The mean ordered magnetic moment per cation, determined by neutron diffraction, in $La_3Ni_{2-x}Cu_xB'O_9$ at 3 K.

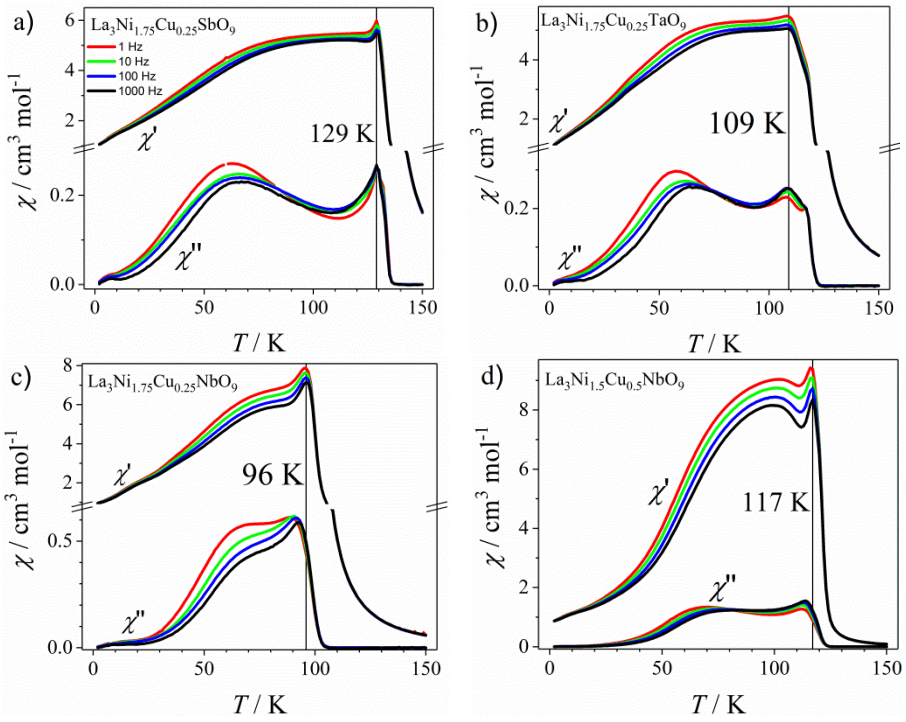


Figure 6.6. Temperature and frequency dependence of the real and imaginary components of the ac molar susceptibility of (a) $La_3Ni_{1.75}Cu_{0.25}SbO_9$, (b) $La_3Ni_{1.75}Cu_{0.25}TaO_9$, (c) $La_3Ni_{1.75}Cu_{0.25}NbO_9$ and (d) $La_3Ni_{1.5}Cu_{0.5}NbO_9$ collected at 1 (red), 10 (green), 100 (blue) and 1000 (black) Hz.

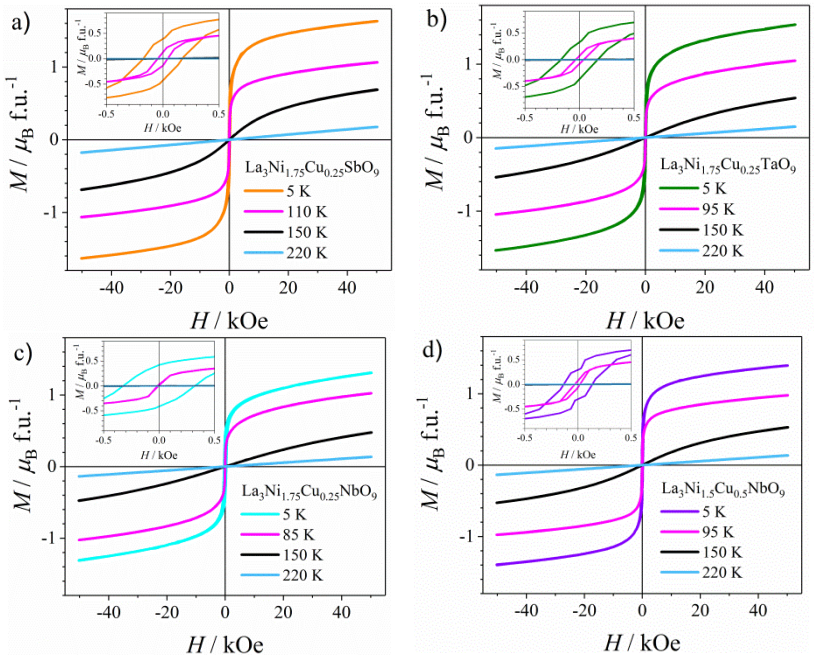


Figure 6.7. Field dependence of the magnetisation per formula unit of (a) $La_3Ni_{1.75}Cu_{0.25}SbO_9$, (b) $La_3Ni_{1.75}Cu_{0.25}TaO_9$, (c) $La_3Ni_{1.75}Cu_{0.25}NbO_9$ and (d) $La_3Ni_{1.5}Cu_{0.5}NbO_9$ at four different temperatures. The insets show the same function for a smaller range of *H*.

The *B*/*B*'–site distribution determined at room temperature was held constant during the Rietveld analyses of the neutron diffraction patterns collected at lower temperatures using both λ = 1.622 and 2.4395 Å. The shorter wavelength was used to deduce the structural parameters whereas the data collected using the longer wavelength provided better counting statistics for the refinement of the magnetic structure. The patterns collected at 3 K and the calculated fits are presented in Figures 6.8 and S6.5 – S6.7. In preliminary refinements the displacement parameters, U_{ISO}, of some oxide anions became negative. However, the values were within one standard deviation of zero and they were therefore fixed at that value in subsequent refinements. The atomic parameters, together with some selected bond lengths and bond angles, are included in Tables 6.2 – 6.5, S6.1 and S6.2. Additional intensity was seen in the 011 reflection of the perovskite phase below the magnetic transition temperature for all compounds using both wavelengths, and hence it was assumed to be magnetic in origin. This extra scattering could be accounted for by adding a G–type magnetic structure with the ordered moments aligned along [100]. The magnetic structure has 100 % and 33 % magnetic occupancy of the 2*c* and 2*d* sites, respectively. When two magnetic cations occupy the same site, the only quantity that can be determined is the mean magnetic moment per site; no partition between the two disordered species can be derived from the data. The magnetic form factor of Ni^{2+} was therefore used for all the magnetic cations and they were all assumed to have the same atomic moment, see Table 6.6. An additional NPD dataset was collected from $La_3Ni_{1.75}Cu_{0.25}TaO_9$ at 95 K using λ = 2.4395 Å. The pattern could be fitted, see Figure S6.8, using the magnetic model used to account for the data collected at 3 K. The mean magnetic moment per site at 95 K was found to be 0.7(1) μ_B.

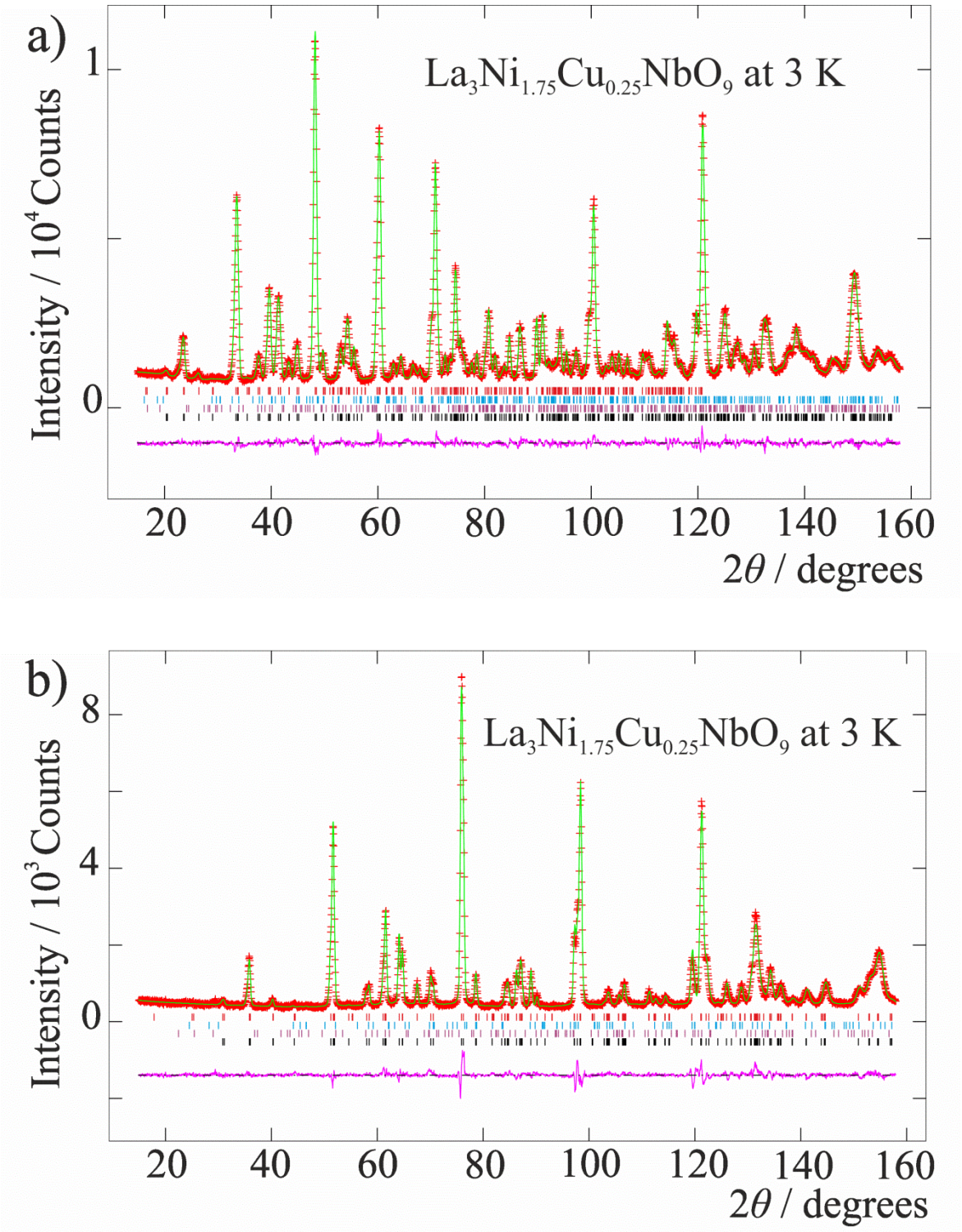


Figure 6.8. Observed (red crosses) and calculated (green line) NPD profiles of $La_3Ni_{1.75}Cu_{0.25}NbO_9$ at 3 K using λ = (a) 1.622 and (b) 2.4395 Å. A difference curve (purple) is shown below. Reflection markers are shown for the magnetic (red) and structural (black) perovskite phases, $LaNbO_4$ (cyan) and La_3NbO_7 (purple).

6.4 Discussion

The data described above show that it is possible to substitute at least 12.5 % of the Ni^{2+} cations in $La_3Ni_2B'O_9$ with Cu^{2+} when *B*' = Sb, Ta or Nb. The space–group symmetry of the structure does not change when Cu^{2+} is introduced and the samples retain a high degree of crystallinity, as judged by both neutron diffraction and electron diffraction. The Cu^{2+} cations share the 2*c* site with Ni^{2+} cations when $x = 0.25$, see Figure 6.3, but the neutron diffraction data collected from $La_3Ni_{1.5}Cu_{0.5}NbO_9$ show that as their concentration increases they also occupy the 2*d* site, albeit in smaller numbers, see Table 6.3. The mean *B*/*B*'–O bond lengths around the 2*c* sites, see Table 6.4, are, as expected, always longer than those around the 2*d* site and they are relatively insensitive to the identity of *B*' when $x = 0.25$. Most noticeably, the pseudo–tetragonal compression of the coordination polyhedron seen in $La_3Ni_2TaO_9$ and $La_3Ni_2NbO_9$[142] is not observed at room temperature in the $x = 0.25$ compositions. It is, however, restored when $x = 0.5$, see Table 6.5. It is impossible to interpret these apparent changes in detail for a number of reasons. Firstly, both sites are occupied by more than one type of cation and the tabulated bond lengths are therefore only mean values. Furthermore, previous analysis of the angular dependence of the background scattering observed in the diffraction pattern of $La_3Ni_2SbO_9$, see Chapter 3, and the diffuse scattering observed in the electron diffraction patterns collected from $La_3Ni_2TaO_9$ and $La_3Ni_2NbO_9$[142] suggests that the distribution of the cations over 2*d* sites in these materials is not always random on a local distance scale. The tendency of Cu^{2+} to occupy a distorted coordination environment as a consequence of the otherwise–degenerate electron configuration of a d^9 cation must also be considered. However, this usually results in the formation of two long bonds and four short bonds in the octahedron of coordinating oxide ions, and no cooperative distortion of this type is seen around the copper–rich 2*c* sites in any of the compounds included in this study. Nevertheless, the possibility that

uncorrelated, local distortions are present within the structure cannot be ruled out. The tendency of the d^0 Nb^{5+} and Ta^{5+} cations to move away from the centre of their octahedra[151] could be an equally important factor in determining the local structure. The likely presence of some combination of these local deviations from the mean structure limits the depth to which the bond lengths derived from a neutron diffraction experiment can be interpreted.

The dc magnetometry data shown in Figures 6.5 and 6.7 suggest that each of the four compounds studied undergoes a transition to a ferromagnetic state on cooling through the temperature range $90 \leq T/K \leq 130$ and the ac data shown in Figure 6.6 are consistent with this conclusion. However, the frequency and temperature dependencies of the latter data below the Curie temperature, T_C, show that none of these compounds is a simple ferromagnet. The observation of magnetic Bragg scattering in the neutron diffraction pattern collected from $La_3Ni_{1.75}Cu_{0.25}TaO_9$ argues against the existence of a re–entrant spin–glass phase[155] at 95 K and the neutron diffraction patterns recorded at 3 K prove that long–range magnetic ordering is always present at that temperature. The G–type structure used to model the data involves antiferromagnetic coupling between spins on nearest–neighbour sites and, as discussed above, the resultant magnetisation is a consequence of there being different concentrations of magnetic cations on these sites. These compounds could therefore be described as ferrimagnets rather than ferromagnets but the latter term will still be used in the following text. Each composition has a magnetisation of ~1.5 μ_B per formula unit in 50 kOe at 5 K. However, the ordered moment determined by neutron diffraction varies by ~33 % across the series, see Table 6.6. It therefore seems likely that, as in the case of $La_3Ni_2SbO_9$[75], long–range ordered regions coexist with ordered domains that are too small to contribute to the magnetic Bragg scattering, although they can be aligned with the net magnetisation by an applied field. The studied crystallites thus consist

of relatively–large, long–range ordered regions interspersed with smaller relaxor regions. The nature of the domain walls between these two types of region is still under investigation but their movement might be responsible for the unusual behaviour of the ac susceptibility at temperatures well below T_C.

The presence of only 12.5 % Cu^{2+} has a remarkable effect on the behaviour of these Ni^{2+}–based oxides. The changes are least marked when *B*' = Sb; $La_3Ni_2SbO_9$ has been shown to have a backbone of long–range ordered spins with relaxor domains also present and the neutron diffraction and magnetometry data collected from $La_3Ni_{1.75}Cu_{0.25}SbO_9$ can be interpreted using a similar model. However, the imaginary component of the ac susceptibility of the copper–free composition does not show a local maximum below T_C and the introduction of 12.5 % Cu^{2+} increases the Curie temperature by ~30 K. More significant changes are seen in the tantalum–based system, wherein, in addition to an enhancement of T_C, the introduction of Cu^{2+} is accompanied by the formation of regions showing long–range magnetic order in addition to the relaxor regions found in the Cu–free composition. The most dramatic changes are seen in $La_3Ni_{2-x}Cu_xNbO_9$. $La_3Ni_2NbO_9$ is a spin glass with T_f ~29 K. The introduction of 12.5 % (25 %) Cu^{2+} causes the onset of long–range G–type magnetic ordering and increases the magnetic transition temperature to 96 K (117 K). In order to eliminate the spin–glass behaviour it is necessary to eliminate or reduce the frustration that causes it. The source of the frustration in $La_3Ni_2NbO_9$ has been discussed previously and concluded that it is most likely to arise from the presence of 180º Ni–O–Nb–O–Ni interactions that compete with Ni–O–Ni interactions. When x = 0.25, the presence of Cu^{2+} introduces 180º Cu–O–Ni, Cu–O–Nb–O–Ni and Cu–O–Nb–O–Cu interactions; further interactions are introduced when Cu^{2+} cations also partially occupy the 2*d* sites, as in $La_3Ni_{1.5}Cu_{0.5}NbO_9$. As a consequence of the different electron configurations of Ni^{2+} and Cu^{2+}, the introduction of the latter cation will lead to changes in the magnitude

and, sometimes, the sign of the relevant exchange constants. Any local variations in the bond lengths around the Jahn–Teller–active Cu^{2+} cations will also have consequences for the magnetic interactions. It is thus easy to understand why the magnetic behaviour might change but, with the data available, very difficult to predict or rationalise the nature of the changes in these heavily disordered compounds. Vasala *et al.*[12] have previously described the consequences of a Jahn–Teller distortion for the magnetic properties of double perovskites containing Cu^{2+} and Mustonen *et al.*[147] have discussed the changes that occur in those materials when a d^0 diamagnetic cation is replaced by a d^{10} cation. The compounds described in this chapter are subject to both these factors, with cation disorder present as an additional complication.

6.5 Conclusion

The introduction of Cu^{2+} cations into $La_3Ni_2B'O_9$ (*B'* = Sb, Ta or Nb) has a marked effect on the magnetic properties. In the case where *B'* = Sb the substituted composition is similar to the parent material[48, 75] in that, at low temperatures, it contains regions that show long–range magnetic order and regions that appear to show relaxor behaviour. The evidence for this comes from magnetometry and neutron diffraction and includes the observation that the ordered moment measured by neutron diffraction is very low compared to the magnetisation measured by magnetometry. The most striking consequence of the substitution in this case is thus that T_C increases by ~30 K. $La_3Ni_2TaO_9$ is a relaxor ferromagnet[142, 152], the low–temperature neutron diffraction pattern of which shows no evidence of long–range magnetic order. Following the introduction of 12.5 % Cu^{2+}, $La_3Ni_{1.75}Cu_{0.25}TaO_9$ shows long–range magnetic order at a temperature ~30 K higher than that at which the copper–free composition begins to behave as a relaxor ferromagnet. However, as in the case *B'* = Sb, the experimental evidence suggests that ordered and relaxor regions coexist below the transition temperature. The most dramatic changes are

seen when *B'* = Nb, in which case the introduction of Cu^{2+} transforms the spin–glass parent composition into a mixed magnetically–ordered/relaxor phase. Although the origins of all these changes remain to be elucidated, the data presented in this chapter demonstrate again the sensitivity of the magnetic properties of these perovskites to chemical composition.

Chapter 7: Structural chemistry and magnetic properties of $SrLa_2Ni_2TeO_9$

7.1 Introduction

Cation ordering in a perovskite is more likely to occur if there is a large mismatch in the charge and size of the two cation species. For instance, Fe^{3+} and Ta^{5+} are randomly distributed in Sr_2FeTaO_6[131] whereas Fe^{3+} and W^{6+} are ordered over two *B* sites in Sr_2FeWO_6[156]. Hence, one would expect the ordered arrangement of the Ni^{2+} and Sb^{5+} in $La_3Ni_2SbO_9$ to be reproduced in a triple perovskite containing Ni^{2+} and hexavalent Te^{6+} cations, for example $SrLa_2Ni_2TeO_9$. To accommodate the change in d^{10} cation, one–third of the La^{3+} cations have been substituted with a divalent cation. In this case Sr^{2+} was chosen to offset the charge imbalance. This subtle alteration introduces the possibility of cation ordering at the *A* site as well as the *B* site. However, as will be discussed later in this chapter, $SrLa_2Ni_2TeO_9$ and $La_3Ni_2SbO_9$ show few similarities. XRPD and NPD, along with electron microscopy and magnetometry data, were collected to characterise $SrLa_2Ni_2TeO_9$, and the results are presented as follows.

7.2 Experimental

$SrLa_2Ni_2TeO_9$ was prepared by mixing and grinding stoichiometric amounts of $SrCO_3$, NiO, TeO_2 and pre–dried La_2O_3 in an agate mortar and pestle. The mixture was initially fired in an alumina crucible at 800 °C and was then pelletised before being heated at 950, 1100, 1200 and finally at 1225 °C, with intermediate regrinding. After a total of six days at 1225 °C the reaction product was cooled to 800 °C in the furnace and then quenched to room temperature.

XRPD data were collected over the angular range $15 \leq 2\theta/° \leq 125$ on a PANalytical Empyrean diffractometer operating with Cu $K_{\alpha 1}$ radiation (λ = 1.54051 Å) at room temperature. Rietveld refinement[92] was performed using GSAS[94] in order to determine the unit cell parameters. NPD data were collected in angular steps of $\Delta 2\theta = 0.05°$ for $10 \leq 2\theta/° \leq 150$ at room temperature, 50 K and 5 K using the instrument D2b at ILL, Grenoble, France. The sample was held in a vanadium can which was mounted in a Displex refrigerator during the data collection at 5 and 50 K. These data were also analysed using the Rietveld method. The background was modelled using an 18–term shifted Chebyshev function whereas a pseudo–Voigt function[123] was employed to model the peak shapes. The unit cell parameters were held at the values determined from the X–ray diffraction data in the analysis of the data collected at room temperature so as to determine the neutron wavelength which turned out to be λ = 1.5937 Å. Further data sets were collected at temperatures of 5 and 50 K on the diffractometer D1b using a wavelength λ = 2.5238 Å. D1b has a higher neutron flux than D2b and data from this instrument were used to search for weak Bragg peaks that might go unnoticed on D2b.

Specimens for electron microscopy were prepared by dispersing crushed $SrLa_2Ni_2TeO_9$ powder in ethanol and depositing a few drops of this solution on a copper grid covered with a holey carbon film. Selected–area electron diffraction patterns were recorded with a Philips CM20 transmission electron microscope. High–resolution HAADF–STEM images and atomic resolution STEM–EDX maps were collected with a FEI Titan 80–300 "cubed" transmission electron microscope equipped with a Super–X detector and operated at 300 kV.

The temperature dependence of the dc molar magnetic susceptibility of $SrLa_2Ni_2TeO_9$ was measured using a SQUID magnetometer. Measurements were made while warming the sample through the temperature range $5 \leq T/K \leq 300$ after it had been cooled either in the

absence (ZFC) of a field or the presence (FC) of a field of 100 Oe. The magnetisation per formula unit (f.u.) was measured as a function of applied magnetic field over the range –50 ≤ H/kOe ≤ 50 at temperatures of 5, 50 and 150 K. The ac susceptibility was measured over the temperature range 2 ≤ T/K ≤ 150 in a field of amplitude 3.5 Oe oscillating at frequencies of 1, 10 and 100 Hz.

7.3 Results

The reaction product was a dark green powder. Fifty crystallites were examined by EDX analysis to rule out the possibility of contamination by Sr_2NiTeO_6[157]; no La–free crystallites were found. Furthermore, Fourier transforms of the appropriate HRTEM images failed to identify any crystallites with the space group, $I2/m$, associated with Sr_2NiTeO_6.

Preliminary Rietveld analysis of the XRPD pattern, see Figure S7.1, suggested that the product consisted principally of a monoclinic, perovskite–like phase contaminated by 1.19(4) wt. % of Sr_3TeO_6[158] and 0.25(3) wt. % of NiO[125]. The perovskite pattern could be indexed in the space group $P2_1/n$ with $a \sim b \sim \sqrt{2}a_p$, $c \sim 2a_p$, $\beta \sim 90$ ° where a_p is the cell parameter of a primitive cubic perovskite. This combination of unit cell size and symmetry allows the presence of two crystallographically–distinct six–coordinate sites in the structure. In the Rietveld refinement, partial cation ordering over the two sites was found. Meanwhile, there was no evidence for the ordering of strontium and lanthanum over the A sites.

The dc molar magnetic susceptibility of $SrLa_2Ni_2TeO_9$ as a function of temperature is shown in Figure 7.1. The data in the temperature range 200 ≤ T/K ≤ 300 exhibits the paramagnetic behaviour described by the Curie–Weiss law and hence the curve was fitted accordingly, resulting in values of 2.21(1) μ_B and +121(2) K for the effective magnetic

moment per Ni^{2+} cation and the Weiss temperature, respectively. The data collected under ZFC and FC conditions differ below 35 K, at which temperature the former show a maximum in $\chi(T)$; the data collected under FC conditions show essentially no temperature dependence below 35 K. The field dependence of the magnetisation per f.u. is shown in Figure 7.2. $M(H)$ is linear at 150 K and nonlinear at 50 K, but no hysteresis is seen at either temperature. However, a hysteresis loop with a finite width below 30 kOe field at 5 K is clearly seen and the curved still shows an increasing trend even in a magnetic field of 50 kOe. The remanent magnetisation is ~0.06 μ_B per f.u. and the coercive field is 2.4 kOe. The ac susceptibility, see Figure 7.3, is a function of frequency and has both real and imaginary components below ~35 K. The transition temperature is frequency–dependent with $\Delta T_f/[T_f\Delta(\log \omega)] = 0.014$, a typical value for a canonical spin glass.

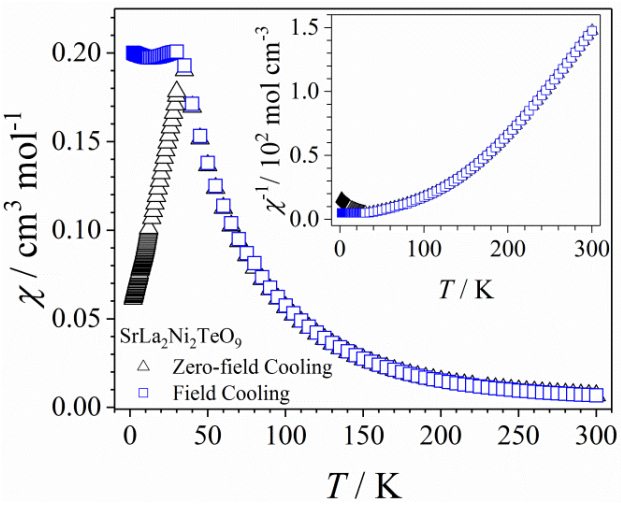


Figure 7.1. The temperature dependence of molar susceptibility and (inset) inverse susceptibility of $SrLa_2Ni_2TeO_9$.

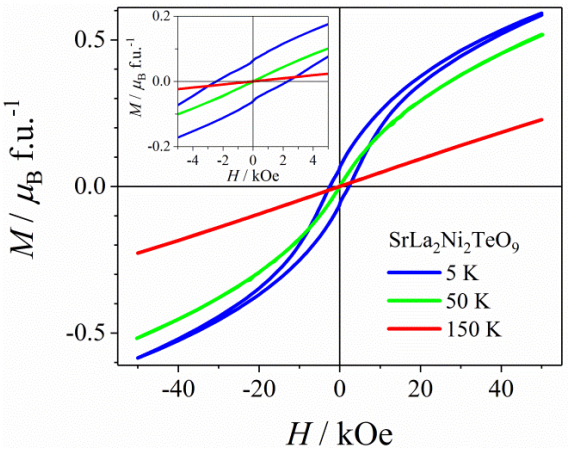


Figure 7.2. Magnetic field dependence of the magnetisation per formula unit of $SrLa_2Ni_2TeO_9$ at 5 (blue), 50 (green) and 150 (red) K.

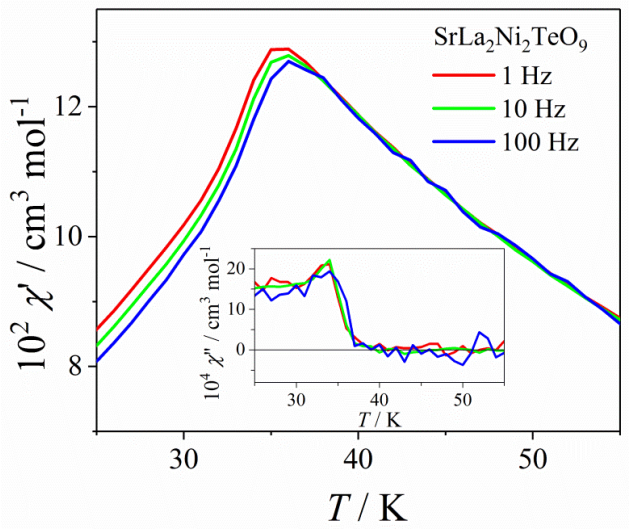


Figure 7.3. Temperature and frequency dependence of the real and imaginary components of the ac susceptibility of $SrLa_2Ni_2TeO_9$ collected at 1 (red), 10 (green) and 100 (blue) Hz.

A Rietveld refinement on the NPD data of $SrLa_2Ni_2TeO_9$ collected at room temperature using D2b was conducted. The analysis confirmed that the perovskite crystallises in the monoclinic space group $P2_1/n$; ~2.3(3) wt. % of Sr_3TeO_6, and ~0.43(3) wt. % of unreacted NiO were detected in this analysis. As in the analysis of the X–ray diffraction data, the nickel and tellurium cations were found to be partially ordered over the octahedral sites. The Ni/Te distribution was refined at room temperature and then held constant during the

analysis of the data collected at 50 and 5 K. The same basic structural model was able to account for all the diffraction patterns. No magnetic Bragg scattering was apparent in any of the datasets collected on D2b. The patterns recorded at room temperature and 5 K are presented, along with the calculated patterns, in Figure 7.4. The refined structural parameters are presented in Table 7.1 and some selected bond lengths and angles are listed in Table 7.2. The parameters and fits resulting from the analysis of the data collected at 50 K are listed in Tables S7.1 and S7.2 and Figures S7.2 and S7.3. The NPD patterns collected at 5 K and 50 K on D1b were superimposable as no additional Bragg scattering was seen at the lower temperature. However, inspection of the data at low angles revealed the presence of a 100 reflection, forbidden in space group $P2_1/n$, and additional intensity in the 101 and 102 reflections of the perovskite phase; the strongest magnetic reflection of nickel oxide was also visible[125, 159]. These reflections, which were apparently too weak to be identified in the data collected on D2b, were not seen in the X–ray diffraction pattern at room temperature. They were therefore assumed to be magnetic in origin. None of the collinear antiferromagnetic ordering patterns associated with the perovskite structure gives rise to this combination of reflections[55]. Hence, in order to fit the data quantitatively it was assumed that two magnetic phases were present, one showing G–type ordering and the other C–type, see Figure 7.5. As a consequence of correlations between the parameters, it was not possible to refine the ordered magnetic moment and the phase fractions of the magnetic phases simultaneously. As a result, the proposed magnetic model consists of these two magnetic phases in which all the 2*c* and 2*d* sites are occupied by Ni^{2+}, and that the magnetic moment is aligned along [100] with a magnitude of 2 μ_B. Refinements, see Figure 7.6, then showed that at 5 K 17(2) and 19(2) wt. % of the sample ordered as G–type and C–type antiferromagnets, respectively. The limitations of these assumptions are discussed below.

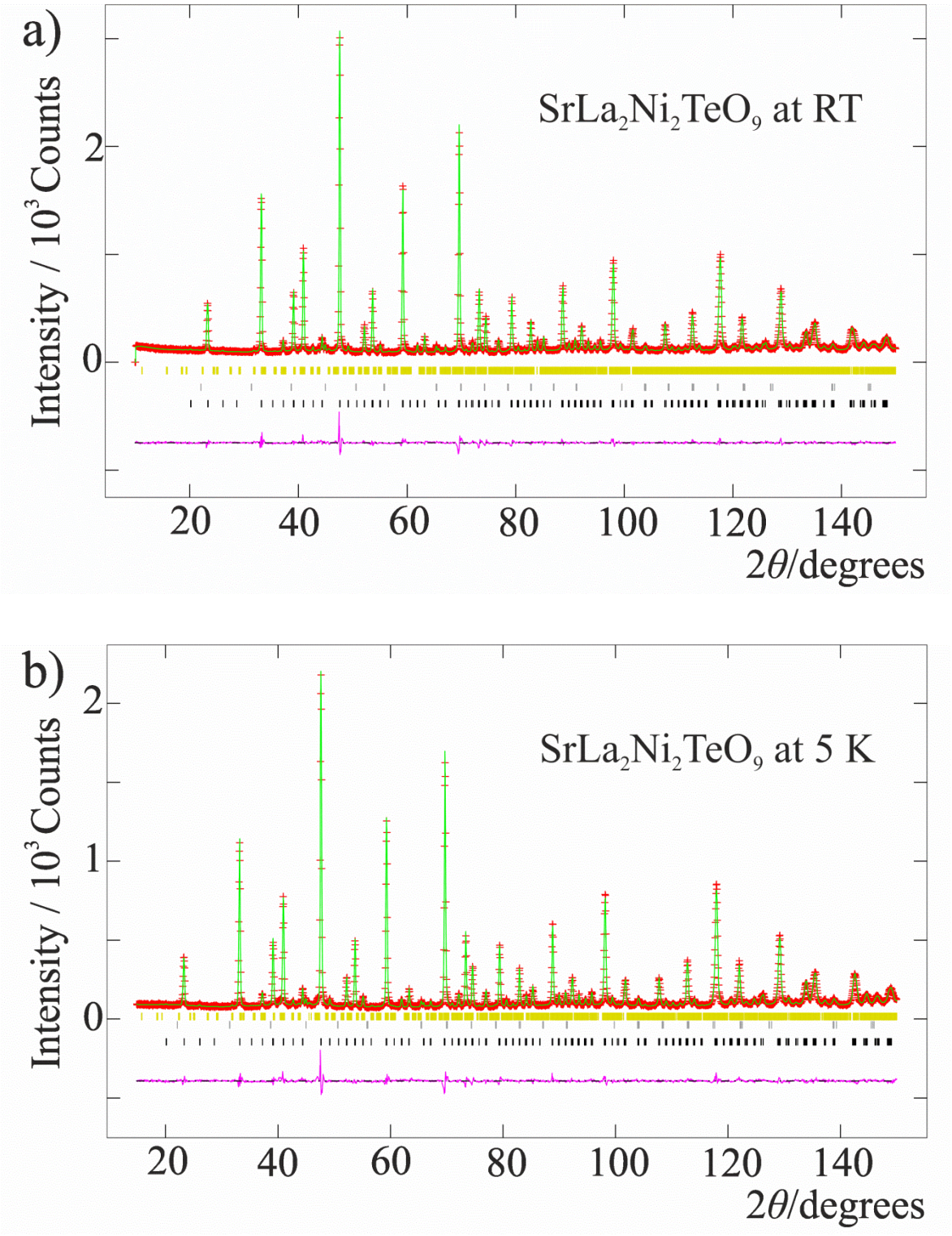


Figure 7.4. Observed (red crosses) and calculated (green line) neutron powder diffraction profiles recorded on D2b of $SrLa_2Ni_2TeO_9$ at (a) room temperature and (b) 5 K. Underneath is a difference curve, purple in colour. Reflection markers are shown, from top to bottom, for Sr_3TeO_6, NiO and $SrLa_2Ni_2TeO_9$.

Table 7.1. Structural parameters of $SrLa_2Ni_2TeO_9$ at RT and 5 K. (Space group $P2_1/n$).

		Room temperature	5 K
a / Å		5.6008(1)	5.5901(1)
b / Å		5.5872(1)	5.5803(1)
c / Å		7.9018(2)	7.8886(2)
β / °		90.021(6)	90.026(5)
V / Å^3		247.27(1)	246.08(1)
$R_{wp\|NPD}$ / %		4.87	5.22
χ^2		4.175	3.709
Sr/La	x	0.5050(8)	0.5061(8)
4*e* (*x y z*)	y	0.5210(5)	0.5237(5)
	z	0.249(2)	0.250(2)
	U_{ISO} / Å^2	0.0275(4)	0.0230(4)
	Sr occupancy	0.3333	0.3333
	La occupancy	0.6667	0.6667
Ni/Te1	U_{ISO} / Å^2	0.0026(19)	0.0004(2)
2*c* (0 ½ 0)	Ni occupancy	0.83(3)	0.83
	Te occupancy	0.17(3)	0.17
Ni/Te2	U_{ISO} / Å^2	0.0026(19)	0.0004(2)
2*d* (½ 0 0)	Ni occupancy	0.50(3)	0.50
	Te occupancy	0.50(3)	0.50
O1	x	0.232(1)	0.231(1)
4*e* (*x y z*)	y	0.224(2)	0.220(2)
	z	–0.0390(8)	–0.0345(12)
	U_{ISO} / Å^2	0.0157(20)	0.0115(20)
O2	x	0.288(1)	0.290(1)
4*e* (*x y z*)	y	0.721(2)	0.721(2)
	z	–0.0309(8)	–0.0366(12)
	U_{ISO} / Å^2	0.009(2)	0.005(2)
O3	x	0.4345(6)	0.4325(7)
4*e* (*x y z*)	y	0.9915(7)	0.9897(6)
	z	0.248(2)	0.246(2)
	U_{ISO} / Å^2	0.0144(7)	0.0095(7)

Table 7.2. Selected bond lengths (Å) and angles (°) of $SrLa_2Ni_2TeO_9$ at RT and 5 K.

	RT	5 K
Sr/La–O1	2.880(13)	2.826(17)
Sr/La–O1	2.638(11)	2.665(15)
Sr/La–O1	2.508(11)	2.513(14)
Sr/La–O2	2.760(13)	2.793(17)
Sr/La–O2	2.479(11)	2.453(15)
Sr/La–O2	2.759(11)	2.713(14)
Sr/La–O3	2.984(4)	3.009(4)
Sr/La–O3	2.659(4)	2.633(4)
Sr/La–O3	2.467(6)	2.460(6)
2*c*–O1	2.041(8) × 2	2.046(8) × 2
2*c*–O2	2.049(6) × 2	2.058(7) × 2
2*c*–O3	2.025(14) × 2	2.037(12) × 2
2*d*–O1	1.977(7) × 2	1.959(8) × 2
2*d*–O2	1.972(7) × 2	1.970(7) × 2
2*d*–O3	1.994(14) × 2	1.980(12) × 2
O1–2*c*–O2	86.3(5) × 2	86.7(5) × 2
O1–2*c*–O3	89.1(2) × 2	89.6(3) × 2
O2–2*c*–O3	89.4(2) ×2	89.5(3) × 2
O1–2*d*–O2	88.6(5) × 2	89.0(6) × 2
O1–2*d*–O3	88.4(2) × 2	89.5(3) × 2
O2–2*d*–O3	89.6(2) × 2	89.6(3) × 2
2*c*–O1–2*d*	159.7(4)	160.8(5)
2*c*–O2–2*d*	159.3(4)	157.4(5)
2*c*–O3–2*d*	158.8(2)	158.1(2)

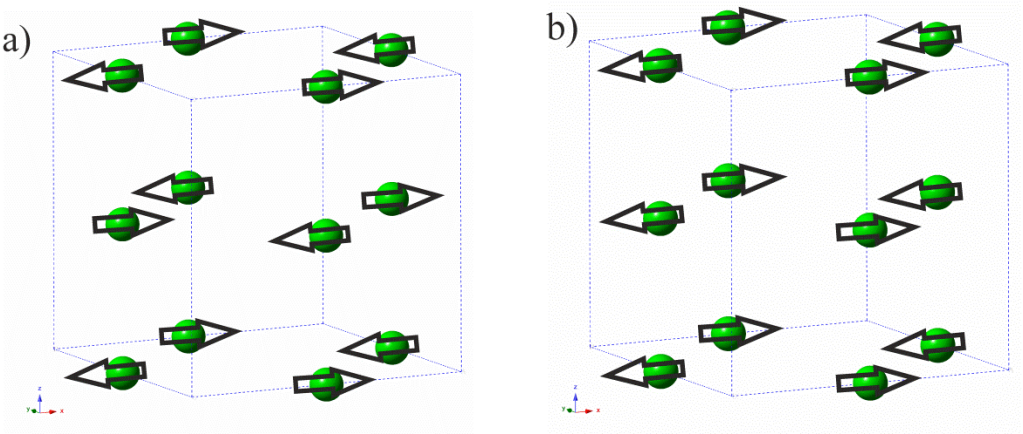


Figure 7.5. (a) G–type and (b) C–type magnetic structures drawn in the unit cell of $SrLa_2Ni_2TeO_9$.

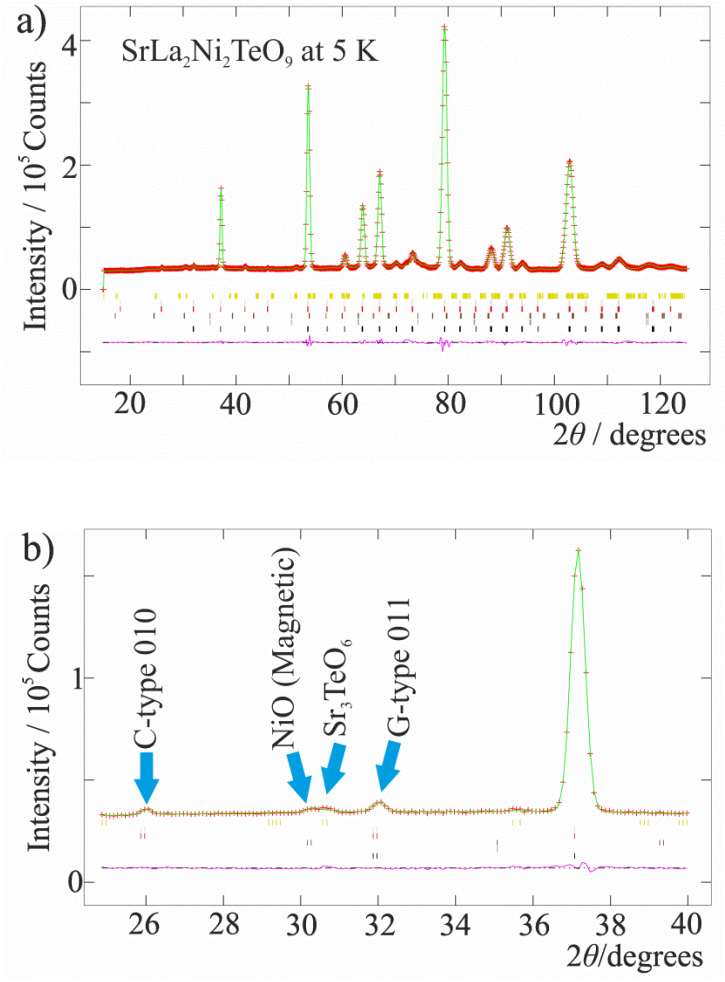


Figure 7.6. Observed (red crosses), calculated (green line) and difference (purple line) neutron powder diffraction profiles of $SrLa_2Ni_2TeO_9$ at 5 K recorded on D1b across (a) the full measured angular range and (b) the low–angle region. Reflection markers are shown from top to bottom for Sr_3TeO_6, C–type magnetic $SrLa_2Ni_2TeO_9$, G–type magnetic $SrLa_2Ni_2TeO_9$, magnetic NiO, structural NiO and structural $SrLa_2Ni_2TeO_9$.

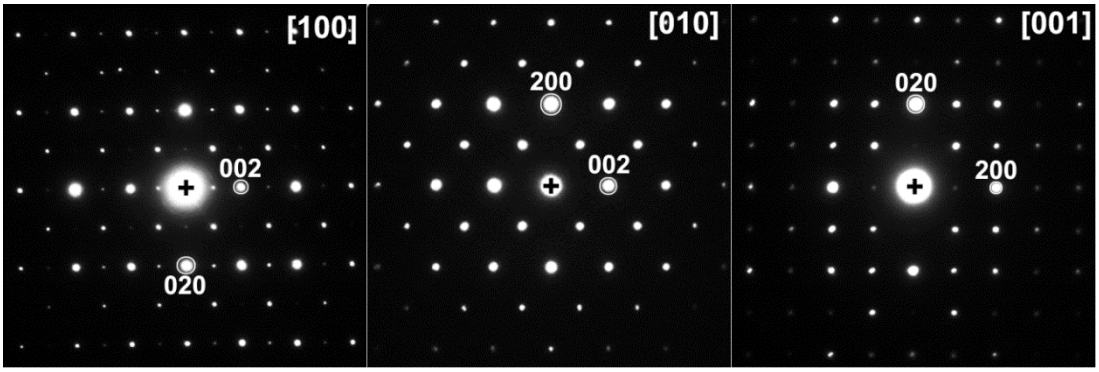


Figure 7.7. Representative selected–area electron diffraction patterns for the main zones of $SrLa_2Ni_2TeO_9$.

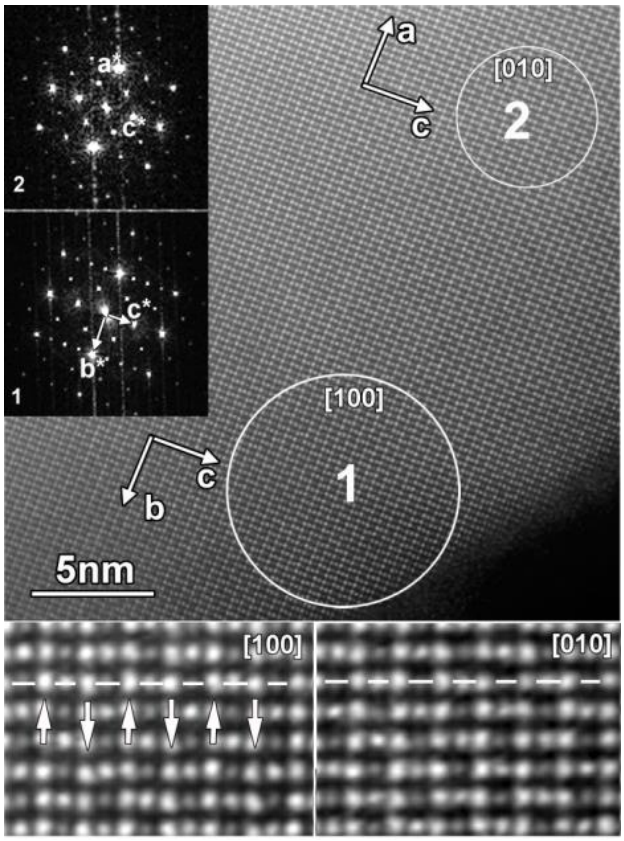


Figure 7.8. Aberration–corrected high–resolution HAADF–STEM image of a $SrLa_2Ni_2TeO_9$ crystal. The crystal is twinned and shows the [010] zone at the top, but the [100] zone at the bottom, as can be seen from the Fourier transforms. Arrows on the enlargements at the bottom show the slight shifts of the rows of *A* cations for [100] and the absence of such shifts in [010], a horizontal line is added as a guide to the eye.

TEM was applied to check for structural differences on a local scale. The electron diffraction analysis, of which the main zones are shown in Figure 7.7, confirms the unit cell and space group derived from X–ray diffraction. More details are given in the Appendix of this

thesis. The *00l:* $l \neq 2n$ reflections are present in [100], violating the reflection condition of the space group $P2_1/n$. However the fact that these reflections are absent in both the [010] pattern and on the [100] Fourier transform, see Figure 7.8, indicates they are observable because of double diffraction. Furthermore, a typical crystal along the [100] zone twinned with a [010] zone is seen in the same figure. The difference between the two orientations is almost imperceptible on the images, but is clear on the Fourier transforms (the Fourier transform for [010] is taken of a smaller area that that of [100] because there is no larger domain available; this should not influence the positions and presence of reflections). In these images, the *A* (La,Sr) columns form a straight line in [010] but a barely–noticeable zig–zag line in [100]. In the Fourier transforms, extra reflections are present in [100] compared to [010], corresponding respectively to the reflection conditions in the space group $P2_1/n$. This twinning is frequent throughout the sample. Note that the reflections 0*kl:* $k = 2n + 1$, $k+l = 2n + 1$ are present on the electron diffraction patterns of [100], consistent with space group $P2_1/n$, while they are absent on the Fourier transform of [100]. This is a consequence of the fact that the brightness of the dots on HAADF–STEM images increases with the average *Z* of the projected columns. Consequently, on the HAADF–STEM image the dots of the purely oxygen columns are invisible. They therefore also do not contribute to the Fourier transform of the HAADF–STEM image. Theoretical diffraction patterns using the RT model given in Table 7.1, with the exclusion of oxygen, were calculated and are shown in Figure S7.4. The exact patterns seen in the Fourier transforms were reproduced from these models.

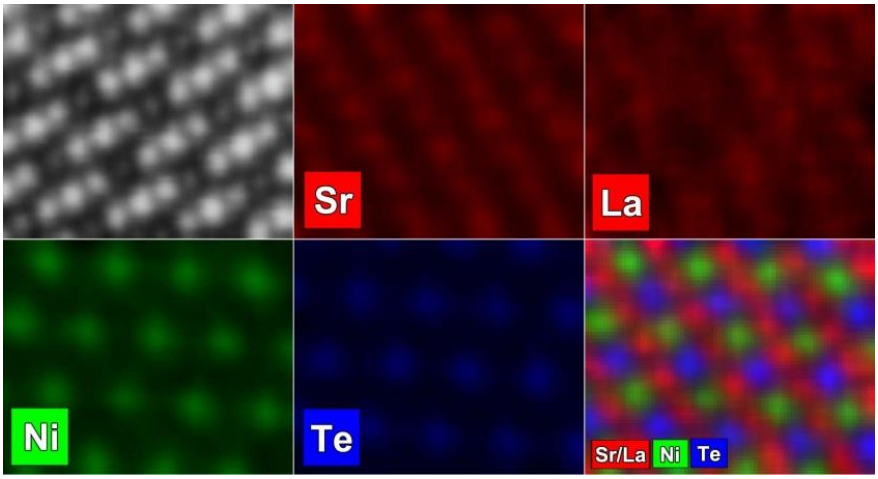


Figure 7.9. Aberration–corrected high–resolution HAADF–STEM and STEM–EDX map of a [010] oriented area of $SrLa_2Ni_2TeO_9$.

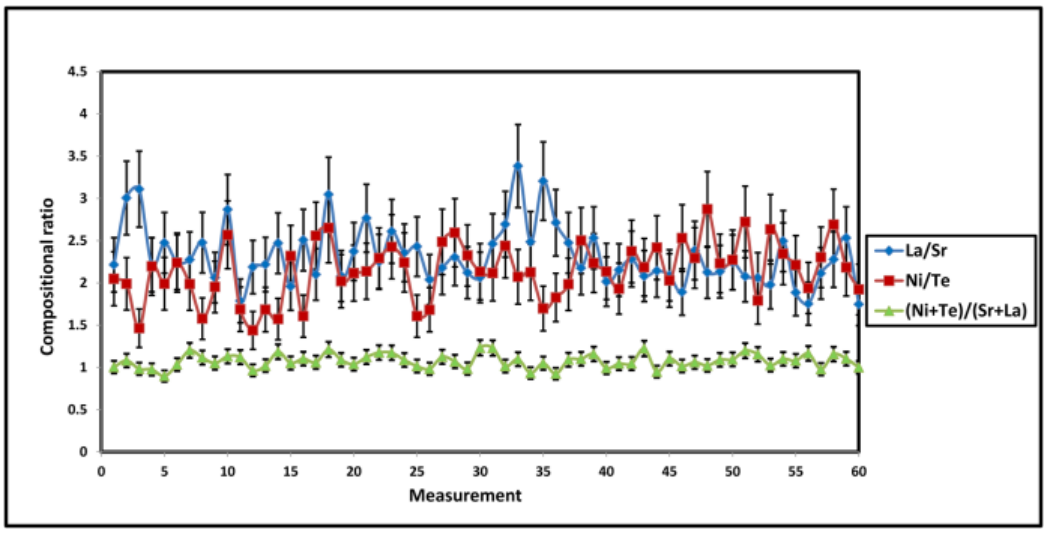


Figure 7.10. STEM–EDX measurements on sixty 4.5 nm × 4.5 nm areas within one crystal of $SrLa_2Ni_2TeO_9$.

Besides twinning, another type of inhomogeneity within the crystals was found using energy dispersive X–ray (EDX) analysis. STEM–EDX was first applied at atomic resolution to confirm the Ni–Te order in the sample, see Figure 7.9. Next, an overview STEM–EDX analysis was done of several crystals to study the homogeneity of the composition throughout the crystal. The composition of a representative crystal with a dimension of 62 nm by 48 nm is measured over 60 square areas of 4.5 nm by 4.5 nm, in low magnification. The measurement was performed with the crystal tilted out of zone to

avoid channelling effects. Figure 7.10 shows the measured ratios between the cations versus the serial number of the measured area. On this graph, the ratio (La+Sr):(Ni+Te) remains relatively constant and stays close to one throughout the measurements, as required for a perovskite structure. The ratios for the Ni:Te and La:Sr cations, however, deviate significantly from areas to areas as the stoichiometric 2:1 ratio for both quantities were not maintained. Nevertheless, when averaging over the whole set of measurements, the overall composition does agree with the stoichiometric one and is found to be $Sr_{0.92(9)}La_{2.07(9)}$ $Ni_{2.03(13)}Te_{0.97(13)}O_x$. The oxygen content was left unspecified as the species cannot be reliably measured from STEM–EDX quantification on a powder sample.

7.4 Discussion

The diffraction data demonstrate that there are a number of potentially–important structural differences between $SrLa_2Ni_2TeO_9$ and $La_3Ni_2SbO_9$. The high values of the displacement parameters of the *A*–site cations and the oxide ions at both room temperature and 5 K, see Table 7.1, could be a consequence of the local static disorder arising from the disordered cation distribution over the *A* site of $SrLa_2Ni_2TeO_9$. The displacement parameters of the anions are also enhanced by the occupational disorder on the *B* sites. In $La_3Ni_2SbO_9$ one of the *B* sites was found, within experimental error, to be totally occupied by Ni^{2+} whereas there is a significant deviation from this ideal ordering pattern in $SrLa_2Ni_2TeO_9$. The reduced degree of ordering is surprising given that Ni^{2+} and Te^{6+} differ by more in both size and charge than do Ni^{2+} and Sb^{5+}. It is worth noting that most of the structural parameters listed have relatively high statistical errors. One of the plausible explanations is that twinning is present throughout the sample. The average structure detected using neutron wavelength could be a combination of two twinned regions, leading to uncertainty in determining the structural parameters during the refinement. If the experimental error is ignored, the mean bond lengths around the two six coordinate sites are both shorter in the

tellurate than in $La_3Ni_2SbO_9$[6], which is consistent with the presence of some Te^{6+} on the six–coordinate site predominantly occupied by Ni^{2+}, see Tables 7.1 and 7.2.

At first sight, both magnetometry data and NPD data of $SrLa_2Ni_2TeO_9$ collected on D2b are indicative of spin–glass behaviour with T_f = 35 K. The additional *B*–site disorder present in $SrLa_2Ni_2TeO_9$ alone is insufficient to elucidate the discrepancy in the magnetic properties of this compound and $La_3Ni_2SbO_9$. The frustration necessary for the formation of a spin glass in the former is only present when next–nearest–neighbour interactions are competitive with nearest–neighbour interactions. More specifically, when 180° Ni–O–Ni interactions between cations ~3.95 Å apart are in competition with Ni–O–O–Ni interactions between cations ~5.6 Å apart. When they are all in competition, a frustrated spin glass will arguably be formed. The relative strength of these interactions will also vary with the local compositional variation within the crystal. For example, the Ni–O–Ni interactions will be less dominant in regions where there is a local excess of tellurium. With the aid of Figure 7.10, it seems plausible to assume the inhomogeneous composition of the crystallites is partly responsible for the formation of a spin–glass phase. Therefore, the local composition may contribute to the difference in the magnetic behaviour of $SrLa_2Ni_2TeO_9$ and $La_3Ni_2SbO_9$. The Ni–O–Ni interactions in the latter dominate within ferromagnetic domains which are ~50 Å long and the boundaries are where the 1:1 cation ordering is lost[75], and hence the next–nearest–neighbour interactions will be more competitive. Yet, no comparable regions were seen in the tellurate. The difference in the magnetic behaviour of the two compounds could then stem from the presence of infrequent but extended disordered regions in $La_3Ni_2SbO_9$ and frequent but local tellurium–rich regions in $SrLa_2Ni_2TeO_9$. The high twinning density in the latter might also be a factor. The presence of extended disordered regions in the antimonate but not in the tellurate is

consistent with the greater difference in size and charge of Ni^{2+} and Te^{6+}, as discussed above.

In the previous paragraph, the complexity of the microstructure of these perovskite has been linked to the magnetic behaviour, but the NPD data collected on D1b hinted that there is a further level of complexity to this case of study since weak magnetic Bragg scattering was observed at 5 K and 50 K. It is uncommon for such observation of magnetic ordering at these temperatures in view of the ordering temperatures of other Ni^{2+}–containing perovskites[129, 160-162]. The proposed magnetic model to account for the observation is a mixture of two magnetic phases, G–type and C–type, co–existing within the predominately glass–like crystallite. If these isolated local regions were allowed to have the same average occupancies of nickel deduced from Table 7.1, these islands would turn into ferrimagnets instead. Clearly this is inconsistent with the magnetometry data. On the other hand, these antiferromagnetic regions of $SrLa_2Ni_2TeO_9$ will be nickel–rich which will ensure the dominance of nearest–neighbour interactions. Meanwhile, there will be other tellurium–rich regions favouring next–nearest–neighbour interactions. Further experimental work will be necessary in order to establish the size of these regions, but the fact that the magnetic scattering persists above the temperature of the susceptibility maximum suggests that they are too large to be described as clusters. A similar model based on phase separation was previously proposed by Martin *et al.* to account for the behaviour of $Pr_{0.1}Sr_{0.9}MnO_3$[163]. The presence of antiferromagnetic regions at relatively high temperatures explains why the effective magnetic moment, 2.21 μ_B per Ni^{2+} cation, derived from the Curie–Weiss law is significantly lower than the spin–only value for Ni^{2+}, 2.83 μ_B. In comparable, perovskite–related compounds the effective magnetic moment is usually enhanced by a small second–order orbital contribution to a value in the range 3.0 – 3.7 μ_B[19–21]. The magnitude of the reduction seen in $SrLa_2Ni_2TeO_9$ is thus consistent with the

conclusion, drawn from the neutron diffraction data, that ~36(3) % of the sample is antiferromagnetic at 5 K.

However, the intensity of the magnetic scattering is so low that the proposed model may not be as definitive. A unique, non–collinear magnetic structure in which the *y* and *z* components of the atomic moments order in C–type and G–type patterns respectively can model the D1b data as well. In this case, again assuming an ordered moment of 2 μ_B per ordered cation, 25(2) % of the Ni^{2+} cations would be part of the long–range ordered structure. Another possibility is a structural model of $SrLa_2Ni_2TeO_9$ with higher occupancy of nickel at one of the octahedral sites as the experimental error in the occupancy of the current model is relatively high. Moreover, the additional Bragg scattering assigned as a C–type magnetic ordering could also be accounted for $\frac{\lambda}{2}$ scattering. Unfortunately, the monochromator of D1b has been changed since the neutron diffraction experiments were carried out. As a result, further investigation is prohibited. However, no $\frac{\lambda}{2}$ contamination of the beam on D1b has been reported previously. Given that the intensity of this Bragg peak was comparable with the magnetic scattering arising from NiO and the structural contribution from Sr_3TeO_6, the C–type magnetic ordering is believed to be genuine. Based on the composition variations described above, the two–phase magnetic model is more likely to give the correct interpretation of the data collected.

7.5 Conclusion

In contrast to $La_3Ni_2SbO_9$, $SrLa_2Ni_2TeO_9$ does not behave as a relaxor ferromagnet. The principal difference in the average structures deduced from NPD data is that the 1:1 cation ordering over the *B* and *B*' sites is imperfect in the latter compound. It is, however, necessary to consider the variations in microstructure between the two compounds when explaining the observed behaviour. By considering the length scale associated with the

cation disorder in each case, a plausible model has been developed. Yet, further investigation is required to validate this magnetic model.

The work has been published as *R. Paria Sena, J. Hadermann, C.–M. Chin, E. C. Hunter and P. D. Battle, Journal of Solid State Chemistry, 2016,* ***243****, 304-311*[164].

Chapter 8: A study of Ca$Ln_2Ni_2WO_9$ (Ln = La, Pr or Nd)

8.1 Introduction

All the perovskites discussed in the earlier chapters of this thesis have only possessed paramagnetic cations on the *B* site with the *A* site cations being diamagnetic. If the *A*, rather than the *B*, site contains the paramagnetic cation, long–range magnetic order can still occur. For example, the magnetic structures of Ni_2InSbO_6 and Ni_2ScSbO_6 are found to be helix–like[165]. The incommensurate magnetic structure of these double perovskites can be thought of as having alternating "magnetic planes" removed. A more complex magnetic structure can form if both the *A* and *B* sites of the perovskite contain paramagnetic *d*–block cations. In the *A*– and *B*–site–ordered perovskite $CaCu_3Fe_2Re_2O_{12}$, the coupling between the Cu^{2+} and Fe^{3+} moments was found to be ferromagnetic with the Re^{5+} cations being antiferromagnetically coupled[166]. The magnetic ordering temperature of the *A* and *B* site cations do not necessarily have to be the same despite the coexistence of paramagnetic cations on both sites. In the case of Mn_2FeReO_6[167, 168], for example, the six–coordinate Fe^{3+} and Re^{5+} cations order ferrimagnetically on cooling below 520 K but the Mn^{2+} sublattice orders at a poorly defined temperature somewhere in the range $70 < T/K < 250$. Unusual magnetic features have also been observed for perovskites with paramagnetic rare–earth cations present on the *A* site. For example, anomalies appear in the magnetic susceptibility of Na$Ln$$CoWO_6$ (Ln = Pr, Gd or Tb) due to magnetic Ln^{3+} cations being polarised by the magnetically ordered Co^{2+} sublattice[169] and negative magnetisation has been reported for $Ca_2PrCr_2NbO_9$ and $Ca_2PrCr_2TaO_9$[170]. In the latter case, in sufficiently low fields, the spins of the Pr^{3+} cations are polarised in a direction that is opposite to the net moment arising from the Cr^{3+} sublattice.

The work presented in this chapter is intended to elucidate the relative importance of the size and electron configuration of the *A* site cation in determining the magnetic properties of a triple perovskite. Ca*Ln*$_2$Ni$_2$WO$_9$ (*Ln* = La, Pr or Nd) was successfully synthesised and studied using XRPD, NPD and magnetometry. In the case of *Ln* = La, the composition was further studied using TEM. The La^{3+} cation in $CaLa_2Ni_2WO_9$ was replaced by paramagnetic Pr^{3+} or Nd^{3+} to introduce the possibility of magnetic coupling between the *A* and *B* sites.

8.2 Experimental

Polycrystalline samples of Ca*Ln*$_2$Ni$_2$WO$_9$ (*Ln* = La, Pr or Nd) were prepared using the traditional ceramic method. In the case of *Ln* = La, stoichiometric quantities of NiO, $CaCO_3$, WO_3 and pre–dried La_2O_3 were mixed and ground in an agate mortar and pestle. The mixture was first heated in air in powder form at 800 °C for 24 hours in order to allow the decomposition of the carbonate. The powder was then pelletised and heated at 1150 °C for 6 days. For the syntheses of $CaNd_2Ni_2WO_9$ and $CaPr_2Ni_2WO_9$, La_2O_3 was replaced by Nd_2O_3 and Pr_6O_{11}, respectively, and the high–temperature firing sequence was 1150 °C for 5 days, 1250 °C for 8 days and 1300 °C for 5 days. All pellets were ground and reformed after every heating cycle, which normally lasted for 48 – 72 hours.

XRPD patterns of the reaction products were collected using a PANalytical Empyrean diffractometer operating with Cu $K_{\alpha 1}$ radiation (λ = 1.54051 Å) at room temperature (RT) over the angular range of $15 \leq 2\theta/° \leq 125$ with a step–size $\Delta 2\theta$ of 0.0066°. NPD patterns were collected at various temperatures using the time–of–flight diffractometer GEM at ISIS, United Kingdom[89]. Data from the detector banks located at 2θ = 34.96 (bank 3), 63.62 (bank 4), 91.30 (bank 5) and 154.40° (bank 6) were analysed using the Rietveld method[92] as implemented in the GSAS program suite[94]. Data collected by bank 1 and bank

2 were deemed to be too noisy and hence were excluded from the Rietveld analysis. The background level and the sample dependent part of the peak shapes were modelled by a 12–term shifted Chebyshev function and a pseudo–Voigt function[123], respectively.

The SQUID magnetometer was used to characterise the magnetic properties of $CaLn_2Ni_2WO_9$. The magnetic susceptibilities of these perovskites were measured in both ZFC and FC conditions as a function of temperature. The samples were warmed through the temperature range $2 \leq T/\mathrm{K} \leq 300$ in the presence of a magnetic field of 100 Oe. For each sample, the field–dependence of the magnetisation per formula unit (f.u.) was measured over the range $-50 \leq H/\mathrm{kOe} \leq 50$ at temperatures that were selected after consideration of the temperature dependence of the magnetic susceptibilities. The ac susceptibility of each composition was measured over the temperature range $2 \leq T/\mathrm{K} \leq 100$ in a field of amplitude 3.5 Oe oscillating at frequencies of 1, 10 and 100 Hz.

$CaLa_2Ni_2WO_9$ was also studied by electron microscopy. Specimens were prepared by dispersing crushed powder in ethanol and depositing a few drops of this solution on a copper grid covered with a holey carbon film. SAED patterns were taken with a Philips CM20 transmission electron microscope. High angle annular dark field stem (HAADF–STEM) images and energy dispersive X–ray (EDX) maps were acquired with a FEI Titan 80–300 “cubed” microscope equipped with a Super–X detector and operated at 300 kV.

8.3 Results

Preliminary XRPD analysis of the dark–green reaction products showed that they all consist of a monoclinic, perovskite–like phase with a small trace of unreacted NiO (at most 0.2(4) wt. %). The Bragg reflections arising from the principal perovskite phase could be successfully indexed in the space group $P2_1/n$ with $a \sim b \sim \sqrt{2}a_p$, $c \sim 2a_p$ and $\beta \sim 90°$, where a_p is the cell parameter of a primitive cubic perovskite. The splitting of the

diffraction maxima that is a signature of non–cubic symmetry was more obvious when *Ln* = Pr or Nd, see Figure S8.1. For all *Ln*, the partial ordering of the Ni^{2+} and W^{6+} cations over the two crystallographically–distinct octahedral sites was revealed by Rietveld analysis. In contrast, there was no evidence to suggest the presence of ordering among the calcium and lanthanide cations that occupy the *A* site.

Figure 8.1 shows the temperature dependence of the dc molar magnetic susceptibility of each composition. In the case of $CaLa_2Ni_2WO_9$, the ZFC and FC susceptibilities overlie above 32 K, the temperature at which a magnetic transition occurs. The latter remains essentially constant below this temperature whereas the ZFC susceptibility decreases. The same general behaviour of $\chi_{ZFC}(T)$ was observed in $CaPr_2Ni_2WO_9$, but the FC susceptibility continues to increase on cooling below the temperature of the maximum in χ_{ZFC}. Both the ZFC and the FC susceptibilities of $CaNd_2Ni_2WO_9$ have a negative temperature gradient throughout the measured range, although they differ slightly below 30 K. The temperature dependence of the reciprocal susceptibility of each composition is also included in Figure 8.1. The Curie–Weiss Law was used to fit the data collected in the temperature range $200 \leq T/K \leq 300$; the resulting values of the molar Curie constant, C_m, and the Weiss temperature, θ_W, are listed in Table 8.1. In order to calculate the effective magnetic moment, μ_{eff}, for the Ni^{2+} cations in each sample, some assumptions were made. Firstly, it was assumed the C_m is simply the sum of the contribution of the Ln^{3+} and Ni^{2+} cations. Assuming the former can be calculated by the Landé formula, the effective magnetic moments of Pr^{3+} and Nd^{3+} cations are 3.58 and 3.62 μ_B respectively. Given that the concentration of the NiO impurity was so small, it was also assumed the antiferromagnetic NiO does not have a significant effect on the bulk magnetic behaviour of the samples. Hysteresis was detected in $M(H)$ for all three compositions at 5 K, see Figure 8.2, and the magnetisation per f.u. increases with the number of unpaired electron present

in the Ln^{3+} cation. The remanent magnetisation, M_R, and the coercive field, H_C, as well as the transition temperature, T_f, of $CaLn_2Ni_2WO_9$ are included in Table 8.1. The field dependence of the magnetisation of each compound at a selection of temperatures is illustrated in Figure S8.2. In each case $M(H)$ was found to be a linear function above 150 K. An additional $M(H)$ dataset was collected at 20 K for $CaPr_2Ni_2WO_9$ due to the slight change in gradient of $\chi(T)$ around this particular temperature. The ac susceptibility of each compound, see Figure 8.3, is frequency dependent and has both real and imaginary components below approximately 30 K. The ratio $\Delta T_f/[T_f\Delta(\log\,\omega)]$[118] was found to be 0.047, 0.034 and 0.017 for $CaLa_2Ni_2WO_9$, $CaPr_2Ni_2WO_9$ and $CaNd_2Ni_2WO_9$ respectively.

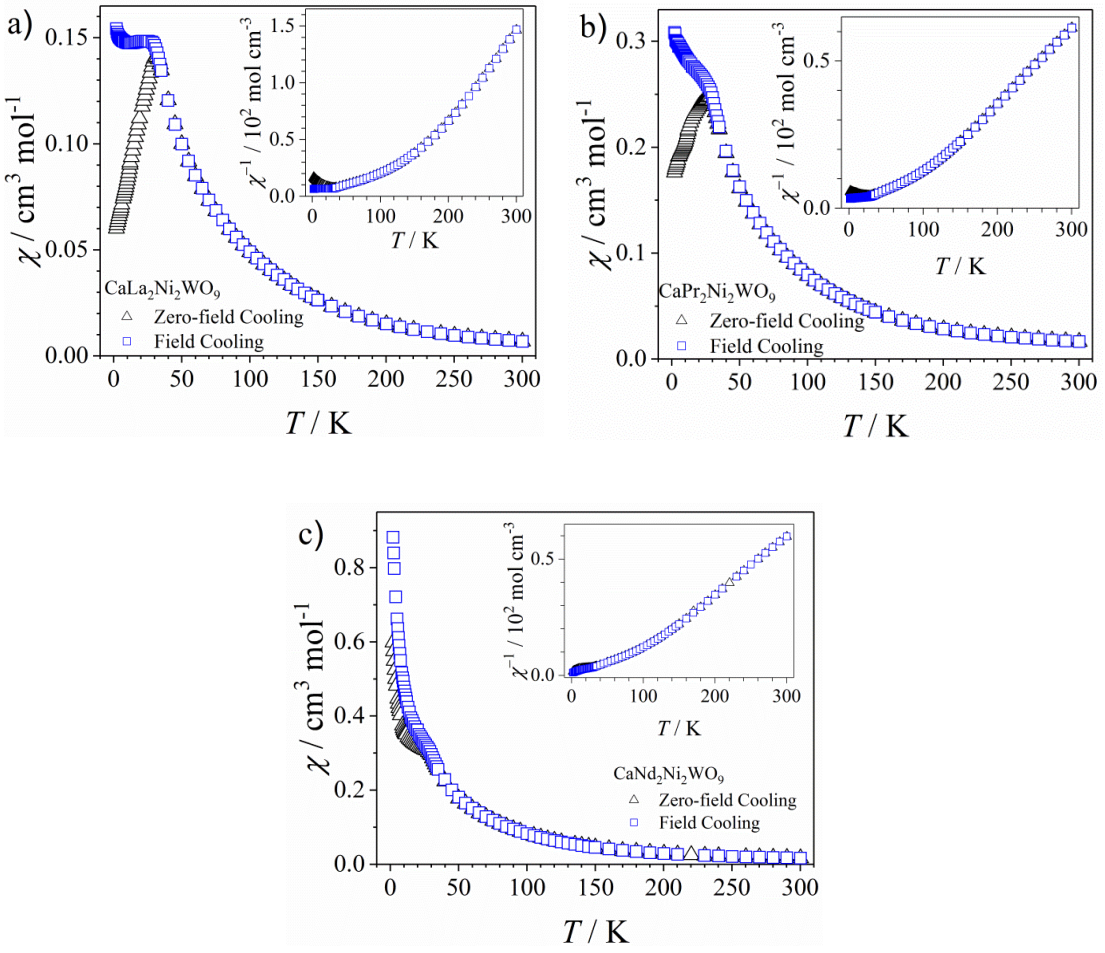


Figure 8.1. Temperature dependence of the molar susceptibility and (inset) inverse susceptibility of (a) $CaLa_2Ni_2WO_9$, (b) $CaPr_2Ni_2WO_9$ and (c) $CaNd_2Ni_2WO_9$.

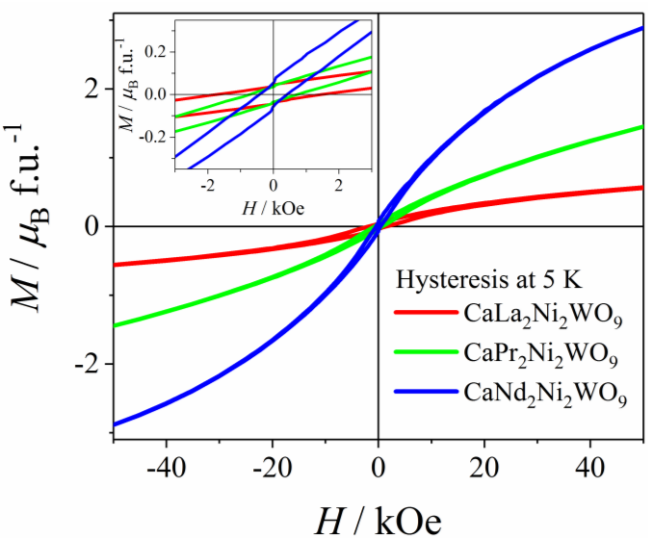


Figure 8.2. Field dependence of the magnetisation per formula unit of $CaLa_2Ni_2WO_9$ (red), $CaPr_2Ni_2WO_9$ (green) and $CaNd_2Ni_2WO_9$ (blue) at 5 K. The inset shows the function for $-3 \leq H/\text{kOe} \leq 3$.

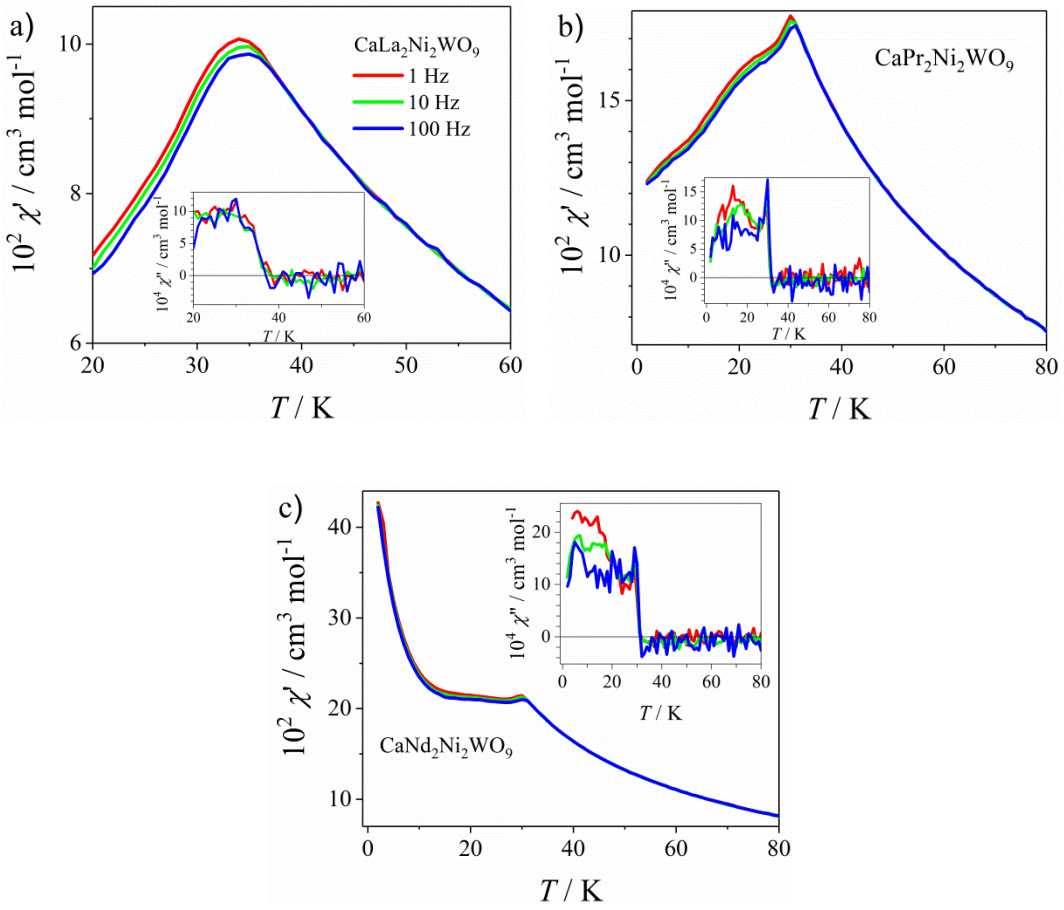
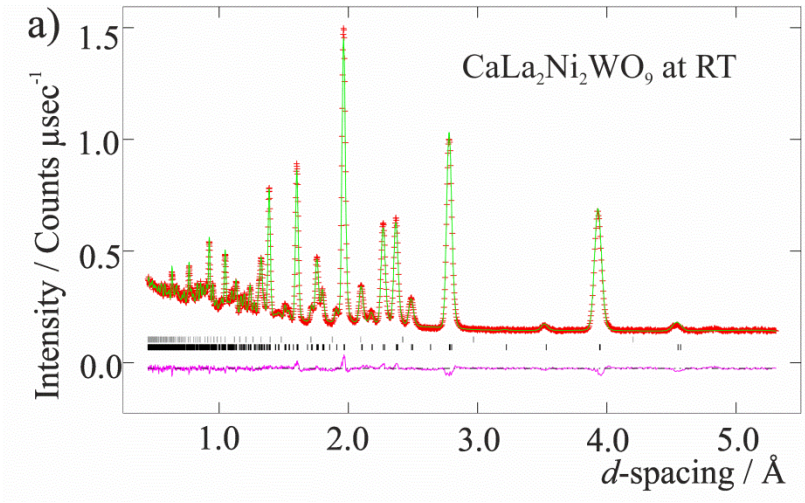


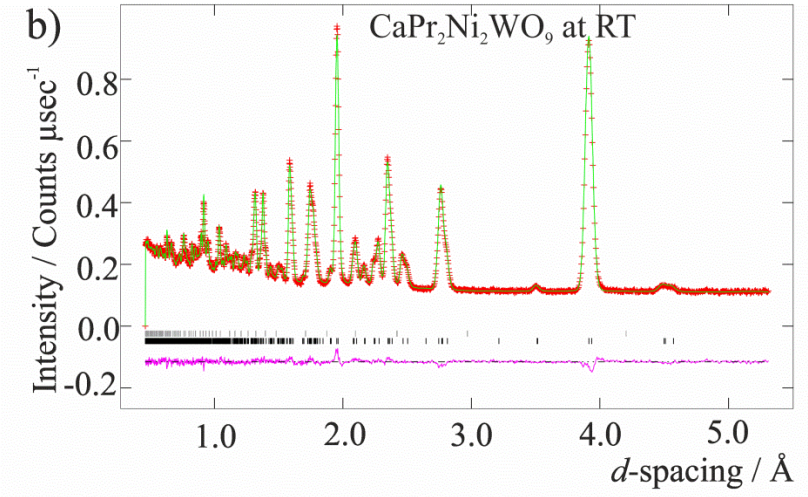
Figure 8.3. Temperature and frequency dependence of the real and imaginary components of the ac susceptibility of (a) $CaLa_2Ni_2WO_9$, (b) $CaPr_2Ni_2WO_9$ and (c) $CaNd_2Ni_2WO_9$ collected at 1 (red), 10 (green) and 100 (blue) Hz.

Table 8.1. Magnetic parameters of $CaLn_2Ni_2WO_9$ (*Ln* = La, Pr or Nd).

Composition	C_m	$\mu_{eff(Ni)}/\mu_B$	θ_W/K	M_R/μ_B	H_C/kOe	T_f/K	$\frac{\Delta T_f}{T_f \Delta(\log \omega)}$
$CaLa_2Ni_2WO_9$	1.242(9)	2.23(2)	+119(3)	0.04	1.5	32	0.047
$CaPr_2Ni_2WO_9$	3.891(2)	1.66(1)	+61(2)	0.036	0.75	29	0.034
$CaNd_2Ni_2WO_9$	3.968(2)	1.71(1)	+63(2)	0.05	0.4	30	0.017

The monoclinic $P2_1/n$ structure deduced from XRPD analysis provides a good fit to the NPD data collected from all three solids at room temperature using GEM; no more than ~0.40(1) wt. % of unreacted NiO was found in any sample. Figures 8.4 and 8.5 illustrate the observed and calculated patterns from bank 3 at room temperature and 5 K, respectively. The fitted patterns for banks 4 – 6 are shown in Figures S8.3 – S8.8. The structural parameters, together with some selected bond distances and bond angles, derived from these data are listed in Tables 8.2 – 8.6. The distribution of the cations over the two crystallographically–distinct six–coordinate sites was allowed to vary, with the Ni:W ratio being constrained to be 2:1, during the analysis of the data collected at room temperature. The 2*c* site of $CaPr_2Ni_2WO_9$ was found to be occupied solely by Ni^{2+} whereas a small percentage of the hexavalent tungsten cations are present on this octahedral site when *Ln* = La or Nd. The Ni/W occupancies were not refined further during the Rietveld analysis of the NPD datasets collected at 5 K. No additional Bragg scattering was observed in any of latter datasets, indicating none of the samples undergoes a structural phase transition or shows long–range magnetic ordering below the corresponding magnetic transition temperatures. An extra data set was collected at 20 K for $CaNd_2Ni_2WO_9$; the fitted pattern is presented in Figure S8.9 whereas the corresponding structural parameters and selected bond lengths and angles are shown in Table S8.1 and S8.2.





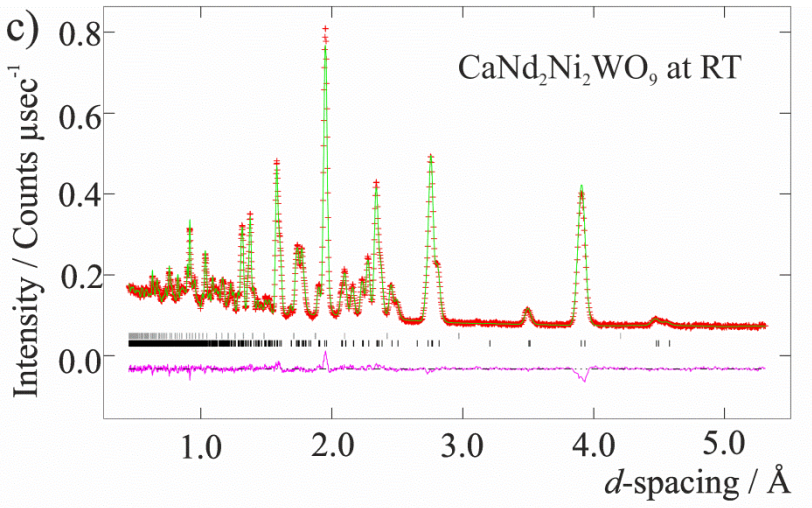


Figure 8.4. Observed (red crosses) and calculated (green line) NPD profiles for (a) $CaLa_2Ni_2WO_9$, (b) $CaPr_2Ni_2WO_9$ and (c) $CaNd_2Ni_2WO_9$ at room temperature. A difference curve (purple) is shown below. Reflection positions are marked for NiO (cyan) and the principal phase (black).

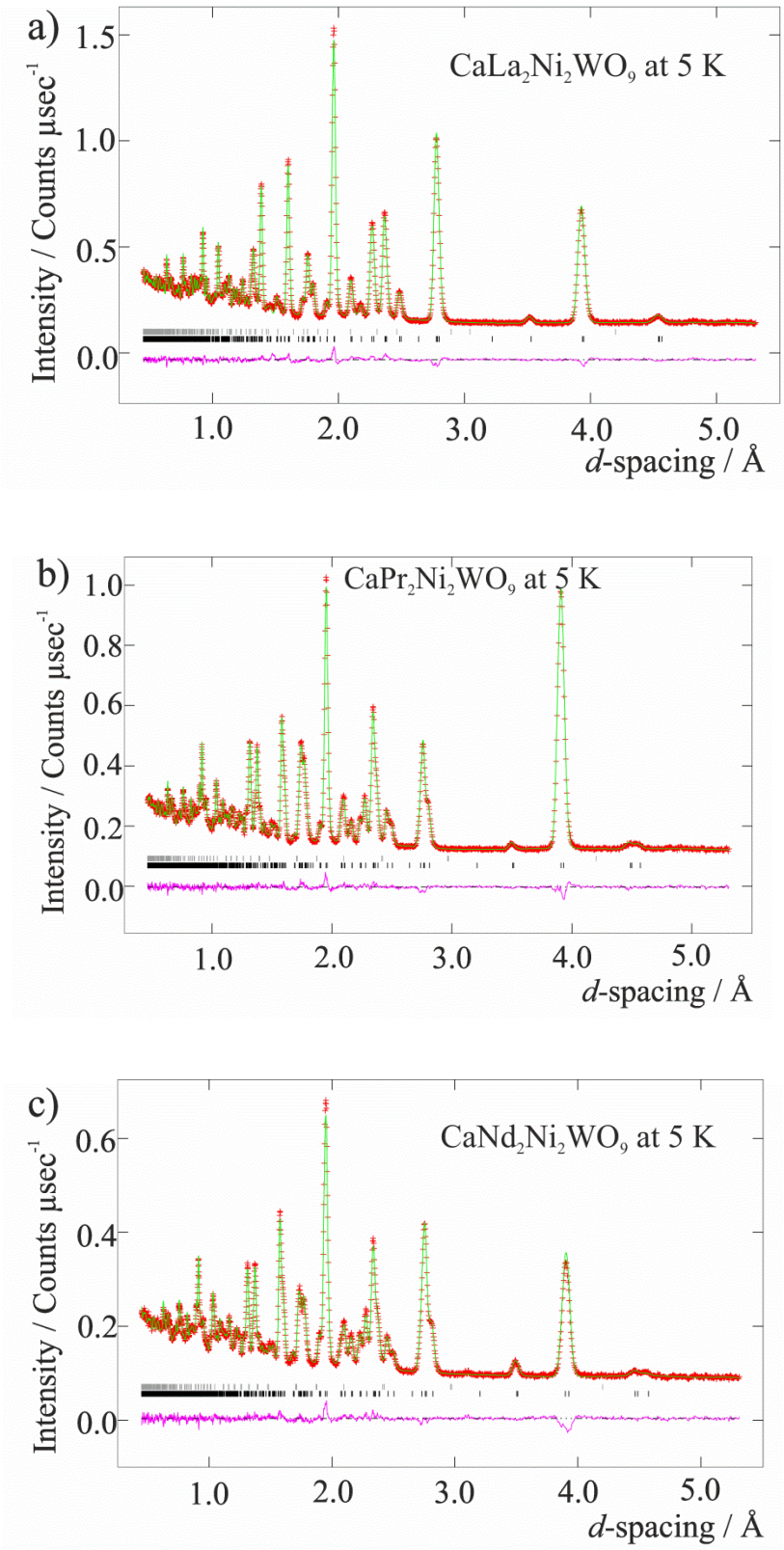


Figure 8.5. Observed (red crosses) and calculated (green line) NPD profiles for (a) $CaLa_2Ni_2WO_9$, (b) $CaPr_2Ni_2WO_9$ and (c) $CaNd_2Ni_2WO_9$ at 5 K. A difference curve (purple) is shown below. Reflection positions are marked for NiO (cyan) and the principal phase (black).

Table 8.2. Structural parameters of $CaLa_2Ni_2WO_9$ at RT and 5 K (Space group $P2_1/n$).

		RT	5 K
a / Å		5.5320(4)	5.5231(9)
b / Å		5.5697(4)	5.5671(9)
c / Å		7.8379(6)	7.8269(12)
β / °		90.01(1)	89.98(1)
V / Å^3		241.50(5)	240.66(11)
$R_{wp\|NPD}$ / %		2.67	3.20
χ^2		3.218	4.634
Ca/La	x	0.4887(3)	0.4870(3)
4*e* (*x y z*)	y	0.4635(2)	0.4619(2)
	z	0.2506(7)	0.2511(8)
	U_{ISO} / Å^2	0.0188(2)	0.0146(2)
	Ca occupancy	0.3333	0.3333
	La occupancy	0.6667	0.6667
Ni/W1	U_{ISO} / Å^2	0.0037(3)	0.0025(3)
2*c* (0 ½ 0)	Ni occupancy	0.965(5)	0.965
	W occupancy	0.035(5)	0.035
	U_{ISO} / Å^2	0.0042(4)	0.0015(4)
Ni/W2	Ni occupancy	0.368(5)	0.368
2*d* (½ 0 0)	W occupancy	0.632(5)	0.632
O1	x	0.7835(6)	0.7819(6)
4*e* (*x y z*)	y	0.7913(7)	0.7934(8)
	z	–0.0438(4)	–0.0352(4)
	U_{ISO} / Å^2	0.0103(8)	0.0078(7)
O2	x	0.7033(6)	0.7004(6)
4*e* (*x y z*)	y	0.2868(7)	0.2869(8)
	z	–0.0326(4)	–0.0426(4)
	U_{ISO} / Å^2	0.0082(8)	0.0059(7)
O3	x	0.5777(3)	0.5780(3)
4*e* (*x y z*)	y	0.0157(2)	0.0159(2)
	z	0.2435(7)	0.2448(9)
	U_{ISO} / Å^2	0.0095(4)	0.0061(4)

Table 8.3. Structural parameters of $CaPr_2Ni_2WO_9$ at RT and 5 K (Space group $P2_1/n$).

		RT	5 K
a / Å		5.4681(3)	5.4537(3)
b / Å		5.5989(3)	5.6011(3)
c / Å		7.7800(4)	7.7651(4)
β / °		90.142(2)	90.174(2)
V / Å^3		238.18(4)	237.20(4)
$R_{wp\|NPD}$ / %		2.46	2.49
χ^2		2.251	2.505
Ca/Pr	x	0.4892(3)	0.4888(3)
4*e* (*x y z*)	y	0.4510(2)	0.4484(1)
	z	0.2521(5)	0.2518(4)
	U_{ISO} / Å^2	0.0203(2)	0.0155(2)
	Ca occupancy	0.3333	0.3333
	Pr occupancy	0.6667	0.6667
Ni/W1	U_{ISO} / Å^2	0.0029(2)	0.0013(2)
2*c* (0 ½ 0)	Ni occupancy	1	1
	W occupancy	0	0
	U_{ISO} / Å^2	0.0036(3)	0.0014(2)
Ni/W2	Ni occupancy	0.3333	0.3333
2*d* (½ 0 0)	W occupancy	0.6667	0.6667
O1	x	0.7903(3)	0.7904(2)
4*e* (*x y z*)	y	0.8027(3)	0.8039(3)
	z	–0.0408(2)	–0.0419(2)
	U_{ISO} / Å^2	0.0077(4)	0.0046(3)
O2	x	0.6945(3)	0.6936(2)
4*e* (*x y z*)	y	0.2896(3)	0.2884(2)
	z	–0.0463(2)	–0.0467(2)
	U_{ISO} / Å^2	0.0073(4)	0.0044(3)
O3	x	0.5842(1)	0.5854(1)
4*e* (*x y z*)	y	0.0235(1)	0.0238(1)
	z	0.2446(2)	0.2441(2)
	U_{ISO} / Å^2	0.0074(2)	0.0043(2)

Table 8.4. Structural parameters of $CaNd_2Ni_2WO_9$ at RT and 5 K (Space group $P2_1/n$).

		RT	5 K
a / Å		5.4441(6)	5.4304(8)
b / Å		5.6097(6)	5.6131(8)
c / Å		7.7597(9)	7.7461(11)
β / °		90.184(2)	90.229(2)
V / Å^3		236.98(8)	236.11(10)
$R_{wp}\|_{NPD}$ / %		2.66	2.92
χ^2		2.253	2.630
Ca/Nd	x	0.4880(2)	0.4882(2)
4*e* (*x y z*)	y	0.4466(1)	0.4446(1)
	z	0.2530(4)	0.2530(4)
	U_{ISO} / Å^2	0.0162(2)	0.0113(2)
	Ca occupancy	0.3333	0.3333
	Nd occupancy	0.6667	0.6667
Ni/W1	U_{ISO} / Å^2	0.0031(1)	0.0007(3)
2*c* (0 ½ 0)	Ni occupancy	0.971(6)	0.971
	W occupancy	0.029(6)	0.029
	U_{ISO} / Å^2	0.0043(5)	0.0012(4)
Ni/W2	Ni occupancy	0.362(6)	0.362
2*d* (½ 0 0)	W occupancy	0.638(6)	0.638
O1	x	0.7922(3)	0.7922(3)
4*e* (*x y z*)	y	0.8046(3)	0.8056(3)
	z	–0.0424(2)	–0.0432(2)
	U_{ISO} / Å^2	0.0071(4)	0.0035(3)
O2	x	0.6924(3)	0.6907(3)
4*e* (*x y z*)	y	0.2903(3)	0.2903(3)
	z	–0.0481(3)	–0.0484(2)
	U_{ISO} / Å^2	0.0074(4)	0.0028(3)
O3	x	0.5874(2)	0.5878(2)
4*e* (*x y z*)	y	0.0253(2)	0.0256(2)
	z	0.2445(3)	0.2437(3)
	U_{ISO} / Å^2	0.0070(2)	0.0027(2)

Table 8.5. Selected bond lengths (Å) and angles (°) in Ca*Ln*$_2$Ni$_2$WO$_9$ (*Ln* = La/Pr/Nd) at RT.

	$CaLa_2Ni_2WO_9$	$CaPr_2Ni_2WO_9$	$CaNd_2Ni_2WO_9$
Ca/*Ln*–O1	2.791(6)	2.679(4)	2.663(3)
Ca/*Ln*–O1	2.628(5)	2.653(3)	2.639(3)
Ca/*Ln*–O1	2.398(5)	2.385(3)	2.370(3)
Ca/*Ln*–O2	2.703(6)	2.735(4)	2.735(3)
Ca/*Ln*–O2	2.445(5)	2.382(3)	2.379(3)
Ca/*Ln*–O2	2.707(5)	2.624(3)	2.599(3)
Ca/*Ln*–O3	2.543(1)	2.450(1)	2.425(1)
Ca/*Ln*–O3	2.417(3)	2.368(2)	2.353(2)
2*c*–O1	2.046(4)×2	2.070(2)×2	2.075(2)×2
2*c*–O2	2.042(3)×2	2.075(1)×2	2.079(2)×2
2*c*–O3	2.057(5)×2	2.045(2)×2	2.046(2)×2
2*d*–O1	1.982(3)×2	1.960(1)×2	1.960(2)×2
2*d*–O2	1.970(4)×2	1.973(2)×2	1.973(2)×2
2*d*–O3	1.959(5)×2	1.961(2)×2	1.959(2)×2
O1–2*c*–O2	88.3(2)×2	89.6(1)×2	89.9(1)×2
O1–2*c*–O3	89.6(1)×2	88.3(1)×2	88.2(1)×2
O2–2*c*–O3	88.8(1)×2	88.7(1)×2	88.7(1)×2
O1–2*d*–O2	89.9(2)×2	89.8(1)×2	89.9(1)×2
O1–2*d*–O3	88.8(1)×2	89.6(1)×2	89.5(1)×2
O2–2*d*–O3	88.0(1)×2	89.8(1)×2	89.8(1)×2
2*c*–O1–2*d*	154.1(2)	152.2(1)	151.2(1)
2*c*–O2–2*d*	156.1(2)	150.4(1)	149.4(1)
2*c*–O3–2*d*	154.8(1)	152.33(4)	151.3(1)

Table 8.6. Selected bond lengths (Å) and angles (°) in Ca*Ln*$_2$Ni$_2$WO$_9$ (*Ln* = La/Pr/Nd) at 5 K.

	$CaLa_2Ni_2WO_9$	$CaPr_2Ni_2WO_9$	$CaNd_2Ni_2WO_9$
Ca/*Ln*–O1	2.730(6)	2.677(3)	2.657(3)
Ca/*Ln*–O1	2.661(6)	2.638(3)	2.629(3)
Ca/*Ln*–O1	2.436(6)	2.382(3)	2.367(3)
Ca/*Ln*–O2	2.761(7)	2.727(3)	2.726(3)
Ca/*Ln*–O2	2.386(6)	2.385(3)	2.379(3)
Ca/*Ln*–O2	2.651(6)	2.610(3)	2.595(3)
Ca/*Ln*–O3	2.534(2)	2.436(1)	2.415(1)
Ca/*Ln*–O3	2.422(3)	2.361(2)	2.347(2)
2*c*–O1	2.048(4)×2	2.076(1)×2	2.080(2)×2
2*c*–O2	2.064(3)×2	2.080(1)×2	2.084(1)×2
2*c*–O3	2.045(7)×2	2.047(2)×2	2.049(2)×2
2*d*–O1	1.955(4)×2	1.956(1)×2	1.956(2)×2
2*d*–O2	1.971(4)×2	1.964(1)×2	1.968(2)×2
2*d*–O3	1.966(7)×2	1.955(2)×2	1.951(2)×2
O1–2*c*–O2	88.0(2)×2	89.9(1)×2	90.0(1)×2
O1–2*c*–O3	88.5(1)×2	88.4(1)×2	88.3(1)×2
O2–2*c*–O3	89.2(1)×2	88.8(1)×2	88.7(1)×2
O1–2*d*–O2	89.7(2)×2	89.7(1)×2	89.9(1)×2
O1–2*d*–O3	89.4(1)×2	89.5(1)×2	89.4(1)×2
O2–2*d*–O3	89.7(1)×2	89.8(1)×2	89.8(1)×2
2*c*–O1–2*d*	156.7(2)	151.7(1)	150.8(1)
2*c*–O2–2*d*	152.7(2)	150.3(1)	149.1(1)
2*c*–O3–2*d*	154.7(1)	151.96(4)	151.2(1)

Selected area electron diffraction (SAED) patterns, including several tilt series, were taken from many different crystals of $CaLa_2Ni_2WO_9$. All the patterns could be indexed using the cell parameters obtained from Rietveld analysis of the XRPD data. Figure 8.6 shows representative SAED patterns from the main zone axes ([100], [010], [001] and [110]). They are in agreement with the reflection conditions for $P2_1/n$: [010] shows clearly that $h0l$: $h+l = 2n$, $h00$: $h = 2n$ and $00l$: $l = 2n$. The presence on some of the other patterns of $h00$: $h = 2n+1$ and $00l$: $l = 2n+1$ reflections, which should be absent in $P2_1/n$, is attributable to double diffraction. The presence of the $0k0$: $k = 2n+1$ reflections is also due to double diffraction, as was verified by tilting around the b^*–axis until these reflections disappeared.

It is noticeable that calculated electron diffraction patterns along [010] and [111] are indistinguishable for this structure in space group $P2_1/n$ (in the parent perovskite they are symmetry equivalent $<110>_p$). It is thus possible to index [111] incorrectly as [010]. However, no other patterns corresponding to $<110>_p$ were found in the sample except the two labelled as [100] and [010] in Figure 8.6. Figure 8.7 shows high resolution HAADF–STEM images taken along two main zones. On both the [100] and the [010] image a clear alternation in brightness is seen in the rows containing the *B* cations, *i.e.* the alternation between columns containing W and no W (W has atomic number $Z = 74$ and thus gives the very bright dots on the image). This is in agreement with the chess board order of the *B* cations found in the $P2_1/n$ model. Figure 8.8 shows the composition of each column viewed along [010] as obtained by high resolution STEM–EDX imaging. Ca and La are seen to be disordered. However, W occupies just one of the two *B* columns along this projection whereas Ni occupies both, but with a higher concentration in the W–free column; oxygen cannot be reliably mapped due to its low atomic number.

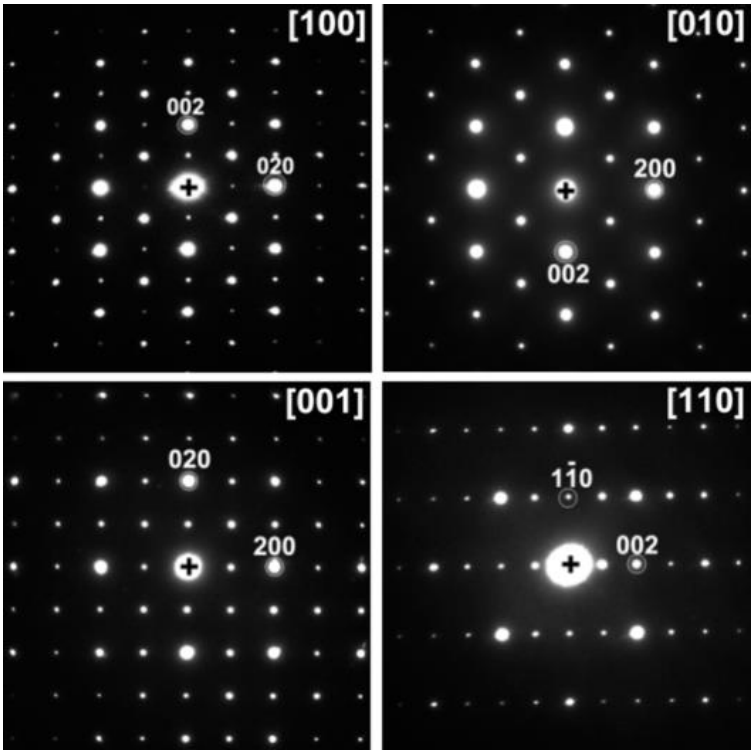


Figure 8.6. Representative selected-area electron-diffraction patterns of $CaLa_2Ni_2WO_9$.

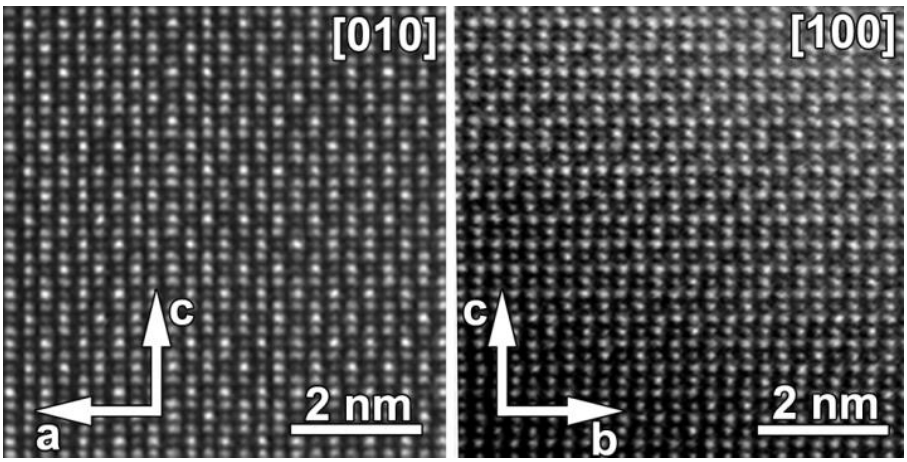


Figure 8.7. High-resolution HAADF STEM image along the [100] and [010] zone axes of $CaLa_2Ni_2WO_9$.The images were corrected for drift and a low band pass filter was applied.

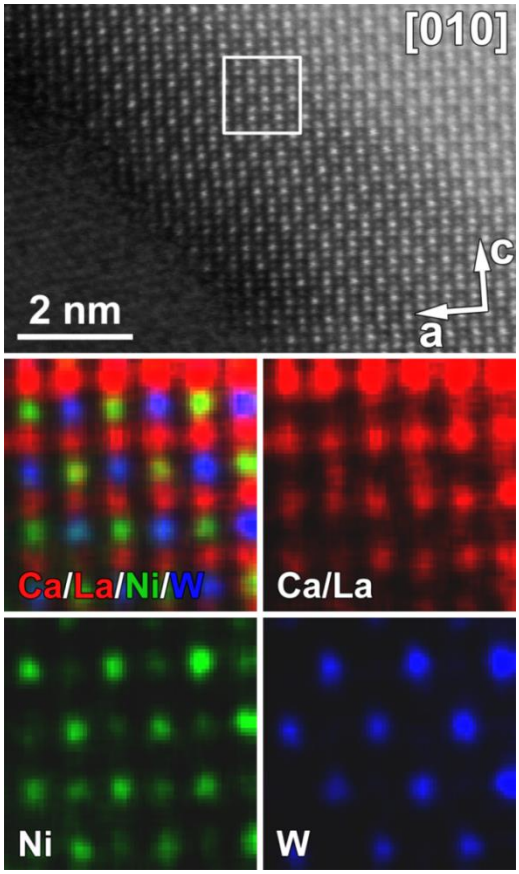


Figure 8.8. High resolution EDX map of the [010] zone. The HAADF-STEM image of the surrounding area is shown at the top, the exact area taken for the EDX map shown below is indicated by a white rectangle.

8.4 Discussion

Across the lanthanide series, the size of the Ln^{3+} cation understandably shrinks as the number of protons increases. As a consequence, it is not surprising to note that the unit cell parameters of $CaLn_2Ni_2WO_9$ decrease at both room temperature and 5 K with increasing atomic number of *Ln*. To accommodate the smaller size of two–thirds of the *A* site cations, distortions away from the ideal cubic symmetry are observed for these compositions. The coordination number of the Ca/*Ln* site is hence reduced from twelve to eight, see Tables 8.5 and 8.6. The decrease in the mean Ca/*Ln*–O bond length between $CaLa_2Ni_2WO_9$ and $CaPr_2Ni_2WO_9$ is more pronounced than the change observed when Pr^{3+} is replaced by Nd^{3+}. Regarding the *B*–site ordering, the distribution of Ni/W seems to randomly vary with

the identities of the Ln^{3+} cations. A bigger sample pool could potentially provide an insight on what factors do cause the variation. Nevertheless, the degree of ordering is always higher than was observed in $SrLa_2Ni_2TeO_9$[164]. As a result, the Ni/W–O bond lengths around the Ni–rich 2*c* site are always longer than those around the W–rich 2*d* site. A pseudo–tetragonal distortion seems to have taken place in both $CaPr_2Ni_2WO_9$ and $CaNd_2Ni_2WO_9$ as the octahedron surrounding the site dominated by the d^0 W^{6+} cation contains two very similar, relatively short 2*d*–O distances and one longer distance. However, this effect is not apparent in the less–precise bond lengths tabulated for *Ln* = La. As the 2*c*–O–2*d* bond angles deviate further from 180° as the ionic radius of *Ln* decreases, the strength of the magnetic superexchange interactions are expected to vary as a function of the Ln^{3+} cation. The study of $CaLa_2Ni_2WO_9$ by electron microscopy did not reveal any anomalies in the microstructure of the compound; the local structure is therefore not similar to that of $La_3Ni_2SbO_9$[48]. The HAADF–STEM and EDX images, see Figures 8.7 and 8.8, show that the crystal selected for detailed study had very well–developed cation ordering over the *B* sites, with W^{6+} only present on one crystallographic site in the chosen region. Due to the signal from Ca being very noisy, the apparent occurrence of some La^{3+}/Ca^{2+} cations on the six–coordinate sites is an artifact. The maps are shown in counts instead of atomic percent for clarity, even though this unfortunately also increases the visibility of the noise related to the Ca map.

There is no indication of long–range magnetic order in any of the compounds from the NPD patterns collected at 5 K as no magnetic Bragg scattering was found. This indirectly verifies one of the assumptions made above when calculating the values of μ_{eff} of Ni^{2+} in the $CaLn_2Ni_2WO_9$; neither the paramagnetic Pr^{3+} or Nd^{3+} couple magnetically with the Ni^{2+} cations. This is not entirely surprising, given that Ln^{3+} has more contracted 4*f* orbitals which have a reduced overlap with the surrounding ions. While the other assumptions

cannot truly be proven, the values of μ_{eff} of Ni^{2+} in $CaLn_2Ni_2WO_9$ derived by fitting the inverse susceptibilities to the Curie–Weiss law, see Table 8.1, are all below the spin–only value. It seems that there are significant short–range antiferromagnetic interactions between nearest–neighbour Ni^{2+} cations that reduce μ_{eff} above 200 K. However, the imbalance in the member of spin–up and spin–down Ni^{2+} cations, which originates from the difference in occupancies of the two octahedral sites, results in a positive θ_W and leads to the presence of uncoupled ferrimagnetic regions. The behaviour of $\chi(T)$ below 50 K, see Figure 8.1, and the hysteresis seen in $M(H)$, see Figure 8.2, suggest the formation of spin–glass phases at low temperature. Nevertheless, presumably because of the differing magnetic properties of Ln^{3+}, all three compounds described in this chapter behave differently; they all have a similar magnetic transition temperature of approximately 30 K but the spins are frozen in different ways. In the case of $CaLa_2Ni_2WO_9$, the FC curve stays constant below 32 K, a temperature which the ZFC reaches a maximum, indicating a canonical behaviour for a spin glass and the spins of the Ni^{2+} cations freeze at 32 K. However, further experiments have to be performed to provide an explanation for the change in the FC susceptibility close to the low–temperature limit of the instrument used. The FC susceptibility of $CaPr_2Ni_2WO_9$ has a negative temperature gradient below 29 K but the ZFC susceptibility decreases with decreasing temperature below the transition temperature. This suggests that both the Ni^{2+} and the Pr^{3+} cations freeze at 29 K. The behaviour of the FC susceptibility below T_f can be ascribed to the presence of entropic clusters[171]. Last but not least, a transition at 30 K in $\chi(T)$ for $CaNd_2Ni_2WO_9$ can clearly be seen, even if both the ZFC and the FC curves shows a negative gradient down to 2 K. The presence of a paramagnetic component in the ZFC curve suggests the Nd^{3+} cations, in contrast to the Ni^{2+} cations, are not frozen throughout the measured temperature range. These conclusions drawn from the dc magnetometry data are consistent with the ac data

shown in Figure 8.3. It is surprising that the magnetic behaviour of the compounds containing Pr^{3+} and Nd^{3+} are markedly different from each other[172]. The answer might lie in the anisotropy difference between the two cations. Further work is required to study the dynamic behaviour of the spins on the paramagnetic cations.

8.5 Conclusion

Long–range magnetic ordering over the *A* and/or *B* site is absent in $CaLn_2Ni_2WO_9$ (*Ln* = La, Pr or Nd). The magnetic transition temperature varies little with the identity of the Ln^{3+} cation. However, the paramagnetic Pr^{3+} and Nd^{3+} cations apparently behave differently when the corresponding perovskites are cooled to 2 K; the Nd^{3+} cations remain paramagnetic whereas the Pr^{3+} cations freeze with the Ni^{2+} on cooling below 30 K. The reason for the difference remains unknown and further studies are required.

With the exception of the ac magnetometry data, the work described in this chapter has been published as *C.-M. Chin, R. Paria Sena, E. C. Hunter, J. Hadermann and P. D. Battle, Journal of Solid State Chemistry, 2017,* ***251****, 224-232*[173].

Chapter 9: Conclusion

The model proposed by Battle *et al.* to explain the relaxor ferromagnetism of $La_3Ni_2SbO_9$ relied on there being a non–random distribution of Ni^{2+} and Sb^{5+} cations over one of the six–coordinate sites in the crystal structure. The experiments described in Chapter 3 show that the tendency of Sb^{5+} cations to avoid occupying next–nearest–neighbouring sites introduces short–range structural correlations and thus provide support for this model. The analysis has shown that the local cation ordering has a correlation length of ~15 Å and that it is accompanied by short–range magnetic ordering with a correlation length of ~9 Å.

A number of chemical substitutions into $La_3Ni_2SbO_9$ template have been made as part of a systematic investigation of relaxor ferromagnetism. The work described in Chapter 4 showed that the magnetic properties of $La_3Ni_2TaO_9$ are similar to those of $La_3Ni_2SbO_9$, whereas those of $La_3Ni_2NbO_9$ are very different, despite Ta^{5+} and Nb^{5+} both being the pentavalent d^0 cations. In fact $La_3Ni_2TaO_9$ was found to be a better example of a relaxor ferromagnet than the antimony–counterpart while $La_3Ni_2NbO_9$ behaves as a spin glass at low temperatures. Electron microscopy and neutron diffraction initially suggested that the difference in behaviour might be due to differences in particle size but a more extensive study of the system $La_3Ni_2Sb_xTa_yNb_{1-x-y}O_9$, see Chapter 5, showed that the difference in energy of the outer *d* orbitals of the pentavalent cations was more likely to be responsible for the observed magnetic behaviour.

Rietveld analysis on the neutron powder diffraction patterns shown in Chapter 6 showed that replacing 12.5 % of Ni^{2+} cations with Jahn–Teller–active Cu^{2+} cations did not result in any observable distortion of the BO_6 octahedra in the average structure of $La_3Ni_{1.75}Cu_{0.25}B'O_9$ when B' = Sb, Ta or Nb. Apart from the β angle being more obtuse, no significant structural change, on either a micro– or macroscopic scale, was detectable.

Nevertheless, the introduction of Cu^{2+} stabilized the magnetic ordering at relatively high temperatures. Perhaps the most surprising feature was the observation of long–range magnetic ordering in $La_3Ni_{1.75}Cu_{0.25}NbO_9$ because the introduction of 12.5 % Cu^{2+} is sufficient to induce ordering in a spin glass.

Surprisingly, given the increase in the charge difference between the cations involved, the high level of cation ordering found in $La_3Ni_2SbO_9$ is not conserved in $SrLa_2Ni_2TeO_9$ which, on the basis of the magnetometry study, was classified as a spin glass below 35 K. However, neutron powder diffraction data revealed weak magnetic Bragg scattering below and above T_f, indicating the coexistence of two magnetic phases (G– and C–type) as well as the spin–glass phase. Electron microscopy revealed a high degree of twinning in the $SrLa_2Ni_2TeO_9$ crystallites studied and the observed magnetic behaviour is proposed to stem from the complexity of the microstructure of $SrLa_2Ni_2TeO_9$.

Cation ordering was restored when Te^{6+} was replaced by d^0 W^{6+} in $CaLn_2Ni_2WO_9$ where *Ln* = La, Pr or Nd and no local structural irregularity was detected by TEM. In each case, irrespective of the Ln^{3+} cation, the absence of observable magnetic Bragg scattering shows that the spins of the Ni^{2+} cations freeze to form a spin glass at low temperatures. However, the temperature dependence of the susceptibility depends on the identity of the Ln^{3+} cation because the moments of the paramagnetic Pr^{3+} and Nd^{3+} cations freeze in a dissimilar fashion below the magnetic transition temperature.

The work described in this thesis thus demonstrates that the magnetic properties of these perovskite–related oxides are determined by the electronic structure of the cations involved, including any diamagnetic cations that lie on the superexchange pathway, the extent to which the cations order over crystallographically–distinct sites, local deviations from that average cation distribution and defects in the microstructure of the compound.

Unfortunately the Goodenough–Kanamori rules alone are not enough to predict the magnetic properties of new materials; the influence of the local structure must not be underestimated.

Bibliography

1. A. Kojima, K. Teshima, Y. Shirai and T. Miyasaka, *Journal of the American Chemical Society*, 2009, **131**, 6050-6051.
2. S. Pang, H. Hu, J. Zhang, S. Lv, Y. Yu, F. Wei, T. Qin, H. Xu, Z. Liu and G. Cui, *Chemistry of Materials*, 2014, **26**, 1485-1491.
3. M. M. Lee, J. Teuscher, T. Miyasaka, T. N. Murakami and H. J. Snaith, *Science*, 2012, **338**, 643-647.
4. M. A. Green, A. Ho-Baillie and H. J. Snaith, *Nature Photonics*, 2014, **8**, 506-514.
5. B. Saparov and D. B. Mitzi, *Chemical Reviews*, 2016, **116**, 4558-4596.
6. T. Siegrist, S. Sunshine, D. W. Murphy, R. J. Cava and S. M. Zahurak, *Physical Review B*, 1987, **35**, 7137-7139.
7. J. Bardeen, L. N. Cooper and J. R. Schrieffer, *Physical Review*, 1957, **106**, 162-164.
8. J. Bardeen, L. N. Cooper and J. R. Schrieffer, *Physical Review*, 1957, **108**, 1175-1204.
9. G. H. Jonker and J. H. Van Santen, *Physica*, 1950, **16**, 337-349.
10. J. H. Van Santen and G. H. Jonker, *Physica*, 1950, **16**, 599-600.
11. J. Volger, *Physica*, 1954, **20**, 49-66.
12. S. Vasala and M. Karppinen, *Progress in Solid State Chemistry*, 2015, **43**, 1-36.
13. V. R. Palkar and S. K. Malik, *Solid State Communications*, 2005, **134**, 783-786.
14. Y. A. Abramov, V. G. Tsirelson, V. E. Zavodnik, S. A. Ivanov and Brown I. D., *Acta Crystallographica Section B*, 1995, **51**, 942-951.
15. D. Weber, *Zeitschrift für Naturforschung B*, 1978, **33**, 1443-1445.
16. D. B. Mitzi, C. A. Feild, Z. Schlesinger and R. B. Laibowitz, *Journal of Solid State Chemistry*, 1995, **114**, 159-163.
17. M. Amano Patino, D. Zeng, S. J. Blundell, J. E. McGrady and M. A. Hayward, *Inorganic Chemistry*, 2018, **57**, 2890-2898.
18. T. J. Prior, V. J. Couper and P. D. Battle, *Journal of Solid State Chemistry*, 2005, **178**, 153-157.
19. C. R. Wiebe, J. E. Greedan, G. M. Luke and J. S. Gardner, *Physical Review B*, 2002, **65**, 144413.
20. C. C. Luhrs, F. Sapiña, D. Beltrán-porter, N. Casañ-pastor and A. Fuertes, *Journal of Materials Chemistry*, 1998, **8**, 209-217.
21. V. M. Goldschmidt, *Naturwissenschaften*, 1926, **14**, 477-485.
22. A. Glazer, *Acta Crystallographica Section B*, 1972, **28**, 3384-3392.
23. P. Woodward, *Acta Crystallographica Section B*, 1997, **53**, 32-43.
24. G. King and P. M. Woodward, *Journal of Materials Chemistry*, 2010, **20**, 5785-5796.
25. M. T. Anderson, K. B. Greenwood, G. A. Taylor and K. R. Poeppelmeier, *Progress in Solid State Chemistry*, 1993, **22**, 197-233.
26. G. Blasse, *Journal of Inorganic and Nuclear Chemistry*, 1965, **27**, 993-1003.
27. J.-W. G. Bos and J. P. Attfield, *Physical Review B*, 2004, **70**, 174434.
28. J. A. Alonso, M. T. Casais, M. J. Martínez-Lope, J. L. Martínez, P. Velasco, A. Muñoz and M. T. Fernández-Díaz, *Chemistry of Materials*, 2000, **12**, 161-168.
29. R. C. Currie, J. F. Vente, E. Frikkee and D. J. W. Ijdo, *Journal of Solid State Chemistry*, 1995, **116**, 199-204.

30. P. A. Seinen, F. P. F. van Berkel, W. A. Groen and D. J. W. Ijdo, *Materials Research Bulletin*, 1987, **22**, 535-542.
31. M. T. Anderson and K. R. Poeppelmeier, *Chemistry of Materials*, 1991, **3**, 476-482.
32. H. A. Jahn and E. Teller, *Proceedings of the Royal Society of London. Series A - Mathematical and Physical Sciences*, 1937, **161**, 220-235.
33. H. A. Jahn, *Proceedings of the Royal Society of London. Series A - Mathematical and Physical Sciences*, 1938, **164**, 117-131.
34. A. W. Sleight and R. Ward, *Inorganic Chemistry*, 1962, **1**, 790-793.
35. M. P. Attfield, P. D. Battle, S. K. Bollen, S. H. Kim, A. V. Powell and M. Workman, *Journal of Solid State Chemistry*, 1992, **96**, 344-359.
36. P. G. Radaelli, D. E. Cox, M. Marezio and S. W. Cheong, *Physical Review B*, 1997, **55**, 3015-3023.
37. V. Caignaert, F. Millange, M. Hervieu, E. Suard and B. Raveau, *Solid State Communications*, 1996, **99**, 173-177.
38. S. Tadashi, Y. Tetsuo and T. Yasuyoshi, *Bulletin of the Chemical Society of Japan*, 1984, **57**, 1859-1862.
39. M. C. Knapp and P. M. Woodward, *Journal of Solid State Chemistry*, 2006, **179**, 1076-1085.
40. F. Galasso, J. R. Barrante and L. Katz, *Journal of the American Chemical Society*, 1961, **83**, 2830-2832.
41. A. Y. Borisevich and P. K. Davies, *Journal of Solid State Chemistry*, 2003, **170**, 198-201.
42. Y. Tang, E. C. Hunter, P. D. Battle, R. P. Sena, J. Hadermann, M. Avdeev and J. M. Cadogan, *Journal of Solid State Chemistry*, 2016, **242**, 86-95.
43. J. A. Alonso, E. Mzayek and I. Rasines, *Materials Research Bulletin*, 1987, **22**, 69-74.
44. J. A. Alonso, E. Mzayek and I. Rasines, *Journal of Solid State Chemistry*, 1990, **84**, 16-22.
45. Y. Yan, S. J. Pennycook, Z. Xu and D. Viehland, *Applied Physics Letters*, 1998, **72**, 3145-3147.
46. P. K. Davies and M. A. Akbas, *Journal of Physics and Chemistry of Solids*, 2000, **61**, 159-166.
47. K. Park, L. Salamanca-Riba, M. Wuttig and D. Viehland, *Journal of Materials Science*, 1994, **29**, 1284-1289.
48. P. D. Battle, S. I. Evers, E. C. Hunter and M. Westwood, *Inorganic Chemistry*, 2013, **52**, 6648-6653.
49. G. A. Bain and J. F. Berry, *Journal of Chemical Education*, 2008, **85**, 532-536.
50. J. Crangle, *The Magnetic Properties of Solids*, Edward Arnold Limited, London, 1977.
51. A. Podlesnyak, S. Rosenkranz, F. Fauth, W. Marti, A. Furrer, A. Mirmelstein and H. J. Scheel, *Journal of Physics: Condensed Matter*, 1993, **5**, 8973.
52. E. J. Cussen, M. J. Rosseinsky, P. D. Battle, J. C. Burley, L. E. Spring, J. F. Vente, S. J. Blundell, A. I. Coldea and J. Singleton, *Journal of the American Chemical Society*, 2001, **123**, 1111-1122.
53. G. Cao, A. Subedi, S. Calder, J. Q. Yan, J. Yi, Z. Gai, L. Poudel, D. J. Singh, M. D. Lumsden, A. D. Christianson, B. C. Sales and D. Mandrus, *Physical Review B*, 2013, **87**, 155136.
54. M. S. Augsburger, M. C. Viola, J. C. Pedregosa, A. Muñoz, J. A. Alonso and R. E. Carbonio, *Journal of Materials Chemistry*, 2005, **15**, 993-1001.
55. E. O. Wollan and W. C. Koehler, *Physical Review*, 1955, **100**, 545-563.

56. J. M. Hudspeth, G. A. Stewart, A. J. Studer and D. J. Goossens, *Journal of Physics and Chemistry of Solids*, 2011, **72**, 1543-1547.
57. A. C. Komarek, S. V. Streltsov, M. Isobe, T. Möller, M. Hoelzel, A. Senyshyn, D. Trots, M. T. Fernández-Díaz, T. Hansen, H. Gotou, T. Yagi, Y. Ueda, V. I. Anisimov, M. Grüninger, D. I. Khomskii and M. Braden, *Physical Review Letters*, 2008, **101**, 167204.
58. W. C. Hamilton, *Physical Review*, 1958, **110**, 1050-1057.
59. Y. Tang, E. C. Hunter, P. D. Battle, M. Hendrickx, J. Hadermann and J. M. Cadogan, *Inorganic Chemistry*, 2018, **57**, 7438-7445.
60. R. Rodriguez, A. Fernandez, A. Isalgue, J. Rodriguez, A. Labrata, J. Tejada and X. Obradors, *Journal of Physics C: Solid State Physics*, 1985, **18**, L401.
61. N. Kashima, K. Inoue, T. Wada and Y. Yamaguchi, *Applied Physics A*, 2002, **74**, s805-s807.
62. M. T. Hutchings and E. J. Samuelsen, *Physical Review B*, 1972, **6**, 3447-3461.
63. W. C. Koehler and E. O. Wollan, *Journal of Physics and Chemistry of Solids*, 1957, **2**, 100-106.
64. G. Pepy, *Journal of Physics and Chemistry of Solids*, 1974, **35**, 433-444.
65. G. Fischer, M. Däne, A. Ernst, P. Bruno, M. Lüders, Z. Szotek, W. Temmerman and W. Hergert, *Physical Review B*, 2009, **80**, 014408.
66. E. C. Hunter, P. D. Battle, R. Paria Sena and J. Hadermann, *Journal of Solid State Chemistry*, 2017, **248**, 96-103.
67. M. Zhu, D. Do, C. R. Dela Cruz, Z. Dun, H. D. Zhou, S. D. Mahanti and X. Ke, *Physical Review Letters*, 2014, **113**, 076406.
68. M. Zhu, D. Do, C. R. Dela Cruz, Z. Dun, J. G. Cheng, H. Goto, Y. Uwatoko, T. Zou, H. D. Zhou, S. D. Mahanti and X. Ke, *Physical Review B*, 2015, **92**, 094419.
69. E. C. Hunter and P. D. Battle, *Journal of Solid State Chemistry*, 2018, **264**, 48-58.
70. C. R. Wiebe, J. E. Greedan, P. P. Kyriakou, G. M. Luke, J. S. Gardner, A. Fukaya, I. M. Gat-Malureanu, P. L. Russo, A. T. Savici and Y. J. Uemura, *Physical Review B*, 2003, **68**, 134410.
71. R. Morrow, K. Samanta, T. Saha Dasgupta, J. Xiong, J. W. Freeland, D. Haskel and P. M. Woodward, *Chemistry of Materials*, 2016, **28**, 3666-3675.
72. J. B. Goodenough, *Physical Review*, 1955, **100**, 564-573.
73. J. B. Goodenough, *Journal of Physics and Chemistry of Solids*, 1958, **6**, 287-297.
74. J. Kanamori, *Journal of Physics and Chemistry of Solids*, 1959, **10**, 87-98.
75. P. D. Battle, M. Avdeev and J. Hadermann, *Journal of Solid State Chemistry*, 2014, **220**, 163-166.
76. A. R. West, *Solid State Chemistry And Its Applications*, John Wiley and Sons, New York, 1984.
77. V. C. Fuertes, M. C. Blanco, D. G. Franco, J. M. De Paoli, R. D. Sánchez and R. E. Carbonio, *Materials Research Bulletin*, 2011, **46**, 62-69.
78. M. Gateshki, J. M. Igartua and E. Hernández-Bocanegra, *Journal of Physics: Condensed Matter*, 2003, **15**, 6199.
79. V. Ting, Y. Liu, R. L. Withers and E. Krausz, *Journal of Solid State Chemistry*, 2004, **177**, 979-986.
80. L. S. Dent Glasser, *Crystallography and its applications*, Van Nostrand Reinhold, New York, 1977.
81. X-ray scattering factors of a few elements, http://pd.chem.ucl.ac.uk/pdnn/diff1/scaten.htm).
82. Neutron Production at ISIS, https://www.isis.stfc.ac.uk/Pages/Characteristics-of-a-pulsed-source.aspx).

83. C. G. Windsor, *Pulsed Neutron Scattering*, Taylor & Francis Limited, London, 1981.
84. G. E. Bacon, *Neutron Diffraction*, Oxford University Press, London, 1962.
85. V. F. Sears, *Neutron News*, 1992, **3**, 26-37.
86. *Empyrean Users' Guide*, PANalytical.
87. K.-D. Liss, B. Hunter, M. Hagen, T. Noakes and S. Kennedy, *Physica B: Condensed Matter*, 2006, **385-386**, 1010-1012.
88. D1b diffractometer layout, https://www.ill.eu/users/instruments/instruments-list/d1b/description/instrument-layout/).
89. A. C. Hannon, *Nuclear Instruments and Methods in Physics Research Section A: Accelerators, Spectrometers, Detectors and Associated Equipment*, 2005, **551**, 88-107.
90. H. Rietveld, *Acta Crystallographica*, 1966, **20**, 508-513.
91. H. Rietveld, *Acta Crystallographica*, 1967, **22**, 151-152.
92. H. Rietveld, *Journal of Applied Crystallography*, 1969, **2**, 65-71.
93. L. B. McCusker, R. B. Von Dreele, D. E. Cox, D. Louer and P. Scardi, *Journal of Applied Crystallography*, 1999, **32**, 36-50.
94. A. C. Larson and R. B. Von Dreele, *General Structure Analysis System (GSAS)*, Report LAUR86-748, 2000.
95. B. Toby, *Journal of Applied Crystallography*, 2001, **34**, 210-213.
96. B. Toby, *Powder Diffraction*, 2006, **21**, 67-70.
97. R. A. Young, *The Rietveld Method*, Oxford University Press, New York, 1995.
98. G. Caglioti, A. Paoletti and F. P. Ricci, *Nuclear Instruments*, 1958, **3**, 223-228.
99. D. E. Jesson and S. J. Pennycook, *Proceedings of the Royal Society of London. Series A: Mathematical and Physical Sciences*, 1995, **449**, 273-293.
100. S. J. Pennycook, *Ultramicroscopy*, 1989, **30**, 58-69.
101. J. R. Stewart, P. P. Deen, K. H. Andersen, H. Schober, J.-F. Barthelemy, J. M. Hillier, A. P. Murani, T. Hayes and B. Lindenau, *Journal of Applied Crystallography*, 2009, **42**, 69-84.
102. O. Schärpf, *Physica B: Condensed Matter*, 1991, **174**, 514-527.
103. O. Schärpf and H. Capellmann, *physica status solidi (a)*, 1993, **135**, 359-379.
104. R. L. McGreevy and L. Pusztai, *Molecular Simulation*, 1988, **1**, 359-367.
105. M. G. Tucker, D. A. Keen, M. T. Dove, A. L. Goodwin and Q. Hui, *Journal of Physics: Condensed Matter*, 2007, **19**, 335218.
106. J. A. M. Paddison, J. R. Stewart and A. L. Goodwin, *Journal of Physics: Condensed Matter*, 2013, **25**, 454220.
107. S. J. Blundell, *Contemporary Physics*, 1999, **40**, 175-192.
108. A. Amato, H. Luetkens, K. Sedlak, A. Stoykov, R. Scheuermann, M. Elender, A. Raselli and D. Graf, *Review of Scientific Instruments*, 2017, **88**, 093301.
109. S. R. Giblin, S. P. Cottrell, P. J. C. King, S. Tomlinson, S. J. S. Jago, L. J. Randall, M. J. Roberts, J. Norris, S. Howarth, Q. B. Mutamba, N. J. Rhodes and F. A. Akeroyd, *Nuclear Instruments and Methods in Physics Research Section A: Accelerators, Spectrometers, Detectors and Associated Equipment*, 2014, **751**, 70-78.
110. J. Clarke, *Scientific American*, 1994, **271**, 46-53.
111. J. Clarke, *Nature*, 1994, **372**, 501-502.
112. B. D. Josephson, *Physics Letters*, 1962, **1**, 251-253.
113. P. W. Anderson and J. M. Rowell, *Physical Review Letters*, 1963, **10**, 230-232.
114. R. Lindell, J. Penttilä, M. Sillanpää and P. Hakonen, *Physical Review B*, 2003, **68**, 052506.

115. A. K. Cheetham and P. Day, *Solid-State Chemistry: Techniques*, Oxford University Press, New York, 1987.
116. R. M. Moon and W. C. Koehler, *Physical Review B*, 1975, **11**, 1609-1622.
117. S. Arajs and R. V. Colvin, *Journal of Applied Physics*, 1962, **33**, 2517-2519.
118. J. A. Mydosh, *Spin Glasses: An Experimental Introduction*, Taylor & Francis Limited, London, 1993.
119. I. Alvarez, M. L. Veiga and C. Pico, *Journal of Alloys and Compounds*, 1997, **255**, 74-78.
120. D. G. Franco, R. E. Carbonio, E. E. Kaul and G. Nieva, *Journal of Magnetism and Magnetic Materials*, 2013, **346**, 196-202.
121. D. G. Franco, R. E. Carbonio and G. Nieva, *IEEE Transactions on Magnetics*, 2013, **49**, 4656-4659.
122. A. A. Bokov and Z.-G. Ye, *Journal of Materials Science*, 2006, **41**, 31-52.
123. W. I. F. David, *Journal of Applied Crystallography*, 1986, **19**, 63-64.
124. A. R. Wildes, *Neutron News*, 2006, **17**, 17-25.
125. G. A. Slack, *Journal of Applied Physics*, 1960, **31**, 1571-1582.
126. K. P. F. Siqueira, R. M. Borges, E. Granado, L. M. Malard, A. M. de Paula, R. L. Moreira, E. M. Bittar and A. Dias, *Journal of Solid State Chemistry*, 2013, **203**, 326-332.
127. C. S. Ltd., http://www.crystalmaker.com/crystalmaker/index.html).
128. N. Metropolis, A. W. Rosenbluth, M. N. Rosenbluth, A. H. Teller and E. Teller, *The Journal of Chemical Physics*, 1953, **21**, 1087-1092.
129. D. Iwanaga, Y. Inaguma and M. Itoh, *Materials Research Bulletin*, 2000, **35**, 449-457.
130. G. Blasse, *Philips Research Reports*, 1965, **20**, 327-336.
131. E. J. Cussen, J. F. Vente, P. D. Battle and T. C. Gibb, *Journal of Materials Chemistry*, 1997, **7**, 459-463.
132. V. C. Fuertes, M. C. Blanco, D. G. Franco, J. M. De Paoli, E. V. Pannunzio Miner, R. D. Sánchez, M. T. Fernández-Díaz and R. E. Carbonio, *Physica B: Condensed Matter*, 2009, **404**, 2717-2719.
133. D. G. Franco, V. C. Fuertes, M. C. Blanco, M. T. Fernández-Díaz, R. D. Sánchez and R. E. Carbonio, *Journal of Solid State Chemistry*, 2012, **194**, 385-391.
134. M. Wakeshima, H. Nishimine and Y. Hinatsu, *Journal of Physics: Condensed Matter*, 2004, **16**, 4103.
135. F. Vullum, F. Nitsche, S. M. Selbach and T. Grande, *Journal of Solid State Chemistry*, 2008, **181**, 2580-2585.
136. Gatan, Digital Micrograph™ software, http://www.gatan.com/products/tem-analysis/gatan-microscopy-suite-software).
137. J. R. Tolchard, M.-L. Fontaine and T. Grande, *Acta Crystallographica Section C*, 2009, **65**, i11-i13.
138. S. Kato, T. Sakamoto, N. Watanabe, M. Sugai, Y. Ohshima, H. Takizawa and M. Shimada, *Materials Letters*, 1994, **21**, 101-104.
139. K. Dey, A. Indra, D. De, S. Majumdar and S. Giri, *ACS Applied Materials & Interfaces*, 2016, **8**, 12901-12907.
140. T. Inprasit, S. Wongkasemjit, P. Limthongkul and S. J. Skinner, *Materials Letters*, 2016, **162**, 37-39.
141. Y. Xu, S. Liu, N. Qu, Y. Cui, Q. Gao, R. Chen, J. Wang, F. Gao and X. Hao, *Journal of Physics: Condensed Matter*, 2017, **29**, 105801.
142. C.-M. Chin, P. D. Battle, S. J. Blundell, E. Hunter, F. Lang, M. Hendrickx, R. Paria Sena and J. Hadermann, *Journal of Solid State Chemistry*, 2018, **258**, 825-834.

143. S. Vasala, J. G. Cheng, H. Yamauchi, J. B. Goodenough and M. Karppinen, *Chemistry of Materials*, 2012, **24**, 2764-2774.
144. S. Vasala, H. Saadaoui, E. Morenzoni, O. Chmaissem, T.-S. Chan, J.-M. Chen, Y.-Y. Hsu, H. Yamauchi and M. Karppinen, *Physical Review B*, 2014, **89**, 134419.
145. D. Iwanaga, Y. Inaguma and M. Itoh, *Journal of Solid State Chemistry*, 1999, **147**, 291-295.
146. T. Koga, N. Kurita and H. Tanaka, *Journal of the Physical Society of Japan*, 2014, **83**, 115001.
147. O. Mustonen, S. Vasala, K. P. Schmidt, E. Sadrollahi, H. C. Walker, I. Terasaki, F. J. Litterst, E. Baggio-Saitovitch and M. Karppinen, *Physical Review B*, 2018, **98**, 064411.
148. O. Mustonen, S. Vasala, E. Sadrollahi, K. P. Schmidt, C. Baines, H. C. Walker, I. Terasaki, F. J. Litterst, E. Baggio-Saitovitch and M. Karppinen, *Nature Communications*, 2018, **9**, 1085.
149. R. Shannon, *Acta Crystallographica Section A*, 1976, **32**, 751-767.
150. M. P. Attfield, P. D. Battle, S. K. Bollen, T. C. Gibb and R. J. Whitehead, *Journal of Solid State Chemistry*, 1992, **100**, 37-48.
151. K. M. Ok, P. S. Halasyamani, D. Casanova, M. Llunell, P. Alemany and S. Alvarez, *Chemistry of Materials*, 2006, **18**, 3176-3183.
152. C.-M. Chin, P. D. Battle, E. C. Hunter, M. Avdeev, M. Hendrickx and J. Hadermann, *Journal of Solid State Chemistry*, 2019, **273**, 175-185.
153. Bokhimi, *Powder Diffraction*, 1992, **7**, 228-230.
154. H. J. Rossell, *Journal of Solid State Chemistry*, 1979, **27**, 115-122.
155. J. Dho, W. S. Kim and N. H. Hur, *Physical Review Letters*, 2002, **89**, 027202.
156. A. K. Azad, S. G. Eriksson, A. Mellergård, S. A. Ivanov, J. Eriksen and H. Rundlöf, *Materials Research Bulletin*, 2002, **37**, 1797-1813.
157. B. Orayech, L. Ortega-San-Martin, I. Urcelay-Olabarria, L. Lezama, T. Rojo, M. I. Arriortua and J. M. Igartua, *Dalton Transactions*, 2016, **45**, 14378-14393.
158. B. Stöger, M. Weil and E. Zobetz, *Zeitschrift für Kristallographie International journal for structural, physical, and chemical aspects of crystalline materials*, 2010, **225**, 125-138.
159. W. L. Roth and G. A. Slack, *Journal of Applied Physics*, 1960, **31**, S352-S353.
160. S. Nomura and T. Nakagawa, *Journal of the Physical Society of Japan*, 1966, **21**, 1068-1071.
161. S. Nomura and T. Nakagawa, *Journal of the Physical Society of Japan*, 1966, **21**, 1679-1684.
162. V. Scatturin, L. Corliss, N. Elliott and J. Hastings, *Acta Crystallographica*, 1961, **14**, 19-26.
163. C. Martin, A. Maignan, M. Hervieu, B. Raveau, Z. Jirák, M. M. Savosta, A. Kurbakov, V. Trounov, G. André and F. Bourée, *Physical Review B*, 2000, **62**, 6442-6449.
164. R. Paria Sena, J. Hadermann, C.-M. Chin, E. C. Hunter and P. D. Battle, *Journal of Solid State Chemistry*, 2016, **243**, 304-311.
165. S. A. Ivanov, R. Mathieu, P. Nordblad, R. Tellgren, C. Ritter, E. Politova, G. Kaleva, A. Mosunov, S. Stefanovich and M. Weil, *Chemistry of Materials*, 2013, **25**, 935-945.
166. W.-t. Chen, M. Mizumaki, H. Seki, M. S. Senn, T. Saito, D. Kan, J. P. Attfield and Y. Shimakawa, *Nature Communications*, 2014, **5**, 3909.

167. M. R. Li, M. Retuerto, Z. Deng, P. W. Stephens, M. Croft, Q. Huang, H. Wu, X. Deng, G. Kotliar, J. Sánchez-Benítez, J. Hadermann, D. Walker and M. Greenblatt, *Angewandte Chemie International Edition*, 2015, **54**, 12069-12073.
168. A. M. Arévalo-López, G. M. McNally and J. P. Attfield, *Angewandte Chemie International Edition*, 2015, **54**, 12074-12077.
169. P. Zuo, H. Klein, C. Darie and C. V. Colin, *Journal of Magnetism and Magnetic Materials*, 2018, **458**, 48-51.
170. E. C. Hunter, S. Mousdale, P. D. Battle and M. Avdeev, *Journal of Solid State Chemistry*, 2019, **269**, 80-86.
171. D. Fiorani, S. Viticoli, J. L. Dormann, J. L. Tholence and A. P. Murani, *Physical Review B*, 1984, **30**, 2776-2786.
172. J. Prado-Gonjal, R. Schmidt, J.-J. Romero, D. Ávila, U. Amador and E. Morán, *Inorganic Chemistry*, 2013, **52**, 313-320.
173. C.-M. Chin, R. Paria Sena, E. C. Hunter, J. Hadermann and P. D. Battle, *Journal of Solid State Chemistry*, 2017, **251**, 224-232.
174. C. J. Howard, B. J. Kennedy and P. M. Woodward, *Acta Crystallographica Section B*, 2003, **59**, 463-471.

Appendices

Appendix 1: Supporting information for Chapter 3

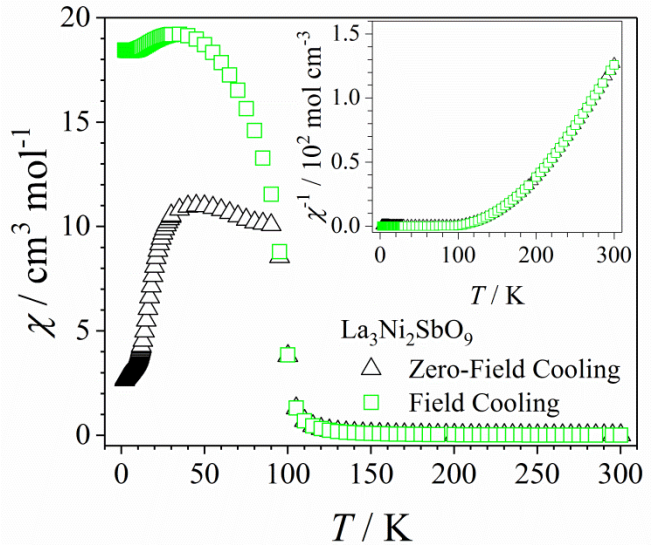


Figure S3.1. The temperature dependence of the dc molar susceptibility and (inset) inverse susceptibility of the sample $La_3Ni_2SbO_9$ used in the polarised neutron experiment.

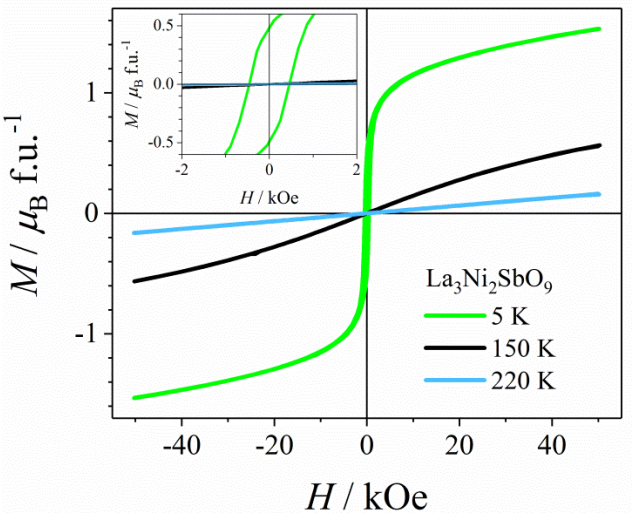


Figure S3.2. The magnetisation per formula unit (f.u.) of $La_3Ni_2SbO_9$ as a function of applied magnetic field. The inset here shows the same function in the range of $-2 \leq H/\text{kOe} \leq +2$.

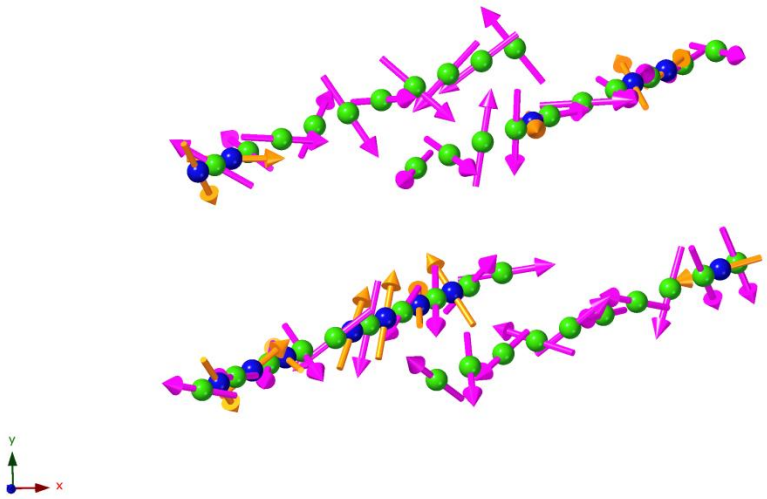


Figure S3.3. A slice of the spin configuration generated using the DMC approach with J_1/k_B and J_2/k_B being –221 and –6 K, respectively. The green spheres which couple with the purple vectors, and the blue spheres which couple with the orange vectors, represent the spin configurations of the Ni^{2+} cations at the 2*c* and 2*d* sites of $La_3Ni_2SbO_9$, respectively.

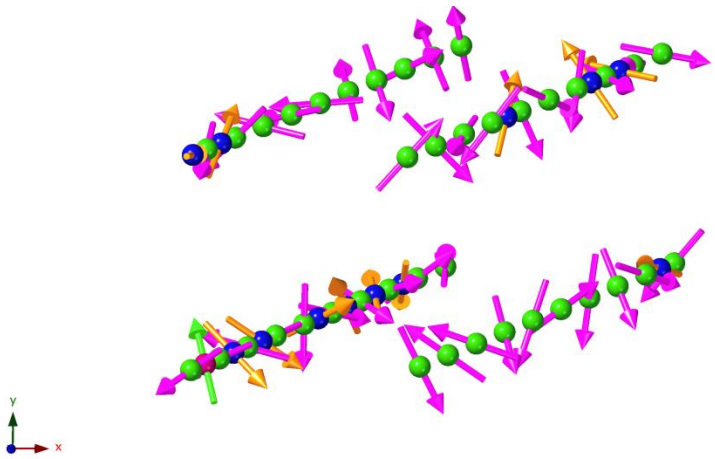


Figure S3.4. A slice of the spin configuration generated using the DMC approach with J_1/k_B, J_2/k_B and J_4/k_B being –221, –7.1 and –0.1 K, respectively. The green spheres which couple with the purple vectors, and the blue spheres which couple with the orange vectors, represent the spin configurations of the Ni^{2+} cations at the 2*c* and 2*d* sites of $La_3Ni_2SbO_9$, respectively.

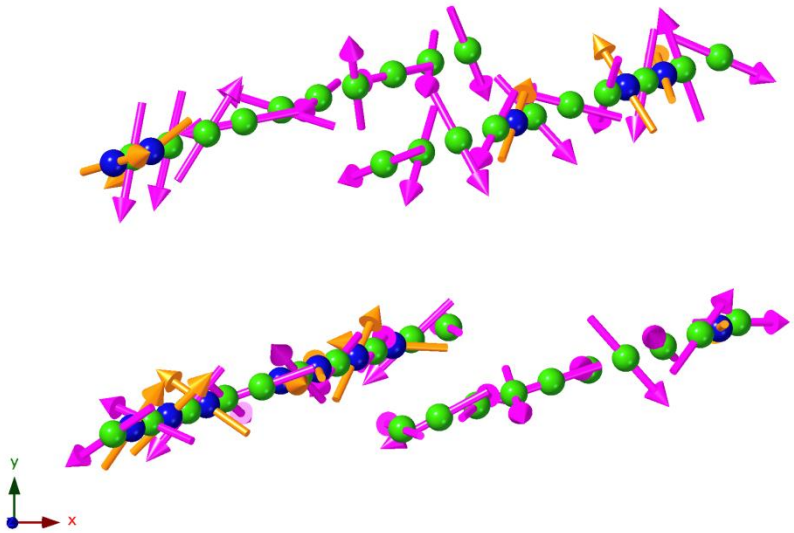


Figure S3.5. A slice of the spin configuration generated using the RMC approach with W = 100. The green spheres which couple with the purple vectors, and the blue spheres which couple with the orange vectors, represent the spin configurations of the Ni^{2+} cations at the 2*c* and 2*d* sites of $La_3Ni_2SbO_9$, respectively.

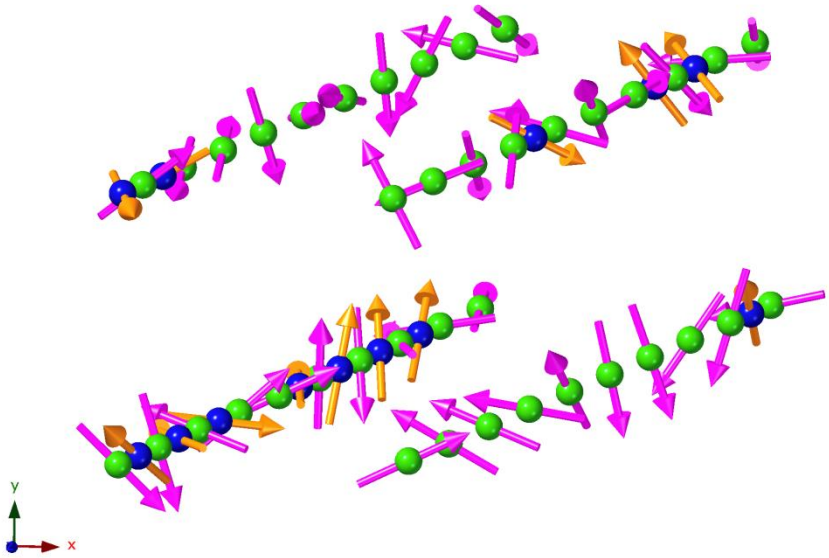


Figure S3.6. A slice of the spin configuration generated using the RMC approach with W = 10000. The green spheres which couple with the purple vectors, and the blue spheres which couple with the orange vectors, represent the spin configurations of the Ni^{2+} cations at the 2*c* and 2*d* sites of $La_3Ni_2SbO_9$, respectively.

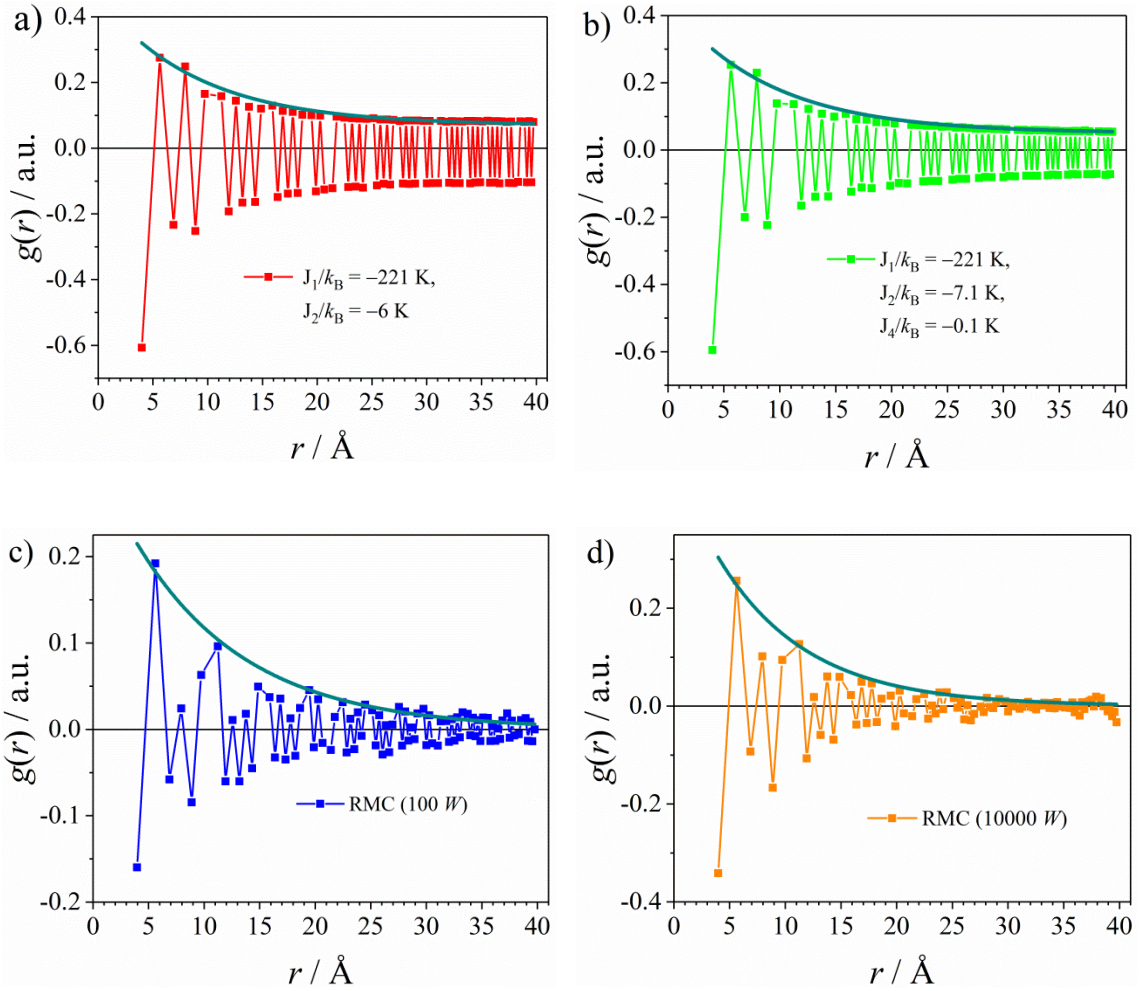


Figure S3.7. The spin correlation functions $g(r)$ of the four simulations described in Figure 3.16. The dark cyan curve represents the exponential fit in each case with $g(r) = Ae^{-r/\xi} + c$.

Appendix 2: Supporting information for Chapter 4

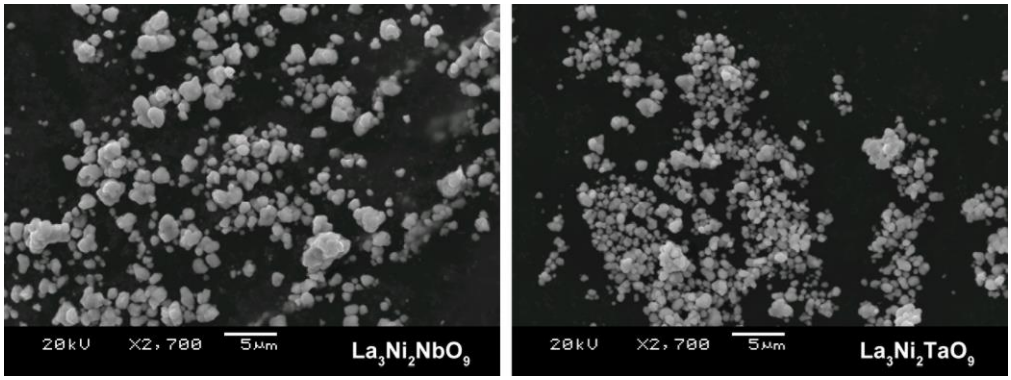


Figure S4.1. Scanning electron microscope (SEM) images of the particles of the $La_3Ni_2NbO_9$ sample (left) and the $La_3Ni_2TaO_9$ sample (right) taken at a voltage of 20kV.

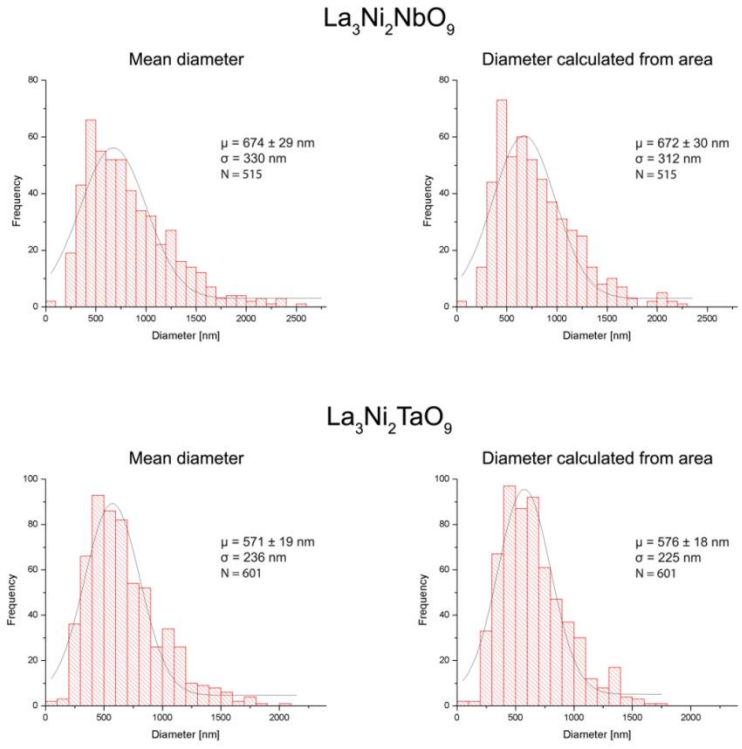


Figure S4.2. Particle size distribution (PSD) for $La_3Ni_2NbO_9$ (top) and $La_3Ni_2TaO_9$ (bottom), where the diameter of each particle is calculated from the mean diameter (left) and from the estimated area (right). The mean particle size (μ), standard deviation (σ) and amount of investigated particles (N) are given for each particle size distribution.

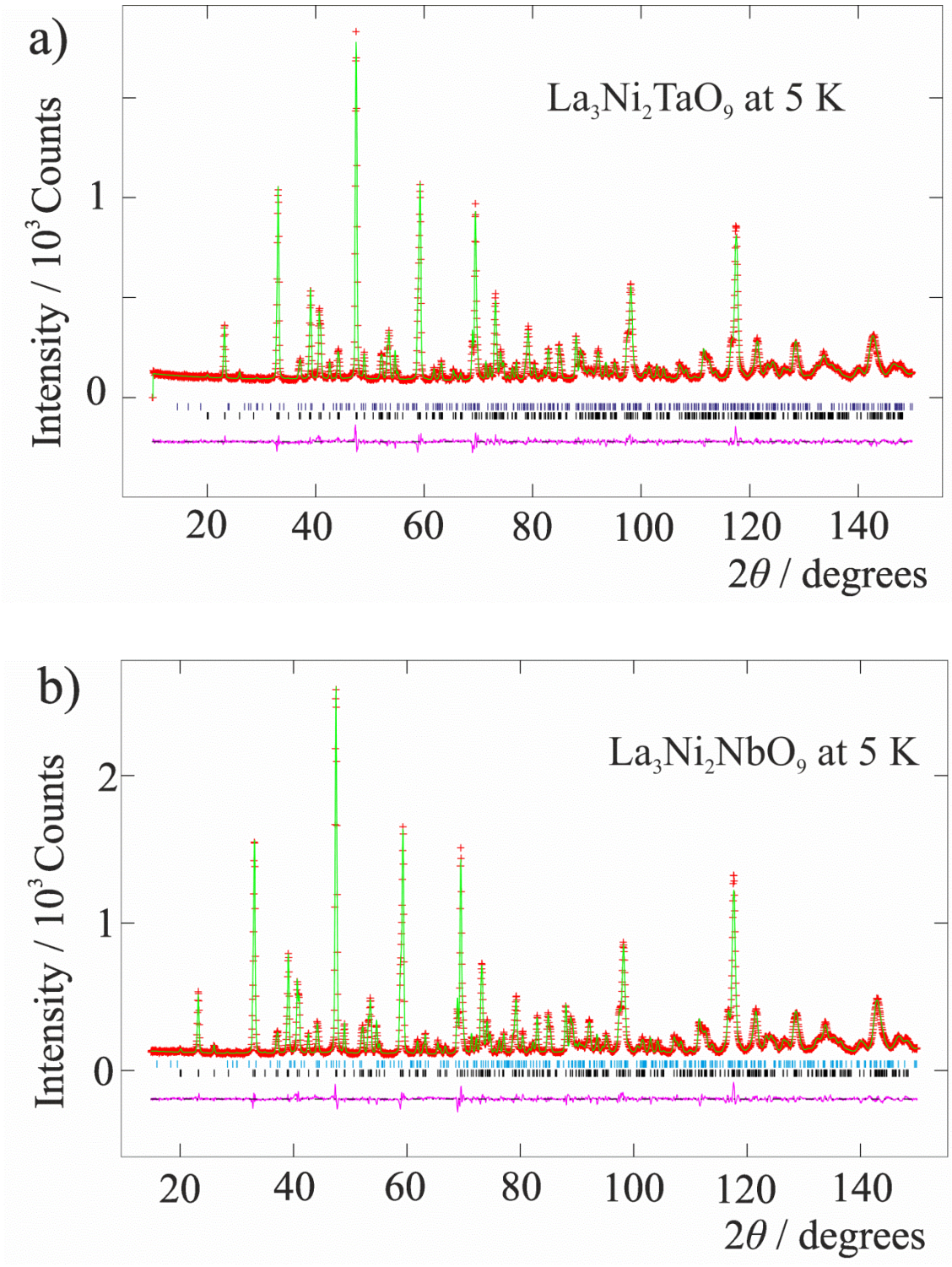


Figure S4.3. Observed (red crosses), calculated (green line) and difference (purple line) NPD profiles of (a) $La_3Ni_2TaO_9$ and (b) $La_3Ni_2NbO_9$ at 5 K measured on D2b. The meaning of the reflection markers is the same as in Figures 4.1 and 4.2.

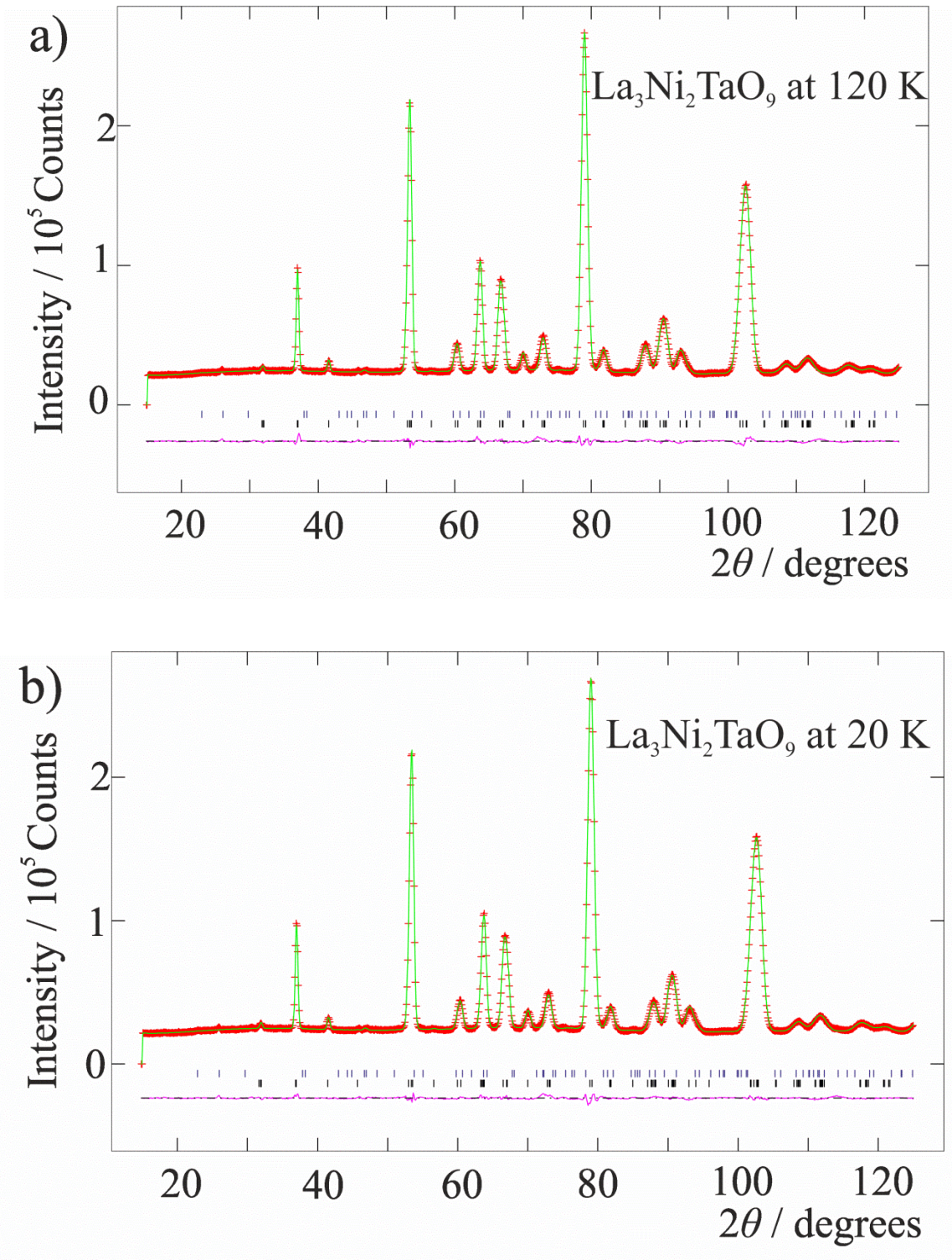


Figure S4.4. Observed (red crosses), calculated (green line) and difference (purple line) neutron powder diffraction profiles of $La_3Ni_2TaO_9$ recorded on D1b at (a) 120 and (b) 20 K. Reflection markers for La_3TaO_7 and $La_3Ni_2TaO_9$ are blue and black respectively.

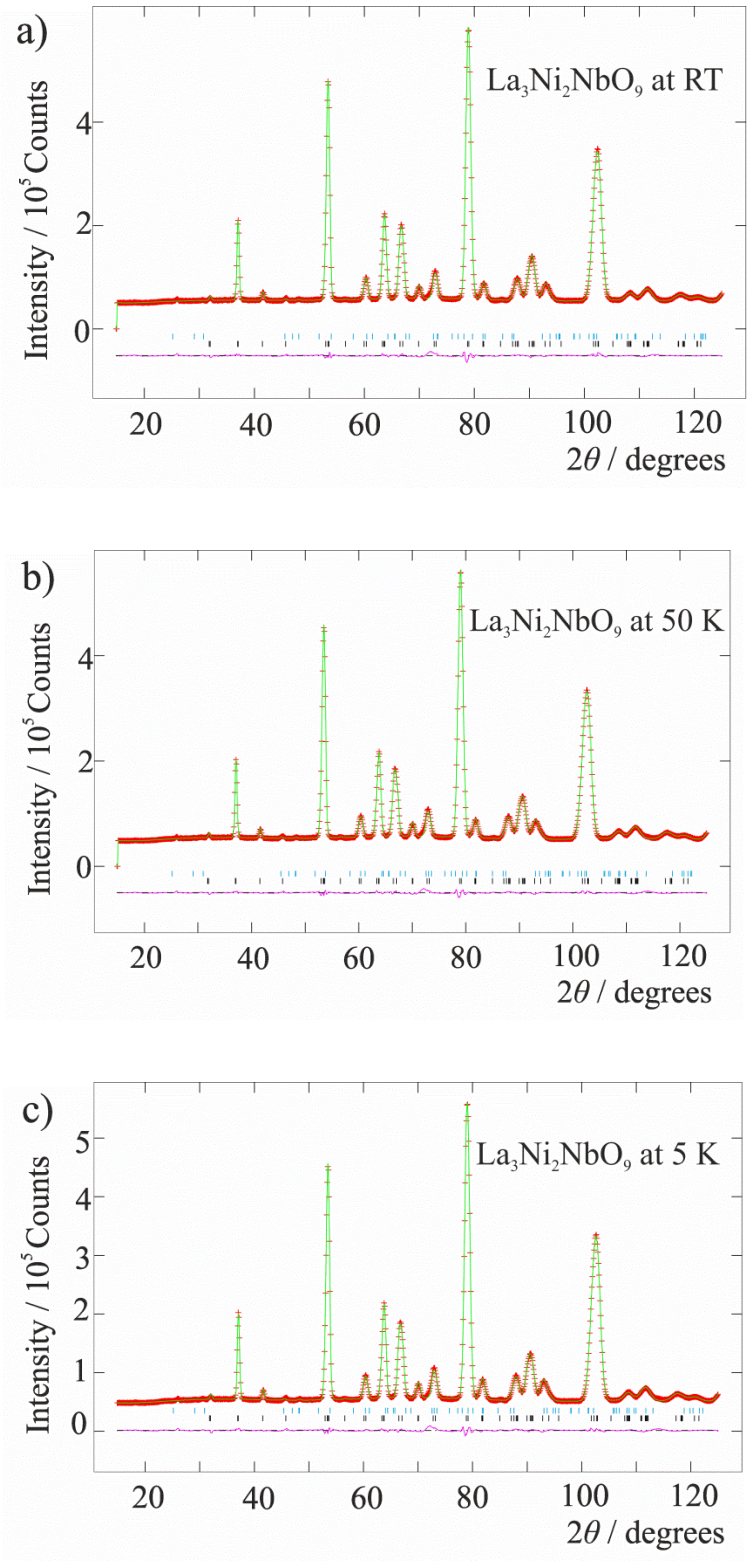


Figure S4.5. Observed (red crosses), calculated (green line) and difference (purple) neutron powder diffraction profiles of $La_3Ni_2NbO_9$ recorded on D1b at (a) RT, (b) 50 K and (c) 5 K. Underneath is a difference curve, purple in colour. The cyan and black vertical markers indicate reflection positions for $LaNbO_4$ and $La_3Ni_2NbO_9$, respectively.

Table S4.1. Structural parameters of $La_3Ni_2B'O_9$ (B' = Ta or Nb) at selected temperatures (Space group $P2_1/n$).

		B' = Ta; T = 120 K	B' = Nb; T = 50 K
a / Å		5.5804(2)	5.5757(1)
b / Å		5.6371(2)	5.6382(1)
c / Å		7.9094(2)	7.9033(2)
β / °		90.064(5)	90.027(8)
V / Å^3		248.82(2)	248.46(2)
$R_{wp\|NPD}$ / %		4.45	4.71
χ^2		3.150	4.598
La	x	0.4917(5)	0.4916(5)
4e (x y z)	y	0.4597(2)	0.4585(2)
	z	0.249(1)	0.2504(12)
	U_{ISO} / Å^2	0.0151(3)	0.0145(3)
Ni/B'1	U_{ISO} / Å^2	0.0014(2)	0.0017(2)
2c (0 ½ 0)	Ni occupancy	0.982	0.964
	B' occupancy	0.018	0.036
Ni/B'2	U_{ISO} / Å^2	0.0014(2)	0.0017(2)
2d (½ 0 0)	Ni occupancy	0.351	0.369
	B' occupancy	0.649	0.631
O1	x	0.789(1)	0.792(1)
4e (x y z)	y	0.797(1)	0.798(1)
	z	–0.0394(8)	–0.0380(7)
	U_{ISO} / Å^2	0.0029(14)	0.0019(12)
O2	x	0.708(1)	0.711(1)
4e (x y z)	y	0.283(1)	0.283(1)
	z	–0.0452(9)	–0.0468(7)
	U_{ISO} / Å^2	0.0066(16)	0.0074(14)
O3	x	0.5776(5)	0.5779(4)
4e (x y z)	y	0.0179(4)	0.0174(4)
	z	0.251(1)	0.251(1)
	U_{ISO} / Å^2	0.0092(5)	0.0094(5)

Table S4.2. Selected bond lengths (Å) and angles (°) in $La_3Ni_2B'O_9$ (*B'* = Ta or Nb).

	B' = Ta; *T* = 120 K	*B*' = Nb; *T* = 50 K)
La–O1	2.756(11)	2.729(9)
La–O1	2.702(9)	2.720(8)
La–O1	2.440(10)	2.435(8)
La–O2	2.806(12)	2.828(10)
La–O2	2.437(9)	2.448(8)
La–O2	2.651(10)	2.621(8)
La–O3	2.536(3)	2.534(2)
La–O3	2.426(4)	2.423(3)
2*c*–O1	2.072(5)×2	2.064(5)×2
2*c*–O2	2.067(5)×2	2.057(6)×2
2*c*–O3	2.024(9)×2	2.017(11)×2
2*d*–O1	2.001(5)×2	2.008(6)×2
2*d*–O2	2.007(6)×2	2.016(6)×2
2*d*–O3	2.030(9)×2	2.033(11)×2
O1–2*c*–O2	89.7(4)×2	89.0(3)×2
O1–2*c*–O3	89.1(2)×2	88.9(2)×2
O2–2*c*–O3	88.4(2)×2	88.0(2)×2
O1–2*d*–O2	87.7(4)×2	87.1(3)×2
O1–2*d*–O3	89.5(2)×2	90.0(2)×2
O2–2*d*–O3	89.3(2)×2	89.1(2)×2
2*c*–O1–2*d*	153.7(4)	153.6(3)
2*c*–O2–2*d*	153.6(4)	153.5(3)
2*c*–O3–2*d*	154.6(1)	154.6(1)

Appendix 3: Supporting information for Chapter 5

Table S5.1. Unit–cell parameters of $La_3Ni_2Sb_xTa_yNb_{1-x-y}O_9$ at RT (Space group $P2_1/n$).

	Composition *x*:*y*					
	0.5:0.0	0.25:0.0	0.5:0.5	0.25:0.75	0.0:0.5	0.0:0.25
a / Å	5.5935(1)	5.5893(1)	5.5956(1)	5.5932(1)	5.5880(1)	5.5860(1)
b / Å	5.6388(1)	5.6405(1)	5.6395(1)	5.6420(1)	5.6411(1)	5.6401(1)
c / Å	7.9244(1)	7.9200(1)	7.9269(1)	7.9253(1)	7.9194(1)	7.9166(1)
β/°	90.003(10)	90.018(6)	90.005(8)	90.039(8)	90.017(7)	90.056(8)
V / Å^3	249.940(7)	249.693(6)	250.146(7)	250.093(7)	249.639(6)	249.417(6)
$R_{wp}\|_{XRPD}$ / %	7.39	7.50	7.19	7.41	6.70	7.11
χ^2	1.74	1.74	1.70	1.53	1.62	1.66

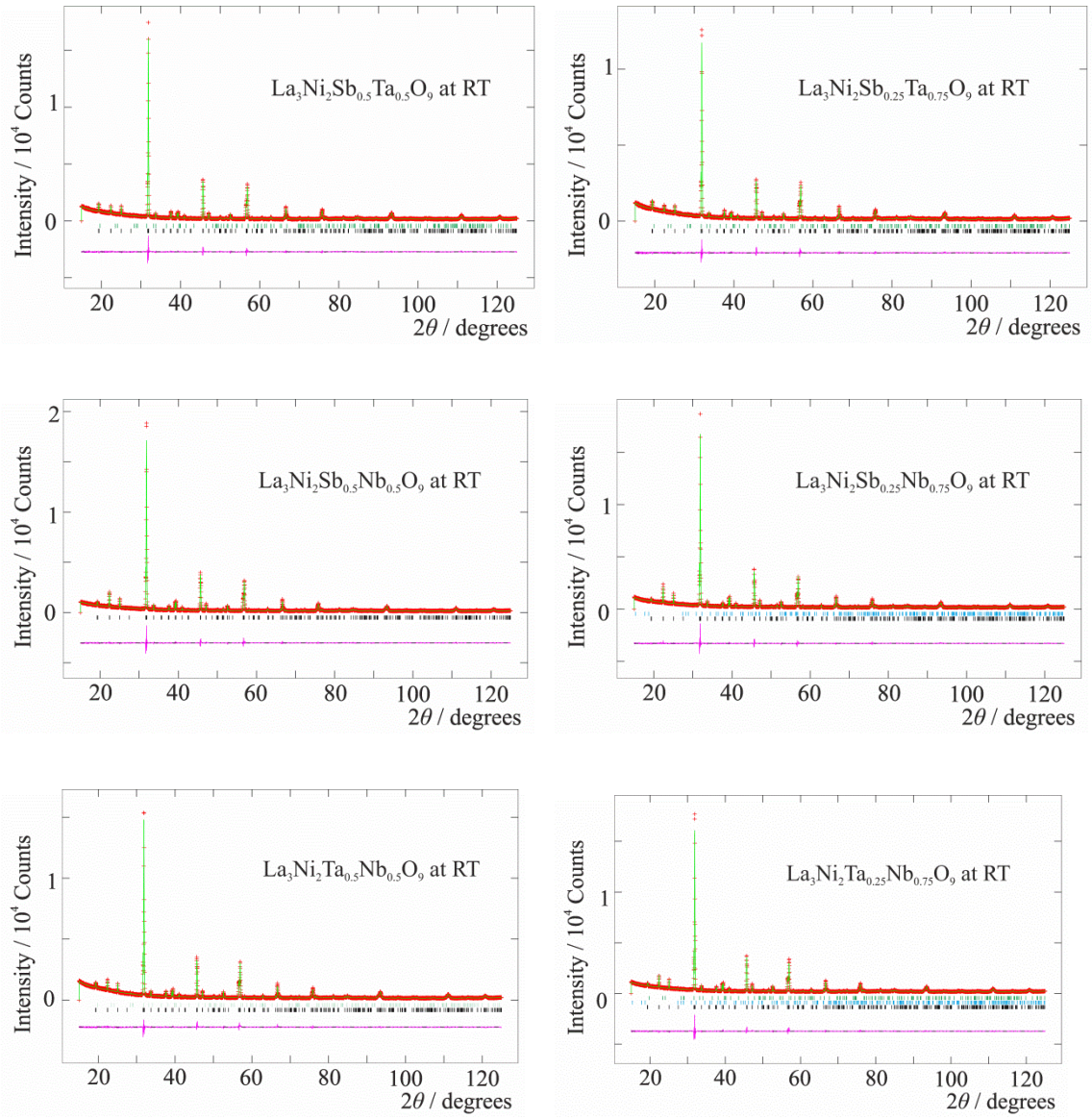


Figure S5.1. Observed (red crosses), calculated (green line) XPRD profiles of $La_3Ni_2Sb_xTa_yNb_{1-x-y}O_9$ collected at room temperature. A difference curve (purple) is shown below. Reflection markers are shown for the principal perovskite phase (black) and for identified impurity phases: $LaNbO_4$ (cyan), $LaTaO_4$ (green).

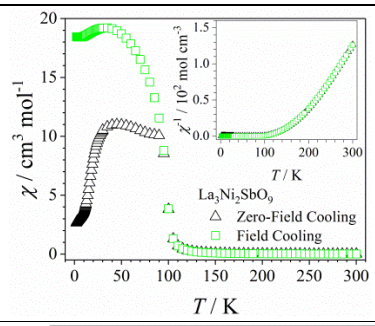
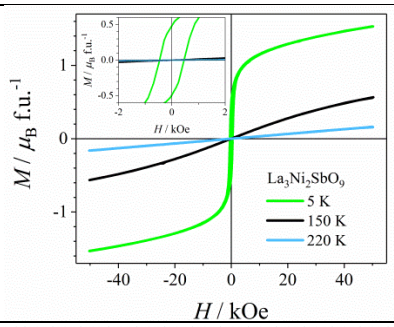
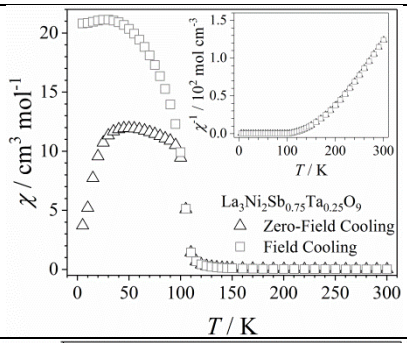
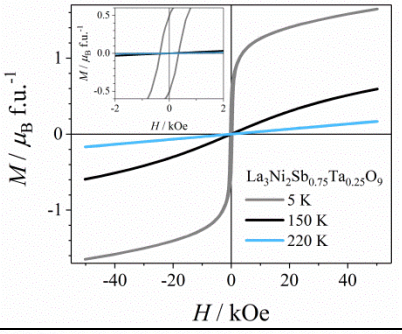
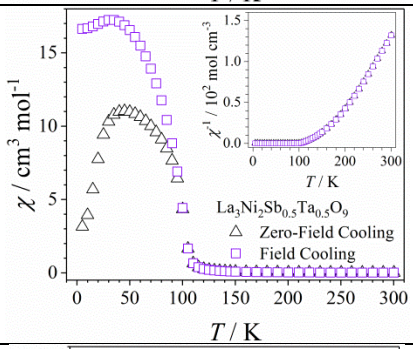
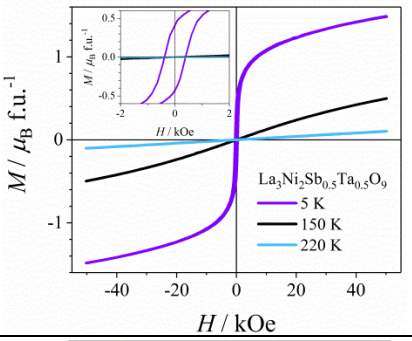
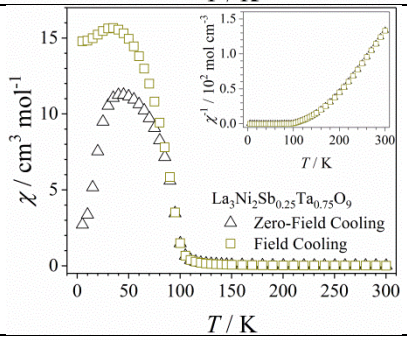
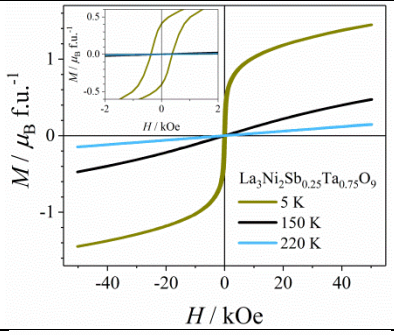
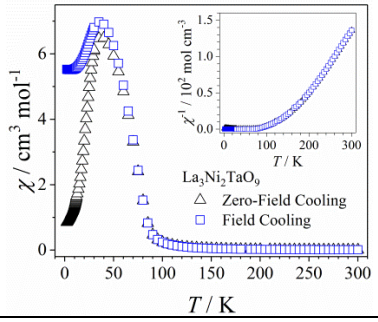
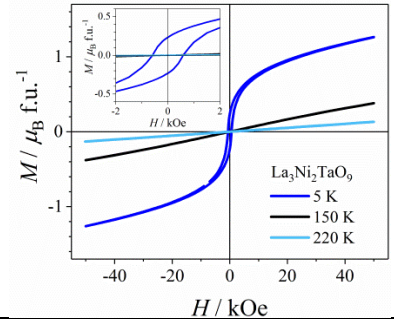
$La_3Ni_2Sb_xTa_yO_9$	$\chi(T)$ [inset: $\chi^{-1}(T)$]	$M(H)$
x:y = 1:0 (i.e. $La_3Ni_2SbO_9$)		
x:y = 0.75:0.25		
x:y = 0.5:0.5		
x:y = 0.25:0.75		
x:y = 0:1 (i.e. $La_3Ni_2TaO_9$)		

Figure S5.2. The molar susceptibility, inverse molar susceptibility (inset) and the field variance of the magnetisation per formula unit of $La_3Ni_2Sb_xNb_yO_9$. For all compositions, both the $\chi_{ZFC}(T)$ and $\chi_{ZFC}^{-1}(T)$ are represented by black triangles whereas $M(H)$ at 150 K and 220 K are in black and cyan respectively.

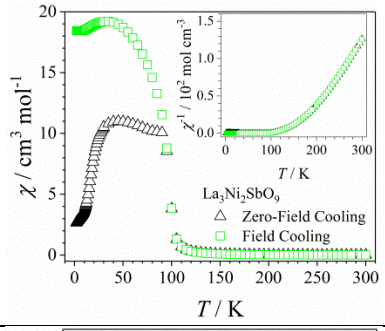
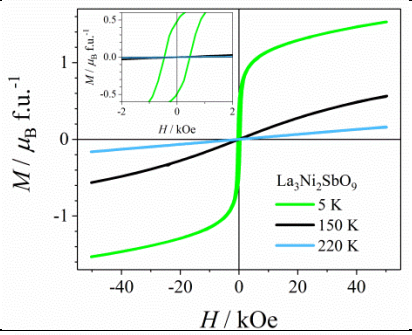
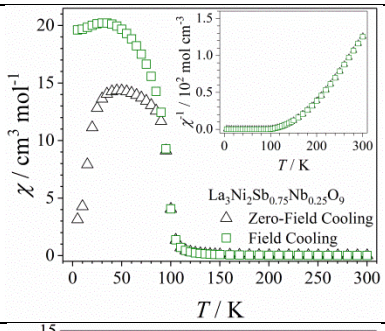
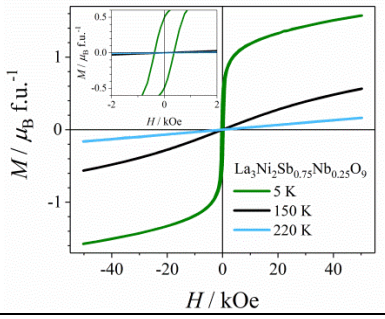
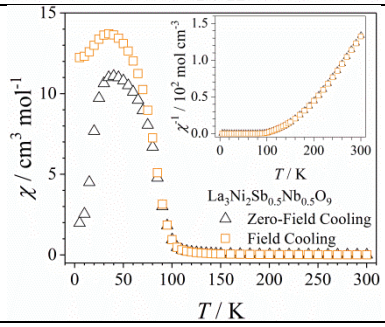
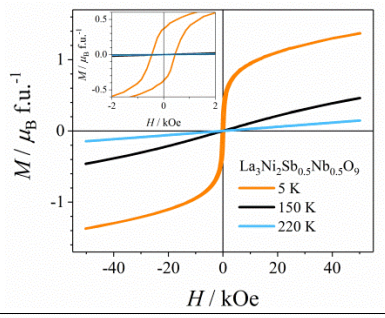
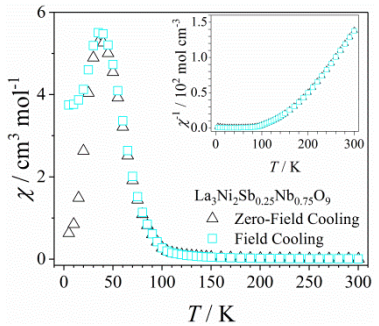
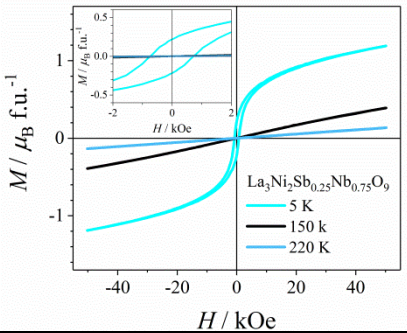
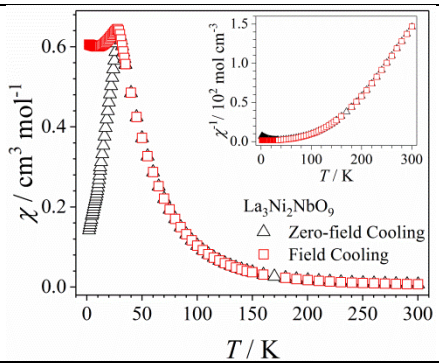
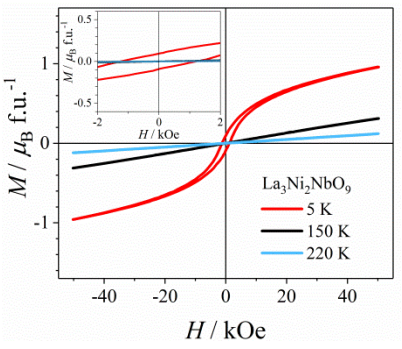
$La_3Ni_2Sb_xNb_{1-x}O_9$	$\chi(T)$ [inset: $\chi^{-1}(T)$]	$M(H)$
$x = 1$ (i.e. $La_3Ni_2SbO_9$)		
$x = 0.75$		
$x = 0.5$		
$x = 0.25$		
$x = 0$ (i.e. $La_3Ni_2NbO_9$)		

Figure S5.3. The molar susceptibility, inverse molar susceptibility (inset) and the field variance of the magnetisation per formula unit of $La_3Ni_2Sb_xNb_{1-x}O_9$. For all compositions, both the $\chi_{ZFC}(T)$ and $\chi_{ZFC}^{-1}(T)$ are represented by black triangles whereas $M(H)$ at 150 K and 220 K are in black and cyan respectively.

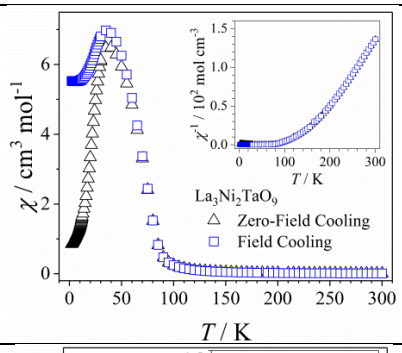
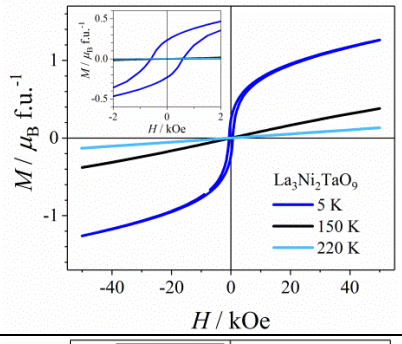
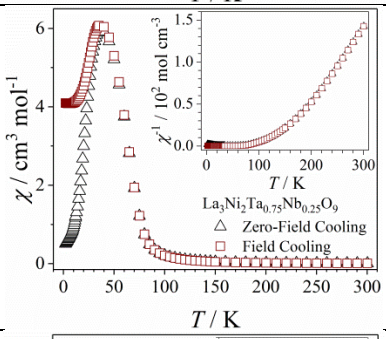
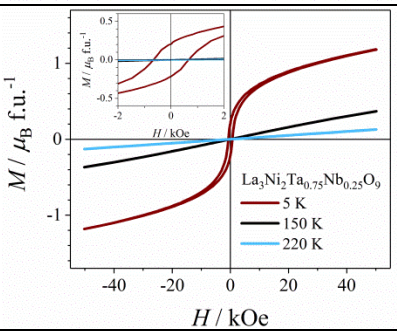
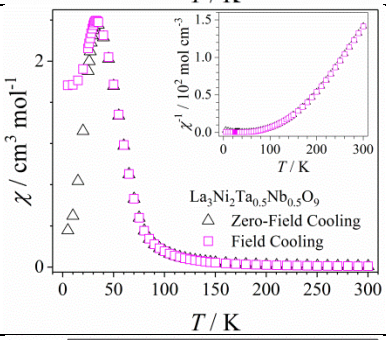
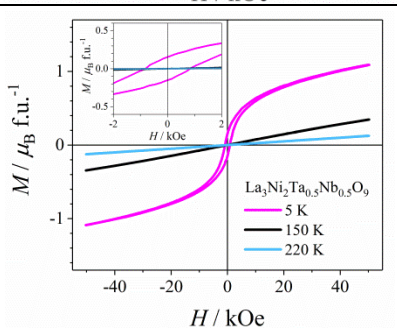
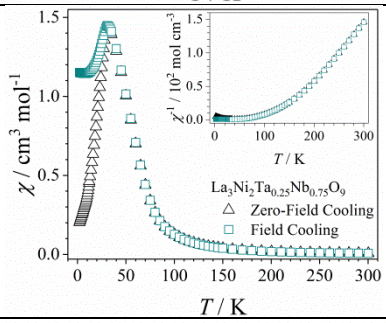
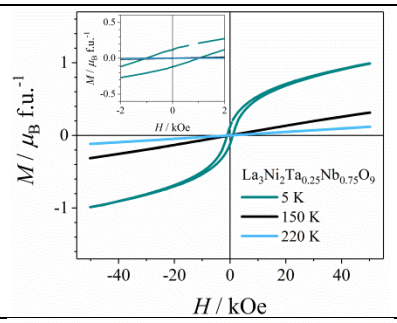
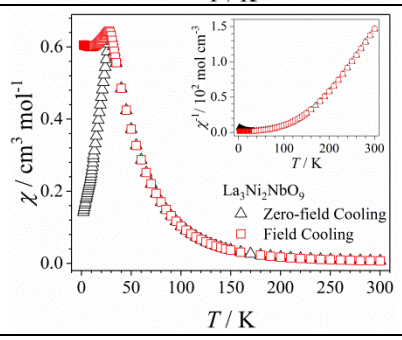
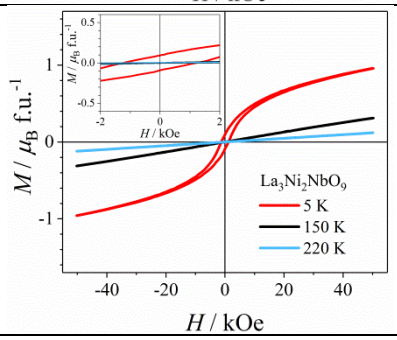
$La_3Ni_2Ta_yNb_{1-y}O_9$	$\chi(T)$ [inset: $\chi^{-1}(T)$]	$M(H)$
$y = 1$ (i.e. $La_3Ni_2TaO_9$)		
$y = 0.75$		
$y = 0.5$		
$y = 0.25$		
$y = 0$ (i.e. $La_3Ni_2NbO_9$)		

Figure S5.4. The molar susceptibility, inverse molar susceptibility (inset) and the field variance of the magnetisation per formula unit of $La_3Ni_2Ta_yNb_{1-y}O_9$. For all compositions, both the $\chi_{ZFC}(T)$ and $\chi_{ZFC}^{-1}(T)$ are represented by black triangles whereas $M(H)$ at 150 K and 220 K are in black and cyan respectively.

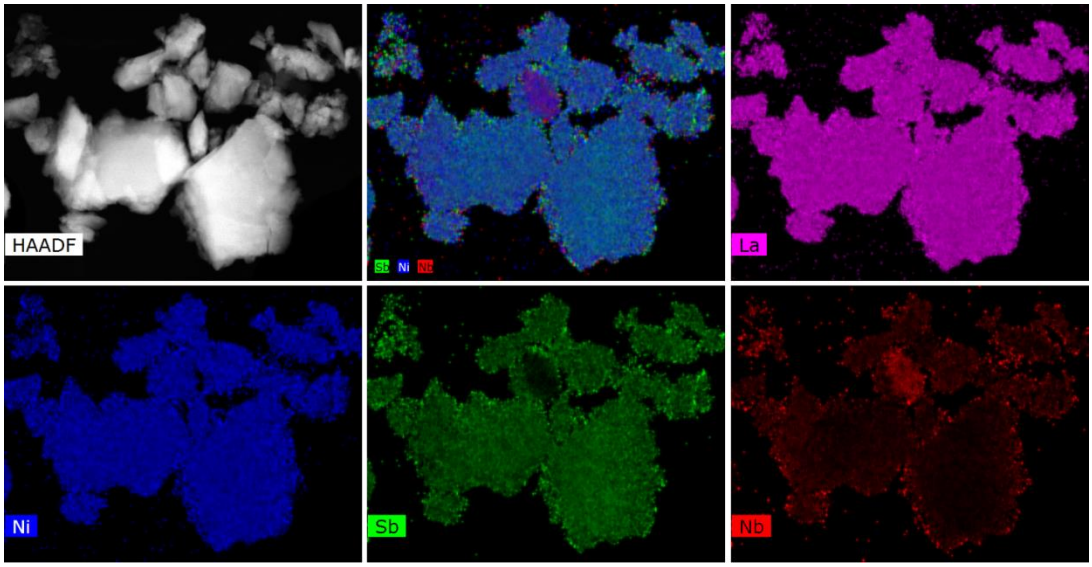


Figure S5.5. HAADF–STEM image of the particles of $La_3Ni_2Sb_{0.75}Nb_{0.25}O_9$ with a mixed (Ni, Sb, Nb) and individual (La/Ni/Sb/Nb) element maps. The element maps are given in counts. The mixed element map clearly shows a particle that contains much more Nb and less Sb than all the other particles.

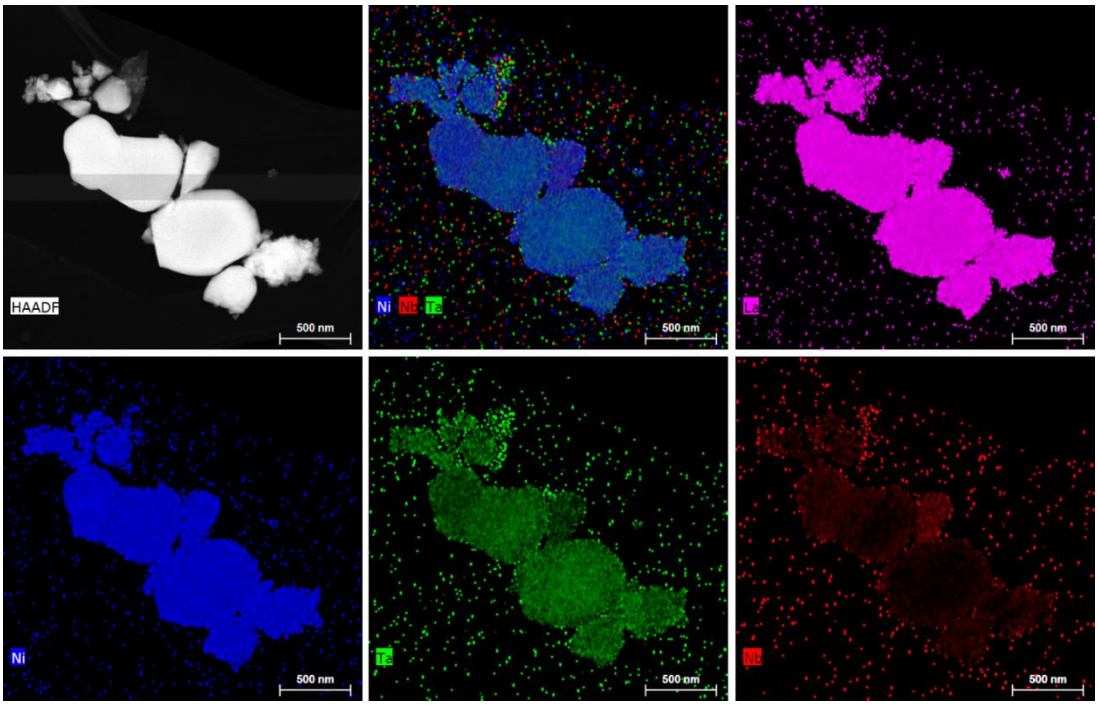


Figure S5.6. HAADF–STEM image of the particles of $La_3Ni_2Ta_{0.75}Nb_{0.25}O_9$ with a mixed (Ni, Nb, Ta) and individual (La/Ni/Nb/Ta) element maps. The element maps are given in counts.

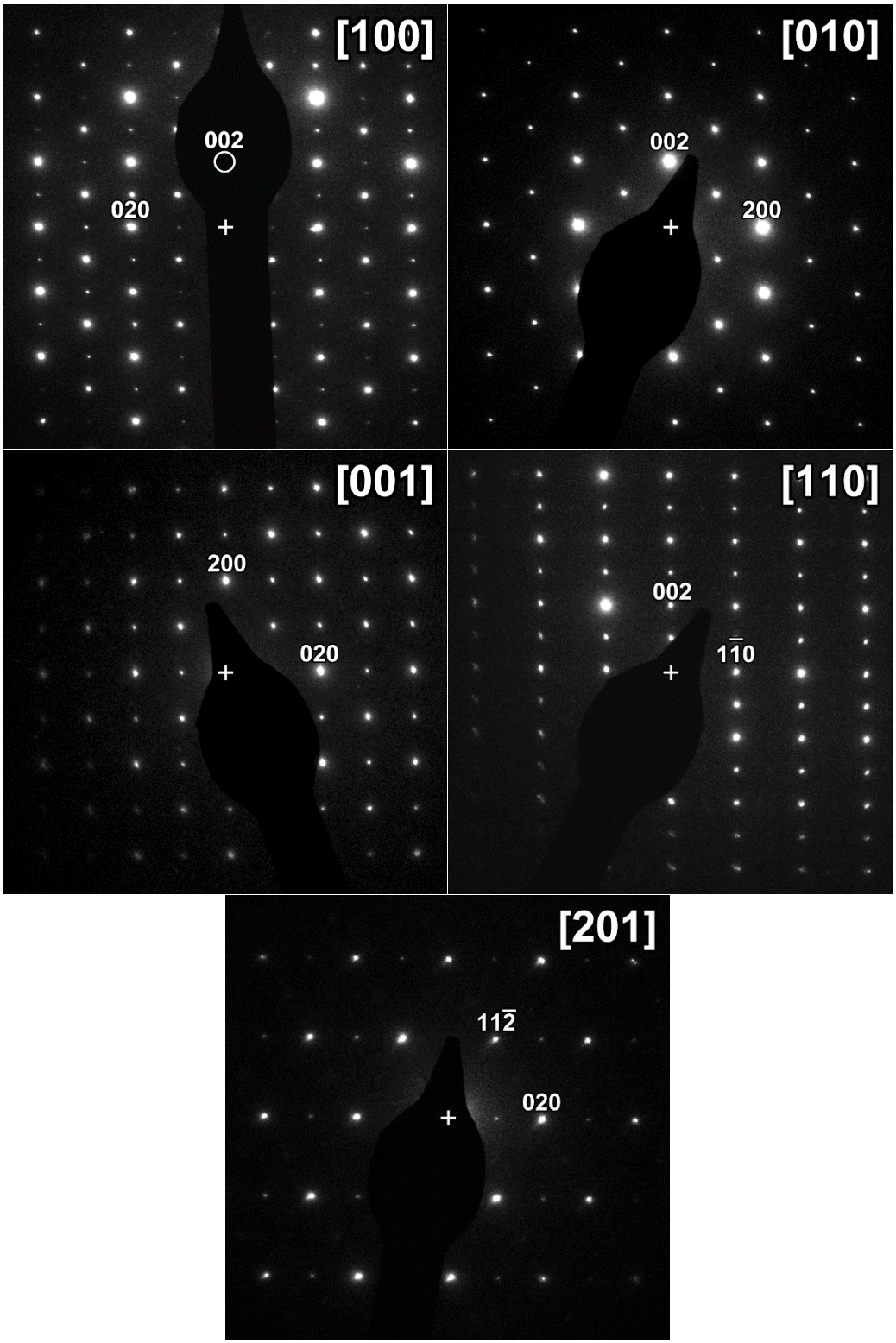


Figure S5.7. SAED patterns of the sample $La_3Ni_2Sb_{0.75}Nb_{0.25}O_9$ along the zone axes [100], [010], [001], [110] and [201] corresponding to space group $P2_1/n$.

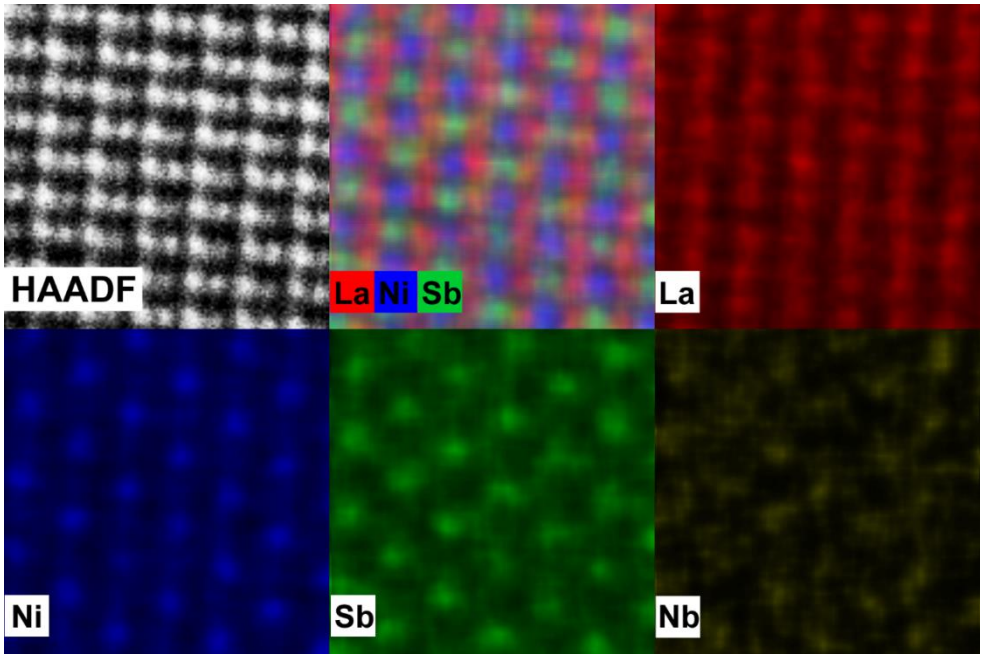


Figure S5.8. Atomic resolution EDX map along the [010] zone axis of $La_3Ni_2Sb_{0.75}Nb_{0.25}O_9$, where La is presented in red and the cations Ni, Sb and Nb in respectively blue, green and yellow. The individual EDX maps of elements Ni, Sb and Nb show ordering between both Ni–Sb and Ni–Nb.

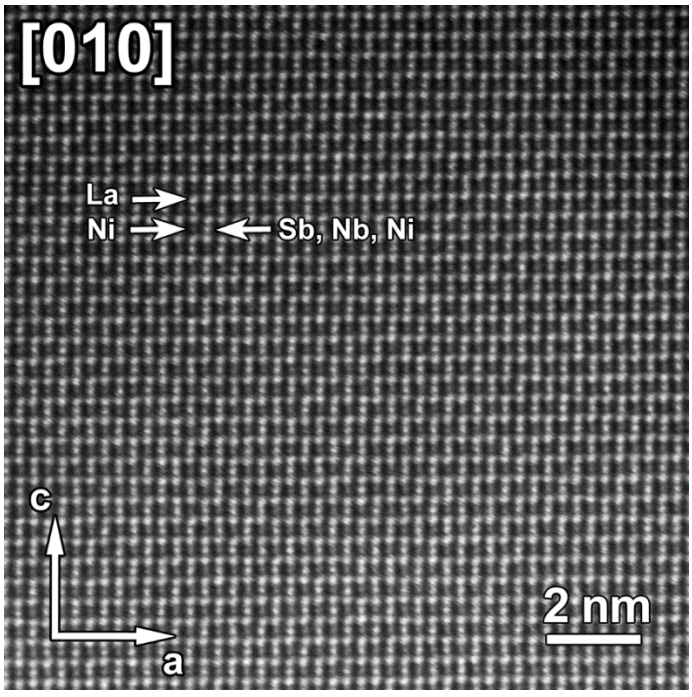


Figure S5.9. HAADF–STEM image of the $La_3Ni_2Sb_{0.75}Nb_{0.25}O_9$ sample along the [010] orientation. The rows of bright atomic columns correspond to the *A* cation La. The rows along the *a*–axis with alternating bright and dark atom columns correspond to Ni and (Sb, Nb and Ni), respectively.

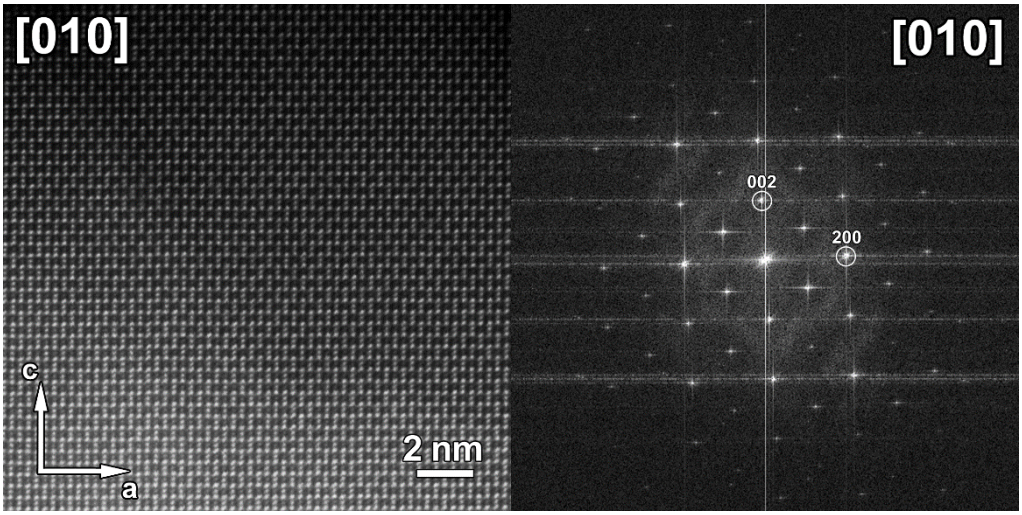


Figure S5.10. Left: HAADF–STEM image of the $La_3Ni_2Sb_{0.75}Nb_{0.25}O_9$ sample along the [010] zone axis, where *B*' cation ordering is clearly present. Right: corresponding fast Fourier Transform (FFT), in which diffuse intensities are observed.

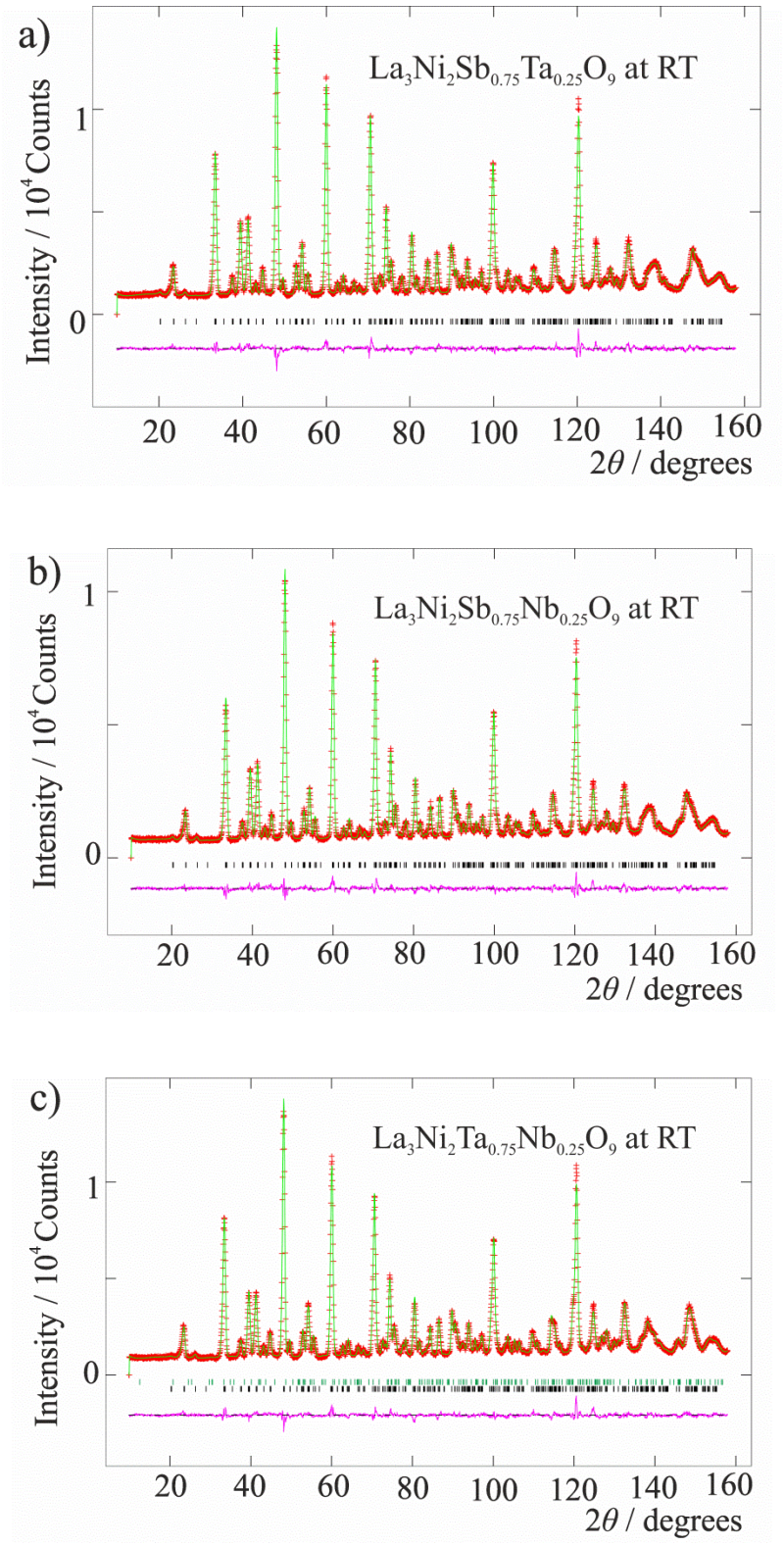


Figure S5.11. Observed (red crosses) and calculated (green line) NPD profiles of (a) $La_3Ni_2Sb_{.75}Ta_{0.25}O_9$, (b) $La_3Ni_2Sb_{.75}Nb_{0.25}O_9$ and (c) $La_3Ni_2Ta_{.75}Nb_{0.25}O_9$ at room temperature using λ = 1.622 Å; a difference curve (purple) is shown below. Reflection markers are shown for any $LaTaO_4$ impurity (top, green) and the principal perovskite phase (bottom, black).

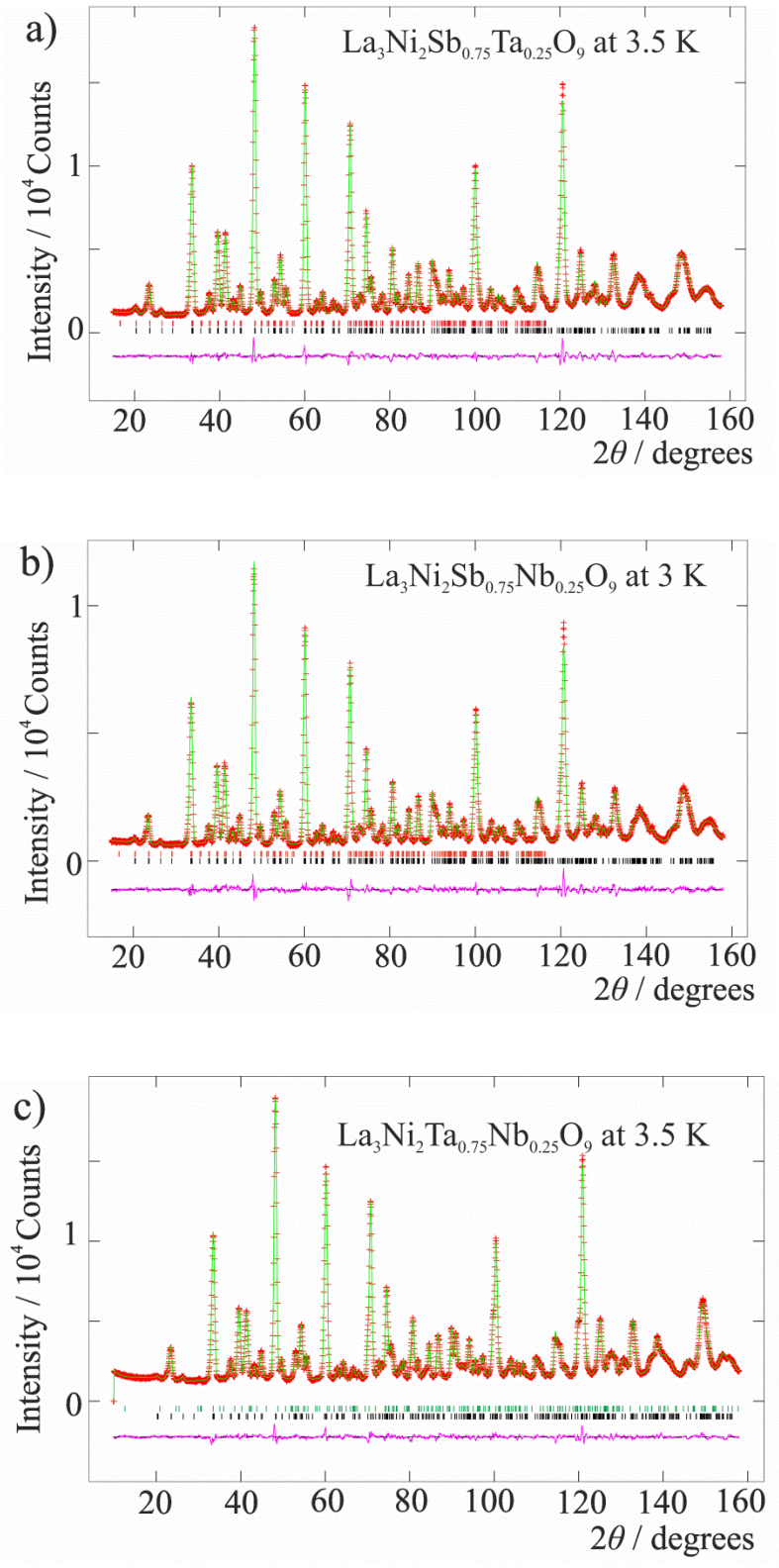
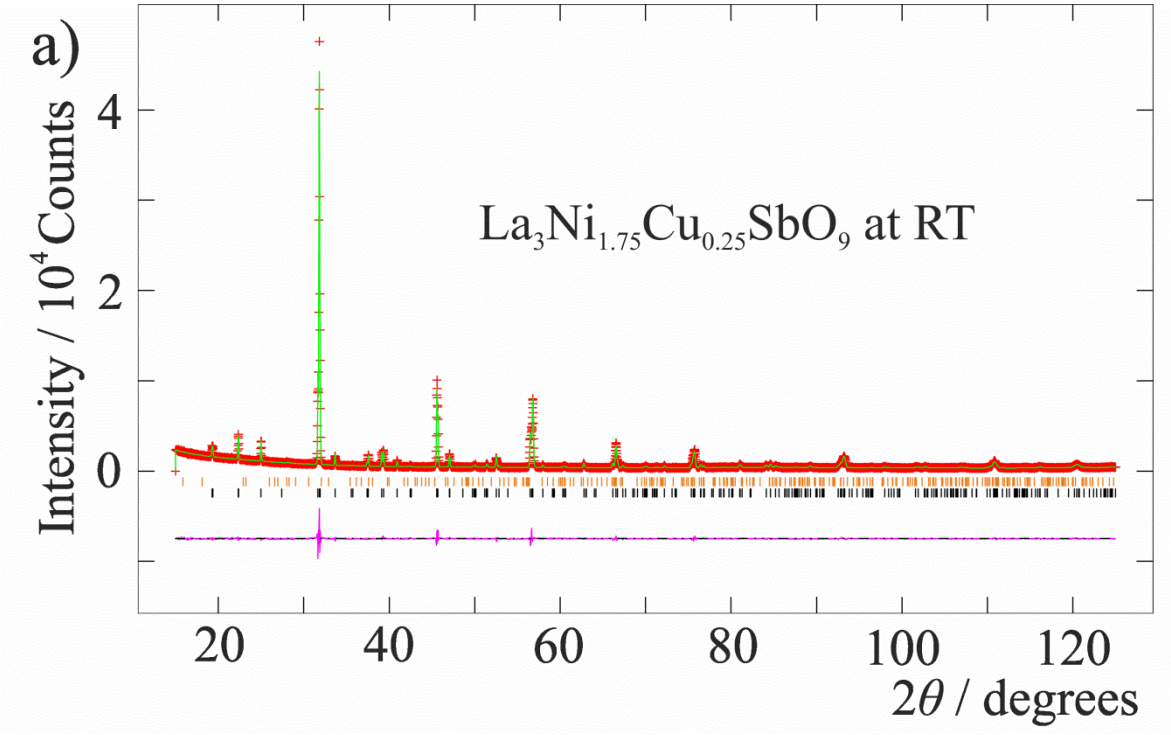
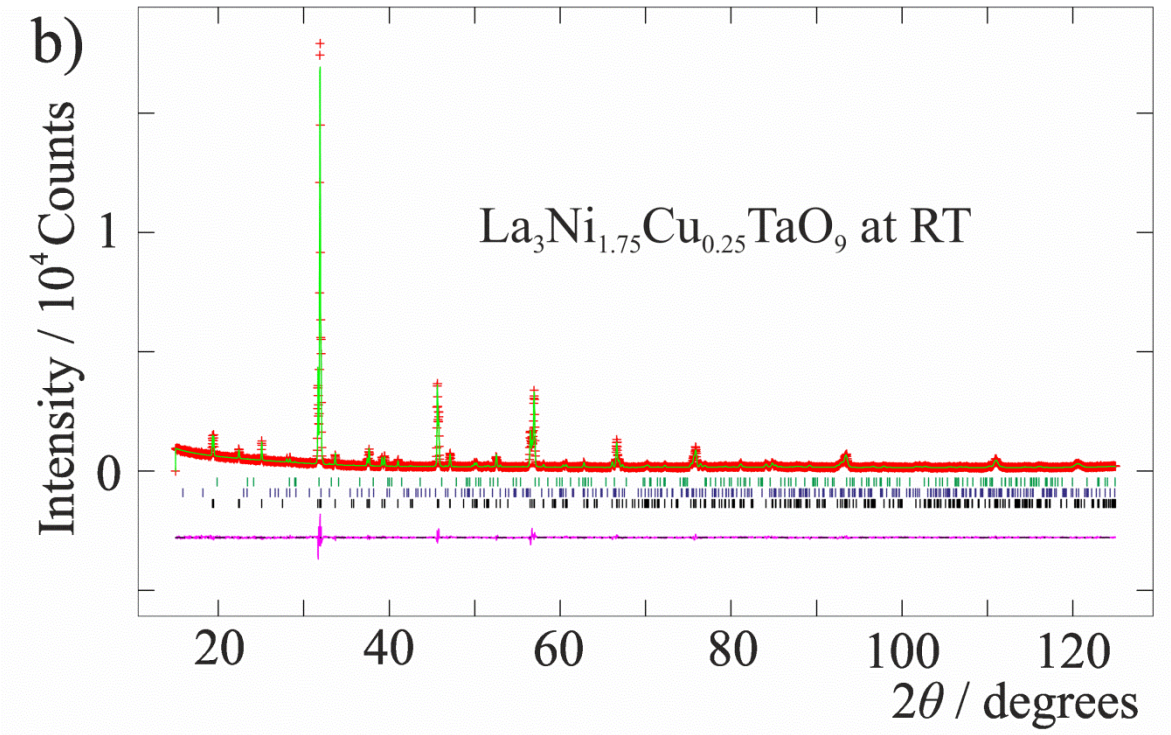
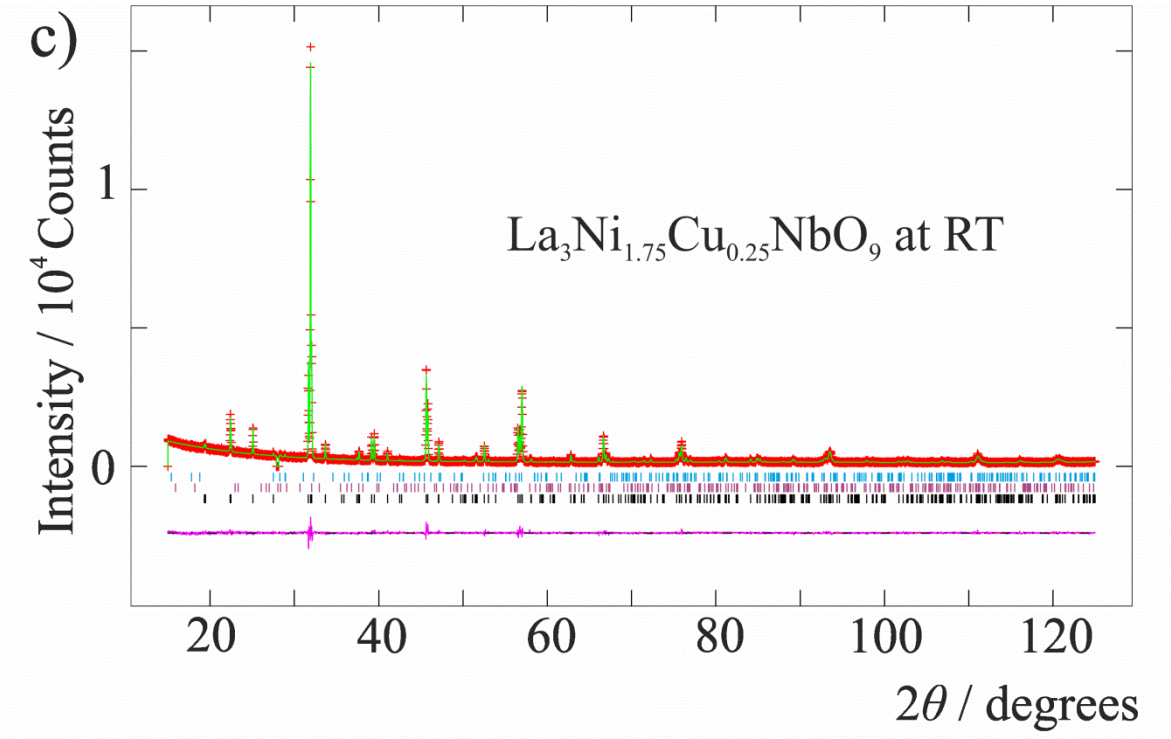


Figure S5.12. Observed (red crosses) and calculated (green line) NPD profiles of (a) $La_3Ni_2Sb_{.75}Ta_{0.25}O_9$, (b) $La_3Ni_2Sb_{.75}Nb_{0.25}O_9$ and (c) $La_3Ni_2Ta_{.75}Nb_{0.25}O_9$ at low T using λ = 1.622 Å; a difference curve (purple) is shown below. Reflection markers are shown for any $LaTaO_4$ impurity (green) and the perovskite phase (magnetic, red; structural, black).

Appendix 4: Supporting information for Chapter 6







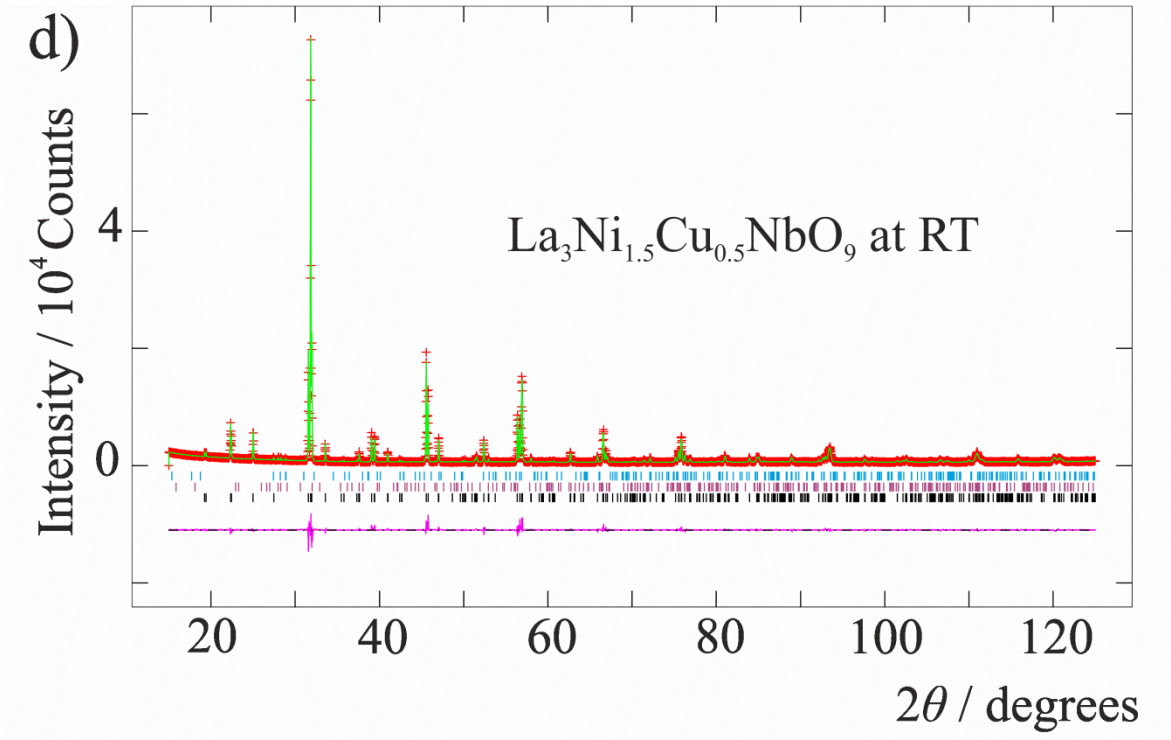


Figure S6.1. Observed (red crosses) and calculated (green line) XRPD profiles of $La_3Ni_{2-x}Cu_xB'O_9$ compositions at room temperature. A difference curve (purple) is shown below. Reflection positions are marked for the principal perovskite phase (bottom, black) and (a) La_3SbO_7 (top, orange); (b) La_3TaO_7 (middle, blue), $LaTaO_4$ (top, green); (c) and (d) La_3NbO_7 (middle, purple), $LaNbO_4$ (top, cyan).

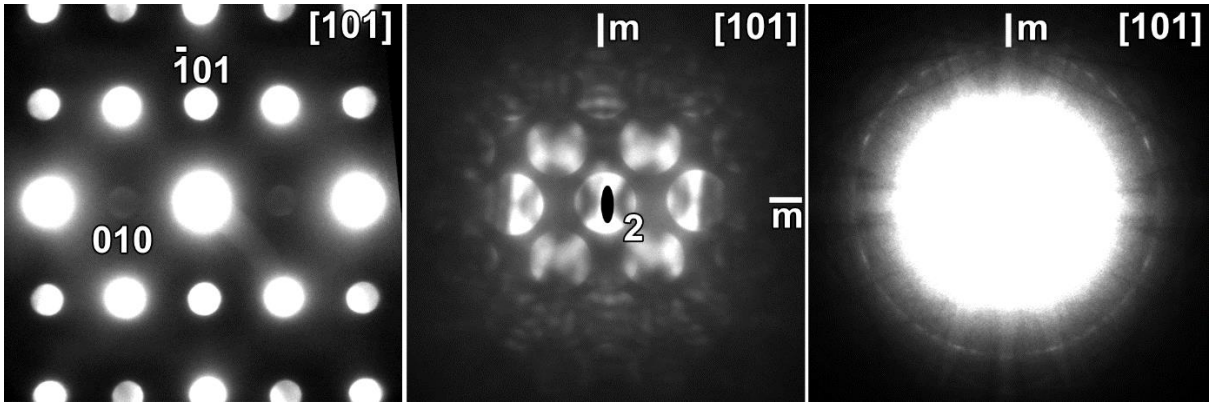


Figure S6.2. CBED patterns of $La_3Ni_{1.75}Cu_{0.25}NbO_{9.}$

The space group for $La_3Ni_{1.75}Cu_{0.25}NbO_9$ was determined from a combination of SAED and CBED data and confirmed using HAADF–STEM images. The SAED patterns of the three main zones were already presented in Figure 6.1 of the main text. Reflections in conflict with the reflection conditions: *h00*, *0k0* and *00l: h, k, l* = 2*n* are present in the SAED patterns of zone axes [100] and [001]. In the SAED pattern of [010] the reflection conditions for *h00* and *00l* are satisfied and thus the reflections *h00* and *00l* corresponding to *h, l* ≠ 2*n* present in other zones can be attributed to double diffraction. In order to check the *0k0* = 2*n* condition, the sample was tilted around the *b*–axis in order to see if the reflections *0k0: k* ≠ 2*n* disappear, but they remained present although very weak, probably because there simply is no orientation in which the double diffraction paths can be completely eliminated. To confirm this, CBED patterns of the orientation [101], see Figure S6.2, were obtained to make sure that the condition *0k0: k* = 2*n* is satisfied. The CBED pattern on the left of Figure S6.2, taken with a small condenser aperture, shows that the ±010 reflections are much weaker than other reflections, although they are still present. However, small dark lines run through these reflections. These are Gjonnes–Moodie lines and they indicate that these reflections are indeed extinct because of a screw axis. Hence the reflection conditions and cell parameters, taken together, are consistent with the space group assignment made on the basis of the XRPD data. The other two CBED patterns in

Figure S6.2 support this conclusion. They were taken with larger condenser apertures, thus allowing the contrast within the discs to be seen. They show the "whole pattern projection symmetry" (middle) and "whole pattern symmetry" (right side) of zone [101]. They indicate that the point group symmetry is 2/*m* (if the crystal class is monoclinic), which supports the assignment of $P2_1/n$ as the space group. Further support for this assignment is provided by Figure S6.3, which shows four HAADF–STEM images, taken along different zone axes, and their fast Fourier Transforms (FFTs); the reflections seen in the FFTs can all be indexed in $P2_1/n$.

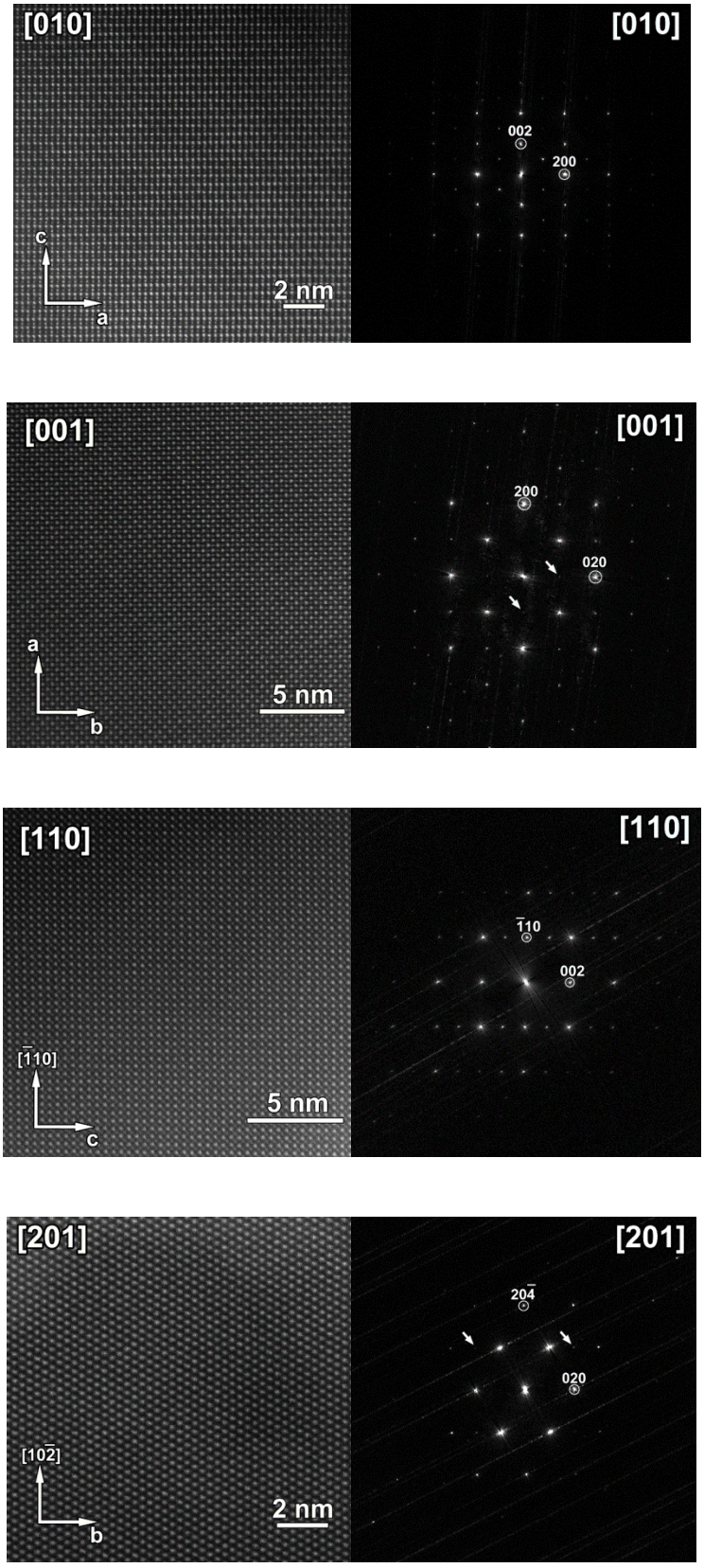


Figure S6.3. Left: High resolution HAADF–STEM image of $La_3Ni_{1.75}Cu_{0.25}NbO_9$ along the [010], [001], [110] and [201] zone axes. Right: the corresponding FFT's are shown in which the arrows indicate the weaker reflections corresponding to the $P2_1/n$ cell.

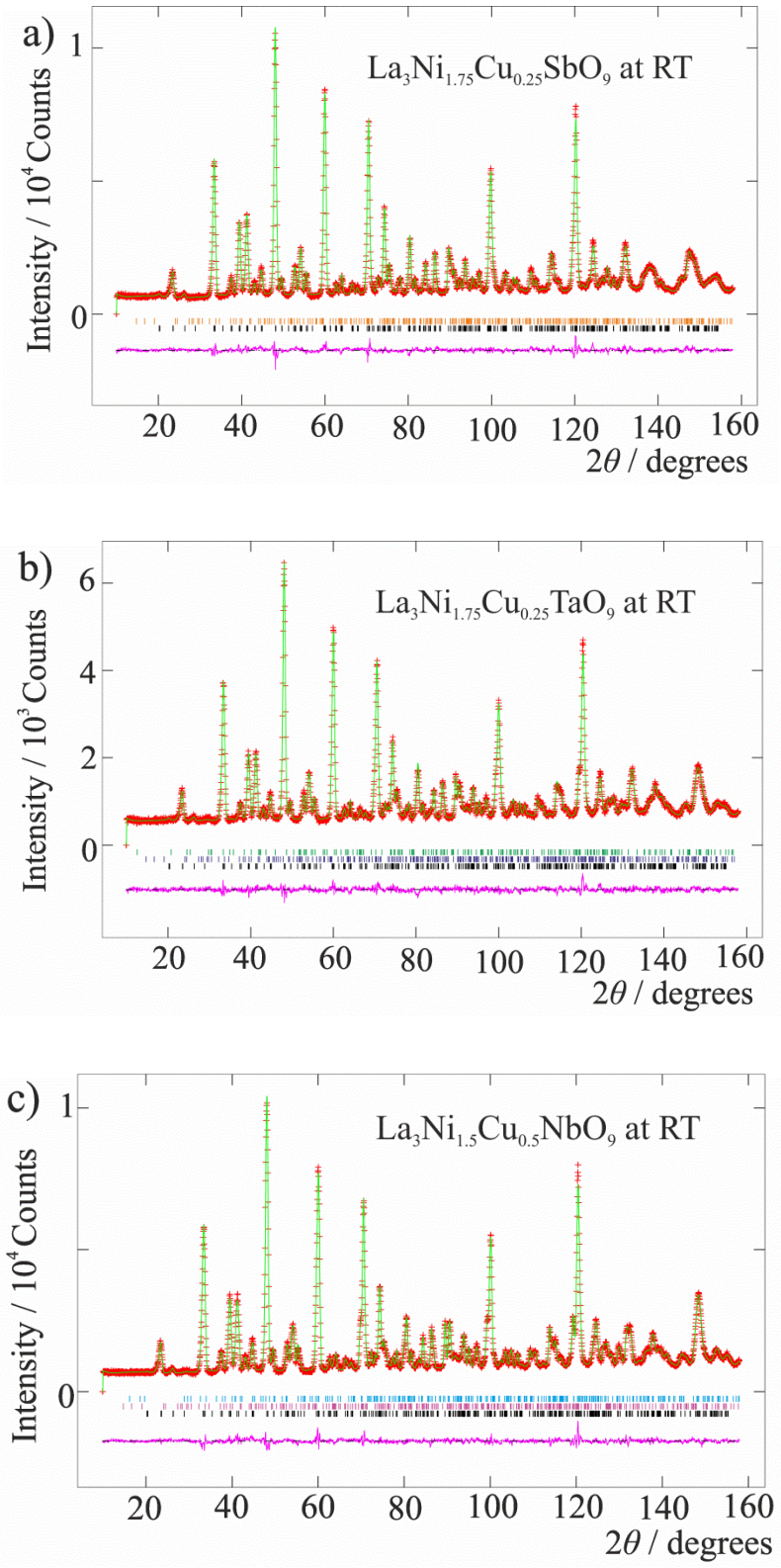


Figure S6.4. Observed (red crosses) and calculated (green line) NPD profiles of $La_3Ni_{2-x}Cu_xB'O_9$ compositions at room temperature using λ = 1.622 Å. A difference curve (purple) is shown below. Reflection positions are marked for the principal perovskite phase (bottom, black) and (a) La_3SbO_7 (top, orange); (b) La_3TaO_7 (middle, blue), $LaTaO_4$ (top, green); (c) La_3NbO_7 (middle, purple), $LaNbO_4$ (top, cyan).

Table S6.1. Structural parameters of $La_3Ni_{1.75}Cu_{0.25}SbO_9$ at RT and 3 K (Space group $P2_1/n$).

		RT	3 K
a / Å		5.6026(2)	5.5921(1)
b / Å		5.6424(1)	5.6397(1)
c / Å		7.9336(2)	7.9203(2)
β / °		90.05(1)	90.06(1)
V / Å^3		250.80(1)	249.79(1)
$R_{wp\|NPD}$ / %		4.37	3.96
χ^2		2.272	2.561
La	x	0.4898(5)	0.4894(5)
4*e* (*x y z*)	y	0.4613(2)	0.4589(2)
	z	0.251(1)	0.254(1)
	U_{ISO} / Å^2	0.0187(3)	0.0148(3)
Ni/Cu/Sb1	U_{ISO} / Å^2	0.0038(2)	0.0018(2)
2*c* (0 ½ 0)	Ni occupancy	0.833	0.833
	Cu occupancy	0.167	0.167
	Sb occupancy	0	0
Ni/Cu/Sb2	U_{ISO} / Å^2	0.0038(2)	0.0018(2)
2*d* (½ 0 0)	Ni occupancy	0.333	0.333
	Cu occupancy	0	0
	Sb occupancy	0.667	0.667
O1	x	0.790(1)	0.788(1)
4*e* (*x y z*)	y	0.795(1)	0.794(1)
	z	–0.0364(6)	–0.0378(6)
	U_{ISO} / Å^2	0.004(1)	0.004(1)
O2	x	0.711(1)	0.706(1)
4*e* (*x y z*)	y	0.282(1)	0.287(1)
	z	–0.0465(7)	–0.0464(7)
	U_{ISO} / Å^2	0.017(1)	0.011(1)
O3	x	0.5789(5)	0.5810(4)
4*e* (*x y z*)	y	0.0174(4)	0.0187(3)
	z	0.245(1)	0.249(1)
	U_{ISO} / Å^2	0.0147(6)	0.0090(4)

Table S6.2. Structural parameters of $La_3Ni_{1.75}Cu_{0.25}TaO_9$ at RT and 3 K (Space group $P2_1/n$).

		RT	3 K
a / Å		5.5935(2)	5.5817(1)
b / Å		5.6510(2)	5.6498(1)
c / Å		7.9250(2)	7.9115(2)
β / °		90.04(1)	90.04(1)
V / Å^3		250.50(1)	249.50(1)
$R_{wp\|NPD}$ / %		4.36	4.05
χ^2		1.676	1.958
La	x	0.4898(7)	0.4915(5)
4*e* (*x y z*)	y	0.4605(2)	0.4580(2)
	z	0.257(1)	0.245(1)
	U_{ISO} / Å^2	0.0171(4)	0.0152(4)
Ni/Cu/Ta1	U_{ISO} / Å^2	0.0031(2)	0.0005(2)
2*c* (0 ½ 0)	Ni occupancy	0.833	0.833
	Cu occupancy	0.167	0.167
	Ta occupancy	0	0
Ni/Cu/Ta2	U_{ISO} / Å^2	0.0031(2)	0.0005(2)
2*d* (½ 0 0)	Ni occupancy	0.333	0.333
	Cu occupancy	0	0
	Ta occupancy	0.667	0.667
O1	x	0.790(1)	0.795(1)
4*e* (*x y z*)	y	0.793(1)	0.798(1)
	z	–0.0367(8)	–0.0375(7)
	U_{ISO} / Å^2	0.004(1)	0.001(1)
O2	x	0.709(1)	0.713(1)
4*e* (*x y z*)	y	0.286(1)	0.283(1)
	z	–0.0470(8)	–0.0457(7)
	U_{ISO} / Å^2	0.016(2)	0.011(1)
O3	x	0.5798(6)	0.5799(5)
4*e* (*x y z*)	y	0.0176(5)	0.0185(4)
	z	0.246(1)	0.243(2)
	U_{ISO} / Å^2	0.0161(8)	0.0123(5)

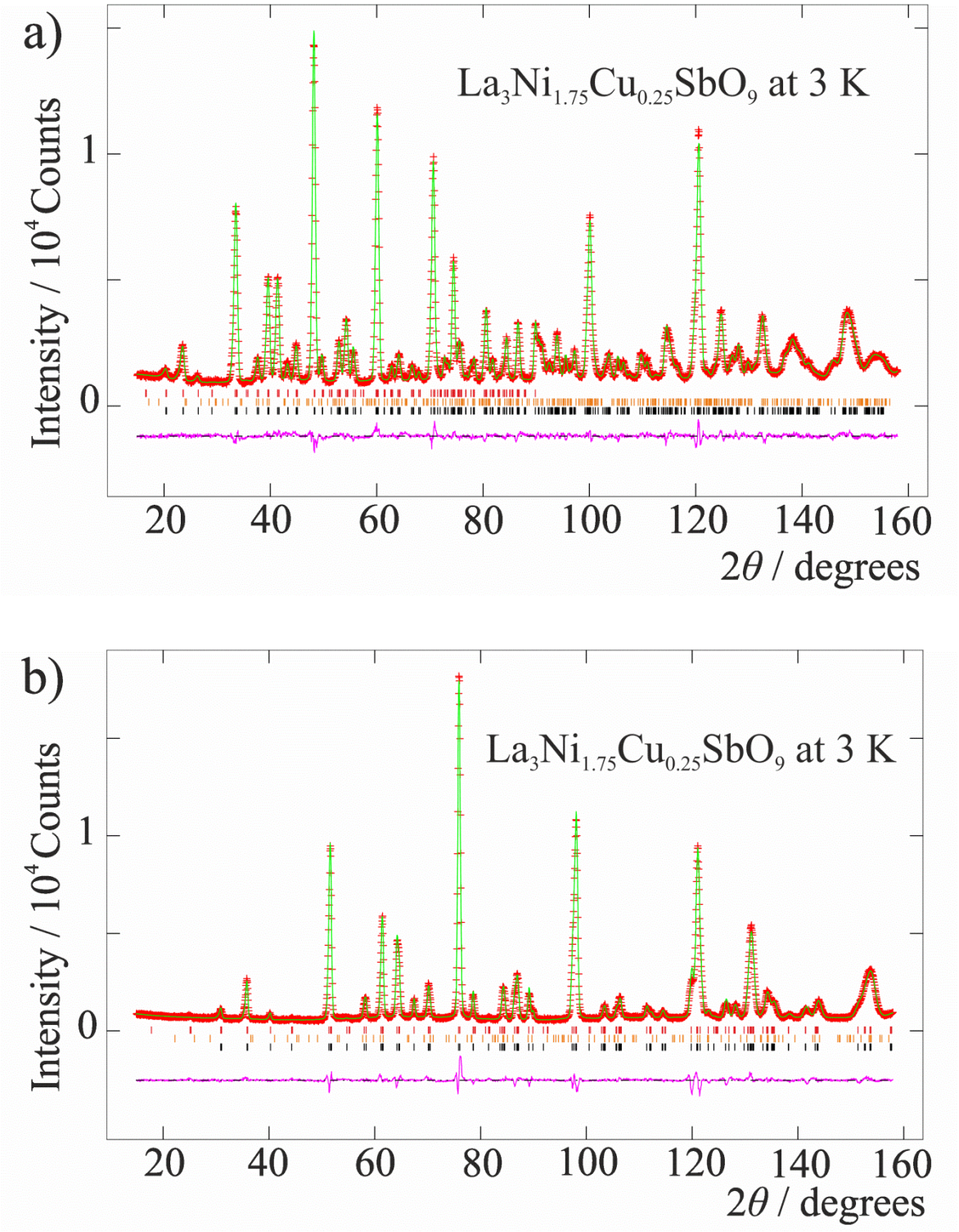


Figure S6.5. Observed (red crosses) and calculated (green line) NPD profiles of $La_3Ni_{1.75}Cu_{0.25}SbO_9$ at 3 K using λ = (a) 1.622 and (b) 2.4395 Å. A difference curve (purple) is shown below. Reflection markers are shown for the magnetic (red) and structural (black) perovskite phases, and La_3SbO_7 (orange).

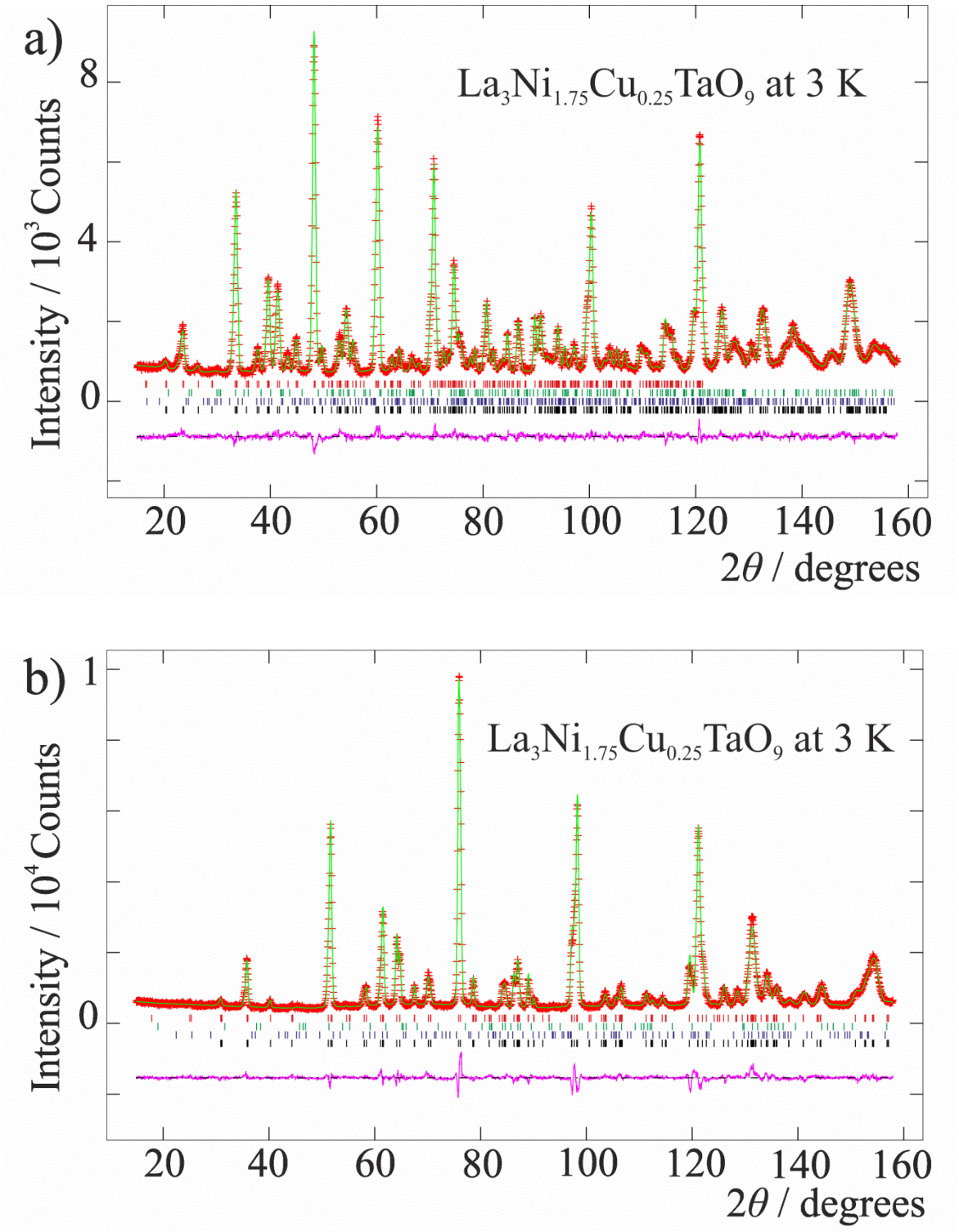


Figure S6.6. Observed (red crosses) and calculated (green line) NPD profiles of $La_3Ni_{1.75}Cu_{0.25}TaO_9$ at 3 K using λ = (a) 1.622 and (b) 2.4395 Å. A difference curve (purple) is shown below. Reflection markers are shown for the magnetic (red) and structural (black) perovskite phases, $LaTaO_4$ (green) and La_3TaO_7 (blue).

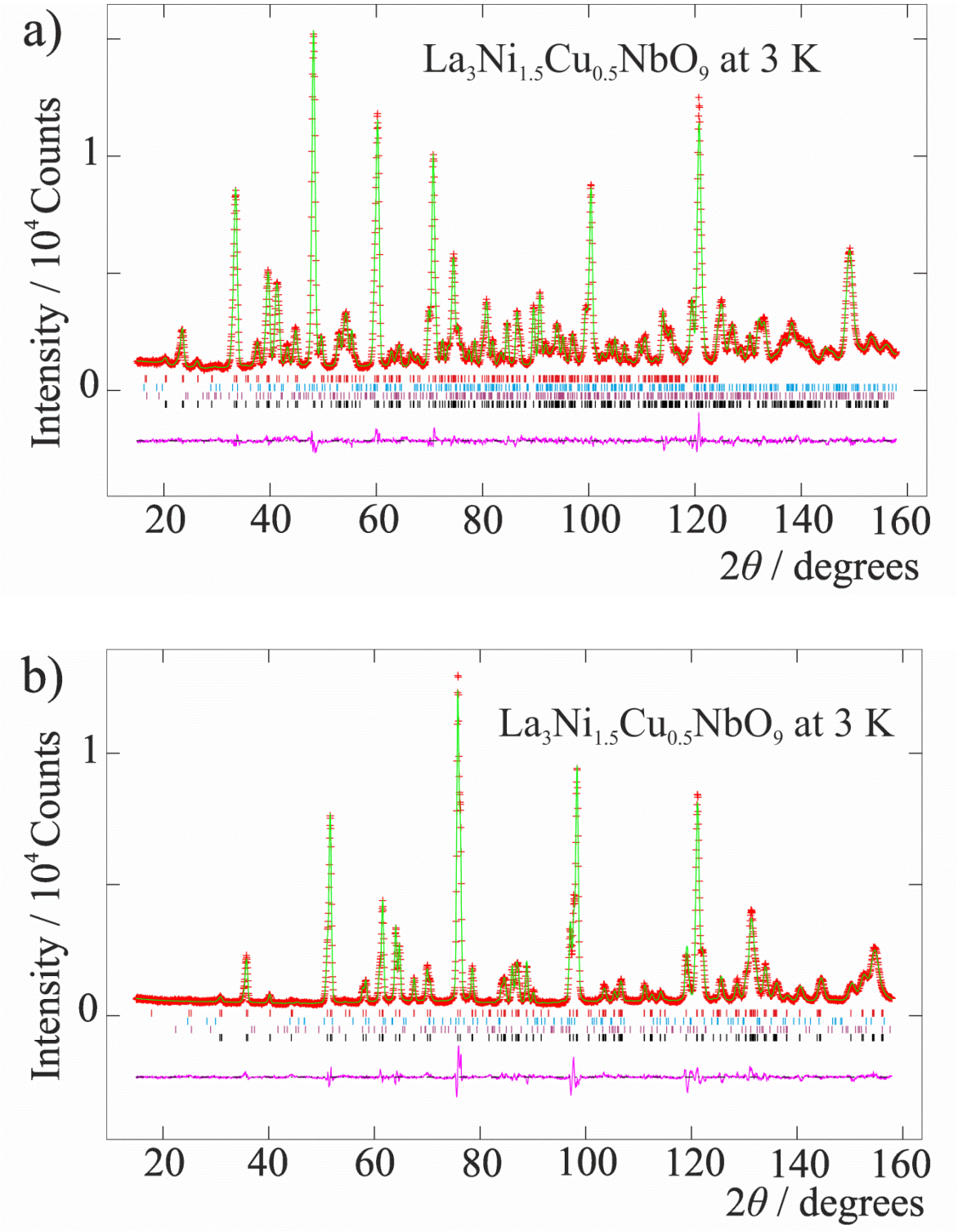


Figure S6.7. Observed (red crosses) and calculated (green line) NPD profiles of $La_3Ni_{1.5}Cu_{0.5}NbO_9$ at 3 K using λ = (a) 1.622 and (b) 2.4395 Å. A difference curve (purple) is shown below. Reflection markers are shown for the magnetic (red) and structural (black) perovskite phases, $LaNbO_4$ (cyan) and La_3NbO_7 (purple).

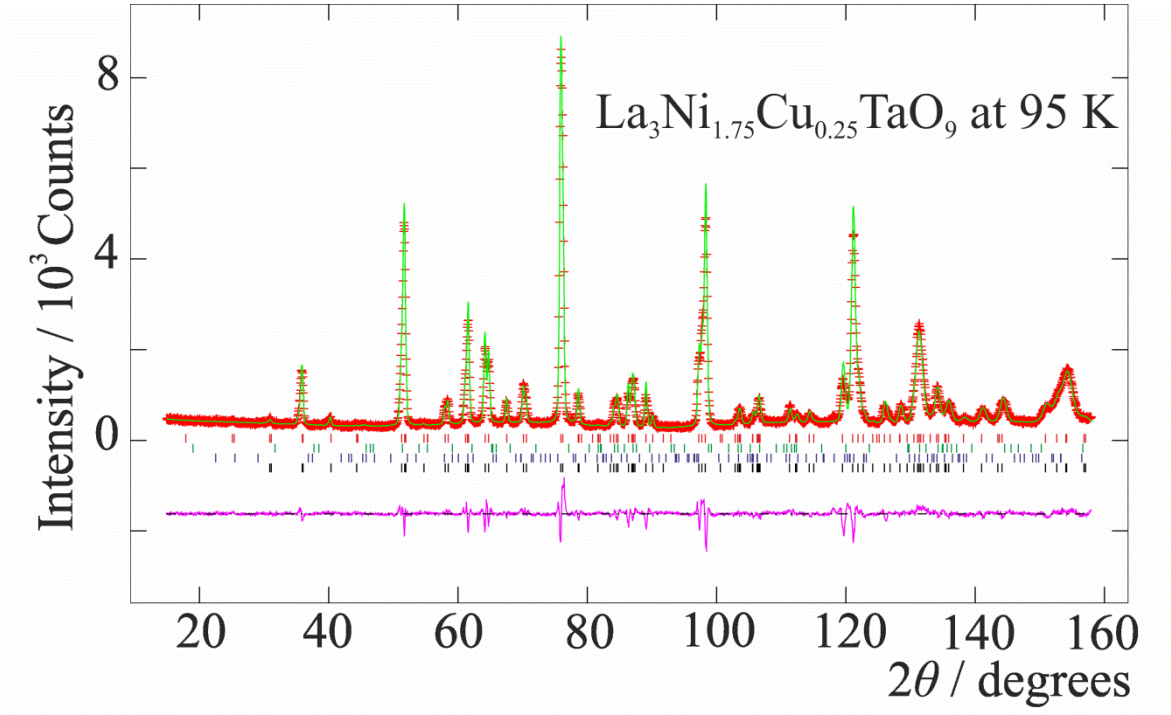


Figure S6.8. Observed (red crosses) and calculated (green line) NPD profiles of $La_3Ni_{1.75}Cu_{0.25}TaO_9$ at 3 K using λ = 2.4395 Å. A difference curve (purple) is shown below. Reflection markers are shown for the magnetic (red) and structural (black) perovskite phases, $LaTaO_4$ (green) and La_3TaO_7 (blue).

Appendix 5: Supporting information for Chapter 7

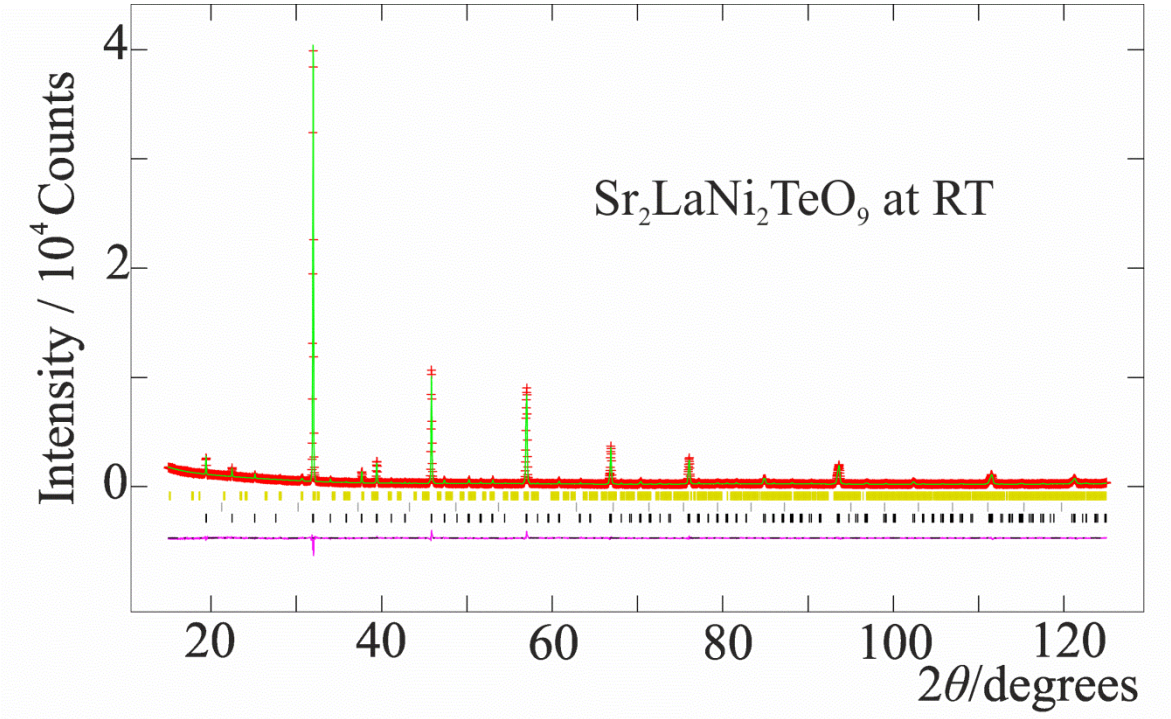


Figure S7.1. Observed (red crosses) and calculated (green line) XRPD profiles of $SrLa_2Ni_2TeO_9$ compositions at room temperature. A difference curve (purple) is shown below. The black, grey and gold vertical makers represent the Bragg reflection markers for $SrLa_2Ni_2TeO_9$, NiO and Sr_3TeO_6, respectively.

Table S7.1. Structural parameters of $SrLa_2Ni_2TeO_9$ at 50 K. (Space group $P2_1/n$).

		50 K
a / Å		5.5902(1)
b / Å		5.5804(1)
c / Å		7.8887(2)
β / °		90.026(5)
V / Å^3		246.09(1)
$R_{wp\|NPD}$ / %		5.33
χ^2		3.859
Sr/La	x	0.5053(9)
4*e* (*x y z*)	y	0.5241(5)
	z	0.250(2)
	U_{ISO} / Å^2	0.0230(4)
	Sr occupancy	0.3333
	La occupancy	0.6667
Ni/Te1	U_{ISO} / Å^2	0.0005(2)
2*c* (0 ½ 0)	Ni occupancy	0.83
	Te occupancy	0.17
Ni/Te2	U_{ISO} / Å^2	0.0005(2)
2*d* (½ 0 0)	Ni occupancy	0.50
	Te occupancy	0.50
O1	x	0.231(1)
4*e* (*x y z*)	y	0.221(2)
	z	–0.0353(13)
	U_{ISO} / Å^2	0.0142(21)
O2	x	0.290(1)
4*e* (*x y z*)	y	0.721(2)
	z	–0.0352(11)
	U_{ISO} / Å^2	0.003(2)
O3	x	0.4322(7)
4*e* (*x y z*)	y	0.9899(7)
	z	0.246(2)
	U_{ISO} / Å^2	0.0101(7)

Table S7.2. Selected bond lengths (Å) and angles (°) in $SrLa_2Ni_2TeO_9$ at 50 K.

	50 K
Sr/La–O1	2.835(15)
Sr/La–O1	2.656(13)
Sr/La–O1	2.518(14)
Sr/La–O2	2.775(16)
Sr/La–O2	2.458(14)
Sr/La–O2	2.727(13)
Sr/La–O3	3.009(4)
Sr/La–O3	2.631(4)
2*c*–O1	2.040(9) ×2
2*c*–O2	2.056(7) ×2
2*c*–O3	2.041(11) ×2
2*d*–O1	1.966(9) ×2
2*d*–O2	1.969(7) ×2
2*d*–O3	1.977(11) ×2
O1–2*c*–O2	86.5(5) ×2
O1–2*c*–O3	89.8(3) ×2
O2–2*c*–O3	89.8(3) ×2
O1–2*d*–O2	88.8(5) ×2
O1–2*d*–O3	89.4(3) ×2
O2–2*d*–O3	89.9(3) ×2
2*c*–O1–2*d*	160.6(6)
2*c*–O2–2*d*	157.7(5)
2*c*–O3–2*d*	158.0(2)

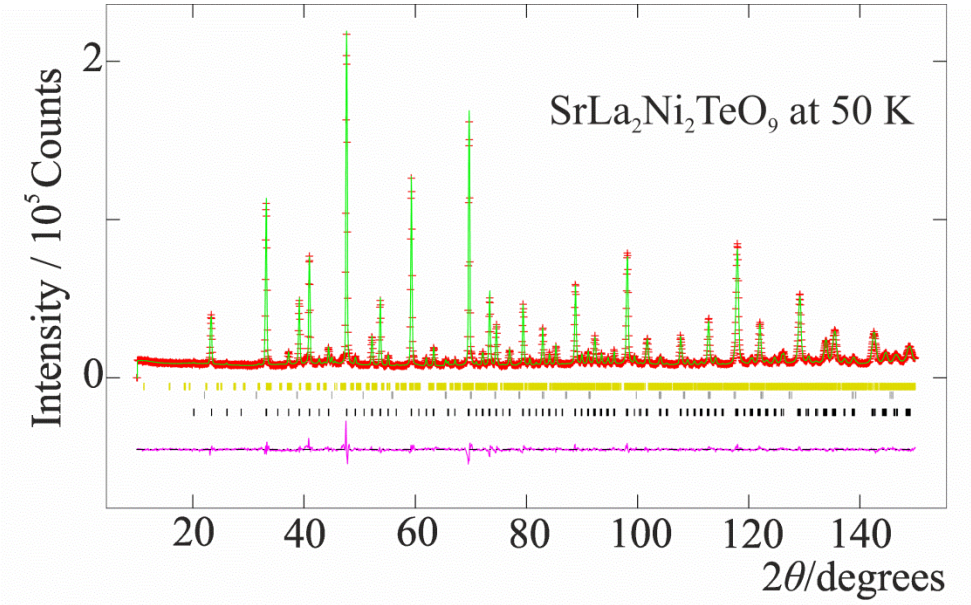


Figure S7.2. Observed (red crosses) and calculated (green line) neutron powder diffraction profiles of $SrLa_2Ni_2TeO_9$ at 50 K recorded on D2b. Underneath is a difference curve, purple in colour. The black, grey and gold vertical makers represent the Bragg reflection markers for $SrLa_2Ni_2TeO_9$, NiO and Sr_3TeO_6, respectively.

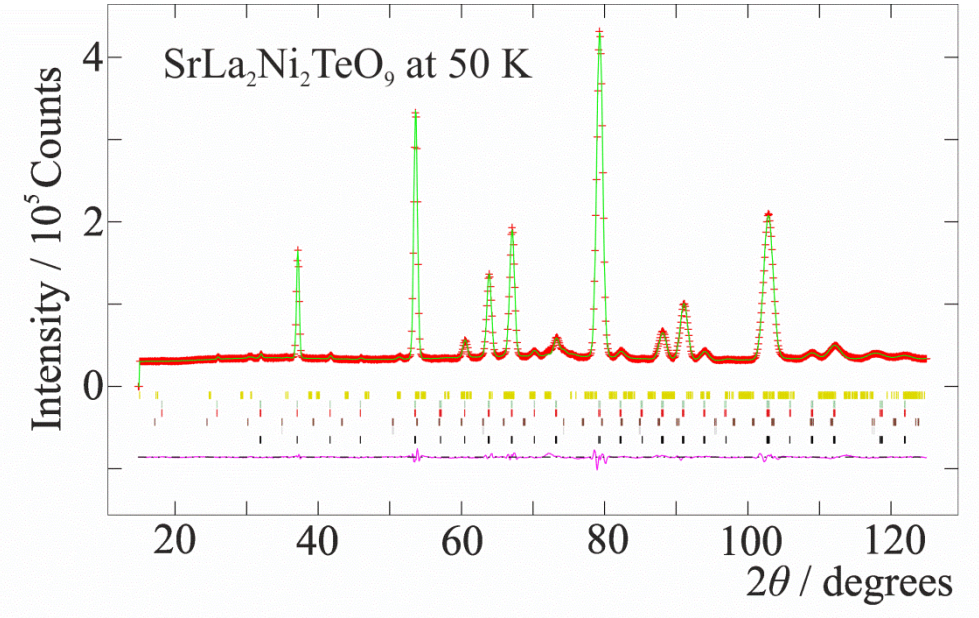


Figure S7.3. Observed (red crosses), calculated (green line) and difference (purple line) neutron powder diffraction profiles of $SrLa_2Ni_2TeO_9$ at 50 K recorded on D1b across the full measured angular range. Reflection markers for structural $SrLa_2Ni_2TeO_9$, structural NiO, magnetic NiO, G–type and C–type magnetic structures of $SrLa_2Ni_2TeO_9$ and Sr_3TeO_6 are black, grey, brown, red, light green and gold, respectively.

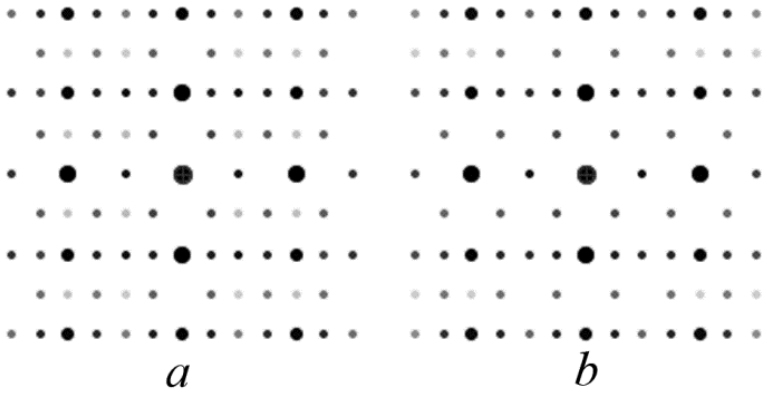


Figure S7.4. Calculated electron diffraction patterns (using JEMS software) for crystals with thickness of 50 nm and for 200 kV, using a 2–beam calculation, for (a) the model proposed in this paper and (b) the same model after removal of all oxygen atoms.

Details of the determination of the space group from electron diffraction patterns and the absence of domains with different symmetry from the HRTEM images

The reflection conditions derived from the electron diffraction patterns in the main text are *hkl*, 0*kl*, *hk*0: no conditions, *h*0*l*: *h*+*l* = 2*n*, *h*00: *h* = 2*n*, 00*l*: *l* = 2*n*.

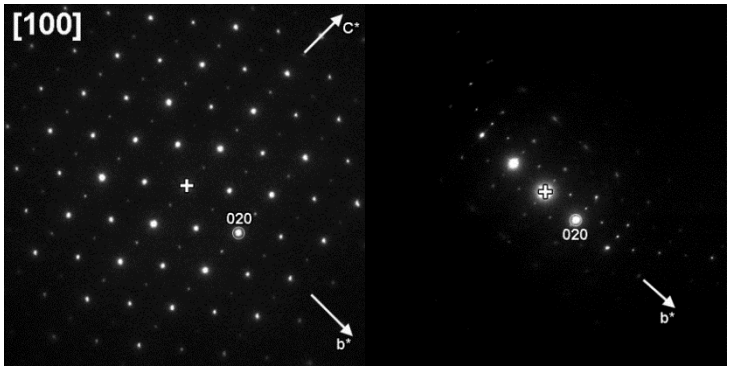


Figure S7.5. Electron diffraction pattern of $SrLa_2Ni_2TeO_9$ titled around the 0*k*0 row of reflections.

The 0*k*0:*k* = 2*n* reflection condition is proven with the tilt shown in the figures below. When tilting around the 0*k*0 row of reflections, the 0*k*0:*k* = 2*n*+1 reflections disappear when the double diffraction paths are destroyed, see Figure S7.5. As this destroys proof that this area is [100] and not [010], a pattern is shown at the right where the necessary extra 0*kl* reflections are still visible, even though this retains some double diffraction. The

0*k*0:*k* = 2*n*+1 are nevertheless barely visible on the right side pattern, with 010 and 030 effectively gone.

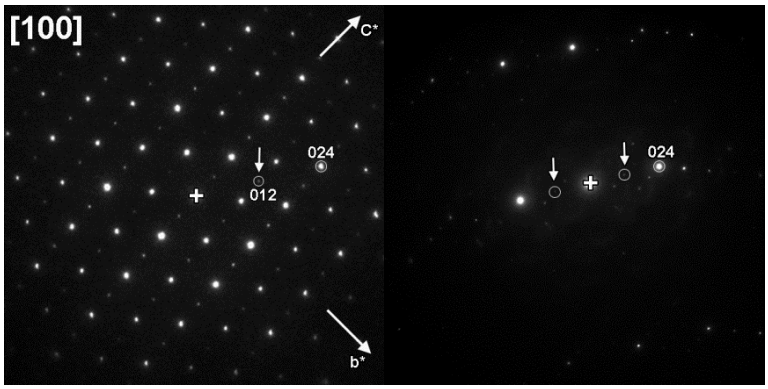


Figure S7.6. Electron diffraction pattern of $SrLa_2Ni_2TeO_9$ titled around the row of reflections 012, 024, …

One could argue that the 0*kl*:*k* = 2*n*+1, *l* = 2*n* could also be due to double diffraction, with reflection conditions 0*kl*:*k* = 2*n*, *h*0*l*:*h*+*l* = 2*n* and overlap of these patterns. However, it has been proven with a similar tilting experiment that these reflections are not due to double diffraction. In Figure S7.6, the pattern was tilted around the row of reflections 012, 024, ... and when all double diffraction paths are destroyed as in the right hand figure, the reflections 012 and 0–1–2 are still clearly present and of the same intensity or higher than the nearest surrounding reflections. This proves that the reflections 0*kl*:*k* = 2*n*+1, *l* = 2*n* are not due to double diffraction.

Therefore the complete set of reflection conditions is *hkl*, 0*kl*, *hk*0: no conditions, *h*0*l*: *h*+*l* = 2*n*, *h*00: *h* = 2*n*, 0*k*0: *k* = 2*n*, 00*l*: *l* = 2*n*. The only space group in agreement with these reflection conditions is $P2_1/n$. No other space groups in monoclinic nor other crystal classes has these reflection conditions.

Then again, electron diffraction patterns are taken from crystals as large as a few hundred nanometers. Domains of smaller size with different symmetry could be present, especially since there is inhomogeneity in the cation distribution. To test this possibility, HRTEM

was performed on several <100>$_p$ crystals. This zone was chosen to prove the absence of different symmetries, because according to the paper by Howard *et al.*[174], group theory leaves only three possible monoclinic space groups in case of cation order (disregarding other uncommon distortions lowering the symmetry even more instead of increasing it), i.e. *I*2/*m* (*C*2/*m*, 12, $a \sim b\sqrt{} \sim 2a_p$, $c = 2a_p$), *C*2/c (15, $a \sim b \sim c \sim 2a_p$) and $P2_1/n$ ($P2_1/c$, 14, $a \sim b\sqrt{} \sim 2a_p$, $c = 2a_p$). It can be concluded from the HAADF–STEM images of the <110>$_p$ zones (as the one shown in the main text) that there are no domains without cation order in the crystallites. For these three space groups a difference is present in the <100>$_p$ zones. For *I*2/*m* these show only the parent cell reflections, for *C*2/*c* one of the three <100>$_p$ zones also shows only this pattern of parent cell reflections. The other two <100>$_p$ zones of *C*2/*c* show reflections at either $h_p/2\ k_p/2\ 0$ with h_p,k_p odd or $h_pk_p/20$ with k_p odd. For $P2_1/n$ one <100>$_p$ shows reflections at $h_p/2\ k_p/2\ 0$ with h_p,k_p odd, two show reflections at $h_pk_p/20$ with k_p odd. There was no evidence in the FTs of the domains for any symmetry other than $P2_1/n$.

The HRTEM images are not included herein as this entails too many images and Fourier transforms.

Appendix 6: Supporting information for Chapter 8

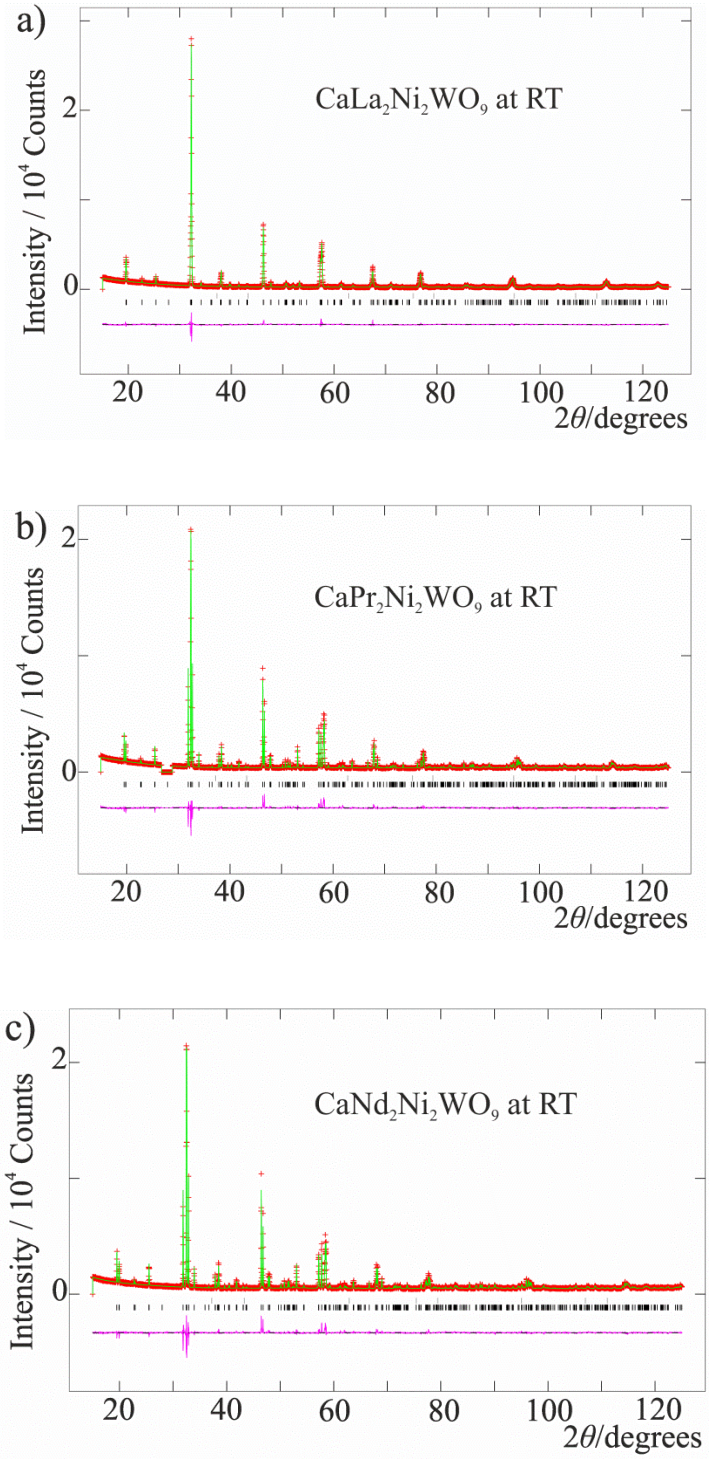


Figure S8.1. Observed (red crosses) and calculated (green line) XRPD profiles of (a) $CaLa_2Ni_2WO_9$, (b $CaPr_2Ni_2WO_9$ and (c) $CaNd_2Ni_2WO_9$ at RT. Below is a difference curve (purple). Reflection positions are marked for NiO (grey) and the principal perovskite phase (black).

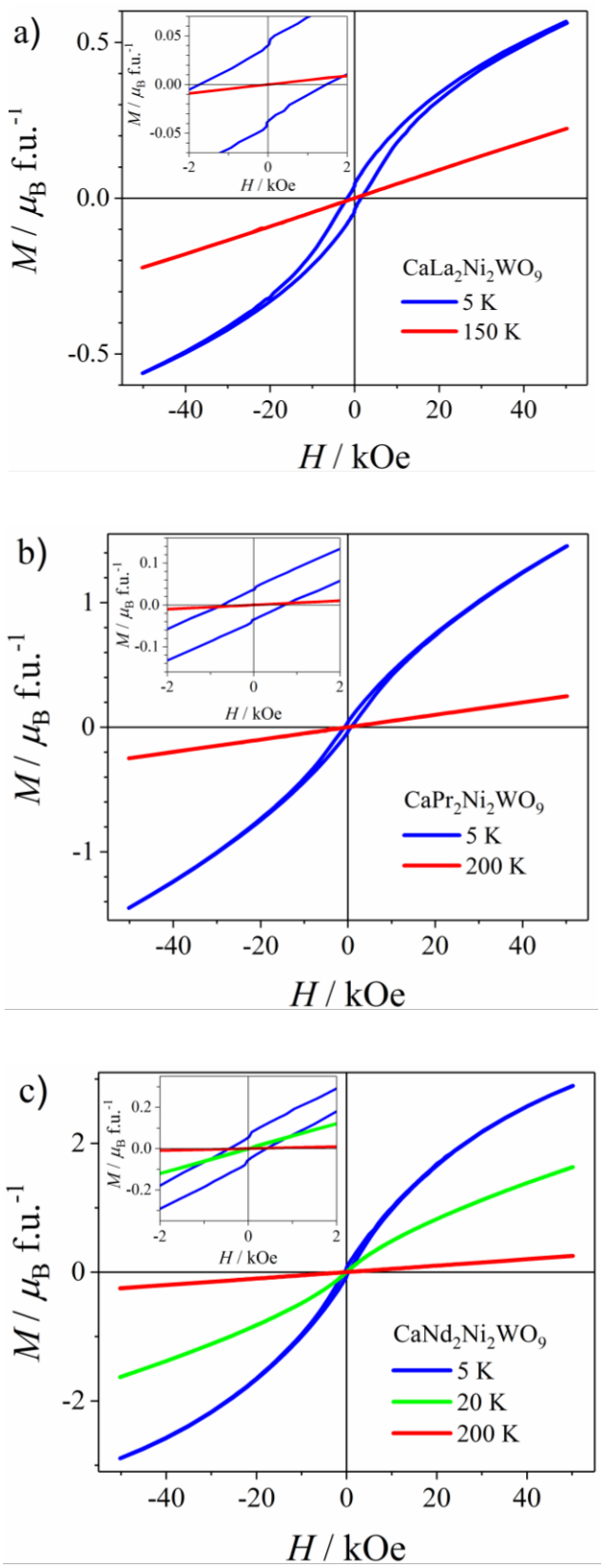
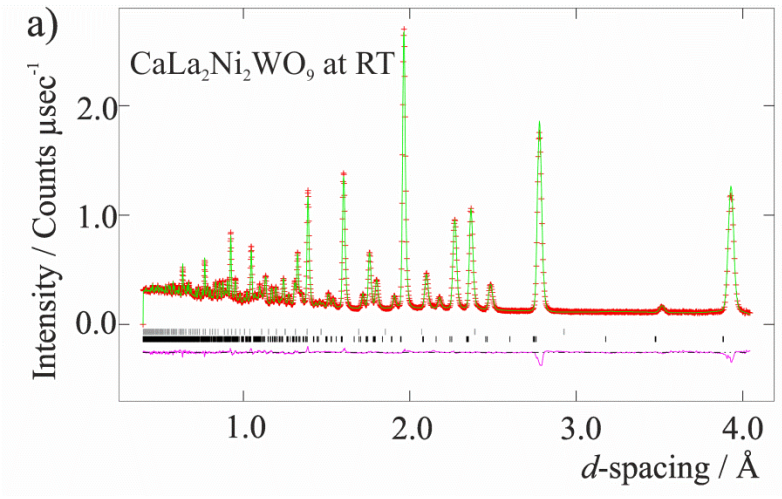
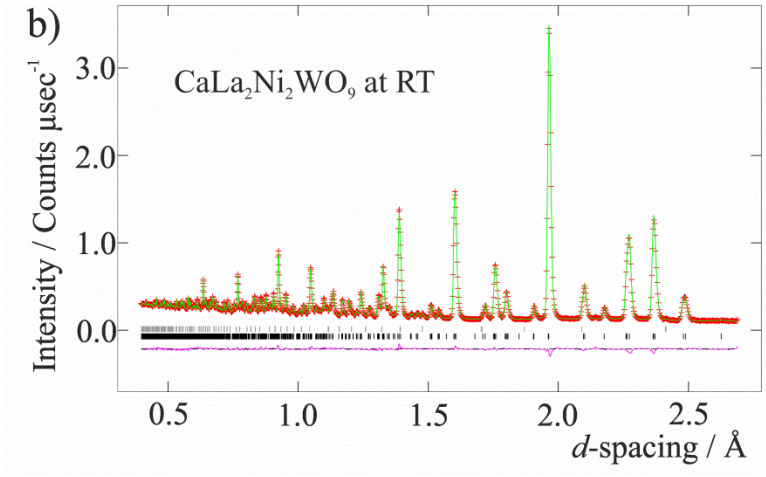


Figure S8.2. The field dependence of the magnetisation per formula unit of (a) $CaLa_2Ni_2WO_9$, (b) $CaPr_2Ni_2WO_9$ and (c) $CaNd_2Ni_2WO_9$ at selected temperatures.





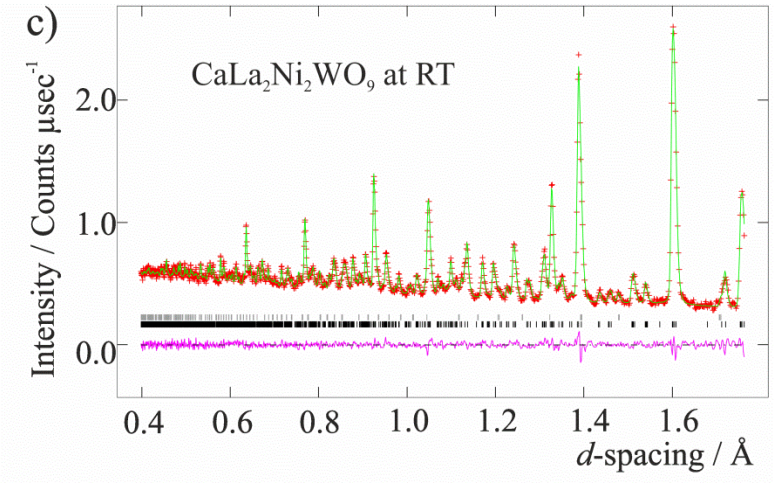


Figure S8.3. Observed (red crosses) and calculated (green line) NPD profiles of $CaLa_2Ni_2WO_9$ at RT. Below is a difference curve (purple). Reflection positions are marked for NiO (grey) and the principal phase (black). The observed patterns shown in (a), (b) and (c) were collected at 2θ = 63.62, 91.30 and 154.40 °, respectively.

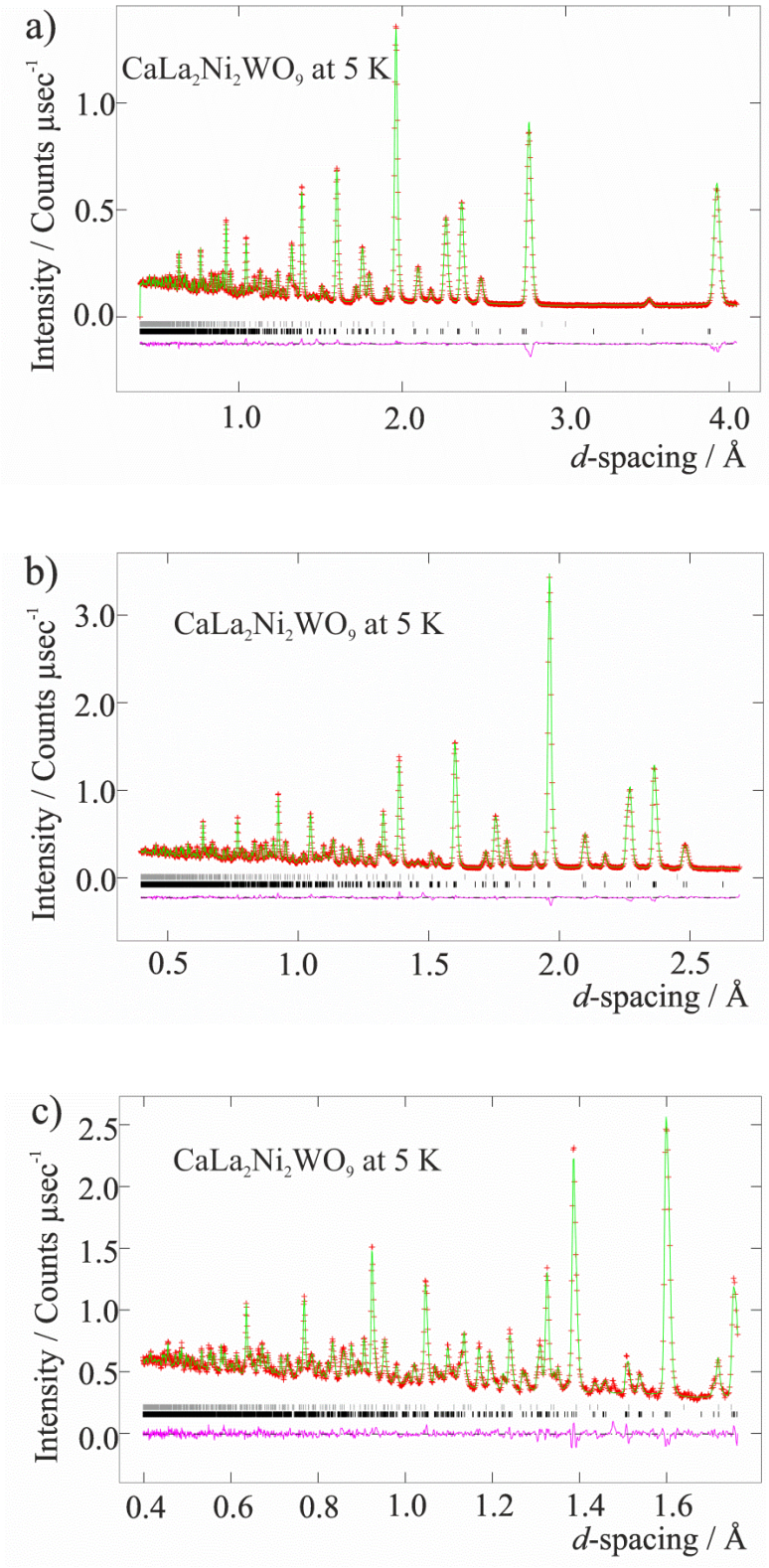
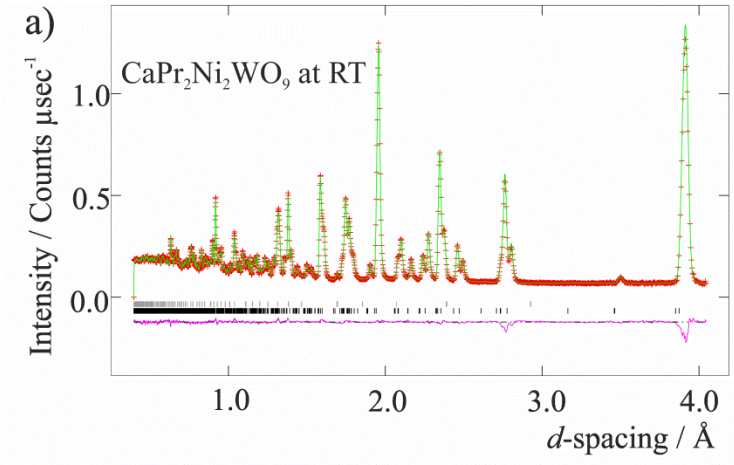
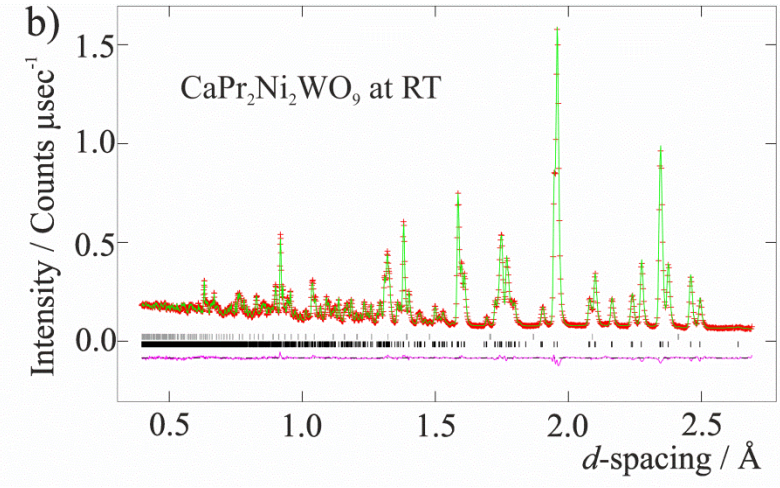


Figure S8.4. Observed (red crosses) and calculated (green line) NPD profiles of $CaLa_2Ni_2WO_9$ at 5 K. Below is a difference curve (purple). Reflection positions are marked for NiO (grey) and the principal phase (black). The observed patterns shown in (a), (b) and (c) were collected at 2θ = 63.62, 91.30 and 154.40 °, respectively.





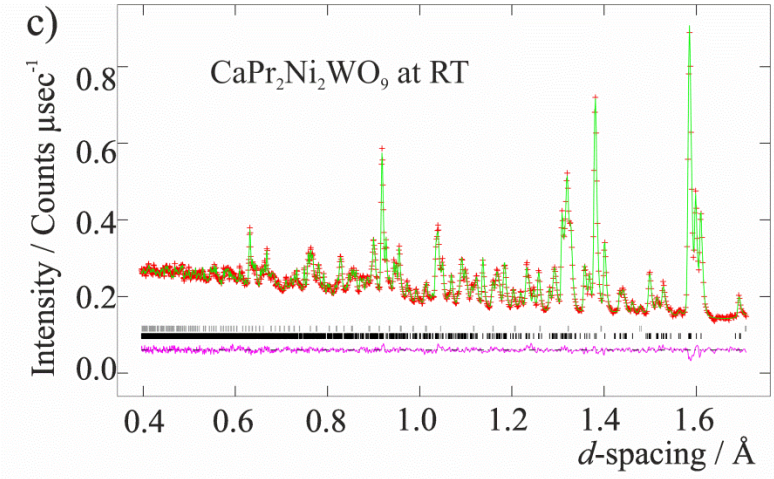
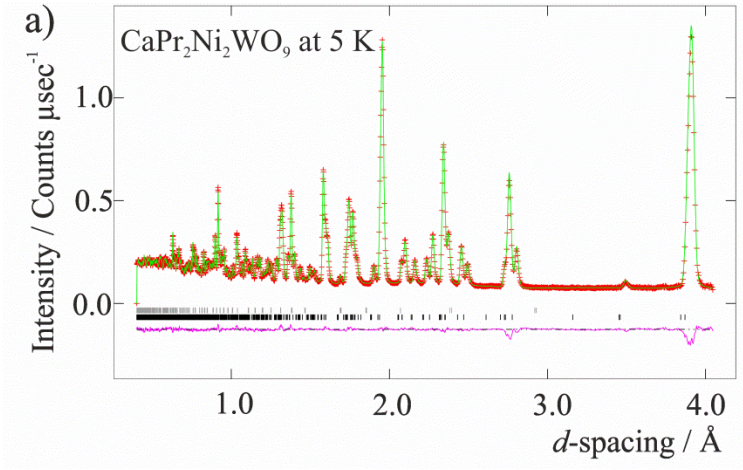
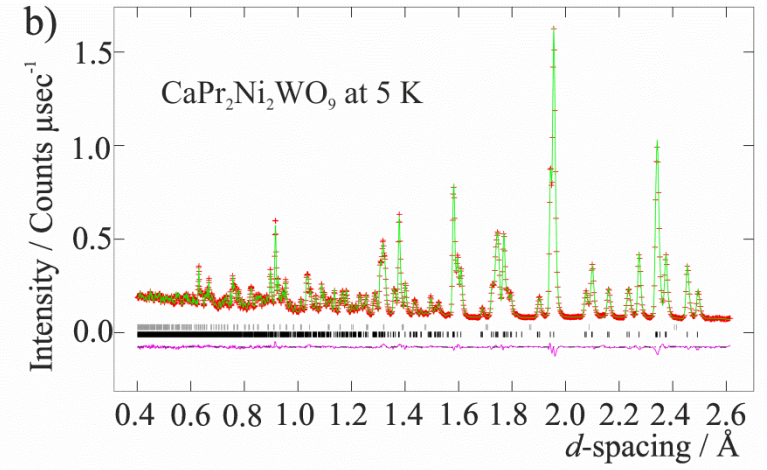


Figure S8.5. Observed (red crosses) and calculated (green line) NPD profiles of $CaPr_2Ni_2WO_9$ at RT. Below is a difference curve (purple). Reflection positions are marked for NiO (grey) and the principal phase (black). The observed patterns shown in (a), (b) and (c) were collected at 2θ = 63.62, 91.30 and 154.40 °, respectively.





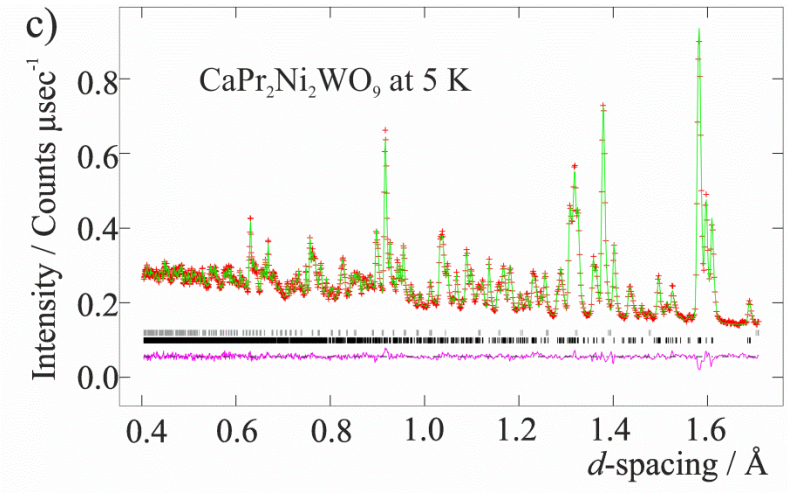


Figure S8.6. Observed (red crosses) and calculated (green line) NPD profiles of $CaPr_2Ni_2WO_9$ at 5 K. Below is a difference curve (purple). Reflection positions are marked for NiO (grey) and the principal phase (black). The observed patterns shown in (a), (b) and (c) were collected at 2θ = 63.62, 91.30 and 154.40 °, respectively.

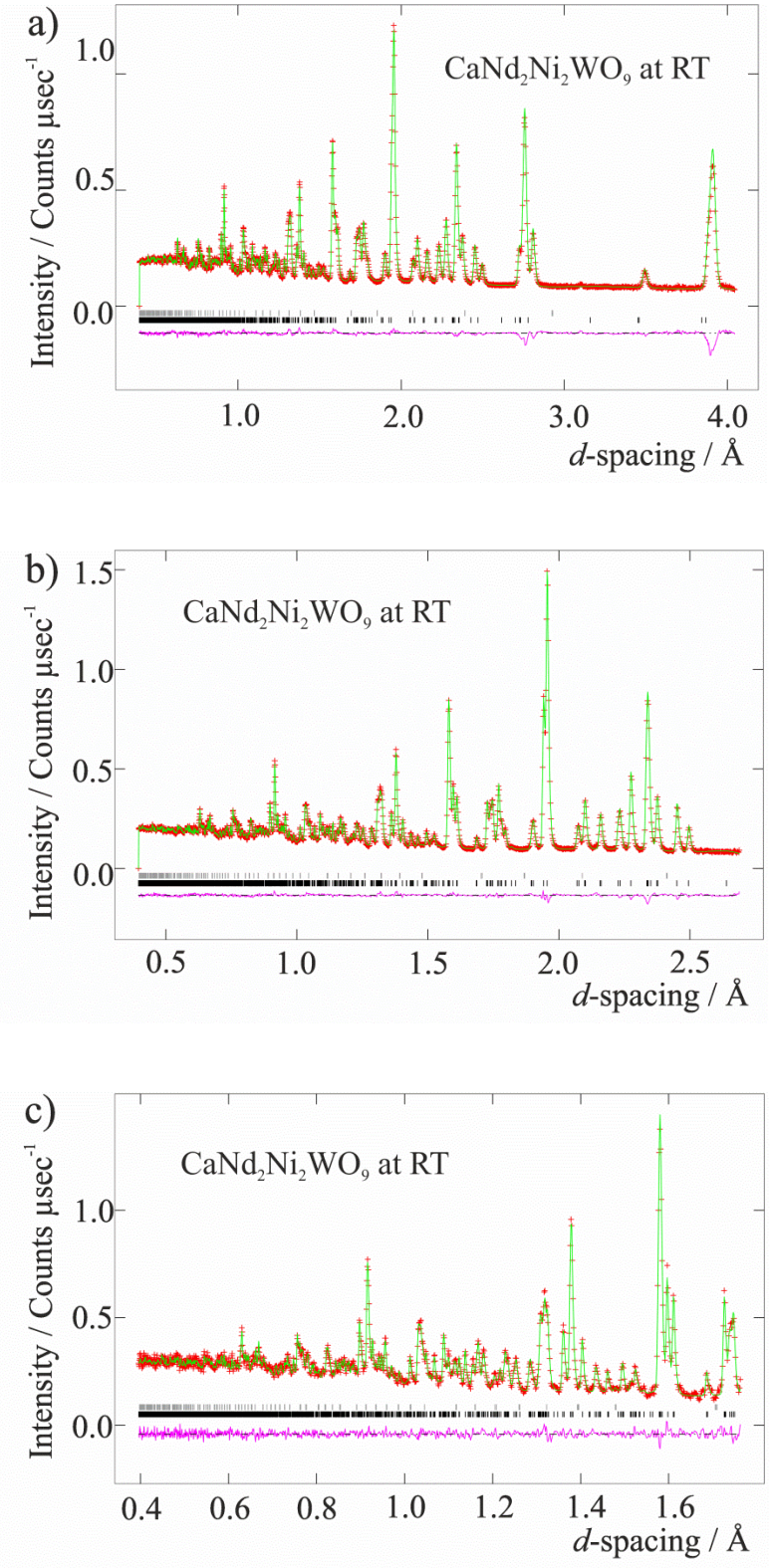


Figure S8.7. Observed (red crosses) and calculated (green line) NPD profiles of $CaNd_2Ni_2WO_9$ at RT. Below is a difference curve (purple). Reflection positions are marked for NiO (grey) and the principal phase (black). The observed patterns shown in (a), (b) and (c) were collected at 2θ = 63.62, 91.30 and 154.40 °, respectively.

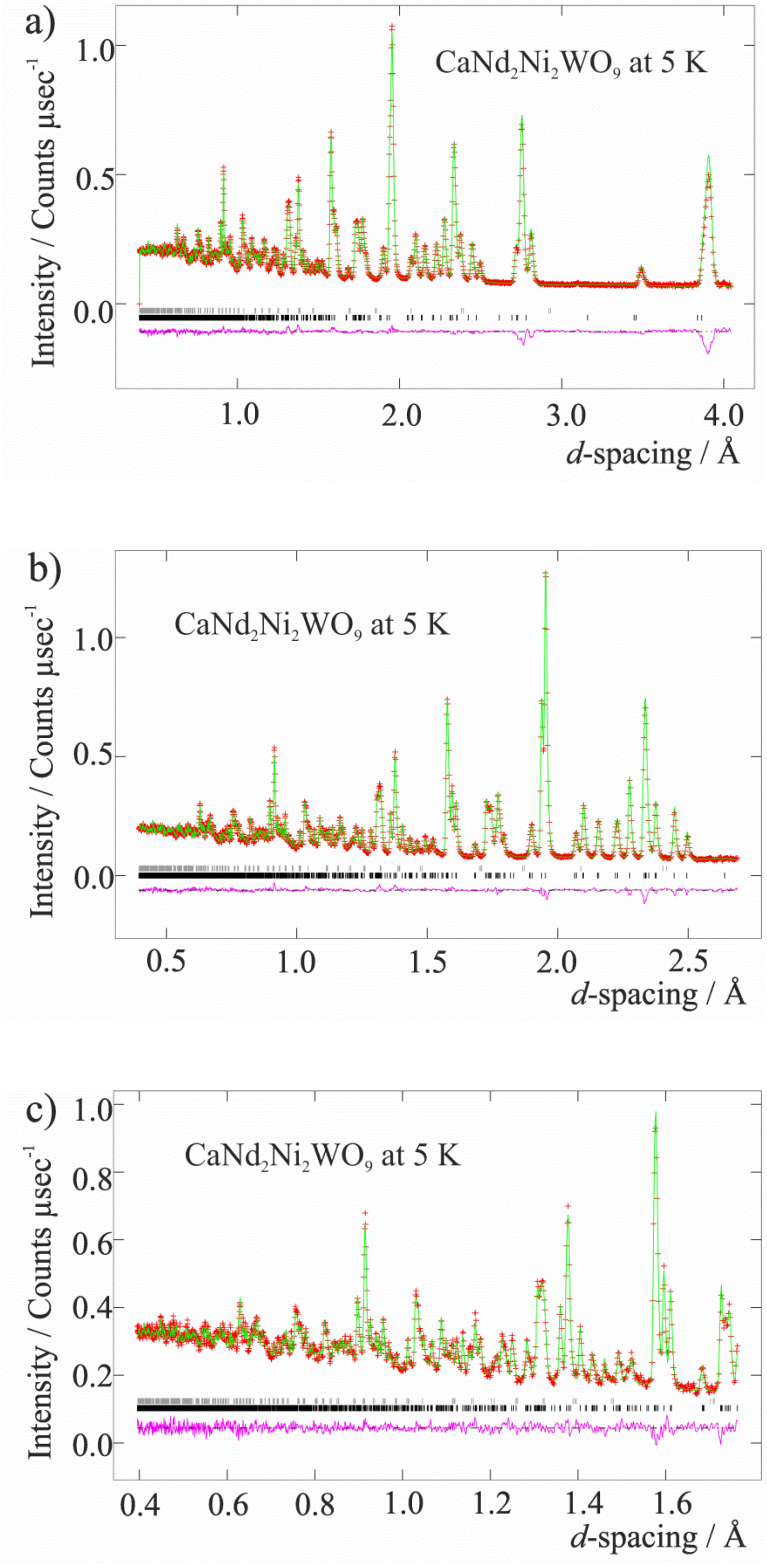
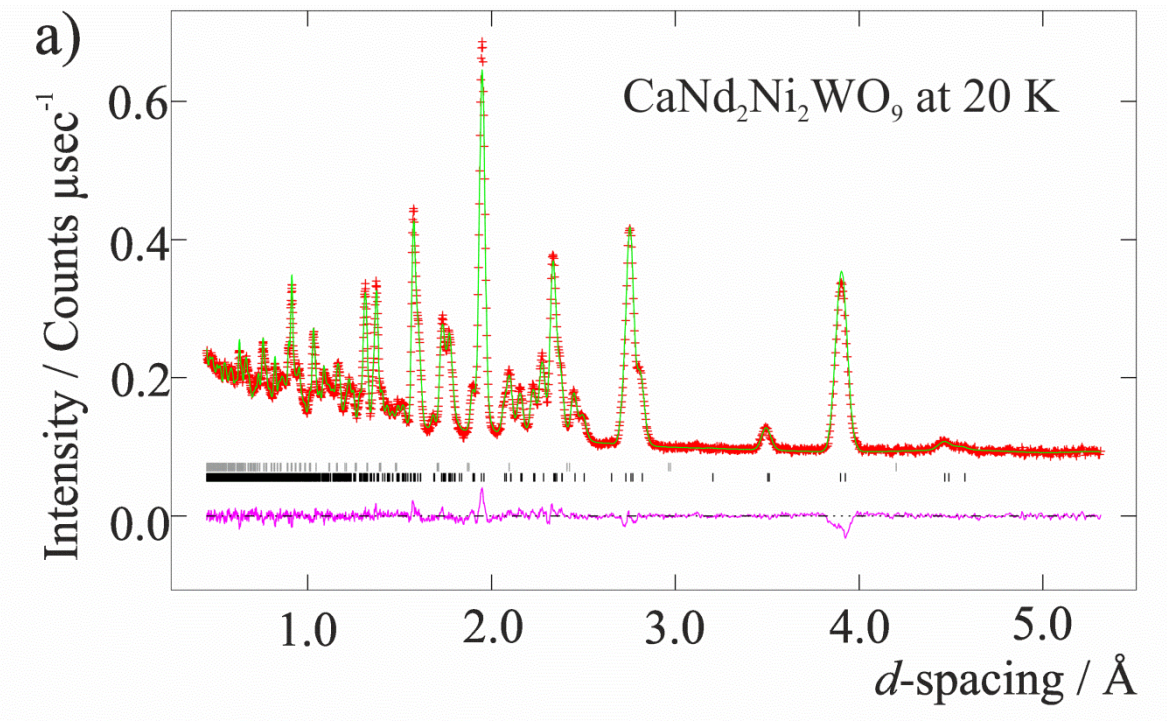
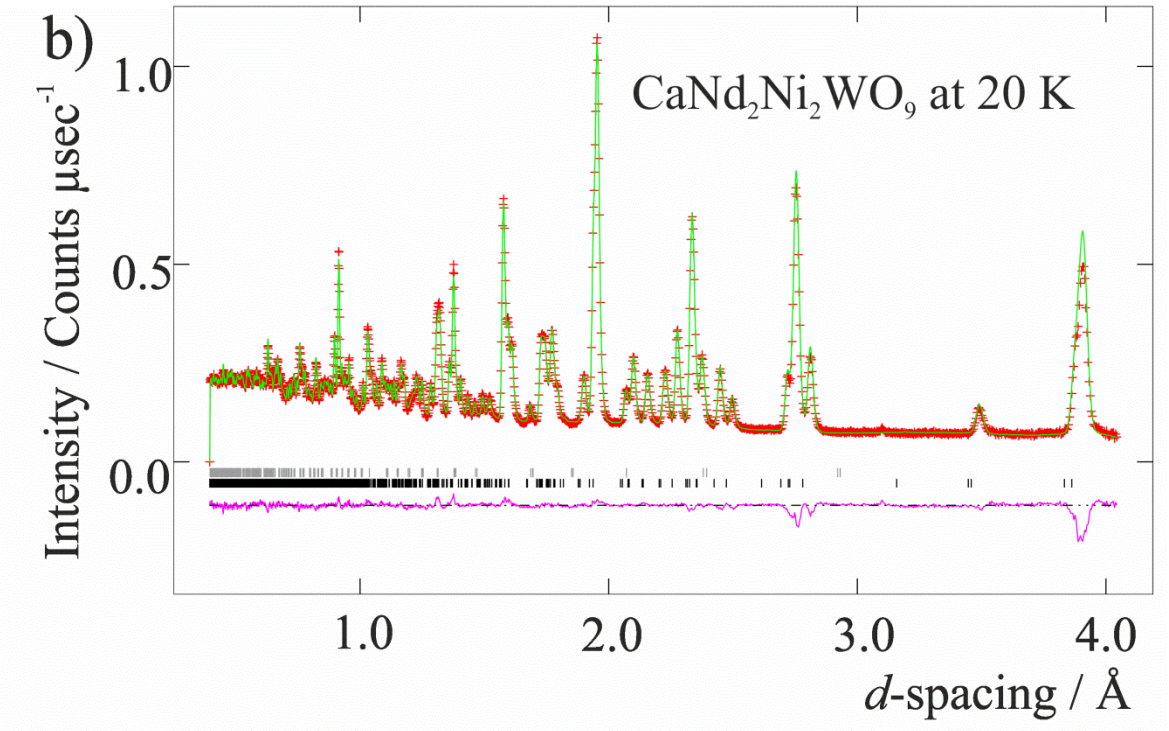


Figure S8.8. Observed (red crosses) and calculated (green line) NPD profiles of $CaNd_2Ni_2WO_9$ at 5 K. Below is a difference curve (purple). Reflection positions are marked for NiO (grey) and the principal phase (black). The observed patterns shown in (a), (b) and (c) were collected at 2θ = 63.62, 91.30 and 154.40 °, respectively.


a)
CaNd2Ni2WO9 at 20 K
Intensity / Counts μsec-1
0.0
0.2
0.4
0.6
1.0
2.0
3.0
4.0
5.0
d-spacing / Å


b)
CaNd2Ni2WO9 at 20 K
Intensity / Counts μsec-1
0.0
0.5
1.0
1.0
2.0
3.0
4.0
d-spacing / Å

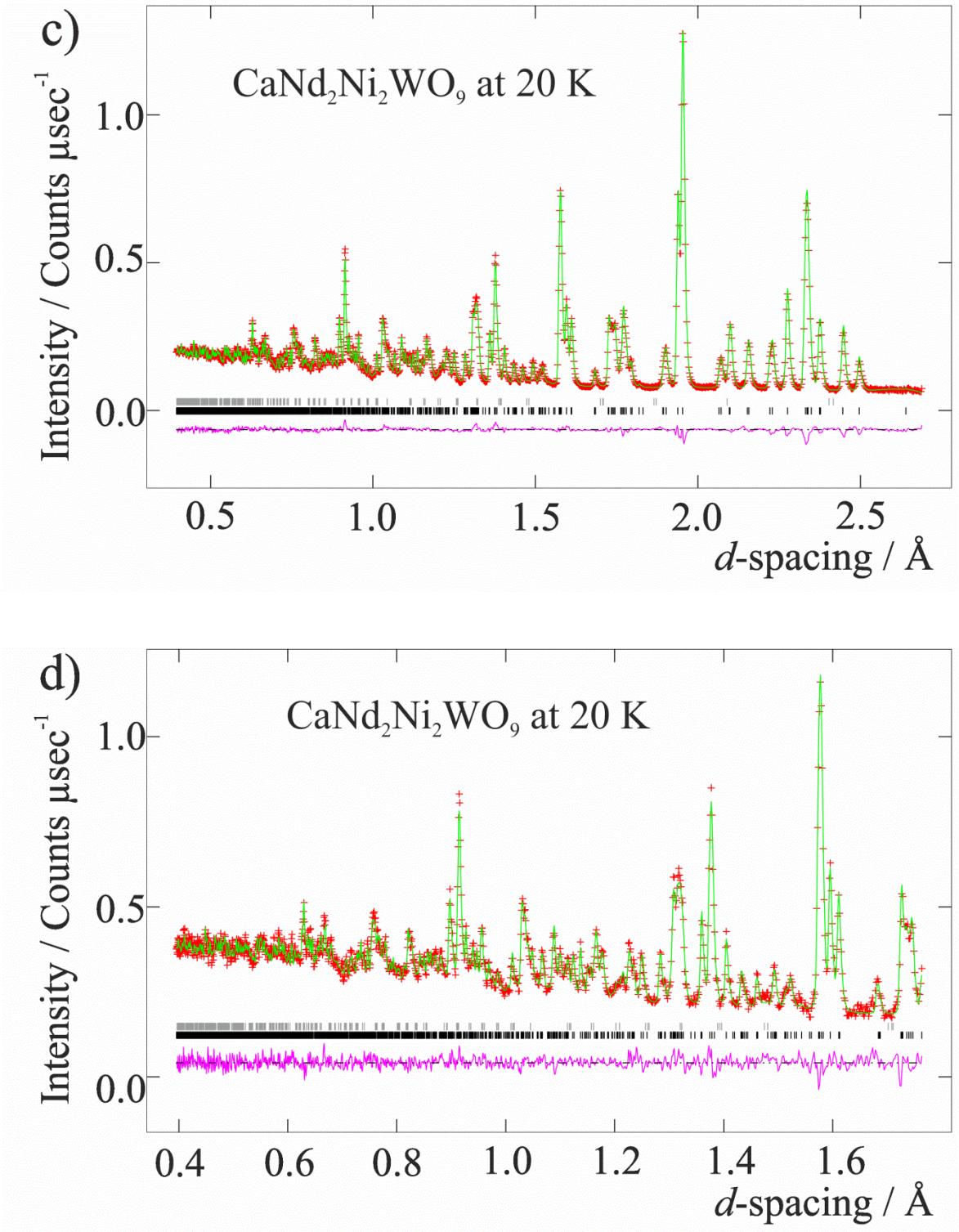


Figure S8.9. Observed (red crosses) and calculated (green line) NPD profiles of $CaNd_2Ni_2WO_9$ at 20 K. Below is a difference curve (purple). Reflection positions are marked for NiO (grey) and the principal phase (black). The observed patterns shown in (a), (b), (c) and (d) were collected at 2θ = 34.96, 63.62, 91.30 and 154.40 °, respectively.

Table S8.1. Structural parameters of $CaNd_2Ni_2WO_9$ at 20 K (Space group $P2_1/n$).

		20 K
a / Å		5.4310(9)
b / Å		5.6136(9)
c / Å		7.7469(12)
β / °		90.228(2)
V / Å^3		236.18(11)
Total $R_{wp}\|_{NPD}$ / %		2.88
χ^2		2.663
Ca/Nd	x	0.4879(2)
4*e* (*x y z*)	y	0.4444(1)
	z	0.2538(3)
	U_{ISO} / Å^2	0.0110(2)
	Ca occupancy	0.3333
	Nd occupancy	0.6667
Ni/W1	U_{ISO} / Å^2	0.0006(3)
2*c* (0 ½ 0)	Ni occupancy	0.971
	W occupancy	0.029
Ni/W2	U_{ISO} / Å^2	0.0009(4)
2*d* (½ 0 0)	Ni occupancy	0.362
	W occupancy	W: 0.638
O1	x	0.7927(3)
4*e* (*x y z*)	y	0.8055(3)
	z	–0.0430(2)
	U_{ISO} / Å^2	0.0033(3)
O2	x	0.6912(3)
4*e* (*x y z*)	y	0.2902(3)
	z	–0.0487(2)
	U_{ISO} / Å^2	0.0029(3)
O3	x	0.5878(2)
4*e* (*x y z*)	y	0.0257(2)
	z	0.2436(3)
	U_{ISO} / Å^2	0.0028(2)

Table S8.2. Selected bond lengths (Å) and angles (°) in $CaNd_2Ni_2WO_9$ at 20 K.

	20 K
Ca/Nd–O1	2.650(3)
Ca/Nd–O1	2.634(3)
Ca/Nd–O1	2.364(3)
Ca/Nd–O2	2.735(3)
Ca/Nd–O2	2.383(3)
Ca/Nd–O2	2.587(3)
Ca/Nd–O3	2.414(1)
Ca/Nd–O3	2.349(2)
2*c*–O1	2.078(2)×2
2*c*–O2	2.083(2)×2
2*c*–O3	2.049(2)×2
2*d*–O1	1.958(2)×2
2*d*–O2	1.969(2)×2
2*d*–O3	1.950(2)×2
O1–2*c*–O2	89.9(1)×2
O1–2*c*–O3	88.2(1)×2
O2–2*c*–O3	88.6(1)×2
O1–2*d*–O2	90.0(1)×2
O1–2*d*–O3	89.4(1)×2
O2–2*d*–O3	89.8(1)×2
2*c*–O1–2*d*	150.8(1)
2*c*–O2–2*d*	149.1(1)
2*c*–O3–2*d*	151.1(1)